A biomarker and isotope study of Paleoproterozoic ecosystems in the northern Australian McArthur Basin

Galina Vinnichenko

March 2021

A thesis submitted for the degree of Doctor of Philosophy of
The Australian National University

Declaration

This thesis contains no material which has been accepted for the award of any other degree or diploma in any university. To the best of the author's knowledge, it contains no material previously published or written by another person, except where due reference is made in the text.

Galina Vinnichenko

March 2021

Acknowledgements

This research is supported by an Australian Government Research Training Program (RTP) Scholarship and an RSES top-up Ringwood Scholarship. I greatly appreciate their financial support.

I am sincerely grateful to many people who supported me during my PhD life. Firstly, I would like to thank my supervisor Jochen Brocks for introducing me to the world of Precambrian biomarkers and guiding me through these four years with enthusiasm, motivation and patience. I also thank my supervisory panel – Amber Jarrett, Emmanuelle Grosjean and Leanne Armand – for their support and involvement with the project. I am extremely grateful to Janet Hope for technical assistance and for teaching me everything I know about the lab work.

Further, I want to thank the fantastic Biomarker team at RSES – Ilya Bobrovskiy, Lennart van Maldegem, Tharika Liyanage, Jordan Kinsley, Caleb Bishop, Claire Patterson, Neil Williams and Clinton Foster. Your moral support, helpful discussions and inspiration are much appreciated. Additionally, a special thank goes to Ilya, who originally suggested changing my life completely and starting a PhD in Australia.

I would like to acknowledge my collaborators for their help with various analyses and discussions – Marcus Kunzmann, Michael Kipp, Brooke Johnson, Ruslan Khamidullin, Tony Hall, Stewart Fallon, Ian Long, Jacob Sohn and Junhong Chen.

Additionally, I want to highlight many amazing RSES friends for their support during all the ups and downs, a warm atmosphere, unforgettable road trips and other activities: Anya Makushkina, Laura Miller, Monika Misztela, Yamila Cajal Contreas, Thuany Costa de

Lima, Buse Turunctur, Carlos Carrasco Godoy, Shub Agrawal, Matthias Scheiter, Bei Chen, Ziyi Zhu, Chris Mathews, Thomas Duvernay and many more.

I am also grateful to my old friends: Sasha, Jenya, Nelya, Dasha and Tanya. Girls, thank you for always being around despite the huge distances between us.

Finally, I want to thank my family for all their love, motivation, and confidence in me. And I am really grateful to my partner, Lennart, for his continuous support, calmness and enthusiasm.

Abstract

Biomarkers represent an important source of information about ancient environments, especially in the Paleoproterozoic, where the body fossil record is comparatively scarce. The northern Australian McArthur Basin contains currently the oldest known indigenous biomarkers in the 1.64 Ga Barney Creek Formation (Fm). Based on published biomarker data, the oceans were almost exclusively inhabited by prokaryotic microorganisms, while eukaryotes with complex cell structure played an insignificant role. However, newly recognized protosteroids in the Barney Creek Fm may record early stages in eukaryotic evolution. This thesis, which consists of four linked research topics, investigates biological community signatures and paleo-environments in a transect through the Barney Creek Fm succession and circumjacent units; explores the preservation of organic matter associated with the Paleoproterozoic McArthur River zinc-lead ore deposit; and describes the influence of thermal maturity on compound-specific carbon and hydrogen isotopic composition of lipids in the Barney Creek Fm. Additionally, this research presents the discovery of trimethyl aryl isoprenoids from carbonaceous shales of the 1.73 Ga Wollogorang Fm in the McArthur Basin, revealing the activity of phototrophic bacteria and extending the biomarker record back in time by ~90 million years.

Table of Contents

Chapter 1

Introduction

1.1 Evolution of Life during the mid-Proterozoic (1.8–0.8 Ga)

The Proterozoic Eon (2.5–0.54 Ga) records the transition from an Archean anoxic world (Poulton & Canfield, 2011) to a Phanerozoic modern Earth with a mainly oxygenated surface (Holland, 2006). According to Holland (2006), the mid-Proterozoic (1.8–0.8 Ga) represents the 'boring billion' (Figure 1.1), due to the absence of remarkable changes in ocean and atmosphere composition, lack of glaciation events and banded iron formations (Anbar & Knoll, 2002; Holland, 2006). However, in reality, some important changes occurred during this period regarding the evolution of eukaryotic life.

1.1.1 The mid-Proterozoic oceans and atmosphere

The first significant increase in the oxygen concentrations in the atmosphere and surface oceans occurred in the early Proterozoic (around 2.3–2.4 Ga). This complex, multi-stage process is known as the Great Oxidation Event (GOE) (Holland 2002, 2006). The GOE is recorded based on geological and geochemical proxies, such as the disappearance of redox-sensitive detrital minerals, a decrease in the abundance of iron formations due to oxidation and the formation of red beds and oxic paleosols (Holland, 2006; Knoll & Nowak, 2017).

However, despite the oxygenation, the Proterozoic ocean remained oxygen depleted compared to the modern state (Planavsky et al., 2014). The 'Canfield Ocean' model (Canfield, 1998) introduced the concept of a globally euxinic ocean with an oxygenated surface layer and sulphidic deeper waters in the mid-Proterozoic. Later, this model was modified to a dominant ferruginous deep-water ocean state with some areas experiencing occasional sulphidic conditions (Johnston et al., 2010; Planavsky et al., 2011; Poulton & Canfield, 2011). A study by Poulton et al. (2010) suggests that euxinic conditions might have been present in continental margin and slope settings during the mid-Proterozoic.

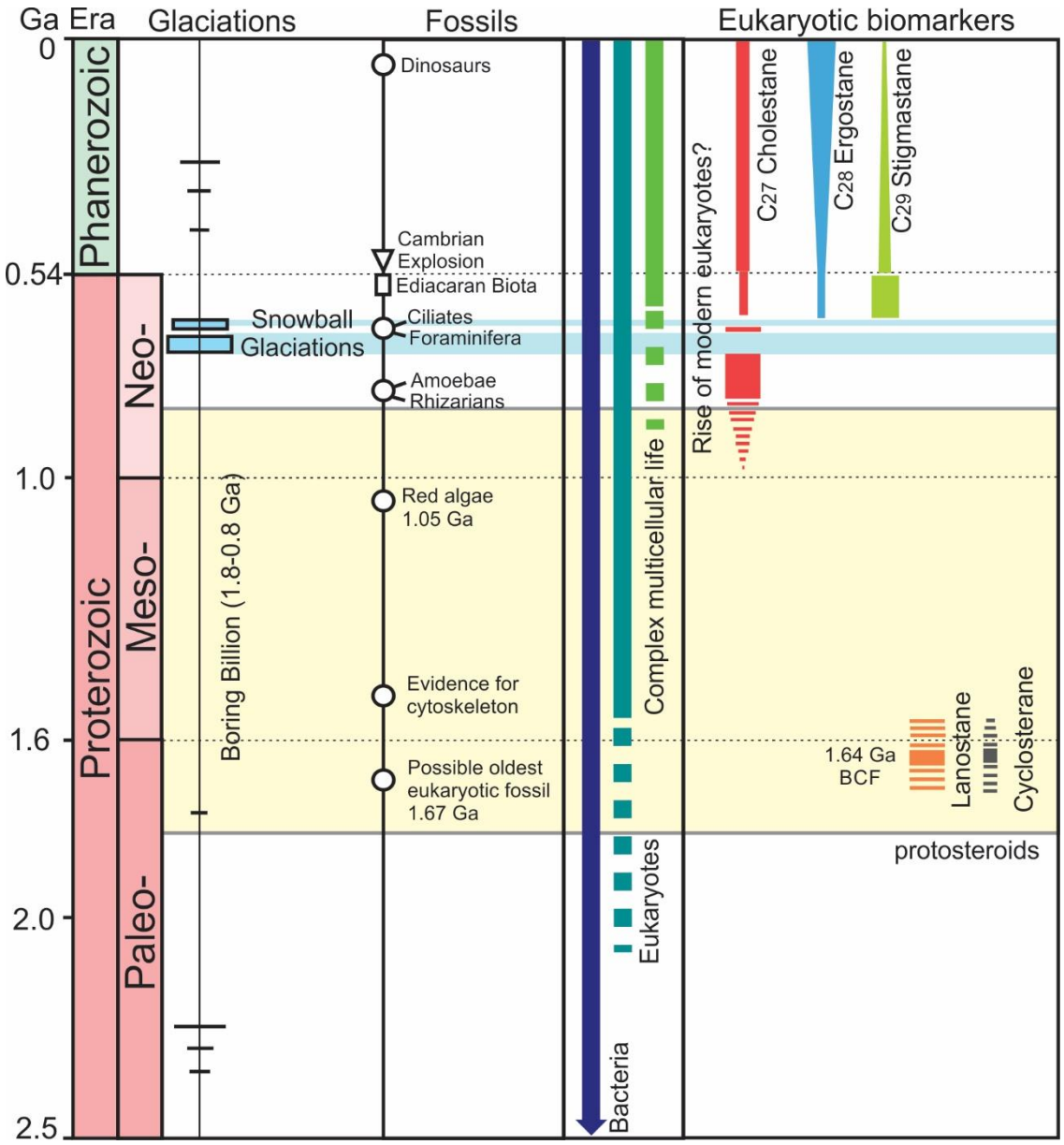

Figure 1.1. The early eukaryotic evolution based on fossils and biomarkers in the context of Earth history. Bacteria exist at least from ~3.4 Ga (Schopf, 1993), eukaryotes emerge in the Paleoproterozoic (Knoll et al., 2006; Lamb et al., 2009), and complex multicellular life is first observed in the Neoproterozoic (Knoll, 2011; Porter & Knoll, 2000). There is a ~0.8 Ga gap between the oldest eukaryotic microfossil (1.67 Ga) and the oldest typical eukaryotic sterane biomarkers (0.8 Ga). However, Nettersheim (2017) detected primitive sterane molecules (protosteranes) in the 1.64 Ga Barney Creek Formation (BCF). The producers of protosteranes are unknown, either eukaryotes or bacteria. The fossil record is reproduced from Figure 1 in Brocks et al. (2017).

1.1.2 Eukaryotic life during the mid-Proterozoic, sterol biosynthesis and biomarkers

Life on Earth is divided into three domains: Archaea, Bacteria and Eukarya (Woese et al., 1990). Bacteria and Archaea are represented by simple prokaryotic cells with circular DNA that floats freely within the cell, whereas eukaryotes are more complex. Eukaryotic cells possess the DNA-containing nucleus, which is surrounded by a double membrane (Embley & Martin, 2006). The domain Eukarya includes plants, fungi and animals, but also a vast diversity of single celled protists and algae.

According to the conventional view, the mid-Proterozoic was dominated by bacteria, while the far more complex, nucleated eukaryotic cells played an insignificant role in ancient ecosystems (Anbar & Knoll, 2002). The question is whether eukaryotes were actually rare during the 'boring billion' or were simply not preserved as body fossils, because early life forms were characterized by soft cells.

Body fossils are rare in the Proterozoic, and the fossil record is dominated by acritarchs – simple organic-walled microfossils of unknown biological origin (Butterfield & Smith, 2015; Huntley et al., 2006). The oldest microfossils of probable eukaryotic origin were found in the 1.673–1.625 Ga old Changzhougou Formation, China (Knoll & Nowak, 2017) (Figure 1.1). However, the oldest preserved fossil reliably assigned to a Crown group eukaryote taxon is a red alga (Butterfield, 2015) from 1.05 Ga carbonates in Arctic Canada (Gibson et al., 2017). Crown Group eukaryotes comprise all living descendants of the last eukaryote common ancestor (LECA) (Penny et al., 2014). Due to an absence of diagnostic characters, some scientists argue that a modest diversity of protists older than the red alga from Arctic Canada could represent Stem Group eukaryotes, which form the trunk and deep branches of the evolutionary tree but did not leave a single living descendant (Knoll, 2014). Nevertheless, phylogenetic logic and

molecular clock calculations suggest that eukaryotes must have evolved long before the first plant and animal fossils emerged (Knoll, 2014) (Figure 1.1).

A major metabolic pathway nearly specific to eukaryotes is the synthesis of sterols. Sterols represent important building blocks in the membranes of complex cells where they regulate membrane fluidity and permeability, permitting adaptation to extreme cold and extreme heat. Since the eukaryotic metabolic pathway is associated with molecular oxygen, the evolution of complex life depends upon the availability of free oxygen (Waldbauer et al., 2011). However, atmospheric oxygen levels in the mid-Proterozoic probably were as low as 0.1% of present atmospheric levels (Planavsky et al., 2014). Therefore, eukaryotic evolution in the mid-Proterozoic may be related to microbial mats inhabited by oxygenic photosynthesizers (Knoll, 2014), as they could produce a significant fraction of oxygen locally within mats.

In general, the fossil record is not sufficient to reconstruct past environments in the Proterozoic. If body fossils are scarce or absent in sediments, hydrocarbon biomarkers can be useful for the reconstruction of ancient ecosystems, particularly in the pre-Ediacaran (>635 Ma) when marine basins were almost exclusively inhabited by microorganisms. Biomarkers are hydrocarbon skeletons, formed due to the defunctionalisation of organic molecules in diagenesis. These molecular fossils are extremely stable and can be preserved in sedimentary rocks. Biomarkers with high taxonomic specificity are the most valuable for paleo-environmental studies (Brocks & Summons, 2005). Molecules with more diverse biological sources might be helpful in screening of changes in ecosystems and environments (Peters et al., 2005). Some biomarkers are used as proxies for redox conditions in the water column and sediments (Brocks & Pearson, 2005; Didyk et al., 1978). Hopanes, the molecular fossils of hopanepolyols, are typical bacterial biomarkers. The most important eukaryotic

biomarkers are the trifecta steranes (cholestane, ergostane and stigmastane), the hydrocarbon fossils of sterols (Figure 1.1). Cholesterol (C_{27}) is one of the most important sterols in animals. Terrestrial fungi mostly produce ergosterol (C_{28}) and plants predominantly produce stigmasterol (C_{29}). Sterol biosynthesis is summarised in Figure 1.2.

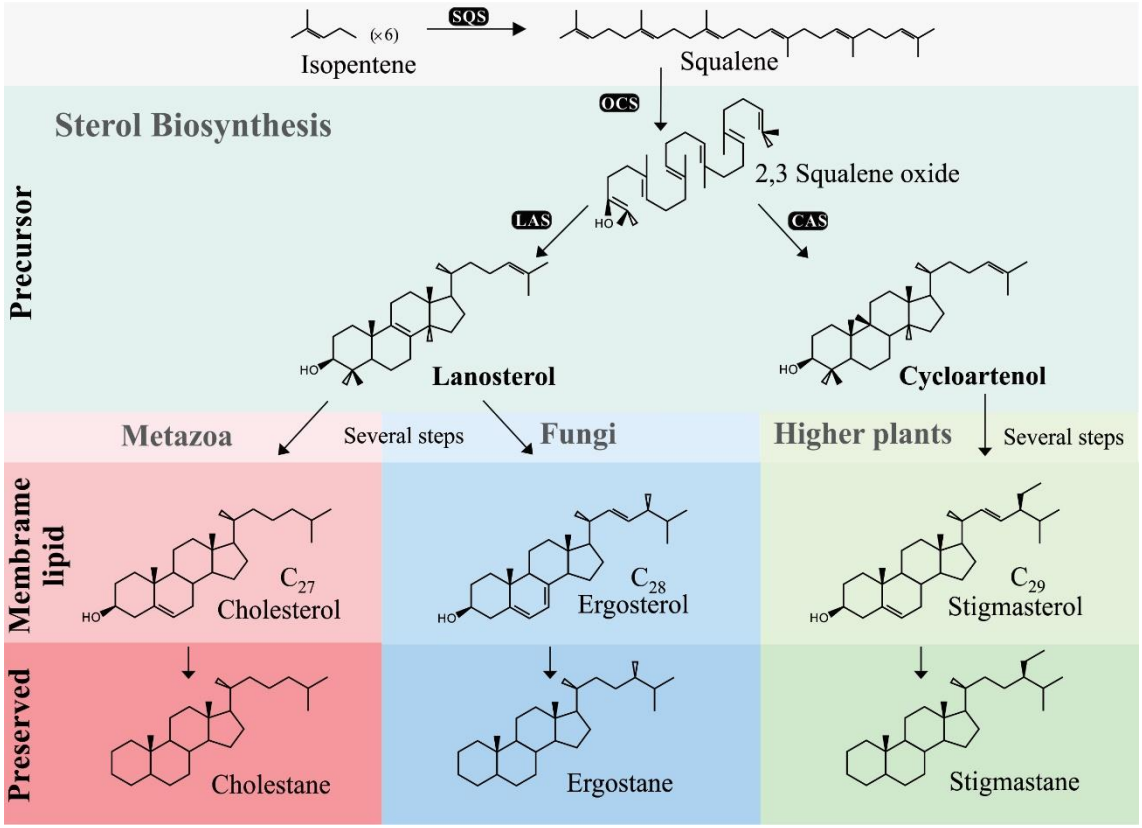

Figure 1.2. Generalised sterol biosynthesis (kindly provided by Lennart van Maldegem).

The acyclic C_{30} isoprenoid oxidosqualene is cyclised to either lanosterol or cycloartenol. From these most primitive 'true steroids' (Nes, 2011) all other steroids are biosynthesised by enzymatic modifications, such as oxidative demethylations and desaturations, that result in the terminal sterol product (Figure 1.2). Most extant eukaryotes employ either the lanosterol (e.g., animals and fungi) or cycloartenol (e.g., plants) route of sterol synthesis.

The Nobel Prize winner Konrad Bloch hypothesised that the sterol biosynthetic pathway parallels sterol evolution and that each of the biosynthetic intermediates could represent a functional end-product at some stage, an improvement over its precursor (Bloch, 1994). In 2012, a study by Dupont et al. suggested a first step towards testing the Bloch's Hypothesis by demonstrating that progression in the ergosterol biosynthetic pathway parallels an improvement in dehydration resistance in fungi. Following Bloch's hypothesis, early eukaryotes may only have produced the initial sterol products lanosterol or cycloartenol. The addition of each enzymatic step must have been an adaptation to new evolutionary pressures and in theory this sterol evolution should be recorded in the ancient rock record.

The organic geochemical laboratory at RSES has investigated the geological record of steranes from 1.6 to 0.5 Ga and found that the sterane trifecta disappears in rocks older than 0.8 Ga (Figure 1.1). Instead, primordial steranes (lanostane and unknown compounds, which may be derived from cycloartane), which are the product of a primitive, abbreviated biosynthetic pathway, were found (Nettersheim, 2017). Proto-steroid producers may belong to Stem Group eukaryotes or bacteria, as a limited number of bacteria can synthesize simple sterols (Lee et al., 2018; Pearson et al., 2003; Wei et al., 2016). However, there are no known bacteria that can methylate the side chain in the sterol skeletons and therefore more complex steranes can be attributed to eukaryotic biomarkers (Knoll, 2014).

The discovery of protosteranes in mid-Proterozoic rocks offers a possibility to test the hypothesis that primordial Stem Group eukaryotes were abundant in mid-Proterozoic environments. In the current thesis, I will try to answer the question of the origin of proto-steroids and will investigate the type of environments in which their producers lived.

1.2 Specific biomarker compounds for the current thesis

1.2.1 Lanostane and cyclosterane

Lanostane

Nettersheim (2017, chapter 9) detected two peak doublets (**1** to **4**) in Barney Creek Fm samples in the MRM *m/z* 414>259 transition (Figure 1.3 a). These C_{30} compounds have a lanostane-like fragmentation with M^+ 414 and prominent fragments of *m/z* 259, 190 and 274 (Figure 1.4). Nettersheim (2017) determined that peak **4** shows the same mass spectrum and elution time as 8*β*(H),9*α*(H)-lanostane and peaks **1** to **3** represent lanostane-like isomers. According to pyrolysis experiments (Nettersheim 2017), the biological precursor for these molecules with lanostane-type fragmentation (**1–4**) could be either lanosterol or cycloartenol. In the current study, I designate the sum of the concentrations of molecules 1 to 4 as lanostane compounds (LA).

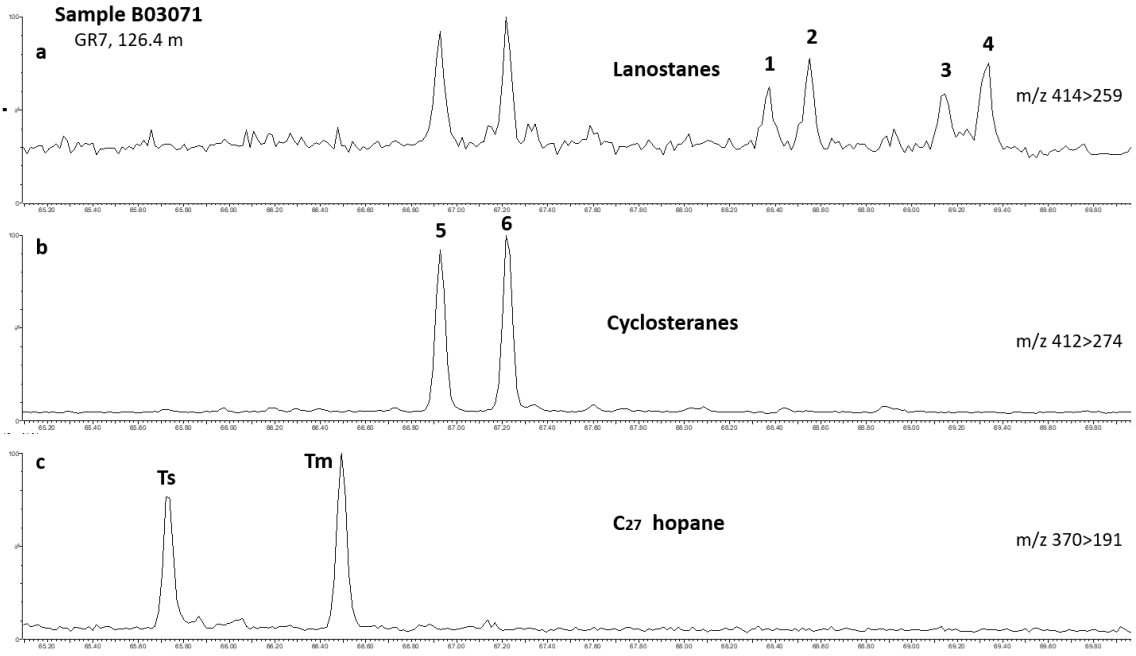

Figure 1.3. MRM transitions for the sample B03071 from 126.4 m depth in drill core GR7. a) *m/z* 414>259, peak **4** is 8β(H),9α(H)-lanostane and peaks **1–3** are C_{30} lanostane-type isomers; b) *m/z* 412>274, peaks **5** and **6** represent doublet of unknown C_{30} triterpenoid, probably derived from cycloartenol; c) *m/z* 370>191 with C_{27} hopanes.

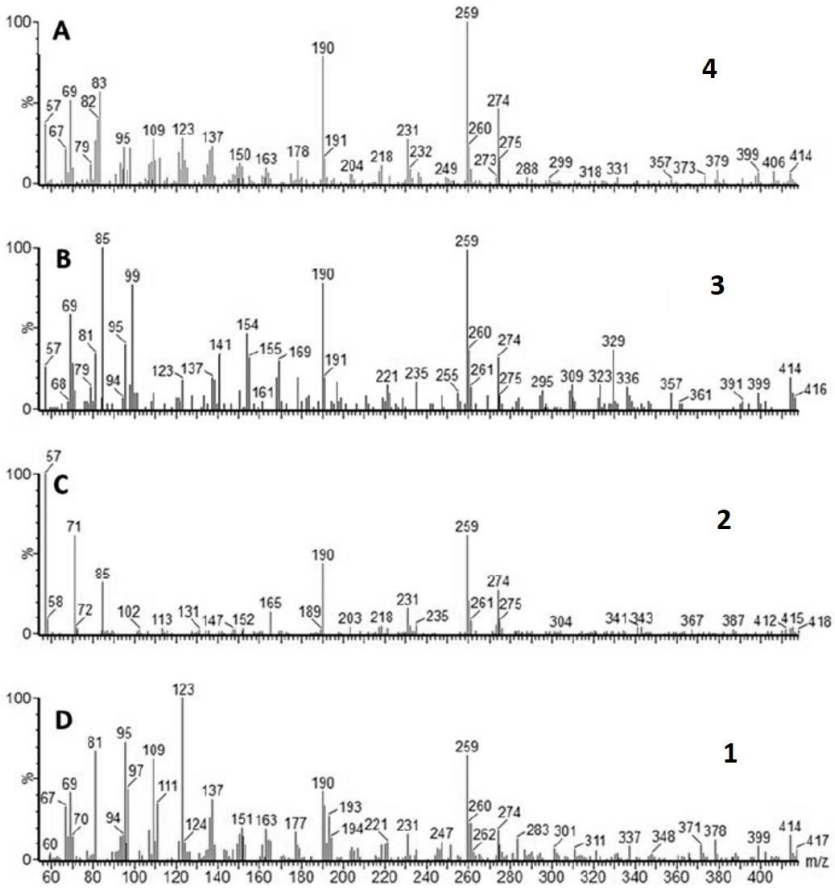

Figure 1.4. Mass spectra of Barney Creek Fm peaks **1** to **4** in the sample B03178 from 199.08 m in GR7 (reproduced from Figure 9-26 in Nettersheim, 2017).

Cyclosterane

In 1988, Summons et al. discovered an unknown doublet of peaks in Barney Creek Fm samples. These pentacyclic C_{30} compounds with cholestane-like side chain elute between the C_{27} and C_{29} hopanes. Nettersheim (2017, chapter 9) also detected these peaks (**5** and **6**) in drill core GR7 in the MRM *m/z* 412>274 transition (Figure 1.3 b). Based on investigation of the mass spectra, Nettersheim (2017) suggested that cycloartenol is the most plausible biological precursor for these triterpenoids; I will call them cyclosteranes. The mass spectrum of peak **5** shows patterns similar to cycloartane from the NIST database (Figure 1.5). Figure 1.6 illustrates the most probable structures of cyclosteranes

with a carbon-bridge in the C-ring (**I**, **II** and **III**) according to Nettersheim (2017). In this work, I use the sum of 5 and 6 peaks as a cyclosterane compound (CA).

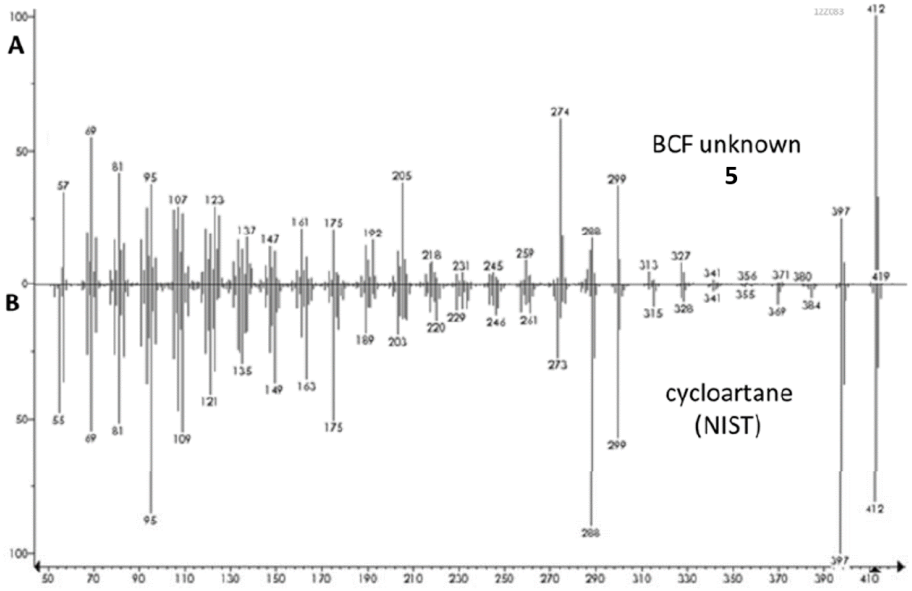

Figure 1.5. Mass spectra of A) Barney Creek Fm **5** peak illustrate a good agreement (63% probability) with B) cycloartane from NIST library (reproduced from Figure 9-12 in Nettersheim, 2017).

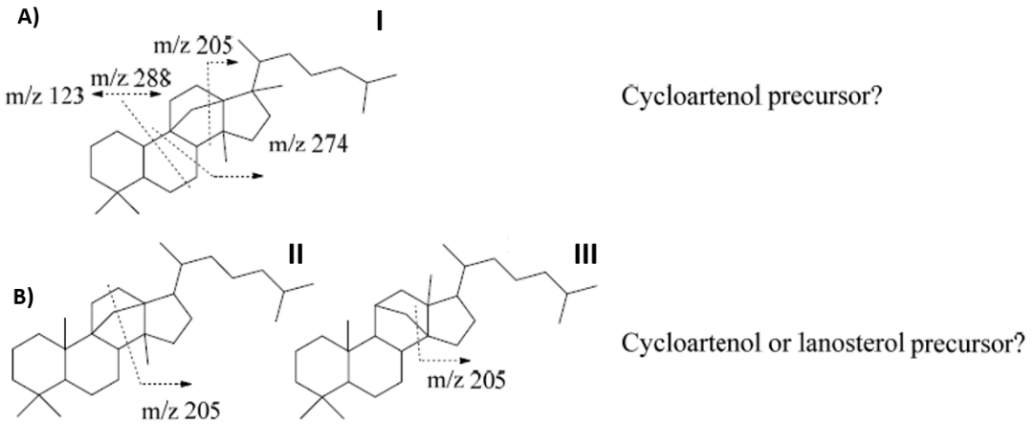

Figure 1.6. Possible structures for C_{30} cyclosterane compounds (peaks **5** and **6**) and plausible biological precursor (taken from Figure 9-18 in Nettersheim, 2017).

1.2.2 Triaromatic steroids (TAS) $C_{26–27}$

In 2005, Brocks et al. reported prominent *m/z* 231 and 245 series indicative of triaromatic steroids in the Barney Creek Fm. These sediments are dominated by C–4

methylated compounds (**IV**, Figure 1.7 a) with mass spectral base peak *m/z* 245 (more than 90% of all TAS, (Brocks et al., 2005)). The chromatograms of the main TAS in the Barney Creek Fm are illustrated in Figure 1.7. Peaks **7** and **8** represent S and R isomers of C_{27} 4-methyl triaromatic cholesteroid (Figure 1.7 a). Peaks **9** and **10** are S and R isomers of C_{26} triaromatic cholesteroid (Figure 1.7 b). Nettersheim (2017) suggested that C_{26} and C_{27} TAS might represent the aromatic equivalents of the protosteranes and originate from lanosterol or cycloartenol. However, during aromatization, protosteranes lose some of their diagnostic properties and it becomes impossible to resolve the actual precursor molecule for TAS – lanosterol or cycloartenol.

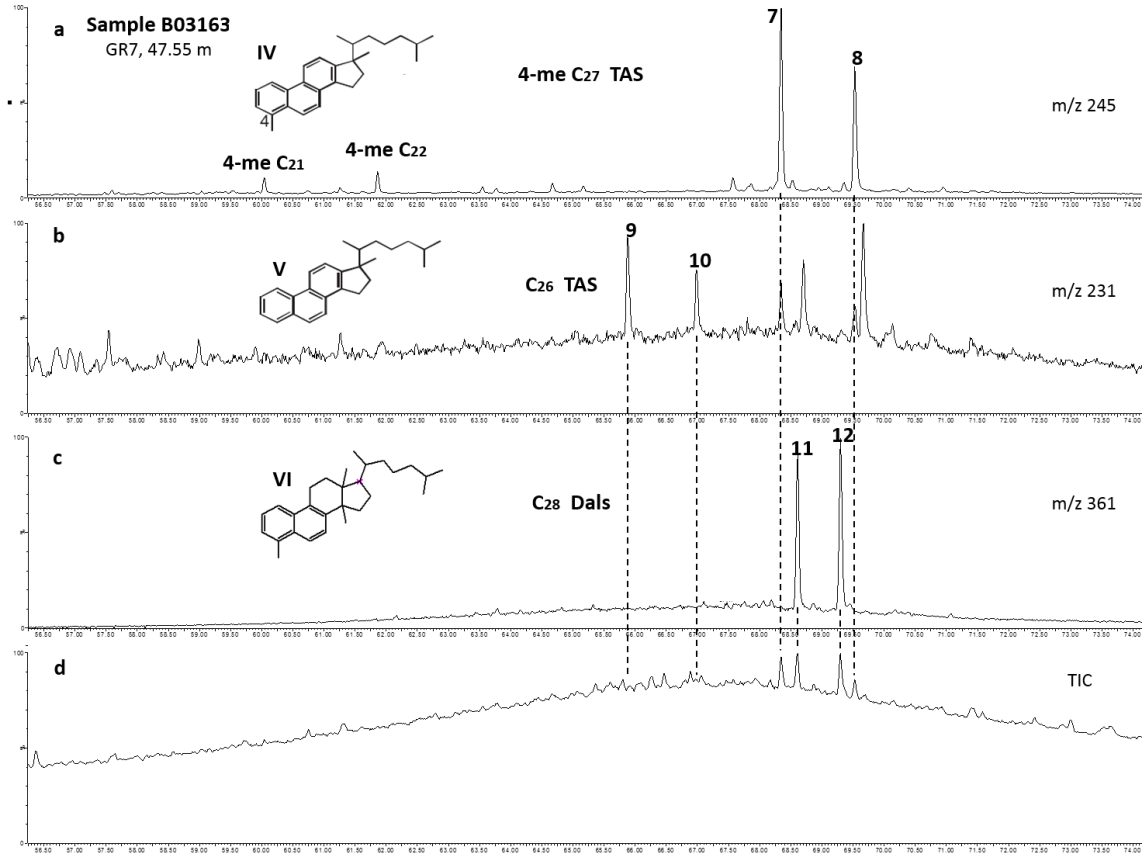

Figure 1.7. Triaromatic (TAS) and diaromatic (Dals) steroids in the sample B03163 (GR7, 47.55 m depth). a) *m/z* 245 trace, peaks **7** and **8** are 4-methylated C_{27} triaromatic steroids (S and R, M^+358), C_{21} (M^+274) and C_{22} (M^+288) homologues. b) *m/z* 231 trace, peaks **9** and **10** are C_{26} triaromatic steroids (S and R). c) *m/z* 361 trace, peaks 11 and 12 are C_{28} diaromatic steroids (S and R) d) Total Ion Chromatogram.

1.2.3 Diaromatic steroids (Dals) C_{28}

Nettersheim (2017) detected C_{28} diaromatic lanosteroids (Dals) in the high boiling range of Barney Creek Fm samples from GR7. S and R isomers of C_{28} Dals (peaks **11** and **12**) elute between the two 4-methylated TAS (Figure 1.7 c) and have similar mass spectra (Figure 1.8). According to mass fragmentation, Nettersheim (2017) proposed a structure for C_{28} Dals (**VI**), which is consistent with aromatization of a lanostane-type precursor. In general, Dals are quite scarce due to difficulties in aromatization of A and B-rings without proceeding to TAS.

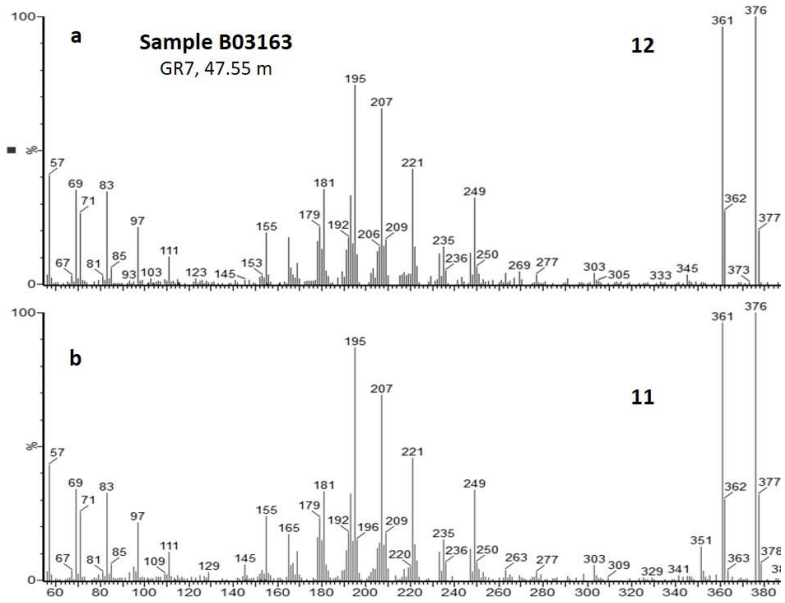

Figure 1.8. Mass spectra of Barney Creek Fm peaks **11** and **12** (Dals) in the sample B03163 (GR7, 47.55 m depth).

1.2.4 Monoaromatic steroids (Mals) C_{29}

Nettersheim (2017) discovered B-ring C_{29} monoaromatic lanosteroids with an *m/z* 379 base ion in the Barney Creek Fm samples of the GR7 drill core (Figure 1.9). Based on pyrolysis experiments conducted upon cycloartenol and lanosterol, he also proposed that C_{29} Mals from the Barney Creek Fm might be intermediates in the aromatization pathway of C_{30} sterols towards di- and triaromatic steroids (Nettersheim, 2017). During

the aromatization of cycloartenol, the diagnostic carbon-bridge breaks resulting in an aromatic steroid indistinguishable from an aromatized lanosterol. The structure of the B-ring monoaromatic lanosteroid (**VII**) is illustrated in Figure 1.9.

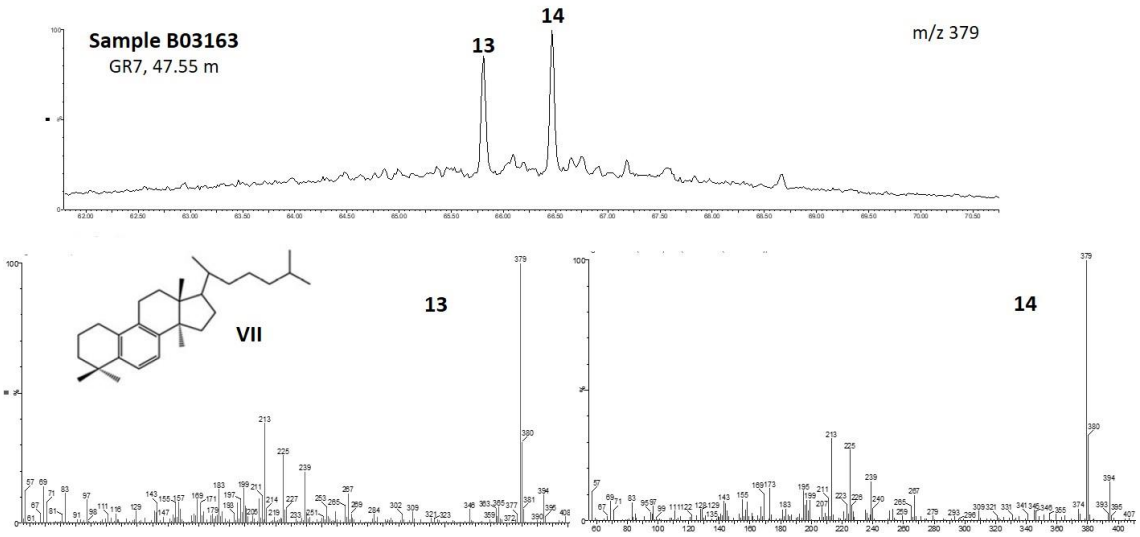

Figure 1.9. Monoaromatic (Mals) lanosteroids in the sample B03163 (GR7, 47.55 m depth) and mass spectra. *M/z* 379 trace, peaks **13** and **14** are S and R isomers of B-ring C_{29} Mals.

1.2.5 Aromatic hopanoids

Aromatic hopanoids in the Barney Creek Fm include low concentrations of benzohopanes ($C_{32–35}$, *m/z* 191) and a series of monoaromatic 8,14-secohopanoids. Based on their mass spectra and elution positions, two peaks (**15** and **16**) with *m/z* 365 base ions were interpreted by Nettersheim (2017) as regular C_{29} and C_{30} monoaromatic 8,14-secohopanoids (Figure 1.10).

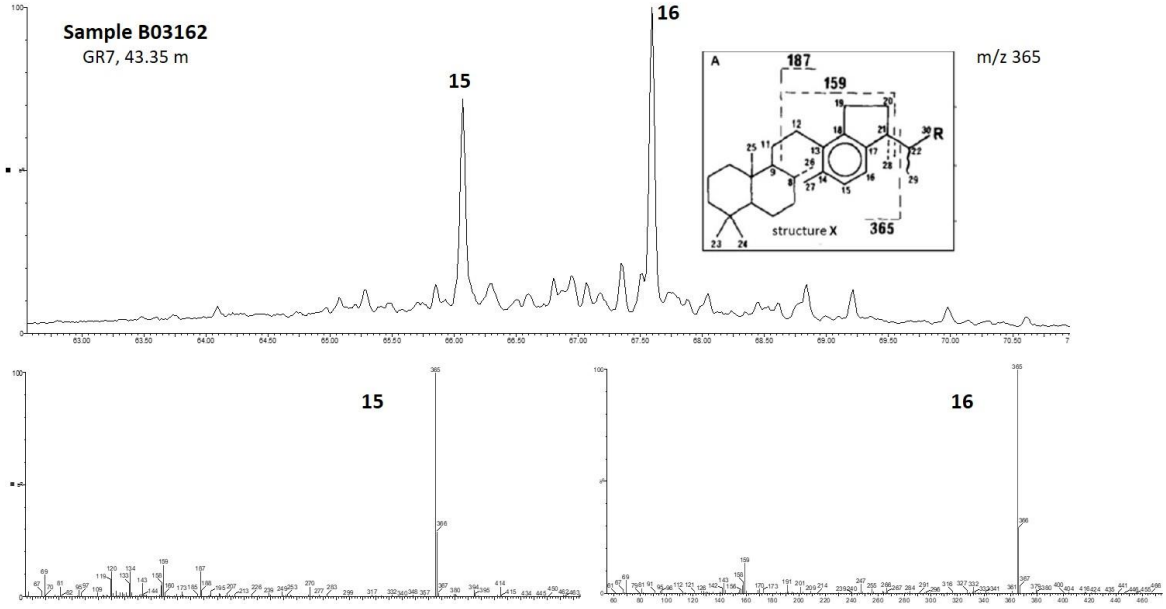

Figure 1.10. *M/z* 365 trace of sample B03162 (GR7, 43.35 m depth) with peaks **15** and **16** that represent C_{29} and C_{30} regular monoaromatic 8,14-secohopanoids (upper panel) and mass spectra of the two peaks (lower panel). The structure of the C_{30} compound was reproduced from Hussler et al. (1984), R=H.

Three peak doublets in the *m/z* 351 partial ion chromatogram represent monoaromatic C_{28}–C_{30} 28-nor-secohopanoids (Figure 1.11 a, peaks **17–22**). These compounds were referred to by Killops (1991) as demethylated seco-hopanoids (DSH). The structure of the C_{29} DSH (peaks **19**, **20**) proposed by Killops (1991) is illustrated in Figure 1.11 e.

A list of main biomarker parameters and ratios for this thesis is represented in Table 1.1.

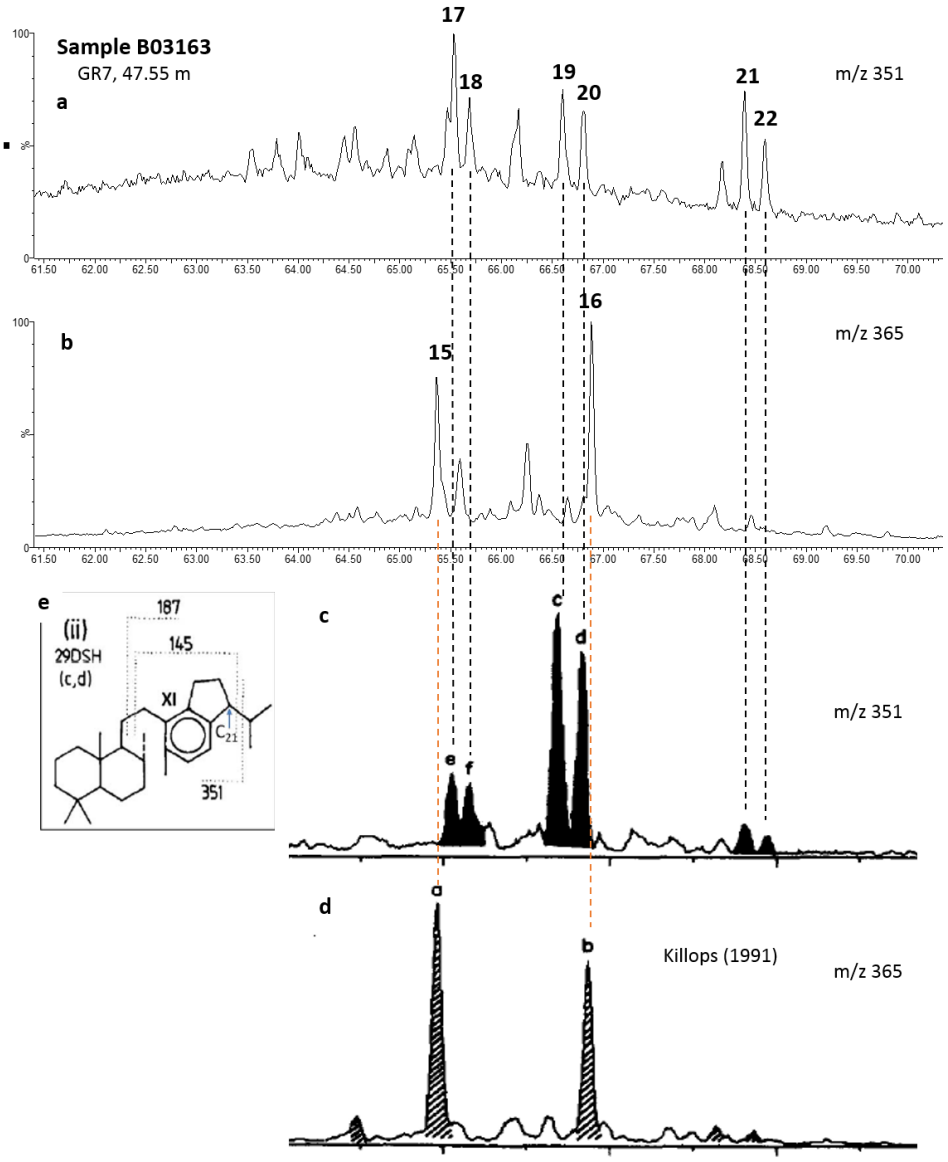

Figure 1.11. Comparison of selected ion chromatograms of a) *m/z* 351 and b) *m/z* 365 of Barney Creek Fm sample B03163 (GR7, 47.55 m), and c) *m/z* 351 and d) *m/z* 365 from Killops (1991), e) structure and fragmentation proposed by Killops (1991) for **19**, **20** (modified from Nettersheim, 2017).

Table 1.1 List of biomarker parameters and ratios

Parameter	**Definition**
Pr/Ph	Acyclic isoprenoids Pristane/Phytane (i-C_{19}/i-C_{20})
(Pr+Ph)/(C_{17}+C_{18})	Acyclic isoprenoids Pristane+Phytane versus sum of C_{17} and C_{18} *n*-alkanes
Ts/(Ts+Tm)	C_{27} hopane ratio with Ts – 18α-22,29,30-trisnorneohopane and Tm – 17α-22,29,30-trisnorhopane
C_{29} Ts/(Ts+H)	C_{29} hopane ratio with Ts - 18α-30-norneohopane and H - 17β,21α-30-norhopane
Moretane ratio	C_{30} βα-hopane/(C_{30} βα-hopane+C_{30} αβ-hopane)
GI (Sinninghe Damsté et al., 1995)	Gammacerane index, GI = gammacerane/ (gammacerane+C_{30} αβ-hopane)
2MHI (Summons et al., 1999)	2α-methyl-hopane index 2MHI = C_{31} 2α-methyl-hopane/(C_{31} 2α-methyl-hopane+C_{30} αβ-hopane)
3MHI (Brocks et al., 2005)	3β-methyl-hopane index 3MHI = C_{31} 3β-methyl-hopane/(C_{31} 3β-methyl-hopane+C_{30} αβ-hopane)
HHI	Homohopane index using 17α,21β(H)-homohopanes: 100*C_{35}(S+R)/Σ$C_{31–35}$(S+R)
3MeHHI	Methyl-homohopane index using 3β-methylhopanes: 100*C_{35}(S+R)/Σ$C_{31–35}$(S+R)
C_{30}DiaH/(DiaH+H)	C_{30} diahopane ratio with DiaH = C_{30} diahopane and H = C_{30} αβ+βα hopane
C_{26}T/C_{25}T	Tricyclic terpane ratios (or cheilanthanes)
C_{19}T/C_{23}T	
(C_{20}+C_{21})/(C_{23}+C_{24})	
Cl/(Cl+Ok)	Ratio of chlorobactane (Cl) over okenane (Ok)
G/(G+P)	G = Σ$C_{13–39}$ 2,3,6- trimethyl aryl isoprenoids (AI) and P = Σ$C_{13–39}$ 2,3,4-AI
G/Cl	Σ$C_{13–39}$ 2,3,6-AI/chlorobactane
P/Ok	Σ$C_{13–39}$ 2,3,4-AI/okenane
GAIR	Aryl isoprenoid ratio (AIR) for green sulphur bacterial carotenoids, GAIR = Σ($C_{13–17}$)/Σ($C_{18–22}$) 2,3,6-AI
PAIR	Aryl isoprenoid ratio (AIR) for purple sulphur bacterial carotenoids, PAIR = Σ($C_{13–17}$)/Σ($C_{18–22}$) 2,3,4-AI
LA/(LA+hop)	LA = Σpeaks$_{\mathbf{1-4}}$ lanostane, hop = dia ($C_{29–35}$)+αβ($C_{27–35}$)+ βα($C_{29–30}$) hopanes, sum of all hopanes
CA/(CA+hop)	CA – unknown protosterane, probably derived from cycloartane, CA= Σpeaks$_{\mathbf{5–6}}$ cyclosterane, hop – sum of all hopanes
PS/(PS+hop)	PS – protosteranes, PS = LA+CA; hop – sum of all hopanes
LA/(LA+DiaH) and CA/(CA+DiaH)	LA = Σpeaks$_{\mathbf{1-4}}$ lanostane, CA= Σpeaks$_{\mathbf{5–6}}$ cyclosterane, DiaH = Σ$C_{29–35}$ diahopanes

LA/(LA+cheil) and CA/(CA+cheil)	LA = $\Sigma peaks_{\mathbf{1-4}}$ lanostane, CA= $\Sigma peaks_{\mathbf{5-6}}$ cyclosterane, cheil = ΣC_{19-25} cheilanthanes
LA/(LA+gam) and CA/(CA+gam)	LA = $\Sigma peaks_{\mathbf{1-4}}$ lanostane, CA= $\Sigma peaks_{\mathbf{5-6}}$ cyclosterane, gam = gammacerane
Mals/(Mals+TAS)	Mals – C_{29} monoaromatic lanosteroid, TAS – C_{26} triaromatic cholesteroids and 4-methylated C_{27} triaromatic cholesteroids; C_{29}(S+R) Mals/(C_{29}(S+R) Mals+C_{26-27} TAS)
Dals/(Dals+TAS)	Dals – C_{28} diaromatic lanosteroid, TAS – C_{26} triaromatic cholesteroids and 4-methylated C_{27} triaromatic cholesteroids; C_{28}(S+R) Dals/(C_{28}(S+R) Dals+C_{26-27} TAS)
ArH	Aromatic hopanoids, ArH = ΣC_{32-35} benzohopanoids+ ΣC_{28-30}(S+R) 28-nor regular monoaromatic 8,14-secohopanoids+ΣC_{29-30} regular monoaromatic 8,14-secohopanoids
TAS/(TAS+ArH)	TAS – C_{26} triaromatic cholesteroids and 4-methylated C_{27} triaromatic cholesteroids, ArH – aromatic hopanoids
ArS/(ArS+ArH)	ArS – sum of aromatic steroids, ArS = (C_{29}(S+R) Mals+C_{28}(S+R) Dals+C_{26-27} TAS); Mals – C_{29} monoaromatic steroids, Dals – C_{28} diaromatic steroids, TAS – C_{26} triaromatic and 4-methylated C_{27} triaromatic cholesteroids. ArH – aromatic hopanoids
ArS/(ArS+PS)	ArS – sum of aromatic steroids, PS – protosteranes, PS = LA+CA.
MDI (Chen et al., 1996)	Methyl diamantane index, MDI = 4-MD/(1-MD+3-MD+4-MD) %
MAI (Chen et al., 1996)	Methyl adamantane index, MAI = 1-MA/(1-MA+2-MA) %
MPI-1 (Radke & Welte, 1983)	Methylphenanthrene index, MPI-1 = 1.5(2-MP+3-MP)/(P+1-MP+9-MP), where P is phenanthrene and MP is methylphenanthrene
Rc from MPI-1 (M Radke & Welte, 1983)	Calculated vitrinite reflectance, %Rc(MPI) = 0.6MPI-1+0.4 for 0.65 to 1.35% Rm (mean vitrinite reflectance), %Rc(MPI) = -0.6MPI-1+2.3 for 1.35 to 2% Rm
MPDF (Kvalheim et al., 1987)	Methylphenanthrene distribution factor, MPDF = (3-MP+2-MP)/(3-MP+2-MP+9-MP+1-MP)
Rc(MPDF) (Kvalheim et al., 1987)	Calculated vitrinite reflectance %Rc(MPDF) = 2.242*MPDF - 0.166
MPR (Radke, 1988)	Methylphenanthrene ratio, MPR = 2-MP/1-MP
Rc(MPR) (Radke, 1988)	Calculated vitrinite reflectance %Rc(MPR) = 1.1*$\log_{10}$(MPR)+0.95
TNR (Alexander et al., 1985)	Trimethylnaphthalene ratio TNR-1 = 2,3,6-TMN/(1,4,6-TMN+1,3,5-TMN)

1.3 Organic matter and thermal maturity

Sedimentary organic matter (OM) is a complex mixture of organic compounds derived from living organisms, such as plants, animals and algae (Tissot & Welte, 1984; Vassoyevich et al., 1970). After living organisms die, their remains sink through the water column and ~90% or more of OM is recycled during this process (Killops & Killops, 2005). Therefore, <10% of OM reaches the bottom sediments after which, during diagenesis (involving both biological and chemical transformation), the OM turns into kerogen, or macromolecular sedimentary OM, that is insoluble in organic solvents (Vandenbroucke & Largeau, 2007). Kerogen is characterised by four major types depending on the OM nature and depositional environments: I (lacustrine), II (marine), III (terrestrial) and IV (oxidized OM) (Tissot & Welte, 1984; Killops & Killops, 2005). Type I generally forms in lakes from lipid-rich OM (algae and bacteria) and generates predominantly oil. Type II is usually related to marine sediments and OM derived from a mixture of phytoplankton, zooplankton, and microorganisms. Type II kerogen has the potential to generate both oil and gas. Type III is gas-prone and essentially derives from continental plants deposited in fluvial/deltaic environments. Type IV represents highly oxidized plant remains and has only low potential to produce gas. Different kerogen types can be distinguished using several geochemical parameters (Table 1.2). With increasing burial, pressure and temperature from 60° to 150 °C, kerogen cracks into smaller molecules generating bitumen (Tissot & Welte, 1984). Bitumen represent molecules in sediments and sedimentary rocks that are extractable with organic solvents. Bitumen contains biomarkers, organic molecules with a diagnostic biological precursor, which can be analysed by gas chromatography-mass spectrometry (GC–MS) and used to reconstruct ancient environments.

Table 1.2 Kerogen Types and their geochemical characteristics[a].

Kerogen Type	Atomic H/C	Atomic O/C	HI (mg HC/g TOC)	S2/S3	Main fluid type
I	>1.2	<0.1	>600	>10	oil
II	1–1.2	~0.15	300–600	5–10	oil and gas
III	0.8–1.0	≤0.3	50–300	1–5	gas
IV	<0.8	≤0.3	<50	<1	none

[a]For thermally immature rocks. HI: hydrogen index. S2: hydrocarbon potential. S3: CO_2 potential. Modified from Peters (1986), Peters and Cassa (1994), Baskin (1997).

Diagenesis represents the first stage in OM alteration and occurs in the water column and immediately after sedimentation at temperatures <60 °C (Tissot & Welte, 1984). During diagenesis, biomolecules lose their functional groups through biological, physical and chemical processes and turn into hydrocarbons (Brocks & Pearson, 2005). Catagenesis is the process of further transformation of hydrocarbons, occurring under increased pressure and temperature (60–150 °C) over millions of years at burial depth ~1.5–4 km (Tissot & Welte, 1984; Hunt, 1995; Peters et al., 2005). Metagenesis is the next stage, where kerogen is affected by temperatures >150 °C (Hunt, 1995).

The alteration of kerogen and bitumen with increasing temperatures is referred to as thermal maturation (Peters & Cassa, 1994). One of the most common and reliable methods used to estimate thermal maturity in the Phanerozoic is vitrinite reflectance (%Ro) measurement. Vitrinite is a maceral originating from woody plant tissues found in sedimentary rocks. The reflectance of vitrinite particles in incident light increases with rising temperature applied to rocks during their geological history. This method measures the maximum temperature to which the vitrinite, and hence the sedimentary OM, has been exposed as the process of vitrinite maturation is irreversible. Sediments are considered immature in the diagenesis stage with Ro <0.6% (Figure 1.12). Thermally mature organic-rich sediments in the oil window zone return Ro values from 0.6 up to 1.2–1.3% and start to generate oil through thermal cracking of kerogen. Sediments with Ro >1.3%

have reached the overmature stage or gas window zone and produce mainly wet and dry gas (Peters & Cassa, 1994).

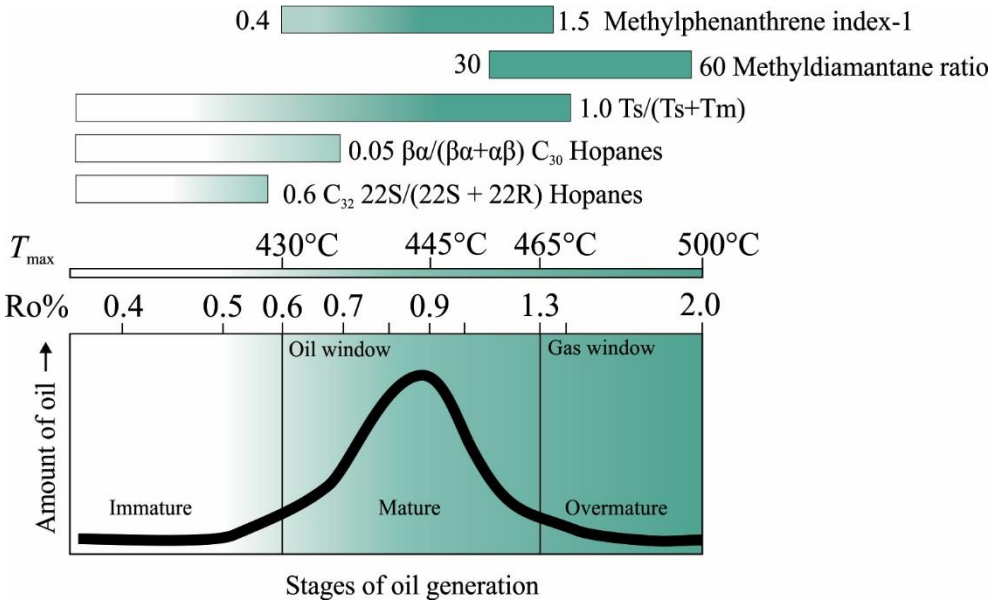

Figure 1.12. Stages of oil generation and thermal maturation with gradations of vitrinite reflectance, Rock-Eval Tmax and hydrocarbon indices. The solid bars represent approximate ranges for each parameter. Figure modified after Peters et al. (2005) and van Maldegem (2017).

Biomarkers are generally preserved in sedimentary rocks ranging in maturity from immature to the main oil window. However, the detection of indigenous biomarkers in the Proterozoic and Archean is a challenge, since biologically informative molecules of such antiquity are commonly destroyed by metamorphism or overprinted by drilling fluids and other anthropogenic contaminants (Brocks et al., 2008; French et al., 2015). Since vitrinite is absent in rocks older than Silurian age, other maturity parameters must be applied in the Proterozoic, for example Rock-Eval pyrolysis and various hydrocarbon ratios (e.g., Peters et al., 2005). For comparison purposes, Rock-Eval (Tmax) and aromatic hydrocarbon parameters can be re-calculated to vitrinite reflectance equivalents (Figure 1.12; Table 1.1). Biomarker ratios provide information about thermal alteration through changes in the relative abundance of isomers with different resistances to thermal

stress. For example, the ratio of Ts/(Ts+Tm) isomers of C_{27} hopane measures the gradual transformation of the less stable 17α(H) Tm to the more stable 18α(H) Ts configuration and reaches a thermodynamic equilibrium in the overmature area (Figure 1.12). Besides burial temperatures, the presence of magmatic intrusions and hydrothermal fluids can also alter sedimentary OM and lead to rapid maturation. Maturity parameters may illustrate some discrepancies around such heat anomalies due to overall poor calibration (Illing et al., 2019).

It is generally important to assess the influence of maturity on OM, since thermal maturation processes affect the preservation and original distributions of biomarkers. In this thesis, I will explore in more detail the influence of thermal maturity on OM preservation in the mid-Proterozoic.

1.4 Stable carbon and hydrogen isotopes

Stable carbon (C) and hydrogen (H) isotope measurements of kerogen and bitumen, as well as compound-specific analyses performed upon individual molecules, can provide important information about biological sources of OM. There are two stable carbon isotopes – ^{12}C and ^{13}C. They are chemically identical, having the same number of protons and electrons, but mechanically different, since they possess a different number of neutrons (one more in ^{13}C). ^{12}C is more abundant and constitutes 98.9% of Earth's carbon, while ^{13}C accounts only for 1.1% of the total abundance (Killops & Killops, 2005). The $^{13}C/^{12}C$ ratio of the carbon of any given sample versus that of a known standard provides a $\delta^{13}C$ measurement of the sample carbon (1.1). Carbonate of the Pee Dee Belemnite is typically used as a standard with its $\delta^{13}C$ value set equal to zero (Hoefs, 2009). The values of $\delta^{13}C$ are represented in per mil notations (‰, or parts per thousand).

$$\delta^{13}C_{Sample} = \left(\frac{(^{13}C/^{12}C)_{Sample}}{(^{13}C/^{12}C)_{VPDB}} - 1\right) \times 1000 \quad (1.1)$$

A majority of studies have looked at the carbon isotopes of inorganic carbon in carbonates and demonstrated that $\delta^{13}C_{carb}$ values through time average around 0‰ with occasional depletions and enrichments throughout the early Paleoproterozoic and late Neoproterozoic (Halverson et al., 2005; Krissansen-Totton et al., 2015; Schidlowski, 2001) (Figure 1.13). This signature is predominantly controlled by atmospheric CO_2 values, providing little information about biology in deep time. It is has been suggested that photosynthesis, which evolved well over 2.0 Ga, represents the primary source of organic carbon fixation in the Proterozoic (Nisbet et al., 2007; Schidlowski, 2001). Since living organisms discriminate against ^{13}C, the $\delta^{13}C$ of organic carbon in the Proterozoic is depleted relative to $\delta^{13}C_{carb}$ by ~20–30‰ in photoautotrophs (Hayes, 1994; Nier &

Gulbransen, 1939; Schidlowski, 2001) and up to ~130‰ in methanotrophs (Hinrichs et al., 1999).

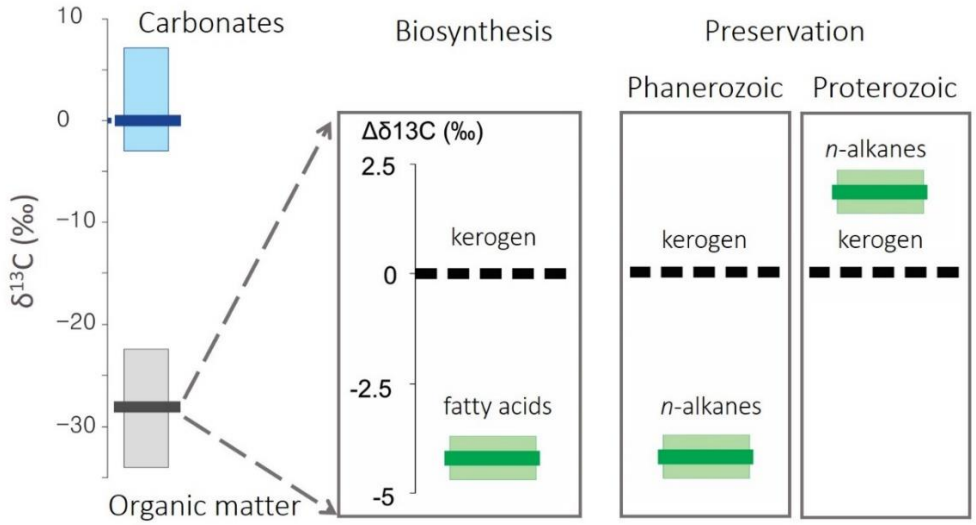

Figure 1.13. Schematic carbon isotope measurements of carbonates and organic matter, with $\delta^{13}C$ biosynthesis and preservation signatures of kerogen and lipids. Data are from Krissansen-Totton et al. (2015), Hayes (2001), Bidigare et al. (1997), Logan et al. (1995).

Bulk sedimentary organic matter is heterogeneous and consists of kerogen and bitumen, which, in turn, contains various individual hydrocarbon molecules. Due to the biosynthetic pathway of standard photosynthesis, there is a general $\delta^{13}C$ offset of ~4.5‰ between kerogen and individual compounds, such as fatty acids (Bidigare et al., 1997) (Figure 1.13). Kerogen predominantly derives from primary producers, while fatty acids are generated by both phototrophs and heterotrophs. In the Phanerozoic, the biosynthetic offset is generally preserved in the sediments, with *n*-alkanes (molecular fossils of fatty acids) being depleted relative to kerogen by ~4.5‰ (Hayes, 2001). However, in the Proterozoic, an inverse isotopic ordering is observed, where *n*-alkanes are enriched relative to kerogen by ~1.5‰ (Logan et al., 1995) (Figure 1.13). According to Logan et al. (1995), this difference is because OM in the modern ocean sinks comparatively fast through the water column and is comparatively weakly affected by continuous trophic

cycling. In the Precambrian however, the slowly floating, smaller particles of OM were more intensively affected by heterotrophic reworking, resulting in enriched ^{13}C values of *n*-alkanes (Logan et al., 1995; 1997). Other hypotheses for Precambrian inverse isotopic ordering include stratification, mixing of different carbon pools and community influence (Close et al., 2011).

Stable hydrogen isotopes are represented by ^{1}H and ^{2}H, and demonstrate an overall predominance of ^{1}H (99.985%) (Killops & Killops, 2005). Hydrogen isotopic compositions are measured relative to the Vienna Mean Ocean Water standard (Werner & Brand, 2001) (1.2).

$$\delta^2 H_{Sample} = \left(\frac{(\,^2H/\,^1H)_{Sample}}{(\,^2H/\,^1H)_{VMOW}} - 1\right) \times 1000 \quad (1.2)$$

Environmental water represents the main source of inorganic hydrogen. While δ^2H values for marine water average at ~0‰, meteoric waters are quite variable in isotopic composition depending on geographic location (Craig & Gordon, 1965; Sessions, 2016). Biological fixation of hydrogen leads to ~170 ± 50‰ ^{2}H-depletion of fatty acids relative to seawater (Li et al., 2009; Sessions, 2016). Water isotopes and biosynthetic fractionations largely define the primary hydrogen isotopic composition of hydrocarbons. During diagenesis and catagenesis, several processes, including hydrogen exchange, kinetic fractionations, biodegradation, fluid migration and water washing, can affect and complicate the original δ^2H signatures (Alexander et al., 1982; Tang et al., 2005; Sessions, 2016 and references therein).

1.5 Research objectives

My research centres on the investigation of mid-Proterozoic ecosystems using biomarkers and stable isotopes in combination with inorganic geochemical proxies. The aim of this study is to investigate the ecology, paleo-environments and organic matter preservation (including biomarkers and compound-specific isotopes) of Paleoproterozoic successions by examining material from the northern Australian McArthur Basin, which contains the oldest known indigenous biomarkers.

This thesis consists of four major research topics:

(1) Characterisation of the paleo-environments and biomarker distributions of the ~1.64 Ga middle McArthur Group, northern Australia. The goal of this project is to perform a multi-proxy analysis throughout the exceptionally well-preserved LV09001 drill core in the southern McArthur Basin. This study also aims to determine the potential biological sources of protosterane molecules found within the core and their distributions with respect to different depositional environments.

(2) Investigation of the influence of thermal maturity on compound-specific carbon and hydrogen isotopes in the mid-Proterozoic utilising material from the 1.64 Ga Barney Creek Formation, Australia.

(3) Preservation of organic matter associated with the activity of hydrothermal fluids. This project focuses on the organic geochemistry of the 1.64 Ga McArthur River (HYC) ore deposit.

(4) Extending the biomarker record back in time by testing the presence of indigenous molecular fossils in the ~1.64 Ga Teena Dolostone and 1.73 Ga Wollogorang Formation, McArthur Basin.

1.6 Thesis outline

This thesis contains eight chapters:

Chapter 2 describes the samples and methodologies utilised for this work.

Chapter 3 outlines the geological setting of the southern McArthur Basin in northern Australia.

Chapter 4 focuses on the paleo-environments and biological signatures of the ~1.64 Ga middle McArthur Group in the LV09001 drill core and investigates the origin and paleoecology of protosteroid producers in the Paleoproterozoic. This study presents the discovery of the oldest known hopanes and intact aromatic carotenoids in the ~1.64 Ga Teena Dolostone, which underlies the Barney Creek Formation. Chapter 4 also includes a discussion of the organisms, which may have produced the protosterane molecules found in the Barney Creek Formation, and the types of environments in which these creatures might have lived.

Chapter 5 describes a substantial thermal maturity effect upon the carbon and hydrogen isotopic compositions of *n*-alkanes in the 1.64 Ga Barney Creek Formation, Australia. This is the first study to compare maturity and compound-specific isotopes in the Proterozoic. Chapter 5 illustrates strong linear correlations between maturity parameters and isotopic values and demonstrates the highest recorded ^{13}C-enrichment of *n*-alkanes caused by thermal maturation (6.8‰). Using simple numerical models, this study suggests that δ^{13}C *n*-alkane slope inversion from positive to negative is controlled by the changing importance of different generation and degradation processes.

Chapter 6 re-examines the thermal preservation of organic matter in the Paleoproterozoic McArthur River (HYC) zinc/lead ore deposits. This is the first hydrocarbon analysis through the foot wall, orebody, inter-ore layers and hanging wall of

the HYC sulphide deposit. It demonstrates that kerogen in the orebody suffered alteration at temperatures consistent with thermochemical sulphate reduction. Hydrocarbons in the mineralized zone migrated into the orebody from surrounding sediments and do not record the temperature of mineralizing fluids, negating earlier temperature estimates.

Chapter 7 illustrates a discovery of the low molecular weight 2,3,4- and 2,3,6-trimethyl aryl isoprenoids in the 1.73 Ga Wollogorang Formation, Australia. These breakdown products of aromatic carotenoids represent the oldest known clearly indigenous molecules of biological origin and extend the biomarker record by ~90 million years. This chapter also describes the limitations of biomarker analysis at the edge of detectability.

Chapter 8 outlines the overarching conclusions for this thesis.

Appendices A–D contain supplementary material for Chapters 4–7.

1.7 Publications from this thesis

Chapter 5 – Vinnichenko, G., Jarrett, A. J., van Maldegem, L. M., & Brocks, J. J. (2021). Substantial maturity influence on carbon and hydrogen isotopic composition of *n*-alkanes in sedimentary rocks. *Organic Geochemistry*, 152, 104171.

Galina Vinnichenko designed the study, performed analytical work for LV09 and HYC samples, including the biomarker analysis and isolation of *n*-alkanes, and interpreted results. Jochen Brocks conducted the biomarker analysis for GR7 samples and Galina Vinnichenko performed the subsequent isolation of *n*-alkanes. Amber Jarrett analysed BB5 and BB6 samples at Geoscience Australia, Jochen Brocks conducted the modelling, Lennart van Maldegem participated in discussions about the interpretation. Galina Vinnichenko and Jochen Brocks wrote the paper with contribution from all authors.

Chapter 6 – Vinnichenko, G., Hope, J. M., Jarrett, A. J., Williams, N., & Brocks, J. J. (2021). Reassessment of the thermal preservation of organic matter in the Paleoproterozoic McArthur River (HYC) Zn-Pb ore deposit, Australia. *Ore Geology Reviews,* 133, 104129.

Galina Vinnichenko and Jochen Brocks designed the study. Neil Williams and Jochen Brocks collected the samples. Galina Vinnichenko performed analytical work with help from Janet Hope, including the biomarker analysis, isolation of *n*-alkanes and kerogen isolation. Galina Vinnichenko interpreted results. Amber Jarrett performed Rock-Eval and isotope analyses at Geoscience Australia. Galina Vinnichenko and Jochen Brocks wrote the paper with contribution from all authors.

Chapter 7 – Vinnichenko, G., Jarrett, A. J., Hope, J. M., & Brocks, J. J. (2020). Discovery of the oldest known biomarkers provides evidence for phototrophic bacteria in the 1.73 Ga Wollogorang Formation, Australia. *Geobiology*, 18(5), 544-559.

Galina Vinnichenko designed the study, collected the samples, performed analytical work with help from Janet Hope, including the biomarker analysis and isolation of *n*-alkanes. Galina Vinnichenko interpreted results. Amber Jarrett conducted the isotope analysis at Geoscience Australia. Galina Vinnichenko and Jochen Brocks wrote the paper with contribution from all authors.

References

Alexander, R., Kagi, R., Rowland, S., Sheppard, P., & Chirila, T. (1985). The effects of thermal maturity on distributions of dimethylnaphthalenes and trimethylnaphthalenes in some ancient sediments and petroleums. *Geochimica et Cosmochimica Acta, 49*(2), 385-395.

Alexander, R., Kagi, R. I., & Larcher, A. V. (1982). Clay catalysis of aromatic hydrogen-exchange reactions. *Geochimica et Cosmochimica Acta, 46*(2), 219-222.

Anbar, A. D., & Knoll, A. H. (2002). Proterozoic Ocean Chemistry and Evolution: A Bioinorganic Bridge? *Science, 297*(5584), 1137-1142. doi:10.1126/science.1069651

Bloch, K., (1994). 'Evolutionary perfection of a small molecule, Blondes in Venetian Paintings, the Nine-Banded Armadillo, and Other Essays in Biochemistry'. *Yale University Press*, New Haven and London.

Baskin, D. K. (1997). Atomic H/C ratio of kerogen as an estimate of thermal maturity and organic matter conversion. *AAPG Bulletin, 81*(9), 1437-1450.

Bidigare, R. R., Fluegge, A., Freeman, K. H., Hanson, K. L., Hayes, J. M., Hollander, D., . . . Milder, J. (1997). Consistent fractionation of 13C in nature and in the laboratory: Growth-rate effects in some haptophyte algae. *Global Biogeochemical Cycles, 11*(2), 279-292.

Brocks, J., & Summons, R. (2005). Biomarkers for Early Life. *Biogeochemistry, 8*, 63.

Brocks, J. J., Grosjean, E., & Logan, G. A. (2008). Assessing biomarker syngeneity using branched alkanes with quaternary carbon (BAQCs) and other plastic contaminants. *Geochimica et Cosmochimica Acta, 72*(3), 871-888.

Brocks, J. J., Jarrett, A. J. M., Sirantoine, E., Hallmann, C., Hoshino, Y., & Liyanage, T. (2017). The rise of algae in Cryogenian oceans and the emergence of animals. *Nature, 548*(7669), 578-581. doi:10.1038/nature23457

Brocks, J. J., Love, G. D., Summons, R. E., Knoll, A. H., Logan, G. A., & Bowden, S. A. (2005). Biomarker evidence for green and purple sulphur bacteria in a stratified Palaeoproterozoic sea. *Nature, 437*, 866. doi:10.1038/nature04068

Brocks, J. J., & Pearson, A. (2005). Building the biomarker tree of life. *Reviews in Mineralogy and Geochemistry, 59*(1), 233-258.

Butterfield, N. J., & Smith, A. (2015). Early evolution of the Eukaryota. *Palaeontology, 58*(1), 5-17. doi:10.1111/pala.12139

Canfield, D. E. (1998). A new model for Proterozoic ocean chemistry. *Nature (London), 396*(6710), 450-453. doi:10.1038/24839

Chen, J., Fu, J., Sheng, G., Liu, D., & Zhang, J. (1996). Diamondoid hydrocarbon ratios: novel maturity indices for highly mature crude oils. *Organic geochemistry, 25*(3-4), 179-190.

Close, H. G., Bovee, R., & Pearson, A. (2011). Inverse carbon isotope patterns of lipids and kerogen record heterogeneous primary biomass. *Geobiology, 9*(3), 250-265. doi:10.1111/j.1472-4669.2011.00273.x

Craig, H., & Gordon, L. I. (1965). Deuterium and oxygen 18 variations in the ocean and the marine atmosphere.

Didyk, B., Simoneit, B., Brassell, S. t., & Eglinton, G. (1978). Organic geochemical indicators of palaeoenvironmental conditions of sedimentation. *Nature, 272*(5650), 216-222.

Dupont, S., Lemetais, G., Ferreira, T., Cayot, P., Gervais, P., & Beney, L. (2012). Ergosterol biosynthesis: a fungal pathway for life on land? *Evolution, 66*(9), 2961-2968. doi:10.1111/j.1558-5646.2012.01667.x

Embley, T. M., & Martin, W. (2006). Eukaryotic evolution, changes and challenges. *Nature, 440*(7084), 623-630. doi:10.1038/nature04546

French, K. L., Hallmann, C., Hope, J. M., Schoon, P. L., Zumberge, J. A., Hoshino, Y., . . . Summons, R. E. (2015). Reappraisal of hydrocarbon biomarkers in Archean rocks. *Proc Natl Acad Sci U S A, 112*(19), 5915-5920. doi:10.1073/pnas.1419563112

Gibson, T. M., Shih, P. M., Cumming, V. M., Fischer, W. W., Crockford, P. W., Hodgskiss, M. S., . . . Skulski, T. M. (2017). Precise age of Bangiomorpha pubescens dates the origin of eukaryotic photosynthesis. *Geology, 46*(2), 135-138.

Halverson, G. P., Hoffman, P. F., Schrag, D. P., Maloof, A. C., & Rice, A. H. N. (2005). Toward a Neoproterozoic composite carbon-isotope record. *GSA bulletin, 117*(9-10), 1181-1207.

Hayes, J. (1994). Global methanotrophy at the Archean-Proterozoic transition. *Early life on Earth*, 220-236.

Hayes, J. M. (2001). Fractionation of carbon and hydrogen isotopes in biosynthetic processes. *Reviews in Mineralogy and Geochemistry, 43*(1), 225-277.

Hinrichs, K.-U., Hayes, J. M., Sylva, S. P., Brewer, P. G., & DeLong, E. F. (1999). Methane-consuming archaebacteria in marine sediments. *Nature, 398*(6730), 802-805.

Hoefs, J. (2009). *Stable isotope geochemistry* (Vol. 285): Springer.

Holland, H. D. (2002). Volcanic gases, black smokers, and the Great Oxidation Event. *Geochimica et Cosmochimica Acta, 66*(21), 3811-3826.

Holland, H. D. (2006). The oxygenation of the atmosphere and oceans. *Philos Trans R Soc Lond B Biol Sci, 361*(1470), 903-915. doi:10.1098/rstb.2006.1838

Hunt, J. M. (1995). Petroleum geochemistry and geology.

Huntley, J. W., Xiao, S., & Kowalewski, M. (2006). 1.3 Billion years of acritarch history: An empirical morphospace approach. *Precambrian Research, 144*(1-2), 52-68. doi:10.1016/j.precamres.2005.11.003

Hussler, G., Connan, J., & Albrecht, P. (1984). Novel families of tetra-and hexacyclic aromatic hopanoids predominant in carbonate rocks and crude oils. *Organic geochemistry, 6*, 39-49.

Illing, C. J., Hallmann, C., Scott, A. C., Collinson, M. E., Briggs, D. E. G., Strauss, H., & Summons, R. E. (2019). Heterogeneity of free and occluded bitumen in a natural maturity sequence from Oligocene Lake Enspel. *Geochimica et Cosmochimica Acta, 245*, 240-265. doi:10.1016/j.gca.2018.10.021

Johnston, D. T., Poulton, S. W., Dehler, C., Porter, S., Husson, J., Canfield, D. E., & Knoll, A. H. (2010). An emerging picture of Neoproterozoic ocean chemistry: Insights from the Chuar Group, Grand Canyon, USA. *Earth and Planetary Science Letters, 290*(1-2), 64-73. doi:10.1016/j.epsl.2009.11.059

Killops, S. (1991). Novel aromatic hydrocarbons of probable bacterial origin in a Jurassic lacustrine sequence. *Organic geochemistry, 17*(1), 25-36.

Killops, S., & Killops, V. (2005). Introduction to Organic Geochemistry, 2nd edn (paperback): Blackwell Science Ltd Oxford, UK.

Knoll, A. H. (2011). The Multiple Origins of Complex Multicellularity. *Annual Review of Earth and Planetary Sciences, 39*(1), 217-239. doi:10.1146/annurev.earth.031208.100209

Knoll, A. H. (2014). Paleobiological perspectives on early eukaryotic evolution. *Cold Spring Harb Perspect Biol, 6*(1). doi:10.1101/cshperspect.a016121

Knoll, A. H., Javaux, E. J., Hewitt, D., & Cohen, P. (2006). Eukaryotic organisms in Proterozoic oceans. *Philos Trans R Soc Lond B Biol Sci, 361*(1470), 1023-1038. doi:10.1098/rstb.2006.1843

Knoll, A. H., & Nowak, M. A. (2017). The timetable of evolution. *Science Advances, 3*(5). doi:10.1126/sciadv.1603076

Krissansen-Totton, J., Buick, R., & Catling, D. C. (2015). A statistical analysis of the carbon isotope record from the Archean to Phanerozoic and implications for the rise of oxygen. *American Journal of Science, 315*(4), 275-316.

Kvalheim, O. M., Christy, A. A., Telnæs, N., & Bjørseth, A. (1987). Maturity determination of organic matter in coals using the methylphenanthrene distribution. *Geochimica et Cosmochimica Acta, 51*(7), 1883-1888.

Lamb, D. M., Awramik, S. M., Chapman, D. J., & Zhu, S. (2009). Evidence for eukaryotic diversification in the ~1800 million-year-old Changzhougou Formation, North China. *Precambrian Research, 173*(1-4), 93-104. doi:10.1016/j.precamres.2009.05.005

Lee, A. K., Banta, A. B., Wei, J. H., Kiemle, D. J., Feng, J., Giner, J.-L., & Welander, P. V. (2018). C-4 sterol demethylation enzymes distinguish bacterial and eukaryotic sterol synthesis. *Proceedings of the National Academy of Sciences, 115*(23), 5884-5889.

Li, C., Sessions, A. L., Kinnaman, F. S., & Valentine, D. L. (2009). Hydrogen-isotopic variability in lipids from Santa Barbara Basin sediments. *Geochimica et Cosmochimica Acta, 73*(16), 4803-4823.

Logan, G. A., Hayes, J., Hieshima, G. B., & Summons, R. E. (1995). Terminal Proterozoic reorganization of biogeochemical cycles. *Nature, 376*(6535), 53-56.

Logan, G. A., Summons, R. E., & Hayes, J. M. (1997). An isotopic biogeochemical study of Neoproterozoic and Early Cambrian sediments from the Centralian Superbasin, Australia. *Geochimica et Cosmochimica Acta, 61*(24), 5391-5409.

Nes, W. D. (2011). Biosynthesis of cholesterol and other sterols. *Chemical reviews, 111*(10), 6423-6451. doi:10.1021/cr200021m

Nettersheim, B. J. (2017). *Reconstructing earth's alien ancient ecology - a multiproxy study of the 1.64 billion-years-old Barney Creek formation, northern Australia.* (PhD Thesis), Australian National University.

Nier, A. O., & Gulbransen, E. A. (1939). Variations in the relative abundance of the carbon isotopes. *Journal of the American Chemical Society, 61*(3), 697-698.

Nisbet, E., Grassineau, N., Howe, C., Abell, P., Regelous, M., & Nisbet, R. (2007). The age of Rubisco: the evolution of oxygenic photosynthesis. *Geobiology, 5*(4), 311-335.

Pearson, A., Budin, M., & Brocks, J. J. (2003). Phylogenetic and biochemical evidence for sterol synthesis in the bacterium Gemmata obscuriglobus. *Proceedings of the National Academy of Sciences, 100*(26), 15352-15357. doi:10.1073/pnas.2536559100

Penny, D., Collins, L. J., Daly, T. K., & Cox, S. J. (2014). The relative ages of eukaryotes and akaryotes. *J Mol Evol, 79*(5-6), 228-239. doi:10.1007/s00239-014-9643-y

Peters, K. (1986). Guidelines for evaluating petroleum source rock using programmed pyrolysis. *AAPG Bulletin, 70*(3), 318-329.

Peters, K., Walters, C., & Moldowan, J. (2005). The biomarker guide, volume 2—biomarkers and isotopes in petroleum exploration and earth history. *Cambridge: Cambridge University Press, 475*, 634.

Peters, K. E., & Cassa, M. R. (1994). Applied source rock geochemistry: Chapter 5: Part II. Essential elements.

Planavsky, N. J., McGoldrick, P., Scott, C. T., Li, C., Reinhard, C. T., Kelly, A. E., . . . Lyons, T. W. (2011). Widespread iron-rich conditions in the mid-Proterozoic ocean. *Nature, 477*(7365), 448-451. doi:10.1038/nature10327

Planavsky, N. J., Reinhard, C. T., Wang, X., Thomson, D., McGoldrick, P., Rainbird, R. H., . . . Lyons, T. W. (2014). Low Mid-Proterozoic atmospheric oxygen levels and the delayed rise of animals. *Science, 346*(6209), 635-638.

Porter, S. M., & Knoll, A. H. (2000). Testate amoebae in the Neoproterozoic Era: evidence from vase-shaped microfossils in the Chuar Group, Grand Canyon. *Paleobiology, 26*(3), 360-385.

Poulton, S. W., & Canfield, D. E. (2011). Ferruginous Conditions: A Dominant Feature of the Ocean through Earth's History. *Elements, 7*(2), 107-112. doi:10.2113/gselements.7.2.107

Poulton, S. W., Fralick, P. W., & Canfield, D. E. (2010). Spatial variability in oceanic redox structure 1.8 billion years ago. *Nature Geoscience, 3*(7), 486-490. doi:10.1038/ngeo889

Radke, M. (1988). Application of aromatic compounds as maturity indicators in source rocks and crude oils. *Marine and Petroleum Geology, 5*(3), 224-236.

Radke, M., & Welte, D. H. (1983). The methylphenanthrene index (MPI): a maturity parameter based on aromatic hydrocarbons. *Advances Organic Geochemistry 1981*, 504-512.

Schidlowski, M. (2001). Carbon isotopes as biogeochemical recorders of life over 3.8 Ga of Earth history: evolution of a concept. *Precambrian Research, 106*(1-2), 117-134.

Schopf, J. W. (1993). Microfossils of the Early Archean Apex chert: new evidence of the antiquity of life. *Science, 260*(5108), 640-646.

Sessions, A. L. (2016). Factors controlling the deuterium contents of sedimentary hydrocarbons. *Organic geochemistry, 96*, 43-64. doi:10.1016/j.orggeochem.2016.02.012

Sinninghe Damsté, J. S., Kenig, F., Koopmans, M. P., Koster, J., Schouten, S., Hayes, J., & de Leeuw, J. W. (1995). Evidence for gammacerane as an indicator of water column stratification. *Geochimica et Cosmochimica Acta, 59*(9), 1895-1900.

Summons, R. E., Jahnke, L. L., Hope, J. M., & Logan, G. A. (1999). 2-Methylhopanoids as biomarkers for cyanobacterial oxygenic photosynthesis. *Nature, 400*(6744), 554-557.

Summons, R. E., Powell, T. G., & Boreham, C. J. (1988). Petroleum geology and geochemistry of the Middle Proterozoic McArthur Basin, Northern Australia: III. Composition of extractable hydrocarbons. *Geochimica et Cosmochimica Acta, 52*(7), 1747-1763. doi:https://doi.org/10.1016/0016-7037(88)90001-4

Tang, Y., Huang, Y., Ellis, G. S., Wang, Y., Kralert, P. G., Gillaizeau, B., . . . Hwang, R. (2005). A kinetic model for thermally induced hydrogen and carbon isotope fractionation of individual n-alkanes in crude oil. *Geochimica et Cosmochimica Acta, 69*(18), 4505-4520. doi:10.1016/j.gca.2004.12.026

Tissot, B., & Welte, D. (1984). Petroleum Formation and Occurrence, 2nd edn, 699 pp: Springer, Berlin.

van Maldegem, L. M. (2017). *Molecular and isotopic signatures of life surrounding the Neoproterozoic Snowball Earth events.* (PhD Thesis), Universität Bremen.

Vandenbroucke, M., & Largeau, C. (2007). Kerogen origin, evolution and structure. *Organic geochemistry, 38*(5), 719-833.

Vassoyevich, N., Korchagina, Y. I., Lopatin, N., & Chernyshev, V. (1970). Principal phase of oil formation. *International Geology Review, 12*(11), 1276-1296.

Waldbauer, J. R., Newman, D. K., & Summons, R. E. (2011). Microaerobic steroid biosynthesis and the molecular fossil record of Archean life. *Proc Natl Acad Sci U S A, 108*(33), 13409-13414. doi:10.1073/pnas.1104160108

Wei, J. H., Yin, X., & Welander, P. V. (2016). Sterol Synthesis in Diverse Bacteria. *Front Microbiol, 7*, 990. doi:10.3389/fmicb.2016.00990

Werner, R. A., & Brand, W. A. (2001). Referencing strategies and techniques in stable isotope ratio analysis. *Rapid Communications in Mass Spectrometry, 15*(7), 501-519.

Woese, C. R., Kandler, O., & Wheelis, M. L. (1990). Towards a natural system of organisms: proposal for the domains Archaea, Bacteria, and Eucarya. *Proceedings of the National Academy of Sciences, 87*(12), 4576-4579.

Chapter 2

Materials and methods

2.1 Samples

This thesis is based on Paleoproterozoic samples of the McArthur and Tawallah Groups from the northern Australian McArthur Basin that hosts the oldest biomarkers so far discovered. For the investigation of ancient biological signatures and paleo-environments (Chapter 4), 45 samples were selected from LV09 drill core, targeting the Lynott Formation (Fm), Reward Dolostone, Barney Creek Fm, and Cooley and Teena Dolostone. Samples were collected in June 2015 and September 2018 at the Northern Territory Geological Survey (NTGS) core library in Darwin, Australia. Maturity influence on compound-specific carbon and hydrogen isotopes is explored in Chapter 5, which is mainly based on samples from four open source drill cores (LV09, GR7, BB5, BB6), also stored at the NTGS core library in Darwin. Organic geochemistry investigation of the McArthur River ore deposit, described in Chapter 6, uses 15 Barney Creek Fm samples from the hanging wall, inter-ore, orebody and foot wall of two drill cores (MRM 2012-03 and BS024-01) from the McArthur River Mine. Chapter 7 is based on 9 Wollogorang Fm samples from two open source drill cores, 14MCDDH001 and 14MCDDH002, stored in Darwin. All analysed samples are provided in Table 2.1.

2.2 Methodology

The biomarker analysis was performed using gas chromatography-mass spectrometry (GC–MS). There are many factors that could affect biomarker distributions such as maturity level, pH conditions, clay catalysis, ecological environments etc. In order to separate these factors and obtain the most reliable geological interpretations, it is better to use biomarker and non-biomarker geochemical parameters together. Therefore, the biomarker study was combined with the following methods:

- X-ray diffraction (XRD) analysis to quantify the mineral composition of the rocks;
- Iron speciation analysis for distinguishing the redox conditions in the water column;
- Rock-Eval analysis for obtaining information about organic matter (OM) sources, quality and thermal maturity. Also, this method (S1 and S2 peaks) could help to differentiate autochthonous and migrated bitumen;
- Compound specific isotope analyses for hydrogen and carbon;
- Nitrogen and organic carbon isotope analyses in collaboration with Michael Kipp from the University of Washington.

2.2.1 Biomarker analysis

Assembly of indigenous biomarker data

It is important to perform so called exterior/interior experiments that provide information about surficial contamination level and the presence of indigenous hydrocarbons. These experiments involve the removal of exterior rock surfaces by diamond cutting (Brocks et al., 2008) and comparison of exterior (E) and interior (I) hydrocarbon contents. The presence of surface contamination is recognised by $E/I >> 1$, whereas $E/I \approx 1$ indicates indigenous hydrocarbons.

In order to evaluate the possible laboratory contaminants, introduced to samples during handling, the cumulative laboratory blanks were analysed. These blanks experienced the whole sequence of procedures along with samples. If no contamination was introduced during laboratory procedure, biomarker concentrations remained below detection limits in the blank.

Sample preparation

Contamination of samples during experimental handling was minimized by combusting all glassware, glass wool and aluminium foil at 300 ºC for 9 h. Metal tools

were rinsed with methanol and dichloromethane (DCM). Silica gel was baked at 280 ºC for 4 h and quartz sand was annealed at 600 ºC for 9 h. This sand was used for cleaning the rock crushing equipment and for the laboratory system blank. Activated copper was washed 3 times with methanol and DCM before usage.

For exterior/interior experiments, samples were cut with a solvent-cleaned precision diamond wafering saw (Buehler IsoMet 1000) or a wet table saw (Nortel Machinery Inc.), depending on sample size and shape. Then exterior and interior rock parts were ground to a < 240-mesh powder using a Rocklabs iron puck mill. The mill was cleaned before use by crushing wet annealed quartz sand for 3 minutes and then rinsing with methanol and DCM. Between samples the mill was cleaned by grinding annealed quartz sand.

Extraction and fractionation of bitumens

Bitumen was extracted from rock powder with a Dionex Accelerated Solvent Extractor (ASE 200) using 90% DCM and 10% methanol. Possible carry-over of samples on the ASE200 was minimized with cleaning cycles between successive runs and analyses of laboratory blanks for each batch of samples. The solvent extracts were reduced in volume to 100 µl under a stream of pure nitrogen gas (N_2). When required, elemental sulphur was removed from the extractable organic matter by filtration over freshly precipitated elemental copper. Extracts were then fractionated into saturated, aromatic, and polar fractions using microcolumn chromatography over annealed and dry-packed silica gel (7 cm). Saturated hydrocarbons were eluted with 1.5 ml of *n*-hexane, aromatic hydrocarbons with 4 ml of *n*-hexane:DCM (1:1, v/v), and polar hydrocarbons with 3 ml of DCM:methanol (1:1, v/v). An internal standard, 18-MEAME (18-methyl eicosanoic acid methyl ester; Chiron Laboratories AS), was added to the saturated and aromatic fractions (1 µg), while 25 ng of D4 (d4-C_{29}-ααα-ethylcholestane; Chiron

Laboratories AS) was added to the saturated fraction only and 50 ng of D10 (d10-pyrene; Chiron Laboratories AS) was added to the aromatic fraction.

Gas chromatography-mass spectrometry (GC–MS)

GC–MS analyses were carried out on an Agilent 6890 GC coupled to a Micromass AutoSpec Premier double-sector MS (Waters Corporation). The GC was equipped with a 60 m DB-5MS capillary column (0.25 mm i.d., 0.25 μm film thickness; Agilent JW Scientific, Agilent Technologies) and helium was used as the carrier gas at a constant flow of 1 ml min^{-1}. Samples were injected in splitless mode into a Gerstel PTV injector at 60 °C (held for 0.1 min) and heated at 260 °C min^{-1} to 300 °C. The MS source was operated at 260 °C in electron ionization mode at 70 eV ionization energy and 8000 V acceleration voltage. The GC oven was programmed from 60 °C (held for 4 min) to 315 °C at 4 °C min^{-1}, with a total run time of 100 min. Full Scan analysis was run for both saturated and aromatic fractions. The concentrations of *n*-alkanes were determined by integration of GC–MS *m/z* 85 signals. Hopanes and methylated hopanes were quantified using metastable reaction monitoring (MRM) analyses using $M^+ \rightarrow 191$ and $M^+ \rightarrow 205$ precursor–product transitions respectively. Triaromatic steroids were quantified using selected ion recording (SIR) of base ion *m/z* 231.2 and 245. Aryl isoprenoids were integrated in SIR mode in *m/z* 134. Because of $FeCl_2$ buildup in the MS ion source, halogenated solvents like DCM might cause deterioration of chromatographic signals (Brocks & Hope, 2013). Therefore, all samples were injected into the GC–MS column in *n*-hexane.

2.2.2 Compound-specific isotope analyses ($\delta^{13}C$ and $\delta^{2}H$)

Isolation of *n*-alkanes from a mixture prior to compound-specific isotope analyses (CSIA) followed the Brocks lab protocol. *n*-Alkanes were separated from other molecules

of the saturated fraction using 0.5 mg of 5Å zeolite molecular sieve (Grace Davison), which was activated at 300 ºC for 9 hours. The molecular sieve and sample were mixed with cyclohexane (3.5 ml), sealed, vigorously mixed, and kept overnight at 90 ºC on a hot plate. The molecular sieve was filtered (filter paper, rinsed with methanol and DCM), washed with cyclohexane (3 x 1 ml), and air-dried for 2–3 hours. The filtrate (= MNA, molecular non-adduct) was collected. The dry molecular sieve was transferred into a Teflon tube and digested with hydrofluoric acid (HF, 32%, 3 ml) to release the *n*-alkanes. *n*-Alkanes were extracted with 3 x 1 ml *n*-hexane under vigorous shaking. The hexane layer containing the molecular adduct was cleaned from remaining particles and HF over a glass column (pasteur pipette), packed with 1 cm of dry silica gel, and eluted with *n*-hexane. Molecular adducts were reduced in volume (~100 µl) and the isotopic composition of *n*-alkanes was analysed as duplicates using gas chromatography–isotopic ratio mass spectroscopy (GC–IRMS) at Geoscience Australia, Canberra. All $\delta^{13}C$ values are reported in permil (‰) notation relative to Vienna Pee Dee Belemnite (VPDB) using internal standards of perdeuterated *n*-alkanes (C_{16}, C_{20}, C_{24}). The standard deviation from the mean was usually better than 0.4‰. The $\delta^{2}H$ values are reported in delta notation relative to Vienna Standard Mean Ocean Water (VSMOW) using internal standards of fatty acid methyl ester (C_{20}, C_{22}, C_{25}).

2.2.3 Nitrogen and organic carbon isotopes

Organic carbon and nitrogen isotope analyses followed the methods described in Kipp et al. (2018) and Stüeken (2013), and were measured at the IsoLab facilities in the Department of Earth and Space Sciences of the University of Washington by Michael Kipp. Rock powders were decarbonised with 6 N HCl, then samples were rinsed in 18 MΩ DI-H_2O and dried in an oven at 60 °C. Carbonate content was evaluated from the

difference in mass of samples before and after decarbonation. For measuring the $\delta^{15}N$ and $\delta^{13}C_{ker}$, carbonate-free powders were analysed with a Costech ECS 4010 Elemental Analyser coupled to a Thermo Finnigan MAT 253 continuous flow isotope-ratio mass spectrometer. Combustion was performed with 20 ml O_2 at 1000 °C, and a magnesium perchlorate trap was used to remove water from the gas stream. The international USGS40 and USGS41 standards were used along with three internal standards (two glutamic acids 'GA1' and 'GA2', and dried salmon 'SA'). Isotopic data are expressed in delta notation relative to air for nitrogen and VPDB for carbon. Analytical blanks resulting from combustion were subtracted from isotopic data.

2.2.4 Isolation of kerogen

Kerogen isolation for HYC samples was undertaken by the author at Geoscience Australia following the in-house protocol. The analysis was performed on 10–11g rock powder that has already undergone solvent extraction with ASE 200 at ANU. For each batch of samples to be analysed, an additional internal standard was processed. This standard is a dilution of one part extracted rock powder (Julia Creek) to 10 parts washed quartz.

Decarbonation of extracted powders is achieved using 15% hydrochloric acid (HCl), with samples then centrifuged 3 times with deionised water (2000 rpm for 5 minutes) for neutralising the HCl. 48% Hydrofluoric acid (HF) was used to remove silicate minerals. Samples were mixed with 100 ml of deionised water and 100 ml of HF and further stirred at room temperature on an agitator plate (150 rpm for 7 hours). The mixture was then allowed to stand for 6 hours, the dilute HF solution decanted and fresh solution (50 ml of water and 50 ml of HF) added. The stirring procedure was repeated and 20 ml of warm (50 °C) saturated boric acid (H_3BO_3) solution was added to each sample, which was still

immersed in HF solution. After the stirring procedure was repeated and samples were settled for 6 hours, the dilute HF/Boric acid solution was siphoned off. Samples were washed with warm (50 °C) deionised water 4 times using centrifugation (2000 rpm for 5 minutes). Treatment with 15 ml of 15% HCl in a water bath set to 65 °C for 2 hours was used as an additional step to remove carbonates. To neutralise the HCl, samples were centrifuged with warm deionised water 3 times. For removal of heavy minerals, 20 ml of sodium polytungstate solution was added to each sample, mixed well and centrifuged. The floats and sinks were collected in separate test tubes and washed with warm deionised water. The kerogen material was dried in an oven at 45 °C.

2.2.5 Rock-Eval pyrolysis

Total organic carbon (TOC) content and hydrocarbon potential were measured using a Rock-Eval 6 Turbo™ (Vinci Technologies, France) at Geoscience Australia or Lomonosov Moscow State University following the methodology described in Jarrett et al. (2018). The analysis was performed on 60 mg of bulk rock powder or 3 mg of isolated kerogen. The samples underwent pyrolysis and combustion. The initial pyrolysis oven temperature was set at 300 °C (held for 5 minutes) and then ramped to 650 °C with 25 °C per minute rate. For the oxidation oven, the temperature was held at 400 °C for 3 minutes followed by a ramping to 850 °C at 20 °C per minute, with a final hold time of 5 minutes. The flame ionisation detector (FID) was calibrated by running IFP standard ‘IFP 160000’. For each batch of samples, the analysis blanks were run and later automatically subtracted from sample data.

The main parameters obtained with this method are S1 (free hydrocarbons), S2 (hydrocarbon potential), S3 peaks (CO_2 potential), Tmax (the pyrolysis temperature at the S2 peak maximum) and TOC (total organic carbon). Also, important indices are

calculated - the hydrogen index (HI = S2 peak area/TOC), oxygen index (OI = S3 peak area/TOC) and production index (PI = S1/(S1+S2)).

2.2.6 XRD

X-ray diffraction (XRD) analyses were undertaken at the Department of Earth Sciences, University of Oxford by Brooke Johnson. The analysis followed the methodology described in Tosca et al. (2010).

2.2.7 Iron speciation

Iron speciation analyses were performed in the Cohen Laboratories of the School of Earth and Environment, University of Leeds by Jordan Kinsley. The methodology was established by Poulton and Canfield (2005). The 'highly-reactive' Fe fraction (Fe_{HR} = Fe_{carb} + Fe_{ox} + Fe_{mag} + Fe_{py}) was evaluated using the sequential extraction individually targeting different iron pools. Carbonate-associated Fe (Fe_{carb}) was extracted with sodium acetate at pH 4.5 for 48 hours; ferric (oxyhydr)oxides (Fe_{ox}) – with sodium dithionite at pH 4.8 for 2 hours; and magnetite (Fe_{mag}) – with ammonium oxalate for 6 hours. Concentrations of Fe fractions (Fe_{carb}, Fe_{ox}, and Fe_{mag}) were quantified using Atomic Absorption Spectroscopy (AAS) against a set of standards. Pyrite-associated iron (Fe_{py}) was extracted separately with chromous chloride distillation and Fe_{py} concentration was measured by weighing precipitated Ag_2S. The ratio of Fe_{HR} to the total pool of iron (Fe_T) distinguishes between anoxic (Fe_{HR}/Fe_T >0.38), equivocal (Fe_{HR}/Fe_T = 0.22–0.38), and oxic (Fe_{HR}/Fe_T <0.22) water-column conditions (Poulton & Canfield, 2005). The degree of pyritization of the Fe_{HR} pool provides more specific information about anoxic depositional environments with Fe_{py}/Fe_{HR} ratios >0.7 and <0.7 indicating sulphidic and ferruginous systems, respectively (Poulton & Canfield, 2011).

Table 2.1. Dataset of analysed McArthur Basin samples.

Formation	ID	Chap. 5 ID	Drill core	Depth, m	Biomarkers	CSIA	$\delta^{13}C_{ker}$, $\delta^{15}N$	Rock-Eval	Fe speciation	XRD
LV09, chapters 4 and 5										
Lynott	19G016i		LV09	271.95	+					
	19G017i		LV09	275.76	+					
	18G014i		LV09	279.35	+			+	+	+
	18G015i		LV09	289.85	+			+	+	+
	19G018i		LV09	295.3	+					
	19G001i		LV09	313.43	+		+		+	
	19G002i		LV09	330.4	+		+		+	
	19G003i		LV09	338.8	+		+		+	
	19G004i		LV09	341.1	+		+		+	
	19G005i		LV09	365.2	+		+		+	
Reward	19G006i		LV09	371.76	+		+		+	
	19G007i		LV09	376.4	+		+		+	
Barney Creek	12B117		LV09	382.22	+					
	18G001i		LV09	393.7	+			+	+	+
	18G002i		LV09	402.4	+		+	+	+	+
	18G003i		LV09	406.7	+		+	+	+	+
	18G004i	#1	LV09	414.75	+	$\delta^{13}C$	+	+	+	+
	12B118		LV09	423.1	+					
	18G005i	#2	LV09	429.7	+	$\delta^{13}C$, $\delta^{2}H$	+	+	+	+
	18G008i		LV09	443.7	+		+	+	+	+
	17G002i	#3	LV09	450.00	+	$\delta^{13}C$, $\delta^{2}H$	+	+	+	+
	19G008i		LV09	452.1	+		+		+	
	19G009i		LV09	457.2	+		+		+	
	18G009i	#4	LV09	461.83	+	$\delta^{13}C$, $\delta^{2}H$	+	+	+	+
	19G010i		LV09	465.3	+		+		+	
	17G007i	#5	LV09	470.7	+	$\delta^{13}C$	+	+	+	+
	19G011i		LV09	474.4	+		+		+	
	17G008i	#6	LV09	477	+	$\delta^{13}C$, $\delta^{2}H$	+	+	+	+
	17G009i	#7	LV09	478.2	+	$\delta^{13}C$, $\delta^{2}H$	+	+	+	+
	17G001i	#8	LV09	485.00	+	$\delta^{13}C$, $\delta^{2}H$	+	+	+	+
	17G010i	#9	LV09	489	+	$\delta^{13}C$, $\delta^{2}H$	+	+	+	+
	12B119		LV09	492.98	+					
	18G007i	#10	LV09	494.5	+	$\delta^{13}C$, $\delta^{2}H$	+	+	+	+
	18G006i	#11	LV09	494.6	+	$\delta^{13}C$, $\delta^{2}H$	+	+	+	+
	18G010i	#12	LV09	498.88	+	$\delta^{13}C$, $\delta^{2}H$	+	+	+	+
	19G012i		LV09	506	+		+		+	
Cooley	19G013i		LV09	515.35	+		+		+	
	18G016i		LV09	522.68	+		+	+	+	+
	18G017i		LV09	527.32	+		+	+	+	+
	18G018i		LV09	542.61	+		+	+	+	+
Teena	18G019i		LV09	552.62	+		+	+	+	+
	19G014i		LV09	558.9	+		+		+	
	18G020i		LV09	561.5	+		+	+	+	+
	17G005i		LV09	577	+		+	+	+	+
	19G015i		LV09	578.5	+		+		+	

Formation	ID	Chapter 6/5 ID	Drill core	Depth, m	Biomarkers	CSIA	$\delta^{13}C_{ker}$	Rock-Eval	Fe speciation	XRD
HYC, chapters 5 and 6										
Barney Creek	17G013i	#1/#20	BS024-01	16.4	+	$\delta^{13}C$, $\delta^{2}H$	+	+		
	17G019i	#2/#21	BS024-01	41.5	+	$\delta^{13}C$	+	+		
	19G019i	#3	BS024-01	63.5	+	$\delta^{2}H$				
	19G020i	#4	BS024-01	85.7	+					
	17G020i	#5/#22	BS024-01	105.1	+	$\delta^{13}C$, $\delta^{2}H$	+	+		
	17G021i	#6	BS024-01	146.1	+			+		
	19G023i	#7	BS024-01	167.5	+					
	19G021i	#8	BS024-01	191.1	+					
	17G011i	#9	MRM 2012-03	157.8	+			+		
	17G018i	#10	BS024-01	201.1	+			+		
	17G016i	#11	BS024-01	210	+			+		
	17G017i	#12	BS024-01	215.7	+		+	+		
	17G014i	#13	MRM 2012-03	190.4	+	$\delta^{13}C$, $\delta^{2}H$	+	+		
	17G015i	#14	MRM 2012-03	197.9	+	$\delta^{13}C$, $\delta^{2}H$	+	+		
	17G012i	#15/#23	MRM 2012-03	210.8	+	$\delta^{13}C$	+	+		
Wollogorang Formation, chapter 7										
Wollogorang	18G021i	#3	14MCDDH001	53.52	+			+		
	18G022i	#5		65	+			+		
	18G023i	#7		70.6	+	$\delta^{13}C$, $\delta^{2}H$		+		
	18G024i	#8		75.4	+			+		
	18G025i	#9		79.7	+			+		
	18G026i	#1	14MCDDH002	72.15	+			+		
	18G027i	#2		75	+			+		
	18G032i	#4		87.9	+			+		
	18G028i	#6		99.75	+	$\delta^{13}C$, $\delta^{2}H$		+		

References

Brocks, J. J., Grosjean, E., & Logan, G. A. (2008). Assessing biomarker syngeneity using branched alkanes with quaternary carbon (BAQCs) and other plastic contaminants. *Geochimica et Cosmochimica Acta, 72*(3), 871-888.

Brocks, J. J., & Hope, J. M. (2013). Tailing of chromatographic peaks in GC–MS caused by interaction of halogenated solvents with the ion source. *Journal of chromatographic science, 52*(6), 471-475.

Jarrett, A., Cox, G., Southby, C., Hong, Z., Palatty, P., Carr, L., & Henson, P. (2018). Source rock geochemistry of the McArthur Basin, northern Australia: Rock-Eval pyrolysis data release. Record 2018/024. *Geoscience Australia, Canberra*.

Kipp, M. A., Stüeken, E. E., Yun, M., Bekker, A., & Buick, R. (2018). Pervasive aerobic nitrogen cycling in the surface ocean across the Paleoproterozoic Era. *Earth and Planetary Science Letters, 500*, 117-126.

Poulton, S. W., & Canfield, D. E. (2005). Development of a sequential extraction procedure for iron: implications for iron partitioning in continentally derived particulates. *Chemical Geology, 214*(3-4), 209-221.

Poulton, S. W., & Canfield, D. E. (2011). Ferruginous Conditions: A Dominant Feature of the Ocean through Earth's History. *Elements, 7*(2), 107-112. doi:10.2113/gselements.7.2.107

Stüeken, E. E. (2013). A test of the nitrogen-limitation hypothesis for retarded eukaryote radiation: nitrogen isotopes across a Mesoproterozoic basinal profile. *Geochimica et Cosmochimica Acta, 120*, 121-139.

Tosca, N. J., Johnston, D. T., Mushegian, A., Rothman, D. H., Summons, R. E., & Knoll, A. H. (2010). Clay mineralogy, organic carbon burial, and redox evolution in Proterozoic oceans. *Geochimica et Cosmochimica Acta, 74*(5), 1579-1592.

Chapter 3

Regional geology of the southern McArthur Basin

3.1 Basin evolution and depositional history

The Paleoproterozoic-Mesoproterozoic McArthur Basin covers approximately 180 000 km^2 in the Northern Territory of Australia (Plumb et al., 1980, Jackson et al., 1987). The basin boundaries are represented by the Pine Creek Orogen in the northwest, the Arnhem Province in the northeast, and the Murphy Province in the southeast (Figure 3.1). The McArthur Basin is unconformably overlain by a series of younger basins - Georgina and Carpentaria Basins in the southwest, and Arafura Basin in the north.

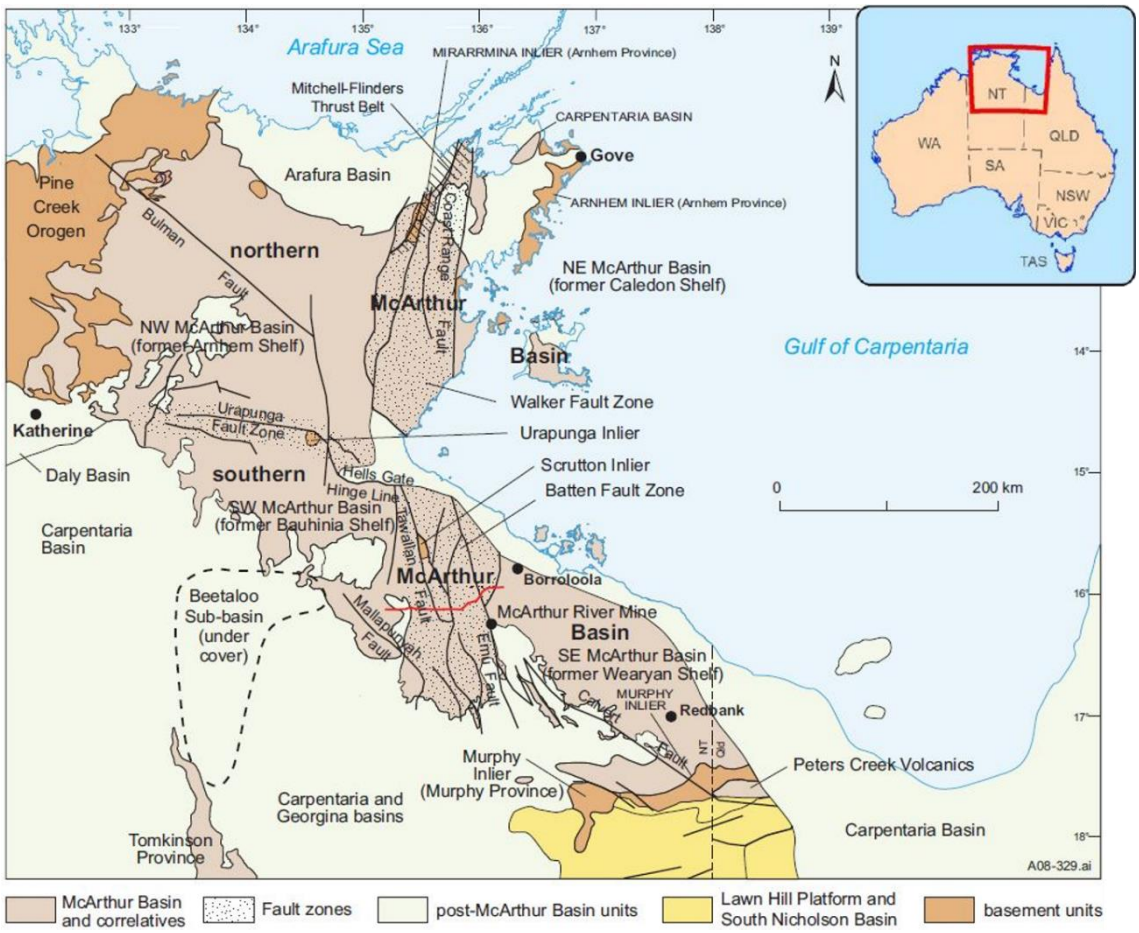

Figure 3.1. Geological settings of the McArthur Basin in northern Australia (after Ahmad et al. (2013)). The position of the southern McArthur Basin deep seismic line 02GA-BT1 (Rawlings et al., 2004) is shown by the solid red line.

Several models about the formation of the McArthur Basin have been proposed by different authors and summarised by Rawlings et al. (2004). However, basin evolution is

still not fully understood. According to the Scott and Rawlings models, the McArthur Basin is a complex basin, which formed in a convergent back-arc tectonic setting due to a variety of subsidence mechanisms (Rawlings et al., 2004).

The main tectonic features of the McArthur Basin are the north-south trending Walker and Batten fault zones, which are separated by the east-west-trending Urapunga Fault Zone (Rawlings et al., 2004). The Urapunga Fault Zone also divides the basin into northern and southern portions. The Walker and Batten fault zones have been interpreted previously as north-trending asymmetric rifts (Plumb & Wellman, 1987). However, the deep seismic survey across the Batten Fault Zone (Figure 3.2), conducted in 2002, showed no evidence for asymmetric rift structures and illustrated up to 8–9 km thick subhorizontal sedimentary succession with zones of faulting (Rawlings et al., 2004).

Plumb (1994) proposed that originally extensional faults experienced several contractional reactivations during basin evolution. The seismic transect (Rawlings et al., 2004) confirms this idea with the presence of an eastward-propagating thrust belt (Figure 3.2). The seismic data (Figure 3.2) illustrate the minor stratigraphic thickening of the McArthur Group adjacent to the complex strike-slip Emu Fault. This increase in thickness might happen in small pull-apart basins, forming negative flower structures. Later post-Roper Group basin inversion resulted in the reactivation of older faults and formation of positive flower structures in the vicinity of the Emu Fault (Rawlings et al., 2004).

3.2 Lithostratigraphy

The McArthur Basin has a complicated lithostratigraphy and contains a relatively undeformed 10–12 km thick succession of siliciclastic and carbonate rocks with volcanic rocks near the base and shallow intrusives (summaries by Ahmad et al., 2013; Munson, 2014). Shallow marine environments are considered the main depositional setting for the McArthur Basin with minor fluvial and lacustrine deposits (Munson, 2014).

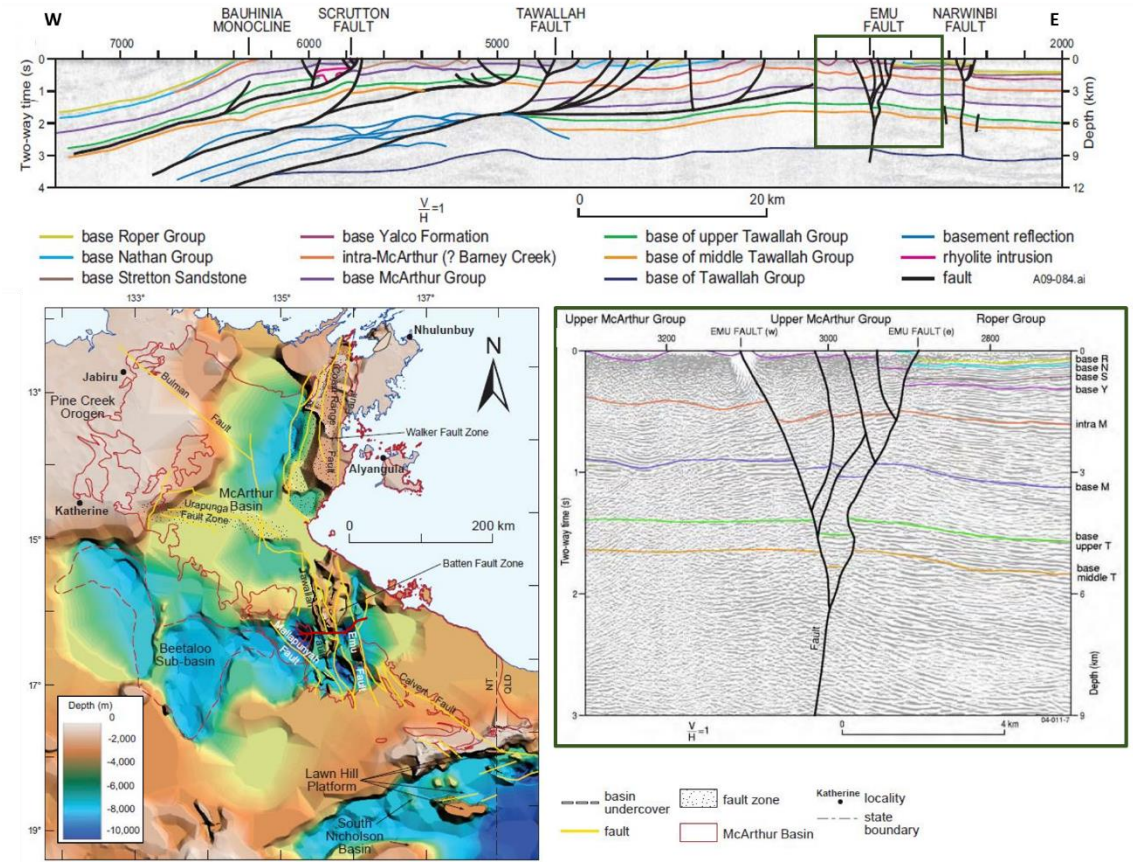

Figure 3.2. Interpreted seismic data for the McArthur Basin deep seismic line 02GA-BT1 (Rawlings et al., 2004: figure 9). The position of the line is shown in Figure 3.1 and SEEBASE depth-to-basement image (after Frogtech Geoscience, 2018), showing interpreted basement highs and depocentres for the McArthur Basin.

The entire basin succession is described in full in Ahmad et al. (2013) and is briefly summarised below. The focus of this study is on the southern McArthur Basin (Figure 3.3). In the Batten Fault Zone, the stratigraphy is subdivided into four major groups,

namely in stratigraphic order, the Tawallah, McArthur, Nathan and Roper groups (Jackson et al., 1987).

The basement unit is represented by the Scrutton Volcanics which are dated at 1851 ± 7 Ma using U/Pb isotopes (Page et al., 2000). These felsic volcanic and plutonic rocks are exposed along the northern Batten Fault Zone (Neudert & McGeough, 1996).

Tawallah Group

The basement unit is unconformably overlain by the Tawallah Group with a maximum thickness of about 6 km. The succession is represented by shallow marine to fluvial red coloured, quartz-rich sandstones with minor carbonates and shales (Rawlings, 1999). The basal age is poorly constrained, however, the top of the succession was dated at 1713 ± 7 Ma (U/Pb, Rawlings, 2004) and 1708 ± 5 Ma (Page et al., 2000) using rare volcanic rocks intercalated with the sediments. The Wollogorang Formation (1730 ± 3 Ma) of the Tawallah Group is about 160 m thick in the southern McArthur Basin and consists of dolostone, sandstone and mudstone (Ahmad et al., 2013), deposited in marine subtidal to supratidal environments on an epeiric platform (Kunzmann et al., 2020; Spinks et al., 2016).

McArthur Group

The McArthur Group, which unconformably overlies the Tawallah Group, is of particular interest because it hosts the famous Zn/Pb ore deposit of the McArthur River Mine and it is also prospective for hydrocarbon exploration. The ~5 km thick succession is dominated by carbonates, mudstones and sandstones (Ahmad et al., 2013; Kunzmann et al., 2019). According to Jackson et al. (1987), depositional environments range from shallow to deep marine and possibly fluvial. The McArthur Group is subdivided by a local unconformity between the Reward Dolostone and Lynott Formation into two subgroups: the Umbolooga and Batten (Figure 3.3). The uppermost part of the

Umbolooga Subgroup is represented by the Barney Creek Formation (Fm). In local sub-basins, which formed along the Emu and Tawallah faults, the Barney Creek Fm thickness can be higher than 1 km (Munson, 2014). The overlying Batten Subgroup is dated at 1625 ± 2 Ma (base) to 1614±4 Ma (top) using U/Pb isotopes (Page et al., 2000) and consists of siliciclastic and dolomitic rocks (Rawlings et al., 2004). The Batten Subgroup marks a significant change in the basin's tectonic regime. The previous extensional tectonics transformed to the compressional regime and this change led to a broad regression (Rawlings et al., 2004).

Nathan Group

The Nathan Group with a thickness of up to 1.6 km rests unconformably on the McArthur Group. The sediments consist of basal breccias and sandstones, overlain by evaporites and stromatolites. It is dated at 1613 ± 4 (base) and 1589 ± 3 (top) Ma using U/Pb isotopes (Rawlings, 1999). The Nathan Group was deposited in marginal marine, peritidal-shelf and continental sabkha environments (Rawlings, 1999).

Roper Group

The Roper Group unconformably overlies the Nathan Group and various older units. The base of the group is dated at 1493±4 Ma (U/Pb, Page et al., 2000). The Roper Group consists of fine- and coarse-grained siliciclastic rocks and represents a series of progradational coarsening upward cycles (Rawlings et al., 2004). Depositional settings for this succession ranged from shallow marine, near shore to shelf environments (Rawlings, 1999).

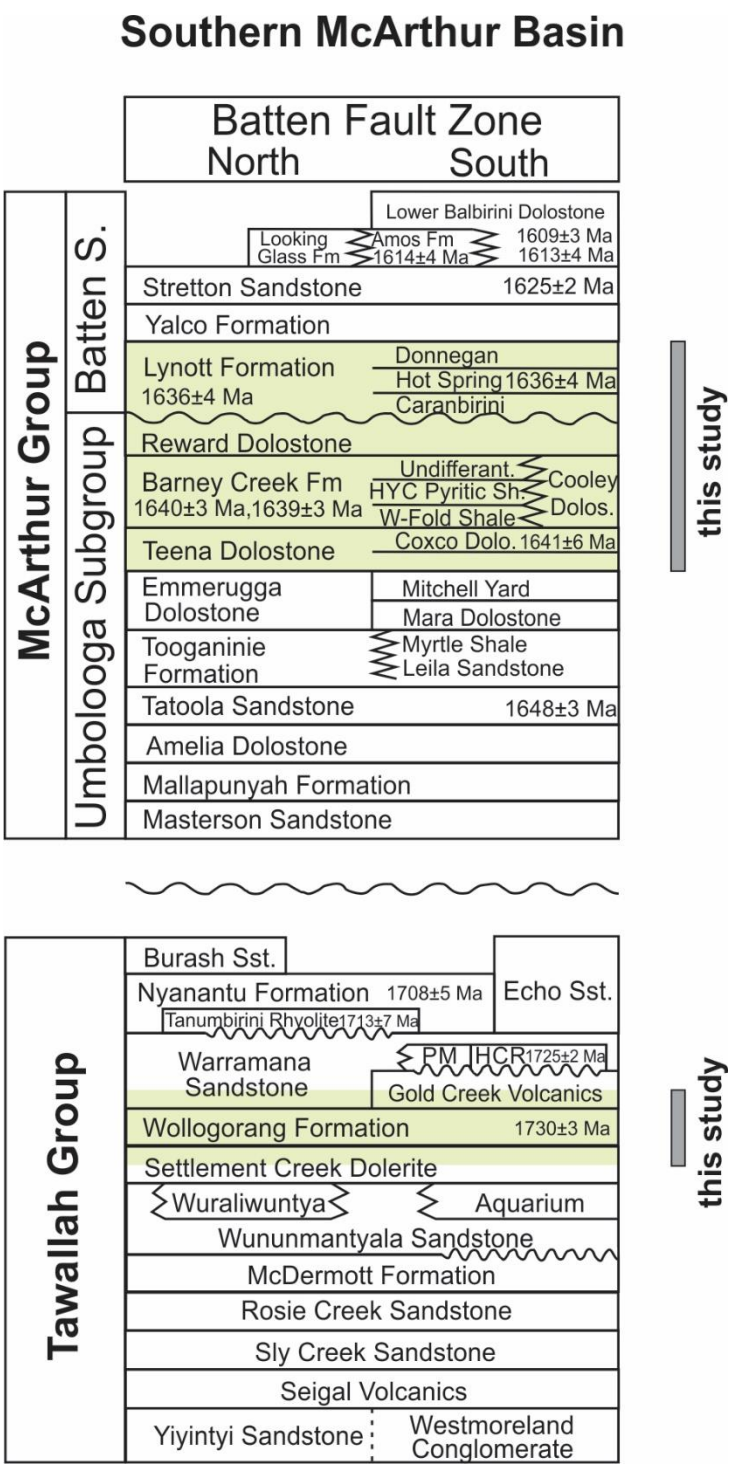

Figure 3.3. Generalized stratigraphy of the Tawallah and McArthur Groups in the southern McArthur Basin. Modified from Ahmad et al. (2013), Page and Sweet (1998) and Page et al. (2000). Formations investigated in this study are highlighted in green.

3.3 Geology of the McArthur Group

The depositional environments of the McArthur Group (~1690 to ~1614 Ma) range from supratidal sabkhas to deep marine (Kunzmann et al., 2019; Rawlings et al., 2004). Based on the seismic survey, Rawlings and colleagues (2004) propose a new geologic model for the McArthur Group. This model suggests a gently east-dipping carbonate ramp with local sub-basins along the Emu Fault. Contrary to most literature, the seismic transect also indicates that deposition was not limited by the Emu Fault, because the McArthur Group succession extends to the east of the fault with significant thickness (Rawlings et al., 2004). The deposition of the McArthur Group occurred during predominant basin subsidence with occasional extensional and compressional periods (Blaikie & Kunzmann, 2020).

The stratigraphic subdivision of the McArthur Group is summarised in Figure 3.3. The middle McArthur Group is a dominantly shallow marine carbonate platform succession that is subdivided by McGoldrick et al. (2010) into three sequences: the oldest Emmerugga, Barney Creek and Lynott depositional sequences. According to McGoldrick et al. (2010), all three depositional sequences are separated by distinctive lithofacies shallowing or local unconformities. The Barney Creek depositional sequence is of particular interest for this study, therefore it will be described in more detail.

Barney Creek Depositional Sequence

The lowermost Teena Dolostone is represented by carbonate platform facies (McGoldrick et al., 2010). In the local subbasins (McGoldrick et al., 2010) and probably across the southern McArthur Basin (Rawlings et al., 2004), the Teena Dolostone is followed by the transitional lithofacies of the W-fold shale Member and deeper water siltstone and carbonaceous shales of the Barney Creek Fm. The Barney Creek Fm is

overlain by the Reward Dolostone that is interpreted by Bull (1998) to be at least partially time-equivalent to the Barney Creek Fm.

The **Teena Dolostone** (1641 ± 6 Ma; Page et al., 2000) consists of mixed carbonate-siliciclastic rocks, breccias, dololutite, dolomitic shale, siltstone and dolarenite (Ahmad et al., 2013). The lower part of the formation formed during basin subsidence, whereas the upper part was deposited in very shallow-water conditions. The Coxco Dolostone Member has been identified in the upper Teena Dolostone based on the presence of 'Coxco Needles' within grey dololutite (Ahmad et al., 2013).

The 1640 ± 3 Ma (Page & Sweet, 1998) **Barney Creek Formation** rests conformably between the Teena Dolostone (below) and the Reward Dolostone (above). The Barney Creek Fm comprises finely laminated to thinly bedded dolomitic, carbonaceous and pyritic siltstone, and shale along with dolostone and locally abundant breccias and tuffs (Jackson et al. 1987). According to Bull (1998) and Kunzmann et al. (2019), the Barney Creek Fm was deposited in a quiet, anoxic, sub-wave-base environment. The Barney Creek Fm and overlying Reward Dolostone record two transgressive-regressive sequences with two maximum flooding surfaces occurring in the Barney Creek Fm (Kunzmann et al., 2019). The thickness of the formation reaches up to 1.2 km in the sub-basins nearby the strike-slip Emu fault (Munson, 2014). The formation thins to the west from the fault zone (<200 m thick) and continues as a relatively thick succession to the east (Rawlings et al., 2004).

In the HYC sub-basin, Jackson et al. (1987) subdivided the Barney Creek Fm into three members: the Cooley Dolostone Member, W-Fold Shale Member and HYC Pyritic Shale Member. Outside the HYC area, the undifferentiated upper part of the Barney Creek Fm overlays these three members (Kunzmann et al., 2019). The Cooley Dolostone Member comprises fault-related chaotic breccia that was locally derived from the

underlying Emmerugga and Teena Dolostones (Munson, 2014). This intraformational unit interfingers with other parts of the Barney Creek Fm along local faults. The W-fold Shale Member consists of green and red dolomitic siltstone and shale, and green vitric tuff (Munson, 2014). This member indicates a transition from the shallow water Coxco Dolostone to the deep water Barney Creek Fm (Large et al., 1998). According to Large et al. (1998), interlayering of green and red deposits represents the mixing of anoxic deep waters with oxic shallow waters. The HYC Pyritic Shale Member that overlies the W-fold member is represented by carbonaceous and pyritic siltstone and shale. Most sediments are finely laminated with occasional presence of graded beds, ripple marks, flame structures and soft-sediment slumping (Jackson et al., 1987). The undifferentiated upper part of the Barney Creek Fm contains dolomitic siltstone and dolarenite (Jackson et al., 1987; Kunzmann et al., 2019).

The **Reward Dolostone**, which generally conformably overlies the Barney Creek Fm, consists of dololutite, silty dololutite, minor dolarenite, shale and local dolostone breccia (Ahmad et al., 2013). This formation was deposited in a peritidal, shallow subtidal to shallow open sea setting (Ahmad et al., 2013).

Lynott Depositional Sequence

The **Lynott Formation** (1636 ± 4 Ma; Page et al., 2000) overlies the Reward Dolostone either conformably or unconformably (Ahmad et al., 2013). The Lynott Fm is subdivided into the Caranbirini, Hot Spring and Donnegan members (Jackson et al., 1987). The Hot Spring Member, represented by stromatolitic dolostone, dolarenite and dololutite, was deposited in subtidal to intertidal environments (Jackson et al., 1987; Kunzmann et al., 2019).

References

Ahmad, M., Dunster, J. N., & Munson, T. J. (2013). Chapter 15: McArthur Basin: in Ahmad M and Munson TJ (compilers).'. *Geology and mineral resources of the Northern Territory'. Northern Territory Geological Survey, Special Publication, 5*.

Blaikie, T., & Kunzmann, M. (2020). Geophysical interpretation and tectonic synthesis of the Proterozoic southern McArthur Basin, northern Australia. *Precambrian Research, 343*, 105728.

Bull, S. (1998). Sedimentology of the Palaeoproterozoic Barney Creek formation in DDH BMR McArthur 2, southern McArthur basin, northern territory. *Australian Journal of Earth Sciences, 45*(1), 21-31.

Frogtech Geoscience (2018). SEEBASE® study and GIS for greater McArthur Basin. *Northern Territory Geological Survey, Digital Information Package* DIP 017.

Jackson, M., Muir, M. D., & Plumb, K. A. (1987). *Geology of the southern McArthur Basin, Northern Territory* (Vol. 220): Australian Government Publishing Service.

Kunzmann, M., Crombez, V., Catuneanu, O., Blaikie, T. N., Barth, G., & Collins, A. S. (2020). Sequence stratigraphy of the ca. 1730 Ma Wollogorang Formation, McArthur Basin, Australia. *Marine and Petroleum Geology, 116*, 104297.

Kunzmann, M., Schmid, S., Blaikie, T. N., & Halverson, G. P. (2019). Facies analysis, sequence stratigraphy, and carbon isotope chemostratigraphy of a classic Zn-Pb host succession: The Proterozoic middle McArthur Group, McArthur Basin, Australia. *Ore Geology Reviews, 106*, 150-175.

Large, R. R., Bull, S. W., Cooke, D. R., & McGoldrick, P. J. (1998). A genetic model for the HYC Deposit, Australia; based on regional sedimentology, geochemistry, and sulfide-sediment relationships. *Economic Geology, 93*(8), 1345-1368.

McGoldrick, P., Winefield, P., Bull, S., Selley, D., & Scott, R. (2010). Sequences, synsedimentary structures, and sub-basins: the where and when of SEDEX zinc systems in the southern McArthur Basin, Australia. *Soc. Econ. Geol. Spec. Publ, 15*, 1-23.

Munson, T. (2014). *Petroleum geology and potential of the onshore Northern Territory, 2014*: Northern Territory Geological Survey.

Neudert, M., and McGeough, M. (1996). A new tectonostratigraphic framework for the deposition of the upper McArthur Group, NT, *In*: BAKER, T. ed. *MIC '96: The McArthur, Mt Isa, Cloncurry Minerals Province – New Developments in Metallogenic Research, Extended Conference Abstracts.'Contribution,* pp. 90 – 93. EGRU

Page, R. W., Jackson, M. J., & Krassay, A. A. (2000). Constraining sequence stratigraphy in north Australian basins: SHRIMP U–Pb zircon geochronology between Mt Isa and McArthur River. *Australian Journal of Earth Sciences, 47*(3), 431-459. doi:10.1046/j.1440-0952.2000.00797.x

Page, R. W., & Sweet, I. P. (1998). Geochronology of basin phases in the western Mt Isa Inlier, and correlation with the McArthur Basin. *Australian Journal of Earth Sciences, 45*(2), 219-232. doi:10.1080/08120099808728383

Plumb, K. (1994). *Structural evolution of the McArthur Basin, NT.* Paper presented at the Australasian Institute of Mining and Metallurgy (AusIMM) annual conference:'Australian mining looks north, the challenges and choices', Darwin, NT.

Plumb, K., Derrick, G., & Wilson, I. (1980). Precambrian geology of the McArthur River—Mount Isa region, northern Australia. *The geology and geophysics of northeastern Australia*, 71-88.

Plumb, K., & Wellman, P. (1987). McArthur Basin, Northern Territory: mapping of deep troughs using gravity and magnetic anomalies. *BMR Journal of Australian Geology and Geophysics, 10*(3), 243-251.

Rawlings, D., Korsch, R., Goleby, B., Gibson, G., Johnstone, D., & Barlow, M. (2004). The 2002 southern McArthur Basin seismic reflection survey. *Geoscience Australia, Record, 17*, 78.

Rawlings, D. J. (1999). Stratigraphic resolution of a multiphase intracratonic basin system: The McArthur Basin, northern Australia. *Australian Journal of Earth Sciences, 46*(5), 703-723. doi:10.1046/j.1440-0952.1999.00739.x

Spinks, S. C., Schmid, S., Pagés, A., & Bluett, J. (2016). Evidence for SEDEX-style mineralization in the 1.7 Ga Tawallah Group, McArthur Basin, Australia. *Ore Geology Reviews, 76*, 122-139. doi:10.1016/j.oregeorev.2016.01.007

Chapter 4

Biological signatures and paleo-environmental reconstructions of the Paleoproterozoic middle McArthur Group, northern Australia

4.1 Introduction

The 1.64 Ga Barney Creek Formation (Fm) in the northern Australian McArthur Basin provides currently the only detailed molecular insights into Paleoproterozoic ecosystems. Previous biomarker studies of the upper Barney Creek Fm from GR7 drill core describe marine restricted environments in the local Glyde River sub-basin with anoxic, sulphate-poor and stratified waters dominated by bacteria (Brocks et al., 2005; Brocks & Schaeffer, 2008; Nettersheim, 2017). While diagnostic eukaryotic steranes were below detection limits in the Barney Creek Fm, Brocks et al. (2005) found abundant triaromatic steroids (TAS). Later, Nettersheim (2017) detected saturated protosterane molecules, lanostane (LA) and cyclosterane (CA), and showed that these primitive steranes are likely the saturated equivalents of the TAS, suggesting that TAS and protosteranes are derived from the same precursors – lanosterol and/or cycloartenol. The exact protosteroid producers in the Barney Creek Fm remain unknown, but they may belong to stem group eukaryotes or bacteria, because a limited number of bacteria can synthesize simple sterols (Lee et al., 2018; Pearson et al., 2003). The discovery of primitive fossil sterol molecules in the Barney Creek Fm (Nettersheim, 2017) records the early stages of sterol evolution.

Nettersheim (2017) found numerous correlations in the GR7 drill core between mineralogy, paleo-redox conditions, and biomarker parameters. He interpreted these cycles with a two-endmember mixing model, in which Barney Creek Fm waters fluctuated frequently, potentially seasonally, between ferruginous and sulphidic conditions, accompanied by intermittent oxidation events. To obtain some information about the ecology of protosteroid producers, we can compare protosteroid abundances in such environmental cycles or different depositional environments. However, due to increasing maturity down core, biomarker data from the GR7 drill core are limited only

to the upper part of the Barney Creek Fm (~250 m out of 883 m). Therefore, we analyse the Barney Creek Fm and circumjacent units from the new LV09001 (LV09) drill core. LV09 was chosen for this study because thermal maturity of the core is within the oil window zone and, therefore, polycyclic biomarkers are exceptionally well preserved throughout the full succession of the Barney Creek Fm and underlying Teena Dolostone. In order to understand the nature and scale of the variations observed by Nettersheim (2017), regional or local, we performed a multi-proxy analysis on samples from LV09 drill core. In this chapter, we combine organic and inorganic proxies to describe biological signatures and paleo-environments of the middle McArthur Group. We will try to provide some insights about the origin of protosteroids and in what type of environments their producers lived.

4.2 Geological setting and samples

Drill core LV09 was drilled in 2009 in the southern McArthur Basin at the Leviathan Anomaly, which is located 40 km south of the McArthur River Mine (HYC) and 80 km south of Borroloola (Figure 4.1). The core intersected 606.2 m of sediments including Paleoproterozoic McArthur Group deposits, with 26.8 m of the Emmerugga Dolostone at its base, 27.1 m of the Teena Dolostone, 41.3 m of the Cooley Dolostone Member, 130.7 m of the Barney Creek Fm, 10.1 m of the Reward Dolostone and 227.5 m of the Lynott Fm (Marcus Kunzmann, personal communication). The general geology of the McArthur Group is discussed in Chapter 3. Depositional environments for LV09 drill core are interpreted to vary between open and restricted shallow marine (Schmid, 2015). This interpretation is consistent with the study by Farkas et al. (2018), who suggested the presence of a temporary basin restriction during the deposition of the organic-rich Barney

Creek Fm in LV09 drill core based on a shift to more radiogenic values of Sr isotopes and lighter $\delta^{13}C$ values. In contrast, the Lynott Fm, Reward, Cooley and Teena Dolostone show less radiogenic values, indicating open marine conditions. However, elevated Sr isotopes in the Barney Creek Fm may also be an artefact due to higher feldspar content (e.g., Veizer, 1989).

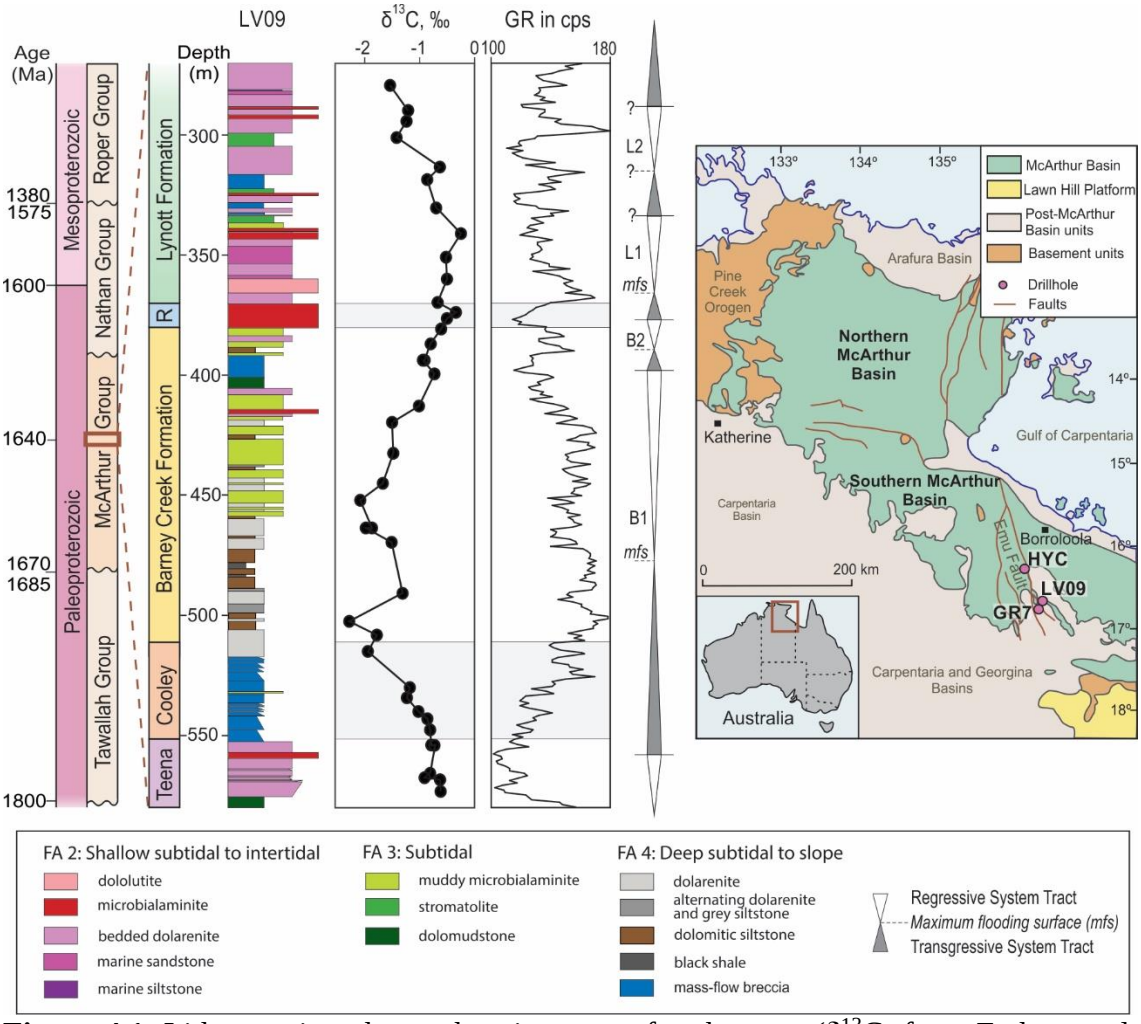

Figure 4.1. Litho-stratigraphy, carbon isotopes of carbonates ($\delta^{13}C$; from Farkas et al. (2018)), gamma ray (GR) curve in counts per second and sequence stratigraphy (Marcus Kunzmann, personal communication) of LV09 drill core; and location of drill cores investigated in this study from the McArthur Basin in northern Australia. R: Reward Dolostone. B1 and B2: Barney Creek Formation sequences. L1 and L2: Lynott Formation sequences.

The litho-stratigraphic interpretation, gamma ray (GR) curve and sequence stratigraphy of LV09 drill core performed by Marcus Kunzmann (personal

communication) are illustrated in Figure 4.1. GR measures natural radioactivity from Th, U and ^{40}K, which are mostly present in shales, organic matter and potassium feldspars. Based on Kunzmann, the Lynott Fm, Reward and Teena Dolostone represent shallow subtidal to intertidal facies, while the Barney Creek Fm and the Cooley Dolostone indicate the deepest water environment with subtidal facies at the top and deep subtidal to slope facies at the base (Figure 4.1). The Barney Creek Fm facies in LV09 are generally shallower than in GR7 drill core. In the local depocenter of the Glyde River sub-basin, GR7 drill core intersects 883 m of the Barney Creek Fm, where depositional environments vary from deep subtidal to slope for the whole preserved formation (Kunzmann et al., 2019).

Samples were collected in June 2015 and September 2018 at the Northern Territory Geological Survey core library in Darwin. For the current project, 45 samples were selected from LV09 drill core for biomarker analysis. 24 samples came from the Barney Creek Fm, 10 from the Lynott Formation, 2 from the Reward Dolostone, 4 from the Cooley Dolostone and 5 from the Teena Dolostone. Additionally, Rock-Eval pyrolysis, XRD, iron speciation, stable carbon ($\delta^{13}C_{org}$) and nitrogen ($\delta^{15}N$) isotope analyses were performed. A detailed methodology for all analyses on the LV09 drill core is presented in Chapter 2.

4.3 Results

The results of inorganic and organic analyses for LV09 drill core are summarized in Table 4.1. The biomarker ratios for all samples are presented in Appendix A.1.

4.3.1 Bulk geochemical characteristics

Figure 4.2 presents the results of X-ray diffraction (XRD) analysis for 24 samples (the raw data are in Appendix A.2). The Barney Creek Fm sediments consist of variable contents of dolomite and silicate minerals. Maximum dolomite content is 85 wt%. Most samples have a significant proportion of dolomite, with 69% (11 out of 16) of samples yielding more than 15 wt%. The other main mineral constituents are quartz (10 to 57%) and feldspars (0 to 42%). XRD data implies that some samples contain up to 20% of pyrite, while the pyrite content should be much lower based on optical inspection of the corresponding rock specimens. Due to these artefacts of unknown origin, and the low number of XRD measurements relative to biomarker analyses, we have excluded the XRD data from statistical evaluation.

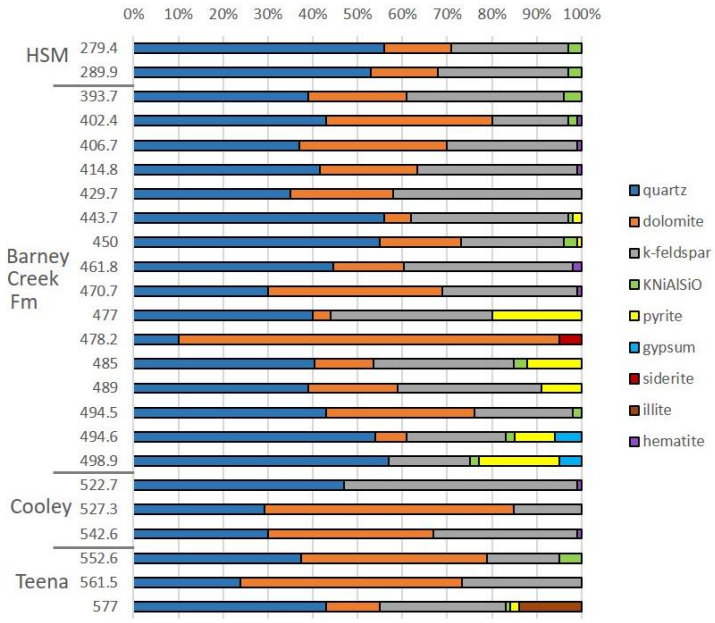

Figure 4.2. Mineralogical composition of LV09 samples (depth in meters) as identified by XRD. Values are normalized to 100%. HSM: Hot Spring Member of the Lynott Fm.

Table 4.1. Bulk geochemical and biomarker parameters for LV09 drill core.

Formation	Lynott	Reward	Barney Creek	Cooley	Teena
Depth, m	142.7–365.7	370.2–380.3	380.3–511.0	511.0–552.3	552.3–579.4
Samples (*n*)	10	2	24	4	5
Parameters	Range Average	Range Average	Range Average	Range Average	Range Average
TOC (%)[a]	0.04–2.7 1.05	0.3–2.1 1.2	0.1–3.8 1.7	0.2–1.2 0.7	0.1–6.6 2.4
Tmax (ºC)	430	No data	423–438 432	420–422 421	432–439 438
$\delta^{13}C_{ker}$ (‰)	-33.5 – -28.9 -32.4	-32.6 – -32.5 -32.6	-33.5 – -31.0 -32.9	-33.1 – -32.8 -32.9	-32.3 – -30.2 -31.1
$\delta^{15}N$ (‰)	5.5–6.6 6.0	6.8–7.5 7.2	5.1–7.8 6.4	5.4–6.2 5.6	6.0–8.0 6.8
Pr/Ph[b]	0.5–0.83 0.65	0.51–0.58 0.55	0.34–0.68 0.5	0.32–0.44 0.37	0.41–0.78 0.58
Ts/(Ts+Tm)	0.21–0.48 0.37	0.46–0.49 0.48	0.52–0.64 0.57	0.6–0.62 0.61	0.63–0.66 0.64
MPI-1[c]	0.18–0.79 0.54	0.46–0.51 0.49	0.46–0.73 0.62	0.54–0.75 0.62	0.4–0.77 0.63
GI (%)[d]	1.2–8.1 3.2	2.2–3.3 2.8	3.2–7.5 4.8	5.1–7.3 6.2	3.8–5.6 4.7
2MHI (%)[e]	0.3–2.4 1.3	0.5–0.8 0.7	0.8–2.1 1.4	0.8–1.5 1.3	0.6–1.2 0.9
3MHI (%)[f]	2.4–16.3 8.0	5.4–5.8 5.6	2.7–8.6 4.5	3.1–4.6 4.1	2.4–3.7 3.1
C_{30}DiaH/ (DiaH+H)[g]	0.10–0.16 0.13	0.09–0.12 0.10	0.13–0.27 0.22	0.18–0.26 0.22	0.17–0.20 0.18
HHI (%)[h]	2.3–4.1 3.1	3.5–3.6 3.5	2.7–5.4 3.7	3.4–4.3 3.8	2.3–4.7 3.8
3MeHHI (%)[i]	3.5–6.5 4.9	5.4	3.9–8.4 6.1	4.6–5.5 5.1	4.4–8.6 6.4
Cl/(Cl+Ok)[j]	0.13–0.38 0.21	0.13–0.14 0.13	0.07–0.34 0.17	0.13–0.25 0.19	0.24–0.45 0.34
G/(G+P)[k]	0.20–0.41 0.29	0.19–0.22 0.20	0.14–0.52 0.21	0.22–0.36 0.30	0.28–0.46 0.34
G/Cl[l]	9–71 37	9–21 15	4–138 48	22–30 26	22–221 84
P/Ok[m]	6–49 25	5–14 10	2–129 39	13–19 16	20–417 131
GAIR[n]	0.12–2.25 0.75	0.07–0.31 0.19	0.04–1.44 0.51	0.06–0.22 0.13	0.22–1.08 0.45
PAIR[o]	0.06–1.62 0.48	0.04–0.14 0.09	0.05–0.58 0.25	0.03–0.22 0.09	0.13–0.56 0.24
PS/(PS+hop) (%)[p]	0–2.42 1.23	1.67–1.75 1.71	0.58–2.77 2.18	1.65–2.23 1.96	0.84–5.37 2.45
Mals/(Mals+TAS)[q]	0.03–0.12 0.07	0.09–0.11 0.1	0.01–0.13 0.06	0.04–0.08 0.06	0.01–0.11 0.04
Dals/(Dals+TAS)[r]	0.04–0.24 0.14	0.18–0.20 0.19	0.02–0.27 0.11	0.12–0.21 0.17	0.03–0.21 0.10
AS/(AS+ArH)[s]	0.40–0.92 0.60	0.42–0.62 0.52	0.39–0.90 0.67	0.43–0.71 0.56	0.19–0.86 0.49
FeHR/FeT	0.48–1.03 0.83	0.96	0.48–1.1 0.89	0.85–1.13 0.95	1.0–1.14 1.06
Fepy/FeHR	0.11–0.63 0.28	0.16–0.55 0.35	0.27–0.83 0.59	0.23–0.8 0.53	0.12–0.72 0.4

[a]Total organic carbon from Elemental Analyser. [b]Pr/Ph = Prystane/Phytane. [c]MPI-1 = 1.5*(2MP+3MP)/(P+1MP+9MP). [d]GI = Gammacerane/(gammacerane+C_{30}αβ-hopane). [e]2MHI = C_{31} 2α-methyl-hopane/(C_{31} 2α-methyl-hopane+C_{30} αβ-hopane). [f]3MHI = C_{31} 3β-methyl-hopane/(C_{31} 3β-methyl-hopane+C_{30} αβ-hopane). [g]C_{30}DiaH/(DiaH+H) = C_{30} diahopane/(C_{30} diahopane+C_{30} αβ+βα hopane). [h]HHI = 100*C_{35}(S+R)/Σ$C_{31–35}$(S+R) using 17α,21β(H)-homohopanes. [i]3MeHHI = 100*C_{35}(S+R)/Σ$C_{31–35}$(S+R) using 3β-methylhopanes. [j]Cl/(Cl+Ok), where Cl = chlorobactane and Ok = okenane. [k]G/(G+P), where G = Σ$C_{13–39}$ 2,3,6- trimethyl aryl isoprenoids (AI) and P = Σ$C_{13–39}$ 2,3,4-AI. [l]G/Cl = Σ$C_{13–39}$ 2,3,6-AI/chlorobactane. [m]P/Ok = Σ$C_{13–39}$ 2,3,4-AI/okenane. [n]GAIR = Σ($C_{13–17}$)/Σ($C_{18–22}$) 2,3,6-AI. [o]PAIR = Σ($C_{13–17}$)/Σ($C_{18–22}$) 2,3,4-AI. [p]PS/(PS+hop) = (Σpeaks$_{\mathbf{1-4}}$ lanostane + Σpeaks$_{\mathbf{5–6}}$ cyclosterane)/(Σpeaks$_{\mathbf{1-4}}$ lanostane + Σpeaks$_{\mathbf{5–6}}$ cyclosterane + (dia($C_{29–35}$)+αβ($C_{27–35}$)+βα($C_{29–30}$) hopanes)). [q]Mals/(Mals+TAS) = C_{29}(S+R) monoaromatic lanosteroids/(C_{29}(S+R) Mals+$C_{26–27}$ triaromatic cholesteroids). [r]Dals/(Dals+TAS) = C_{28}(S+R) diaromatic steroid /(C_{28}(S+R) Dals+$C_{26–27}$ TAS). [s]ArS/(ArS+ArH), where ArS (aromatic steroids) = (C_{29}(S+R) Mals+C_{28}(S+R)Dals+$C_{26–27}$TAS) and ArH (aromatic hopanoids) = Σ$C_{32–35}$ benzohopanoids+ Σ$C_{28–30}$(S+R) 28-nor regular monoaromatic 8,14-secohopanoids+Σ$C_{29–30}$ regular monoaromatic 8,14-secohopanoids.

The results of Rock-Eval pyrolysis for LV09 samples are summarized in Table 4.2 and Figure 4.3. Production index (PI) values around 0.1 suggest immature organic matter and the absence of migrated hydrocarbons for all analysed samples (Peters, 1986). In the following, only HI values in the samples with TOC >1% will be discussed, since the HI is probably underestimated in the samples with low TOC due to mineral matrix effects (Dahl et al., 2004). Early mature Lynott Fm samples with Tmax = 430°C have poor potential to generate gas (TOC = 0.13–0.25 wt%). The Barney Creek Fm has fair to excellent potential to generate oil and gas based on TOC in the range 0.11–4.71 wt% and associated HI values. The HI values in the Barney Creek Fm vary from 344 to 515 mg HC/g TOC, indicating predominantly marine oil-prone type II kerogen. Thermal maturity for the samples ranges from immature to early mature in the beginning of the oil window with Tmax = 423–438°C. The Cooley Dolostone samples have fair to very good potential to generate oil and gas with TOC ranging from 0.6 to 2.52 wt% and HI in the range 451–507 mg HC/g TOC. Tmax values indicate that the formation is immature (Tmax ≈ 420°C).

Two Teena Dolostone samples have poor potential to generate gas (TOC = 0.14–0.42 wt%) and one organic rich sample with 5 wt% TOC has excellent potential to generate oil. Thermal maturity is within the early oil window with Tmax = 432–439°C.

Table 4.2. Rock-Eval parameters for LV09 drill core.

Formation	Sample ID	Depth, m	S1[a]	S2[b]	PI[c]	HI[d]	OI[e]	TOC[f] %	Tmax[g] (ºC)
Lynott	18G014i	279.35	0.04	0.44	0.08	176	16	0.25	430
	18G015i	289.85	0	0.11	0.03	85	123	0.13	436*
Barney Creek	18G001i	393.7	0.01	0.03	0.14	27	145	0.11	437*
	18G002i	402.4	0.15	3.80	0.04	349	11	1.09	435
	18G003i	406.7	0.48	3.83	0.11	435	16	0.88	423
	18G004i	414.75	0.36	3.85	0.09	344	16	1.12	430
	18G005i	429.7	0.78	7.32	0.10	466	9	1.57	433
	18G008i	443.7	1.09	9.88	0.10	430	8	2.3	430
	17G002i	450.0	1.32	10.73	0.11	475	5	2.26	435
	18G009i	461.83	1.02	9.30	0.10	417	7	2.23	431
	17G007i	470.7	0.38	3.46	0.10	398	37	0.87	424
	17G008i	477.0	2.69	22.35	0.11	513	1	4.36	434
	17G009i	478.2	0.14	1.61	0.08	268	48	0.6	431
	17G001i	485.0	2.50	24.24	0.09	515	2	4.71	438
	17G010i	489	1.82	17	0.10	450	4	3.78	435
	18G007i	494.5	0.06	0.73	0.08	162	51	0.45	436
	18G006i	494.6	1.56	13.26	0.11	407	4	3.26	433
	18G010i	498.88	1.88	12.12	0.13	359	4	3.38	427
Cooley	18G016i	522.68	1.23	12.77	0.09	507	2	2.52	420
	18G017i	527.32	0.30	2.62	0.10	437	32	0.6	422
	18G018i	542.61	0.78	5.64	0.12	451	18	1.25	421
Teena	18G019i	552.62	0.07	0.84	0.08	200	48	0.42	432
	18G020i	561.5	0.01	0.09	0.14	64	136	0.14	442*
	17G005i	577.0	1.55	23	0.06	459	2	5.01	439

[a]Free hydrocarbons, mg HC/g rock. [b]Generative potential, mg HC/g rock. [c]Production index PI = S1/(S1+S2). [d]Hydrogen index HI = S2*100/TOC, mg HC/g TOC. [e]Oxygen index OI = S3*100/TOC, mg CO_2/g TOC. [f]Total Organic Carbon. [g]Temperature at maximum of S2 peak. * – low S2 (<0.2), Tmax is unreliable.

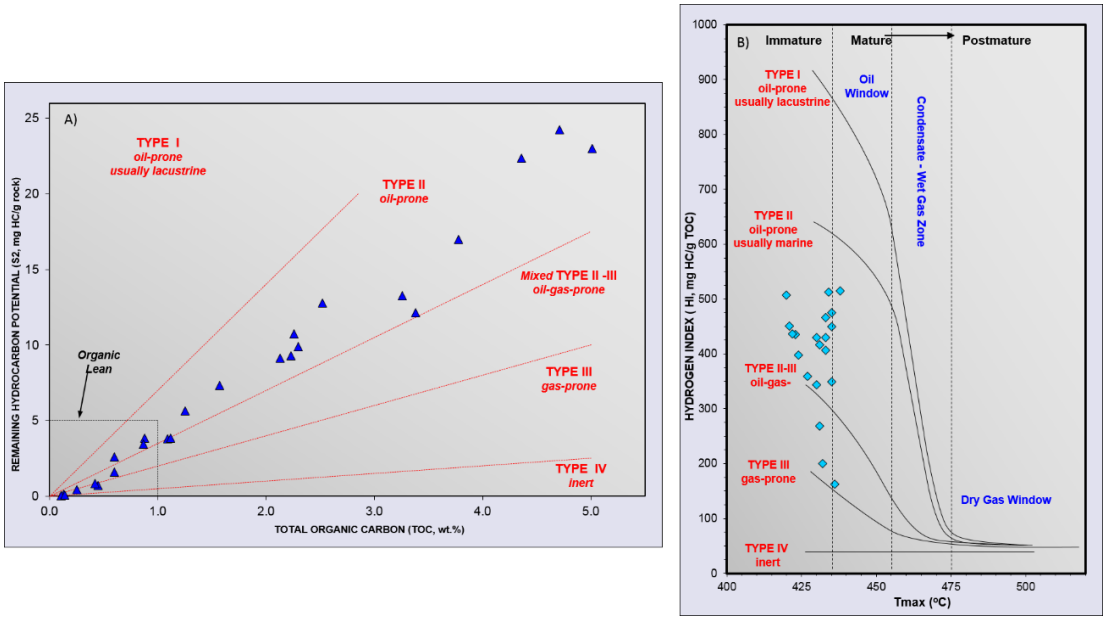

Figure 4.3. Rock-Eval data plots for LV09 drill core. (a) TOC content versus S2 yield; (b) Tmax versus HI.

The results of bulk organic carbon ($\delta^{13}C_{ker}$) and nitrogen ($\delta^{15}N$) isotope analysis for LV09 samples are summarized in Table 4.3. Additionally, Figure 4.4 provides depth trends for a variety of bulk geochemical parameters, including carbon isotopes of carbonates ($\delta^{13}C$) and strontium isotopes ($^{87}Sr/^{86}Sr$) from Farkas et al. (2018), $\delta^{13}C_{ker}$, $\delta^{15}N$, TOC from Elemental Analyser and carbonate content. The $\delta^{13}C_{ker}$ averages at -32.8‰ ± 0.8‰ through the Lynott Fm, Reward Dolostone, Barney Creek Fm and Cooley Dolostone and displays slightly enriched values in the Teena Dolostone of -31.1‰ ± 0.7‰ (Figure 4.4). TOC values range between 0.04–2.7% in the Lynott Fm, 0.3–2.1% in the Reward Dolostone, show an excursion to higher values in the lower Barney Creek Fm (up to 3.8%), decrease in the Cooley Dolostone and the upper Teena Dolostone to 0.1% and reach 6.6% in the lower Teena Dolostone (Figure 4.4; Table 4.3). Carbonate content ('HCl soluble') throughout the whole drill core ranges from 10 to 84% and correlates negatively with TOC ($R^2 = 0.4$; $p < 0.00001$; Figure 4.4). TOC also shows a strong anti-correlation with the sum of carbonate and quartz ($R^2 = 0.64$; $p < 0.00001$). Therefore, variations in TOC might be explained by the dilution of organic matter within samples.

Samples from LV09 drill core show moderately elevated bulk-rock $\delta^{15}N$ values from 5.1 to 8.0‰, consistent with aerobic nitrogen cycling and denitrification occurring in the upper water column (Sigman et al., 1999; Stüeken et al., 2016). C/N values vary between 23.5 and 85.5 and do not correlate with $\delta^{15}N$.

Table 4.3. Bulk isotope data for LV09 drill core

Formation	Sample ID	Depth, m	TOC %	$\delta^{13}C_{ker}$ (‰)	$\delta^{15}N$ (‰)	HCl soluble %	C/N
Lynott	19G001i	313.43	0.25	-33.4	5.5	50	59.5
	19G002i	330.4	0.04	-28.9		35	
	19G003i	338.8	2.65	-32.9	6.0	13	73.3
	19G004i	341.1	0.06	-33.1	5.8	71	50.0
	19G005i	365.2	2.23	-33.5	6.6	14	72.4
Reward	19G006i	371.76	2.06	-32.5	7.5	22	71.3
	19G007i	376.4	0.26	-32.6	6.8	61	56.7
Barney Creek	18G001i	393.7	0.1	-31.0		37	23.5
	18G002i	402.4	0.9	-32.2	6.5	40	59.4
	18G003i	406.7	0.4	-33.3	6.2	38	74.2
	18G004i	414.75	0.9	-33.1	6.5	29	79.4
	18G005i	429.7	1.2	-32.6	6.7	29	81.5
	18G008i	443.7	1.9	-33.0	7.1	10	62.3
	17G002i	450.00	1.9	-32.8	7.1	22	75.8
	19G008i	452.1	0.57	-32.9	6.2	12	56.1
	19G009i	457.2	3.45	-32.8	6.6	12	68.9
	18G009i	461.83	1.8	-33.4	7.8	16	65.7
	19G010i	465.3	0.36	-33.0	5.9	41	47.6
	17G007i	470.7	0.6	-33.0	6.3	58	69.8
	19G011i	474.4	1.68	-32.8	6.6	25	60.6
	17G008i	477	3.8	-32.6	7.1	10	64.8
	17G009i	478.2	0.4	-33.1	5.9	84	53.4
	17G001i	485.00	3.8	-33.5	6.5	21	71.2
	17G010i	489	3.3	-33.5	6.4	27	72.1
	18G007i	494.5	0.5	-32.7	5.6	38	49.1
	18G006i	494.6	3.1	-33.0	6.5	15	66.0
	18G010i	498.88	2.7	-32.5	5.6	11	63.9
	19G012i	506	1.93	-33.1	5.1	15	70.5
Cooley	19G013i	515.35	1.18	-32.8	5.4	24	68.7
	18G016i	522.68		-32.9	5.4		85.5
	18G017i	527.32	0.24	-32.9	5.5	67	63.0
	18G018i	542.61	0.73	-33.1	6.2	58	69.4
Teena	18G019i	552.62	0.33	-30.6	6.2	57	37.3
	19G014i	558.9	0.30	-30.9	8.0	57	41.4
	18G020i	561.5	0.07	-30.2	6.0	67	33.8
	17G005i	577	4.70	-32.3	6.6	15	56.7
	19G015i	578.5	6.62	-31.3	7.4	27	56.5

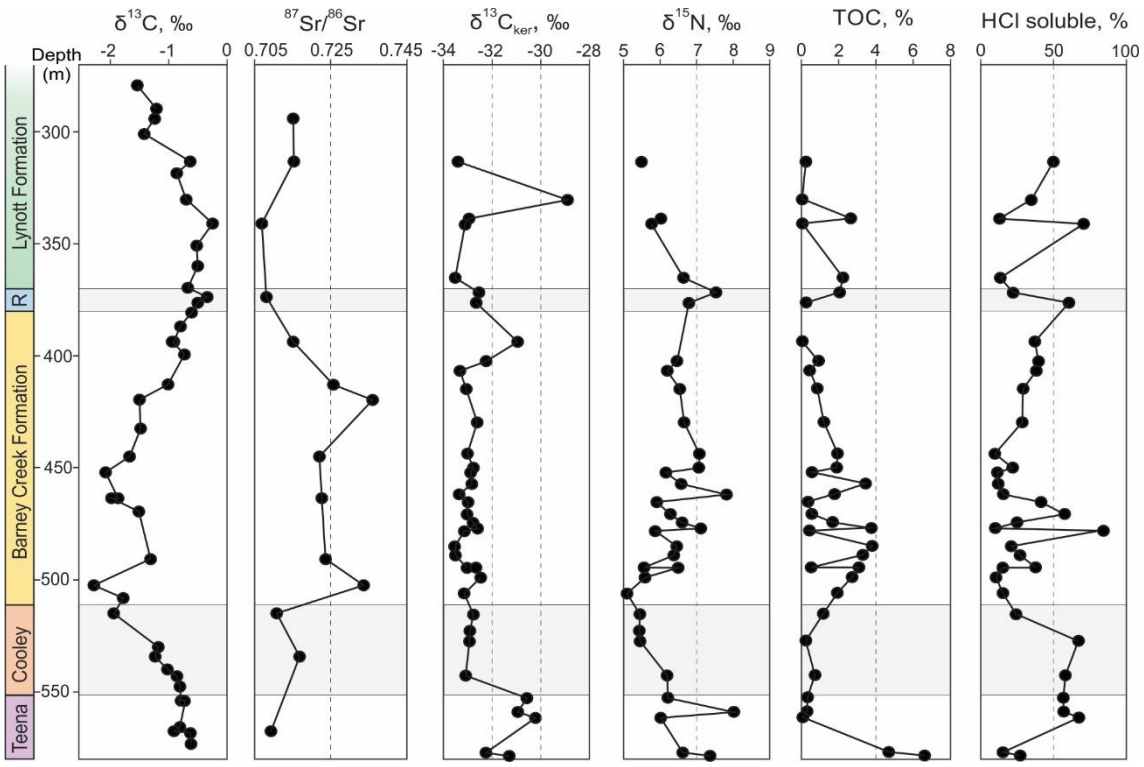

Figure 4.4. Bulk geochemical parameters for LV09 drill core, including carbon isotopes of carbonates ($\delta^{13}C$) and strontium isotopes ($^{87}Sr/^{86}Sr$) from Farkas et al. (2018), $\delta^{13}C_{ker}$, $\delta^{15}N$, TOC from Elemental Analyser and carbonate content. R: Reward Dolostone.

4.3.2 Iron speciation

Table 4.4 presents the results of iron speciation analysis for LV09 drill core on 39 samples from the current study and 21 samples analysed previously by Nettersheim (2017). Generally, iron speciation data in carbonate-rich sediments are unreliable if the total iron concentration (Fe_T) is <0.5% (Clarkson et al., 2014). In LV09 drill core, Fe_T is always >0.5% and varies between 0.54–1.37% in the Lynott Fm and between 0.82–0.95% in the Reward Dolostone. In the Barney Creek Fm, Fe_T increases downcore from 0.62 to 8.3% (473 m) and then decreases back to 1.4% at the bottom of the formation. Fe_T varies in the Cooley Dolostone from 0.84 to 3.9% and in the Teena Dolostone from 0.39 to 2.18%. The ratios of the highly-reactive iron to the total pool of iron (Fe_{HR}/Fe_T) vary between 0.48–1.03% in the Lynott Fm, 0.96 in the Reward Dolostone, 0.48–1.1 in the

Barney Creek Fm, 0.85–1.13 in the Cooley Dolostone and 1.0–1.14 in the Teena Dolostone (Table 4.1; Figure 4.15). Consistent Fe_{HR}/Fe_T >0.38 indicate anoxic depositional environments for the whole LV09 drill core (Poulton & Canfield, 2005). The ratios of the pyrite iron (Fe_{py}) to the Fe_{HR} range between 0.11–0.63% in the Lynott Fm, 0.16–0.55 in the Reward Dolostone, 0.27–0.83 in the Barney Creek Fm, 0.23–0.8 in the Cooley Dolostone and 0.12–0.72 in the Teena Dolostone (Table 4.1; Figure 4.15). The Fe_{py}/Fe_{HR} ratios show strong logarithmic correlation with TOC ($R^2 = 0.8$, logarithmic fit; Figure 4.9d). Based on a strict application of boundary values by Poulton & Canfield (2011), the Lynott Fm and Reward Dolostone with Fe_{py}/Fe_{HR} <0.7 display ferruginous conditions, while the Barney Creek Fm, Cooley and Teena Dolostone represent dominantly ferruginous systems with occasional sulphidic conditions.

Table 4.4. Iron speciation data for LV09 drill core

Formation	Sample ID	Depth, m	Fe_{py}[a]	Fe_{HR}[b]	Fe_T[c]	Fe_{HR}/Fe_T	Fe_{py}/Fe_{HR}
Lynott	18G014i	279.35	0.09	0.39	0.63	0.62	0.23
	18G015i	289.85	0.10	0.73	0.84	0.87	0.14
	19G001i	313.43	0.20	0.79	0.89	0.88	0.25
	12B109*	315.44	0.17	0.46	0.96	0.48	0.37
	19G002i	330.4	0.10	0.72	0.72	1.0	0.14
	19G003i	338.8	0.27	0.49	0.54	0.91	0.55
	19G004i	341.1	0.09	0.85	0.83	1.03	0.11
	12B114*	356.95	0.06	0.56	0.73	0.76	0.11
	19G005i	365.2	0.76	1.21	1.37	0.88	0.63
Reward	19G006i	371.76	0.50	0.91	0.95	0.96	0.55
	19G007i	376.4	0.12	0.79	0.82	0.96	0.16
Barney Creek	12B117*	382.22	0.45	0.92	1.06	0.87	0.49
	18G001i	393.7	0.20	0.62	0.62	1.0	0.32
	18G002i	402.4	0.63	1.11	1.19	0.93	0.57
	18G003i	406.7	0.43	0.88	0.95	0.93	0.49
	18G004i	414.75	0.63	1.17	1.29	0.91	0.54
	12B118*	423.1	1.24	1.89	2.28	0.83	0.65
	18G005i	429.7	0.67	1.22	1.32	0.92	0.55
	12Z171*	430.55	0.94	1.45	1.56	0.93	0.65
	18G008i	443.7	1.46	2.16	2.46	0.88	0.68
	17G002i	450.00	1.10	1.74	1.93	0.90	0.63
	19G008i	452.1	0.71	1.17	1.61	0.73	0.60
	12Z169*	453.65	0.76	1.31	1.57	0.83	0.58
	12Z167*	455.52	0.87	1.19	1.7	0.7	0.73
	12Z168*	455.58	1.25	1.93	2.24	0.86	0.65
	19G009i	457.2	1.42	1.91	2.68	0.71	0.74
	12Z154*	459.25	1.69	2.54	2.93	0.87	0.66

	18G009i	461.83	1.43	2.07	2.18	0.95	0.69
	19G010i	465.3	0.35	1.0	1.18	0.84	0.35
	17G007i	470.7	0.35	1.16	1.20	0.96	0.30
	12Z166*	473.28	2.21	4.01	8.32	0.48	0.55
	19G011i	474.4	2.20	3.10	3.20	0.97	0.71
	17G008i	477	5.53	6.64	6.30	1.05	0.83
	17G009i	478.2	0.52	1.94	1.93	1.01	0.27
	12Z157*	483.95	2.56	3.66	3.74	0.98	0.7
	17G001i	485.00	2.83	3.81	3.43	1.11	0.74
	17G010i	489	2.04	3.05	2.79	1.09	0.67
	12Z155*	489.32	1.13	1.92	2.27	0.85	0.59
	12B119*	492.98	0.77	1.4	1.66	0.84	0.55
	18G007i	494.5	0.68	1.56	1.74	0.90	0.43
	18G006i	494.6	3.34	4.86	4.66	1.04	0.69
	12Z165*	497.87	1.79	2.94	3.42	0.87	0.61
	18G010i	498.88	4.07	5.89	5.88	1.0	0.69
	12Z164*	501.5	1.02	1.61	1.97	0.8	0.58
	12Z163*	501.68	1.61	2.56	3.0	0.81	0.6
	19G012i	506	2.20	3.04	3.07	0.99	0.72
	12Z162*	508.25	0.96	1.67	1.87	0.88	0.56
	12Z161*	508.99	0.65	1.25	1.4	0.83	0.48
Cooley	12Z160*	512.1	0.4	1.04	1.23	0.85	0.38
	19G013i	515.35	0.87	1.58	1.84	0.86	0.55
	12Z158*	517.45	1.71	2.33	2.49	0.94	0.73
	12B120*	522	2.86	3.58	3.9	0.92	0.8
	18G016i	522.68	0.64	1.01	1.13	0.90	0.63
	18G017i	527.32	0.22	0.96	0.93	1.03	0.23
	18G018i	542.61	0.36	0.95	0.84	1.13	0.38
Teena	18G019i	552.62	0.21	0.75	0.66	1.14	0.28
	19G014i	558.9	0.05	0.39	0.39	1.0	0.12
	18G020i	561.5	0.17	0.86	0.83	1.03	0.19
	17G005i	577	1.64	2.4	2.18	1.10	0.68
	19G015i	578.5	1.63	2.26	2.18	1.04	0.72

[a]Pyrite iron. [b]Highly reactive iron. [c]Total iron

* - Samples analysed previously by Nettersheim (2017).

4.3.3 Syngeneity of biomarkers

In general, biomarkers remained below detection limits in the cumulative laboratory blanks. Generally, ~3 mm of the external rock surfaces were removed with a diamond saw from all LV09 samples. To assess the levels of surficial contamination in the drill core, exterior/interior (E/I) ratios were determined on seven samples for *n*-alkanes, isoprenoids, hopanes and cheilanthanes. The presence of surficial contamination is commonly recognised by E/I >>1, whereas E/I ≈ 1 indicates indigenous hydrocarbons and E/I <1 represents evaporation from exterior surfaces (Brocks et al., 2008). Figure 4.5

illustrates the examples of sterane, hopane and *n*-alkane distributions in the interior and exterior parts of samples 17G007 and 17G008.

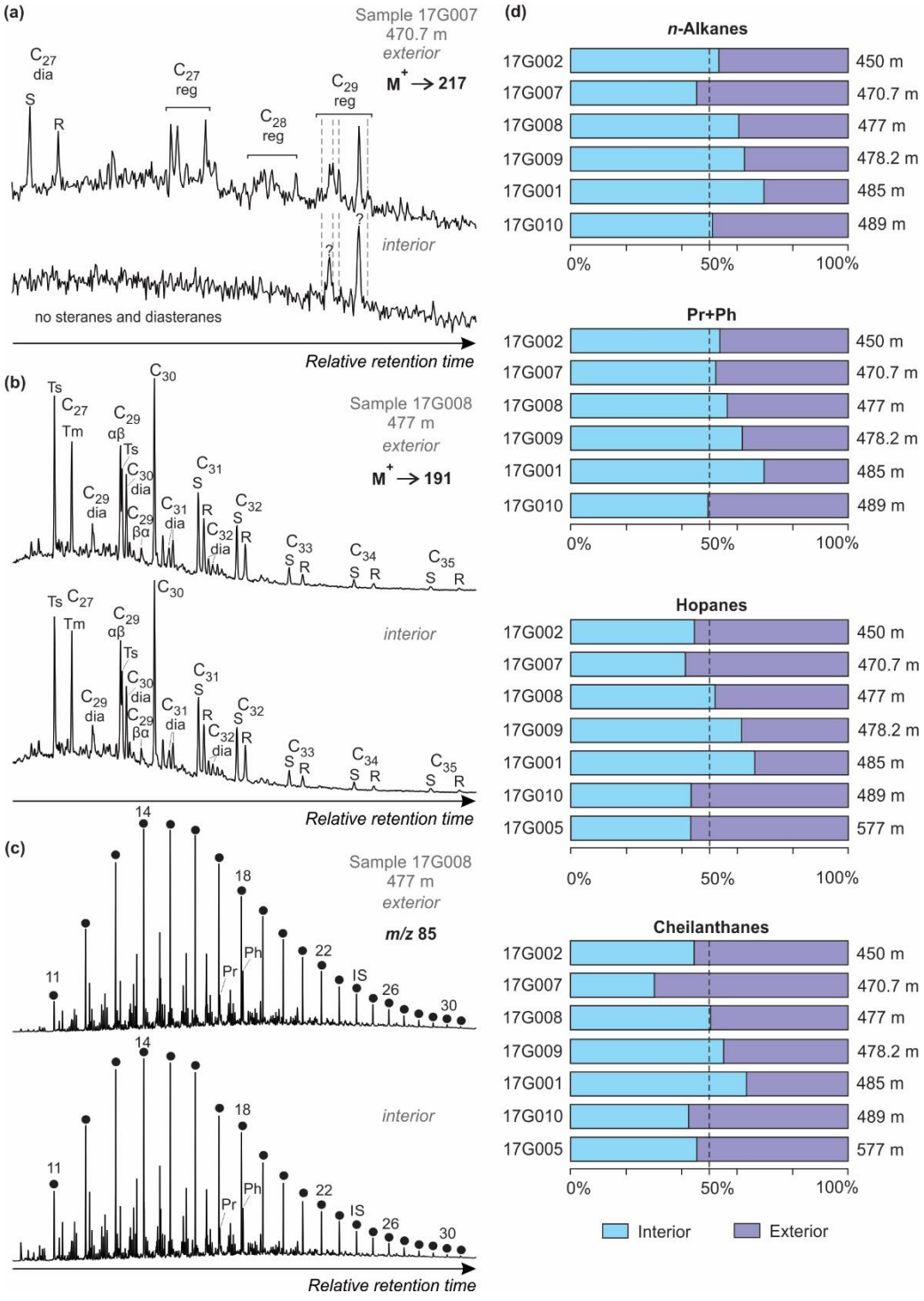

Figure 4.5. The results of exterior/interior experiments on LV09 samples. (a) Summed $M^+ \rightarrow 217$ MRM chromatogram showing sterane distribution. (b) Summed $M^+ \rightarrow 191$ MRM chromatogram showing hopane distribution. (c) Partial *m/z* 85 chromatogram highlighting the distribution of *n*-alkanes. (d) Hydrocarbon distribution between interior and exterior sample portions.

Steranes were not observed in any interior samples or analysed exteriors, except for the exterior of 17G007, where steranes were detected in low abundances and interpreted as contaminants (Figure 4.5a). Absence of regular steranes in all interior LV09 samples and most exteriors indicates that the contamination level of the drill core is very low.

Table 4.5. Biomarker ratios of interior and exterior samples

Sample	Depth	Pr/Ph	Ts/ (Ts+Tm)	GI, %	2MHI, %	3MHI, %	C_{30}DiaH/ (DiaH+H)	HHI, %	$C_{19}T$/ $C_{23}T$
17G002i	450	0.49	0.56	4.43	1.6	3.1	0.24	3.2	1.6
17G002e	450	0.53	0.57	4.57	1.8	4.2	0.24	3.3	1.4
17G007i	470.7	0.38	0.57	4.25	2.1	4.6	0.24	4.4	1.1
17G007e	470.7	0.4	0.57	4.02	2.4	4.2	0.24	4.0	0.4
17G008i	477	0.6	0.57	4.75	1.6	4.0	0.26	3.2	1.6
17G008e	477	0.56	0.58	4.43	1.4	4.0	0.27	2.9	1.4
17G009i	478.2	0.56	0.6	4.24	1.5	3.4	0.18	5.0	1.2
17G009e	478.2	0.56	0.6	4.21	1.1	3.8	0.21	4.8	1.2
17G001i	485	0.5	0.58	4.91	-	2.9	0.26	2.8	1.7
17G001e	485	0.57	0.57	4.93	-	3.3	0.26	2.7	1.3
17G010i	489	0.57	0.57	4.95	1.1	4.6	0.26	2.8	1.4
17G010e	489	0.56	0.59	4.19	1.3	4.4	0.26	2.7	1.4
17G005i	577	-	0.66	3.80	-	2.4	0.19	2.3	1.7
17G005e	577	-	0.65	3.06	-	2.5	0.20	2.4	1.6

Of the seven samples, five showed indigenous distribution of *n*-alkanes with E/I ≈ 1 and E/I <1. *n*-Alkanes in sample 17G007 also indicated indigenous distribution in the range *n*-$C_{12–26}$, but the exterior portion of the sample was slightly contaminated in higher molecular weight *n*-alkanes *n*-$C_{27–33}$ with E/I = 1.7–2.5. Six of seven samples contained indigenous pristane and phytane with E/I ≈ 1. Hopanes also were considered indigenous, since E/I ratios were close to 1 in all analysed samples. Cheilanthanes are largely indigenous with E/I ≈ 1, except for sample 17G007, where E/I = 2.0–3.5 in the range $C_{22–25}$. No significant differences were observed between biomarker abundances in the interior and exterior portions of the samples (Figure 4.5 d). Comparison of biomarker ratios between interiors and exteriors shows that they are nearly identical (Table 4.5), suggesting that surficial contaminants have no impact on the interpretation of biomarker ratios in the analysed samples from LV09 drill core. Overall, interior LV09 samples were

largely unaffected by contamination and E/I experiments were efficient in the removal of surficial contaminants in case they were present.

4.3.4 Saturated fractions

Indigenous extracted bitumens from LV09 drill core are characterized by large unresolved complex mixture (UCM), relatively high methyl-alkane/*n*-alkane ratios, lack of saturated C_{26} to C_{29} steranes and prevalence of hopanes. The total ion chromatograms (TIC) from GC–MS analysis of representative saturated fractions are shown in Figure 4.6.

4.3.4.1 Alkanes, acyclic isoprenoids and biodegradation

One Lynott Fm (19G003), five Barney Creek Fm (12B117, 18G002, 18G004 at the top, 18G006 and 19G012 at the bottom of the formation) and all analysed Reward, Cooley and Teena Dolostone samples are considered moderately (stage 2) biodegraded based on substantially depleted *n*-alkane abundances relative to regular isoprenoids and elevated values of (Pr+Ph)/(*n*-C_{17}+*n*-C_{18})>1 (Figure 4.6; Peters et al., 2005). One Teena Dolostone sample from 577 m depth (17G005) is heavily or severely (stage 3 or higher) biodegraded with no *n*-alkanes and isoprenoids preserved. The (Pr+Ph)/(*n*-C_{17}+*n*-C_{18}) ratios do not co-vary in time series with other biomarker parameters. For example, no correlation was observed between (Pr+Ph)/(*n*-C_{17}+*n*-C_{18}) and Pr/Ph (R^2 = 0.2; p = 0.00042). Therefore, the variability of biomarker ratios is not primarily controlled by biodegradation.

Lynott Fm samples not visibly affected by biodegradation (n = 9) display unimodal distribution of *n*-alkanes in the range C_{10}–C_{31} with a maximum at C_{15} to C_{17} (Figure 4.6, sample 19G005). Barney Creek Fm saturated fractions with (Pr+Ph)/(*n*-C_{17}+*n*-C_{18}) <1 (n = 19) also contain a unimodal distribution of *n*-alkanes ranging from C_{10} to C_{33} with a maximum at C_{14} to C_{20} (Figure 4.6).

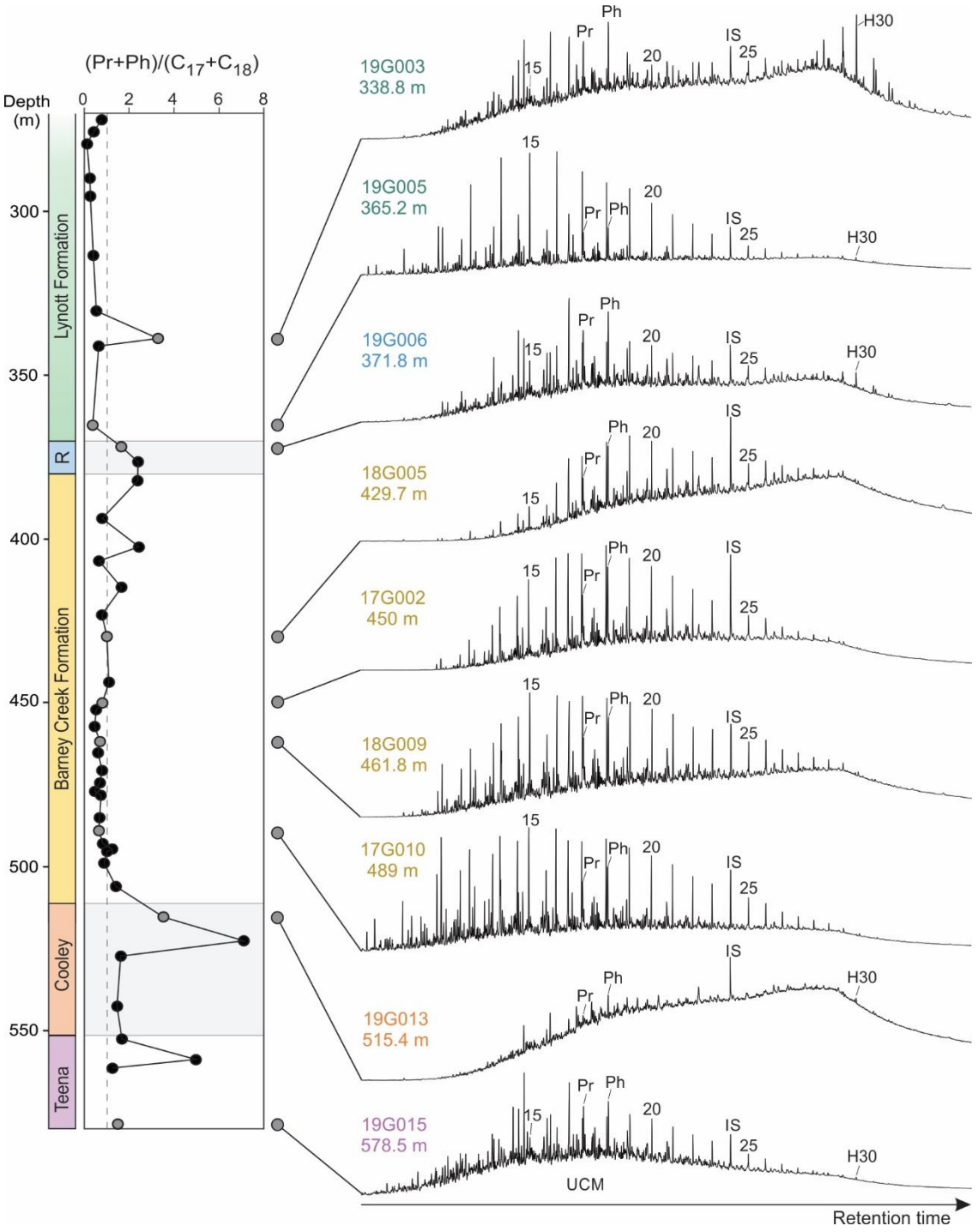

Figure 4.6. Total ion chromatograms (TIC) of the saturated hydrocarbon fractions through all formations in LV09 drill core and depth trend of (Pr+Ph)/(*n*-C_{17}+*n*-C_{18}) ratios. Grey circles on the trend correspond to the TIC profiles displayed. The dotted line in the left panel (Pr+Ph)/(*n*-C_{17}+*n*-C_{18}) = 1 indicates a threshold for moderately biodegraded samples. R: Reward Dolostone; Numbers above peaks represent *n*-alkanes; Pr: pristane; Ph: phytane; IS: internal standard; H30: C_{30} hopane.

Regular isoprenoids pristane (Pr) and phytane (Ph) were detected in significant abundances (Figure 4.6). The Pr/Ph ratio (calculated *m/z* 85 signal areas) decreases from 0.8 to 0.3 through the Teena and Cooley Dolostone. Pr/Ph varies between 0.3–0.7 in the Barney Creek Fm and 0.5–0.6 in the Reward Dolostone. In the Lynott Fm, Pr/Ph slightly increases and varies between 0.5–0.8 (Table 4.1; Figure 4.15).

4.3.4.2 Hopanes, gammacerane and cheilanthanes

In MRM, hopanes were detected in the range from C_{27} to C_{35} with C_{30} 17α,21β-hopane being the most abundant (Figure 4.5b; 4.7). The Ts/(Ts+Tm) ratio consistently increases downcore and varies between 0.21–0.48 in the Lynott Fm, 0.46–0.49 in the Reward Dolostone, 0.52–0.64 in the Barney Creek Fm, 0.60–0.62 in the Cooley Dolostone and 0.63–0.66 in the Teena Dolostone (Table 4.1; Figure 4.13). The moretane ratio (defined as C_{30} βα-hopane/(C_{30} βα-hopane+C_{30} αβ-hopane)) slightly decreases downcore from average 0.08 in the Lynott Fm to average 0.05 in the Teena Dolostone. The homohopane index (HHI, defined as 100*C_{35}(S+R)/Σ$C_{31–35}$(S+R) homohopanes) ranges from 2.3 to 5.4% throughout the core with an average value around 3.6% (Table 4.1; Figure 4.8).

Diahopanes (C_{29}–C_{35} 17α-diahopanes) were detected in all samples (Figure 4.7). The ratio of C_{30} diahopane versus C_{30} hopane (C_{30}DiaH/(DiaH+H)) varies from 0.09 to 0.27 in the LV09 drill core and displays an excursion from lower values in the Teena and Cooley Dolostone to higher values (0.18–0.27) in the Barney Creek Fm between 420–515 m depth and back to lower values in the Lynott Fm and Reward Dolostone (Table 4.1; Figure 4.8). There is a positive correlation (R^2 = 0.53; p < 0.00001) between the C_{30}DiaH/(DiaH+H) and C_{29} Ts/(Ts+H) ratios (Figure 4.9a). The C_{30}DiaH/(DiaH+H) trend also illustrates an apparent anti-correlation with $\delta^{13}C$ (Figure 4.8). However,

measurements of $\delta^{13}C$ (Farkas et al., 2018) and C_{30}DiaH/(DiaH+H) ratios are not aligned in depth, i.e. are largely derived from different sample specimens. Depth trends of $\delta^{13}C$ and C_{30}DiaH/(DiaH+H) have 42 and 45 data points respectively, and only 8 measurements are recorded from matching depths. Therefore, we used an interpolation function in Python to extract missing C_{30}DiaH/(DiaH+H) values from the diahopane trend at depth levels of $\delta^{13}C$ measurements (Figure 4.10; Appendix A.4 for the annotated Python code). The restored C_{30}DiaH/(DiaH+H) ratios show a negative correlation with $\delta^{13}C$ ($R^2 = 0.58$; $p < 0.00001$; Figure 4.10).

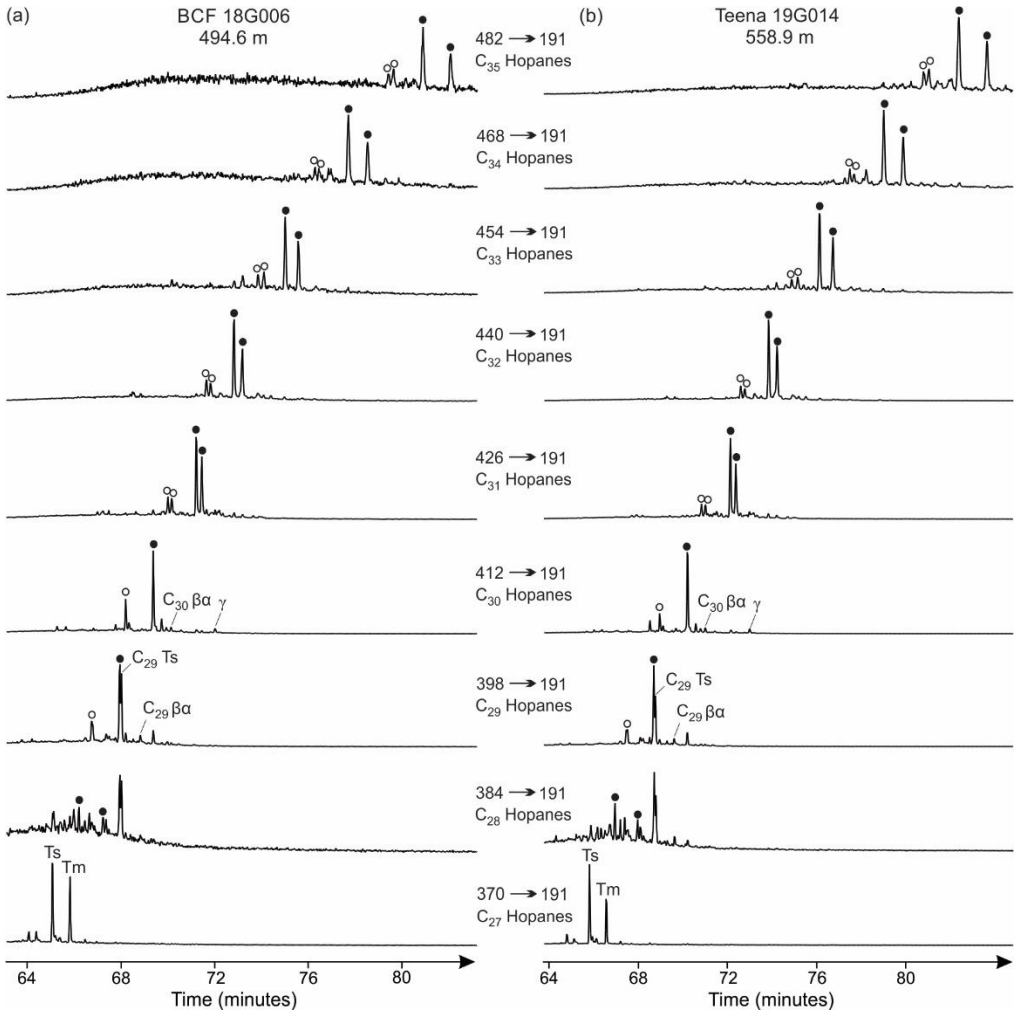

Figure 4.7. MRM chromatograms showing hopane distributions for (a) sample 18G006 from the Barney Creek Fm and (b) sample 19G014 from the Teena Dolostone. Black circles: 17α(H),21β(H)-hopanes; White circles: 17α(H)-diahopanes; Ts: C_{27} 18α(H)-22,29,30-trisnorneohopane; Tm: C_{27} 17α(H)-22,29,30-trisnorneohopane; γ: gammacerane.

For all analysed formations, the 3β-methylhopanes were observed in the range C_{31}–C_{36}, while only C_{31} 2α-methylhopanes were detectable due to much lower concentrations. The 2α-methylhopane index (2MHI, defined as C_{31} 2α-methylhopane/(C_{31} 2α-methylhopane+C_{30} αβ-hopane)) is low throughout the core ranging from 0.3 to 2.4% and averaging at 1.3% (Figure 4.8; Table 4.1). The 2MHI stratigraphic trend largely co-varies in time series with the C_{30} diahopane ratio. For all formations except for the Lynott Fm, the diahopane ratio and the 2MHI display a significant linear correlation ($R^2 = 0.50$, n = 31, $p < 0.00001$). The 2MHI also shows an apparent anti-correlation with $\delta^{13}C$ of carbonates.

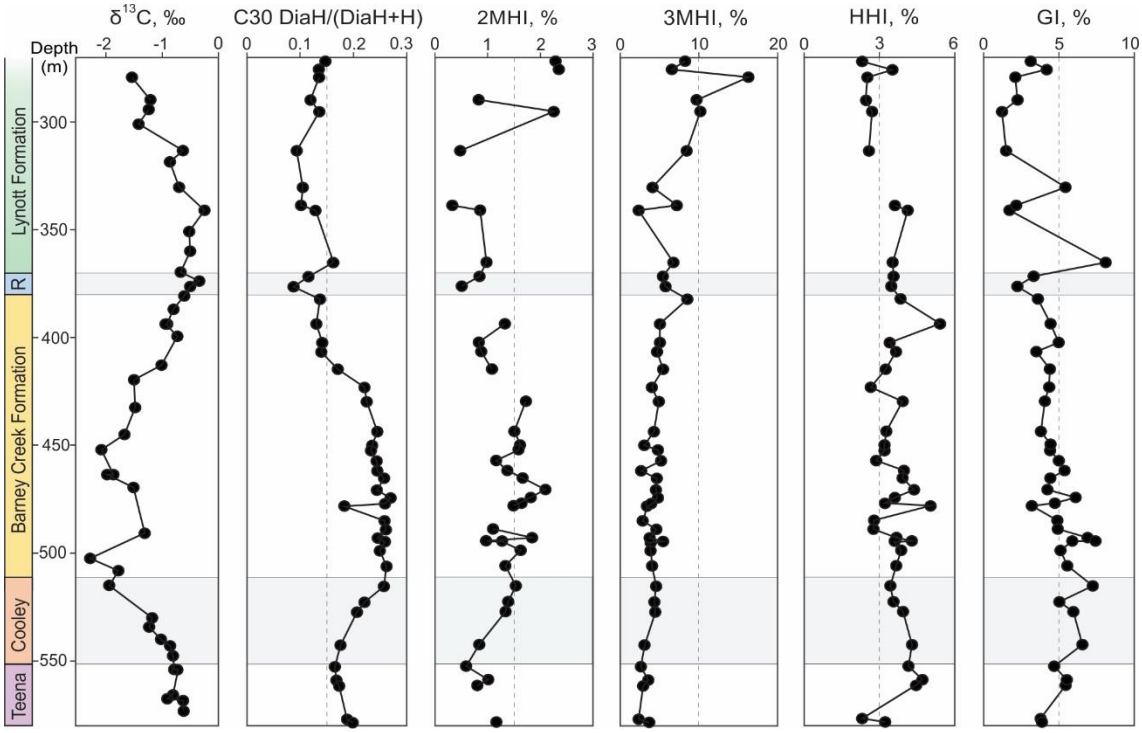

Figure 4.8. Biomarker ratios for LV09 drill core, including carbon isotopes of carbonates ($\delta^{13}C$) from Farkas et al. (2018), C_{30}DiaH/(DiaH+H), 2α-methylhopane index (2MHI), 3β-methylhopane index (3MHI), homohopane index (HHI) and gammacerane index (GI). R: Reward Dolostone.

The 3β-methylhopane index (3MHI, defined as C_{31} 3β-methylhopane/(C_{31} 3β-methylhopane+C_{30} αβ-hopane)) decreases downcore from 16.3% in the Lynott Fm to 2.4%

in the Teena Dolostone (Figure 4.8) and displays a significant negative correlation with Ts/(Ts+Tm) (R^2 = 0.56; p < 0.00001; Figure 4.9b). The 3-methyl-homohopane index (3MeHHI, defined as 100*C_{35}(S+R)/Σ$C_{31–35}$(S+R) 3β-methylhopanes) ranges from 3.5 to 8.6% throughout the core and correlates positively with HHI (R^2 = 0.46; p < 0.00001; Figure 4.9c).

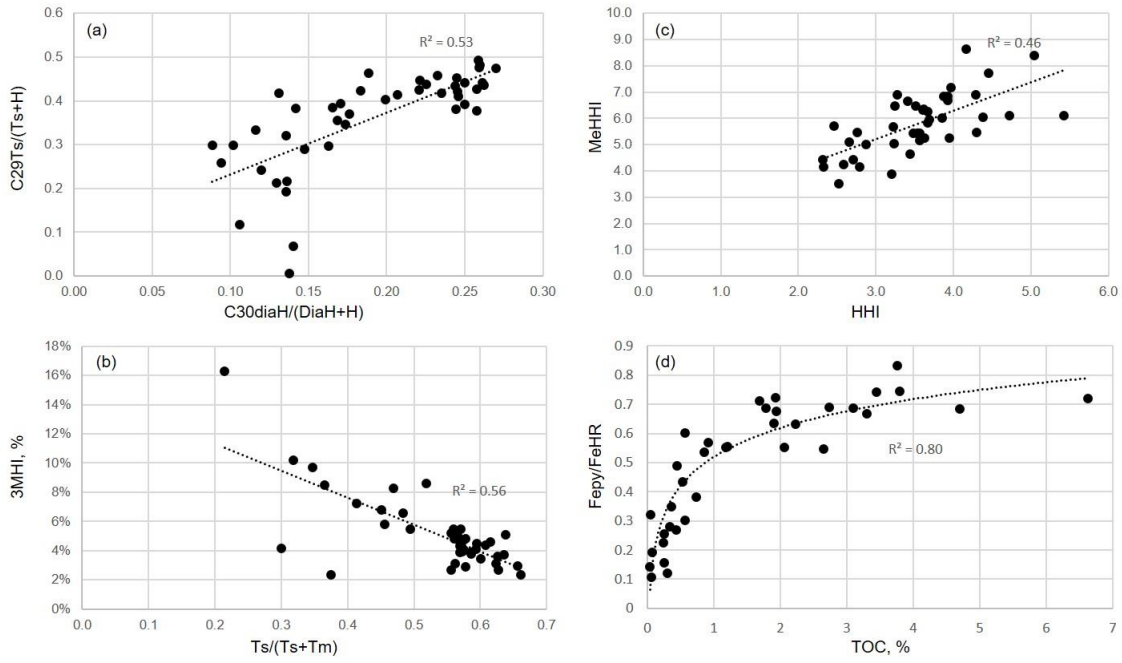

Figure 4.9. Cross-plots of (a–c) hopanoid ratios and (d) Fe_{py}/Fe_{HR} versus TOC, R^2 is from a logarithmic fit. The hopanoid ratios are defined in Table 1.1.

Gammacerane was present in all samples and the gammacerane index (GI) varies between 1.2 and 8.1% (average 4.5%) and does not correlate with other parameters (Table 4.1; Figure 4.8). Tricyclic terpanes (cheilanthanes) in the range from C_{19} to C_{26} and C_{24} tetracyclic terpane were monitored in LV09 samples (Figure 4.11). The ratio of C_{26} to C_{25} cheilanthanes ($C_{26}T/C_{25}T$) ranges between 0.45–1.09 with an average of 0.89 (n = 21). The ratio of C_{19} to C_{23} cheilanthanes ($C_{19}T/C_{23}T$) ranges between 0.2–2.72 with an average of 1.08 ± 0.58 (n = 45). The tricyclic terpane ratio (C_{20}+C_{21})/(C_{23}+C_{24}) varies

slightly around 1.03 ± 0.24 (0.57–1.77, n = 45). The cheilanthane ratios for all samples are presented in Appendix A.1.

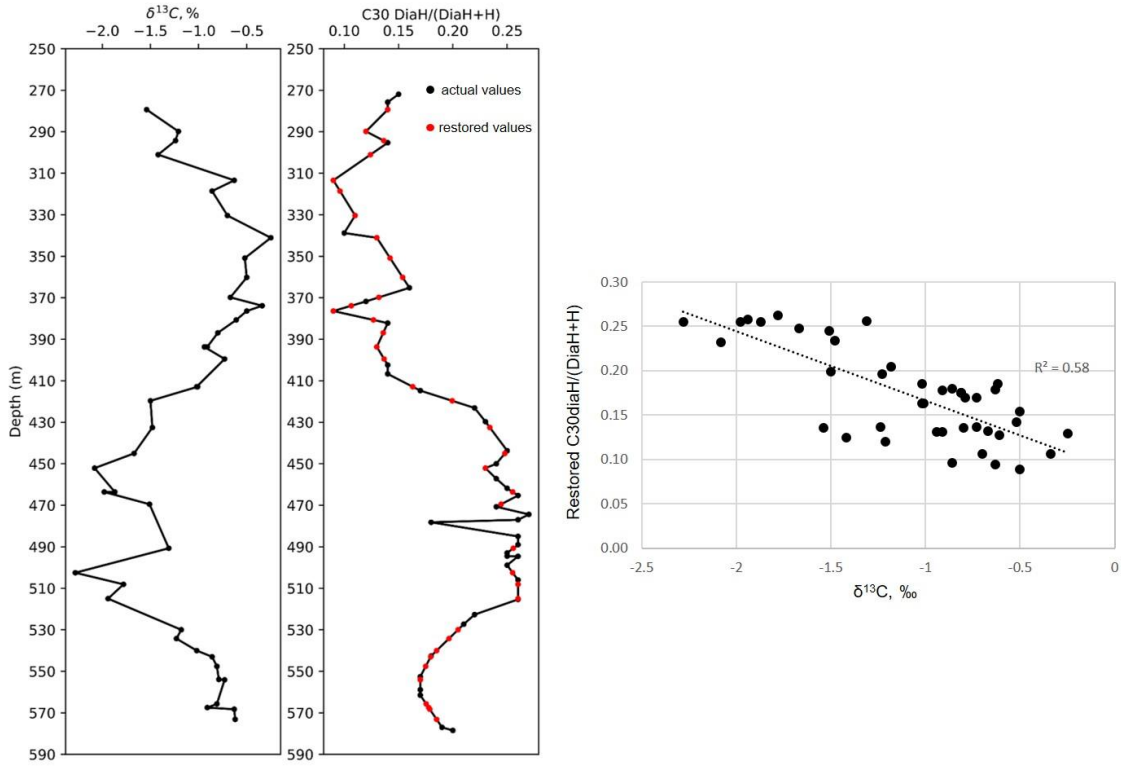

Figure 4.10. Anti-correlation between the C_{30}DiaH/(DiaH+H) trend and $\delta^{13}C$ trend.

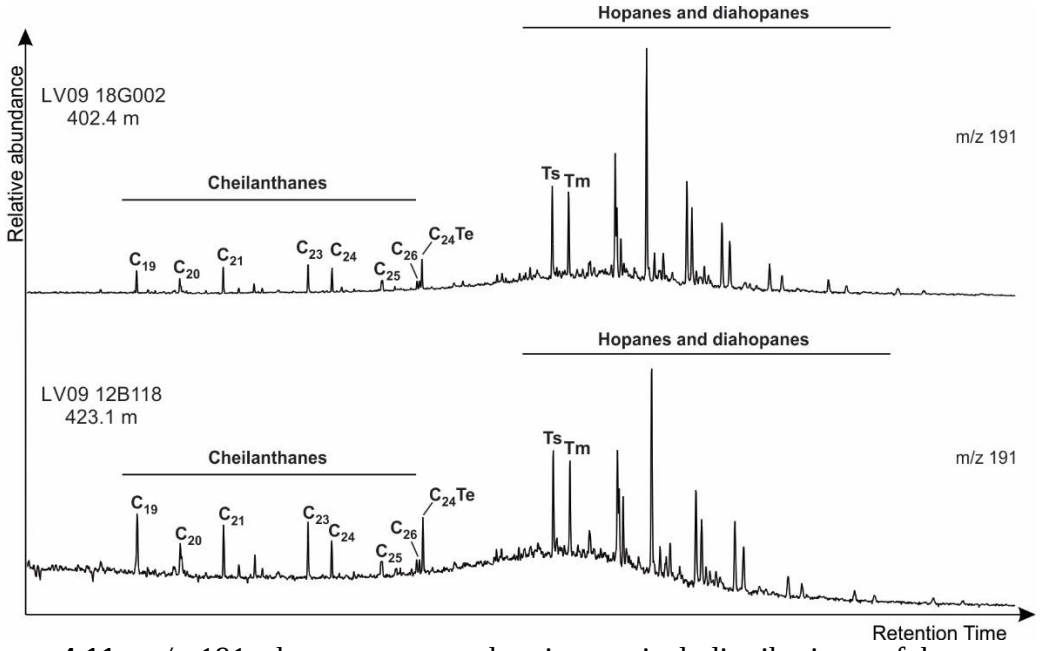

Figure 4.11. *m/z* 191 chromatograms showing typical distributions of hopanes and tricyclic terpanes (cheilanthanes) for samples 18G002 and 12B118 from the Barney Creek Fm. C_{24}Te: tetracyclic terpane.

4.3.4.3 Protosteroids

Nettersheim (2017) found protosterane (PS) molecules in the Barney Creek Fm sediments – lanostanes (LA) and an unknown compound ('cyclosterane', CA), possibly derived from cycloartane (more information is available in section 1.2 of the current thesis). We also detected these protosteranes in the LV09 drill core (Figure 4.12). In analogy to the classic ratio of steranes over hopanes, which is commonly used as an indicator for the relationship between eukaryotic and bacterial biomass input (Peters et al., 2005), Figure 4.12a plots the concentrations of protosteranes relative to hopanes versus depth. The LA/(LA+hop) ratio is low in the Teena Dolostone (0.3–0.9%), increases gradually through the Cooley Dolostone towards the upper part of the Barney Creek Fm to a maximum of 2%, and then quickly drops to ~0.4% at the top of the formation. The ratio remains low in the Reward Dolostone and Lynott Fm (Figure 4.12a). The LA/(LA+hop) shows an apparent correlation with C_{30}DiaH/(DiaH+H) ($R^2 = 0.5$; $p < 0.00001$). The CA/(CA+hop) ratio follows a notably different trend. The ratio fluctuates erratically in the Teena Dolostone, slightly increases in the overlying Cooley Dolostone, and then gradually decreases through the Barney Creek Fm. In the Reward Dolostone and Lynott Fm, the relative CA abundance again behaves erratically, ranging between 0 and 1.8% (Figure 4.12a).

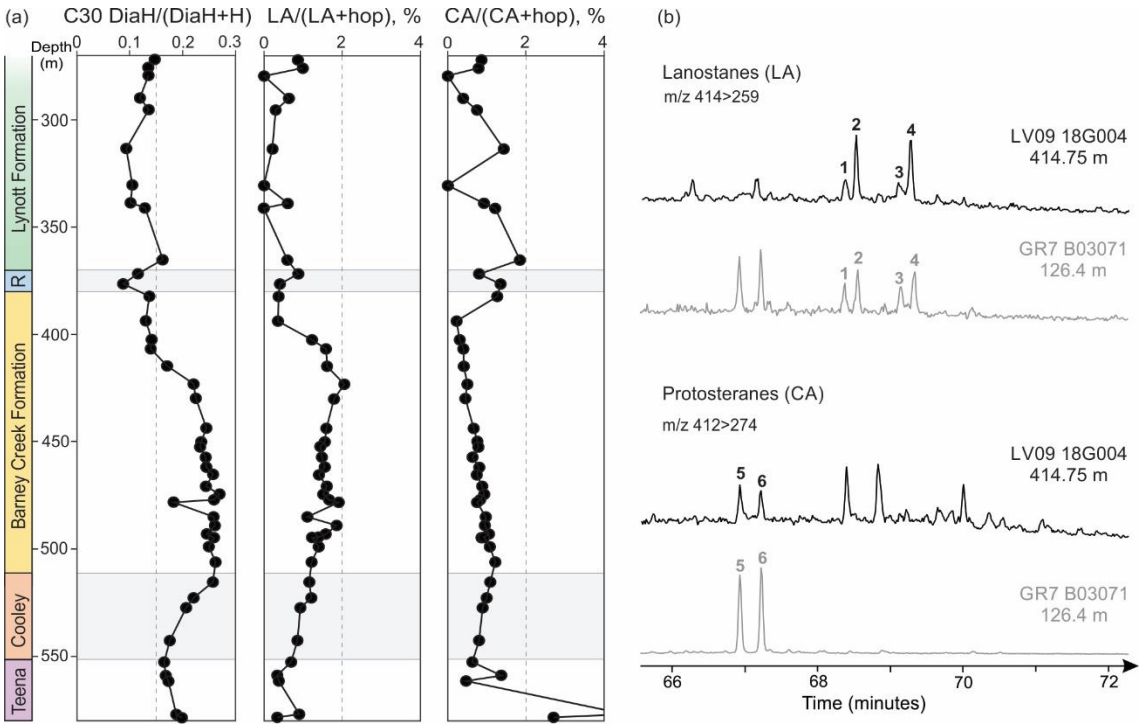

Figure 4.12. (a) C_{30}DiaH/(DiaH+H), LA/(LA+hop) and CA/(CA+hop) depth trends for LV09 drill core. (b) MRM transitions of *m/z* 414>259 and *m/z* 412>274 illustrating the distribution of lanostanes and protosteranes respectively in LV09 drill core (sample 18G004, 414.75 m) with a reference sample from GR7 drill core (B03071, 126.4 m).

4.3.5 Aromatic fractions

The aromatic fractions from LV09 drill core contain aromatic carotenoids and aryl isoprenoids, aromatic steroids, benzohopanoids and polycyclic aromatic hydrocarbons (PAHs) such as naphthalenes, phenanthrene and methyl phenanthrenes, pyrene, chrysene, benzo[e]pyrene and benzo[ghi]perylene. Phenanthrene-based parameters MPI and MPDF (Kvalheim et al., 1987; Radke & Welte, 1983) were used to estimate the thermal maturity (Table 4.1). Figure 4.13 illustrates the distribution of MPI and MPDF values versus depth, revealing a slightly increasing thermal maturity downcore, albeit with considerable scatter. Calculated vitrinite reflectance values Rc(MPI) and Rc(MPDF) range between 0.5–0.9% and 0.3–0.9% respectively and indicate that LV09 samples are immature to early mature in the beginning of the oil window.

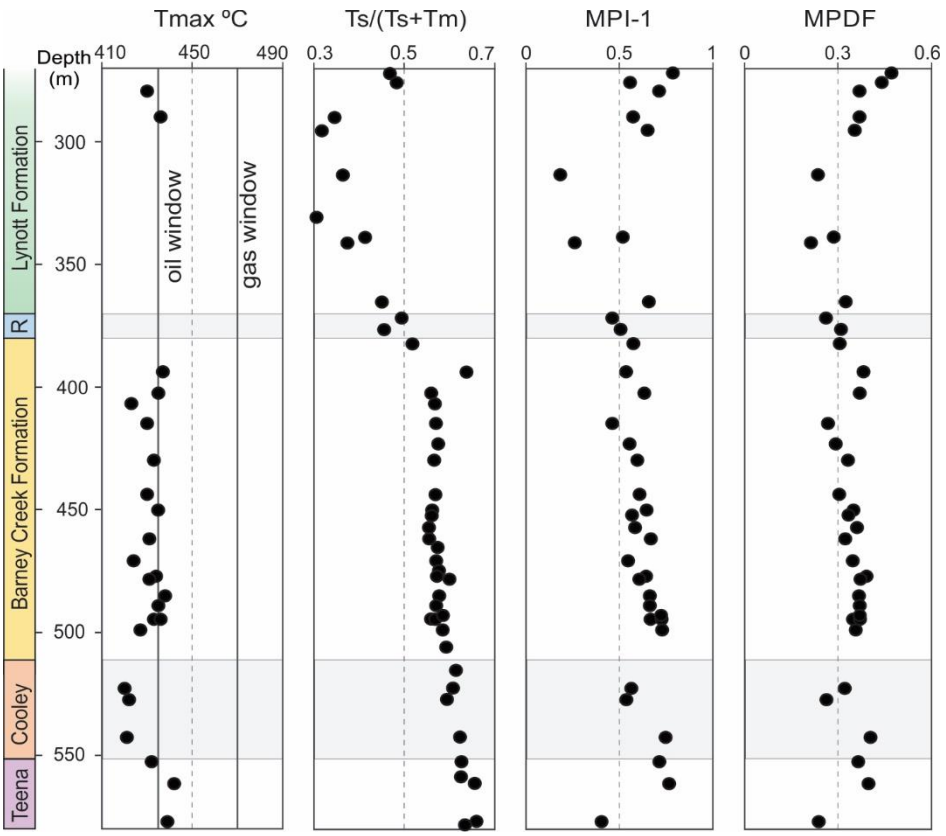

Figure 4.13. Maturity parameters for LV09 drill core, including Tmax values from Rock-Eval, Ts/(Ts+Tm), Methylphenanthrene index (MPI-1) and Methylphenanthrene distribution factor (MPDF). R: Reward Dolostone. Oil window: Tmax between 435 – 470ºC.

4.3.5.1 Aromatic carotenoid derivatives

Intact C_{40} aromatic carotenoid biomarkers, okenane and chlorobactane, and their typical breakdown products 2,3,4- and 2,3,6-trimethyl aryl isoprenoids (AI) have been previously detected in many of the well-preserved Barney Creek Fm samples (Brocks et al., 2005; Brocks & Schaeffer, 2008; Nettersheim, 2017). Okenane is a C_{40} monoaromatic 2,3,4-AI, likely originating from biological okenone, a biomarker for purple sulphur bacteria (PSB, Chromatiaceae) (Brocks & Schaeffer, 2008). Chlorobactane is a C_{40} monoaromatic 2,3,6-AI, derived from biological chlorobactene, accessory pigments in green sulphur bacteria (GSB, Chlorobiaceae) (Brocks & Schaeffer, 2008). In the current study, we identified AI in all analysed samples from all formations using *m/z* 134 selected

ion recording (SIR) chromatograms. The chromatograms reveal a continuous series of signals for C_{13} to C_{39} AI with 2,3,4- and 2,3,6-methylation patterns and C_{40} monoaromatic okenane and chlorobactane (Figure 4.14). Diaromatic C_{40} carotenoids, renieratane and renierapurpurane, were present in low abundances and isorenieratane was below detection limit (Figure 4.14). Concentrations of 2,3,4-AI are higher than 2,3,6-AI in all samples, and abundances of okenane are higher than chlorobactane.

Nettersheim (2017) proposed the ratio of G/(G+P) as a proxy for the relative ecological importance of GSB versus PSB, where G = Σ $C_{13–39}$ 2,3,6-AI and P = Σ$C_{13–39}$ 2,3,4-AI (ratios with C_{40} compounds give the same results). In GR7 drill core, the G/(G+P) ratio for the Barney Creek Fm ranged from 0.26 to 0.73 and showed a good correlation with other environmental proxies (Nettersheim, 2017). In the Barney Creek Fm of LV09, this ratio averages at 0.21 (Table 4.1; Figure 4.15). The G/(G+P) ratio is similar in the Reward Dolostone (avg. 0.2) and slightly higher in the Lynott Fm (avg. 0.29), Cooley (avg. 0.3) and Teena (avg. 0.34) Dolostone (Figure 4.15). The relative abundance of chlorobactane over okenane (Cl/(Cl+Ok)) is generally low throughout the core with average values around 0.2–0.3 (Table 4.1). A positive linear correlation (R^2 = 0.44; p = 0.00013) between G/(G+P) and Cl/(Cl+Ok) indicates that AI are largely derived from intact chlorobactane and okenane. No correlation and covariation of the G/(G+P) ratio with other proxies is observed.

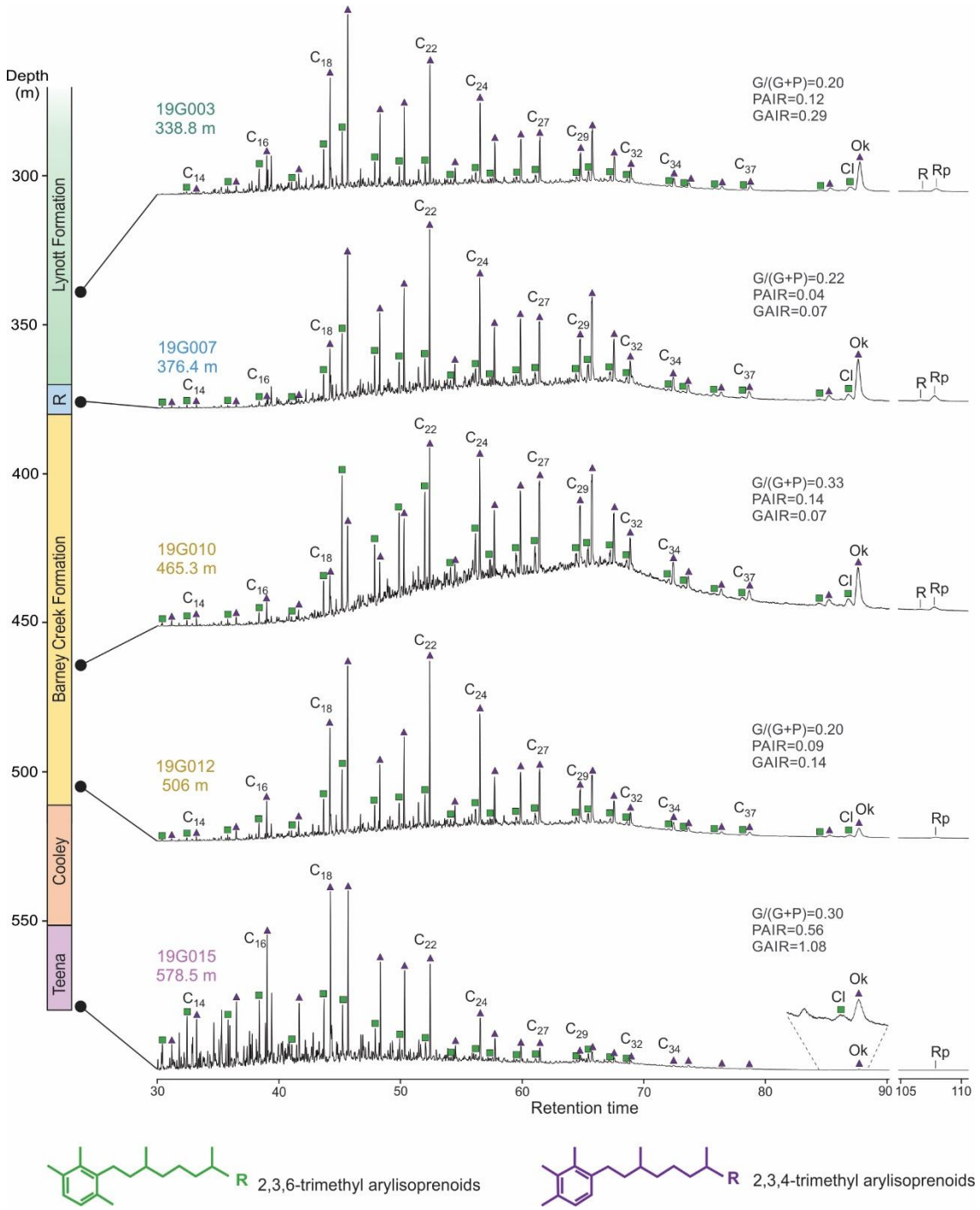

Figure 4.14. *M/z* 134 selected ion recording chromatograms of the aromatic hydrocarbon fractions illustrating the distribution of aryl isoprenoids in all formations of LV09 drill core and chemical structures of the 2,3,6- and 2,3,4-trimethyl aryl isoprenoids (AI). Green squares and purple triangles denote 2,3,6- and 2,3,4-AI respectively, numbers indicate carbon atoms. Cl: Chlorobactane; Ok: Okenane; R: Renieratane; Rp: Renierapurpurane.

Schwark and Frimmel (2004) introduced the aryl isoprenoid ratio (AIR), which evaluates the proportion of short versus intermediate chain-length AI. GAIR and PAIR

represent AIR for green and purple sulphur bacterial carotenoids respectively (Figure 4.15). In this study, GAIR = $\Sigma(C_{13–17})/\Sigma(C_{18–22})$ 2,3,6-AI and PAIR = $\Sigma(C_{13–17})/\Sigma(C_{18–22})$ 2,3,4-AI. GAIR and PAIR illustrate similar trends in LV09 drill core (Figure 4.15). The AIR values are quite low in the Teena and Cooley Dolostone, the upper part of the Barney Creek Fm and the Reward Dolostone (Figure 4.15). The lower Barney Creek Fm (440–506 m) shows three excursions with GAIR up to 1.4 and PAIR up to 0.6 (Table 4.1; Figure 4.15). In the Lynott Fm, GAIR varies between 0.1–2.3 and PAIR between 0.1–1.6 (Table 4.1). A strong linear correlation ($R^2 = 0.87$; $p < 0.00001$; Figure 4.16) between GAIR and PAIR indicates that the source of both series experienced similar degradation conditions.

The relationship between intact C_{40} carotenoids (Cl and Ok) and aryl isoprenoid degradation products ($C_{13–39}$) represents the extreme version of AIR. These proxies are illustrated in Figure 4.15 with depth trends of G/Cl and P/Ok. Both parameters co-vary and show a strong linear correlation ($R^2 = 0.79$; $p < 0.5$; Figure 4.16). The ratios vary slightly in all the formations, except for the lower part of the Barney Creek Fm (440–506 m), where several fluctuations to higher values are observed with G/Cl up to 138 and P/Ok up to 129 (Table 4.1; Figure 4.15).

4.3.5.2 Aromatic steroids and hopanoids

Triaromatic steroid (TAS) series of C_{26} and 4-methylated C_{27} cholesteroids were detected in all LV09 samples (Figure 4.17). TAS homologues without side chain (TA (II) steroids C_{20} and C_{21}) possess a general C_{21} over C_{20} predominance. Diaromatic (Dals) C_{28} and monoaromatic (Mals) C_{29} steroids also were observed in all analysed samples (more information is available in Chapter 1.2). Aromatic hopanoids were represented by $C_{32–35}$ benzohopanes and series of monoaromatic 8,14-secohopanoids.

4.4 Discussion

4.4.1 Thermal maturity

Organic matter is thermally exceptionally well preserved throughout the whole succession in LV09 drill core. Rock-Eval pyrolysis data (Table 4.2; Figure 4.13) demonstrate that the thermal maturities of all formations range from immature to early mature in the beginning of the oil window (Tmax = 420–442ºC). Biomarker-based maturity parameters (Ts/(Ts+Tm), MPI-1, MPDF) are in agreement with Rock-Eval data and illustrate increasing downcore thermal maturity trends within the early oil window (Figure 4.13). The observation of increasing downcore biomarker-based maturity parameters and their consistency with bulk Tmax values (Figure 4.13) provide additional evidence for the syngeneity of biomarkers. A negative correlation between Ts/(Ts+Tm) and 3MHI (Figure 4.9b) may indicate a maturity influence on 3β-methylhopanes. However, since 2MHI (which presumably has equal thermal stability as 3MHI) shows no correlation with Ts/(Ts+Tm), decreasing 3MHI trend is likely not controlled by maturity. Overall, the variability in biomarker parameters is largely independent from differences in thermal maturity, since Ts/(Ts+Tm) and phenanthrene-based ratios do not correlate or co-variate with biomarker ratios.

4.4.2 Redox conditions

We applied iron speciation analyses together with bulk $\delta^{15}N$ isotopes and biomarker proxies to investigate redox conditions in LV09 drill core. The ratio Fe_{HR}/Fe_T >>0.38 indicates that all analysed formations were deposited in anoxic bottom waters (Figure 4.15) (Poulton & Canfield, 2005). However, it seems doubtful that shallow subtidal to intertidal facies of the Lynott Fm were deposited under anoxic conditions. As suggested by Slotznick et al. (2018), the Fe_{HR}/Fe_T proxy can be skewed to higher values in

carbonate-rich samples due to the presence of diagenetic iron in carbonates. Therefore, Fe_{HR}/Fe_T values for LV09 drill core should be interpreted with caution. The Lynott Fm and Reward Dolostone display persistent ferruginous conditions (Fe_{py}/Fe_{HR} <0.7). In contrast, the Barney Creek Fm, Cooley and Teena Dolostone are dominated by ferruginous state with occasional excursions to sulphidic (euxinic) conditions (Figure 4.15). The strong correlation between Fe_{py}/Fe_{HR} and TOC may indicate better organic matter preservation in more reduced conditions. At the same time, moderately elevated bulk-rock $\delta^{15}N$ values (5.1–8.0‰; Figure 4.4) imply aerobic nitrogen cycling and denitrification happening in the upper water column (Sigman et al., 1999; Stüeken et al., 2016), which is in agreement with mildly oxygenated surface waters proposed for the mid-Proterozoic (e.g., Poulton & Canfield, 2011).

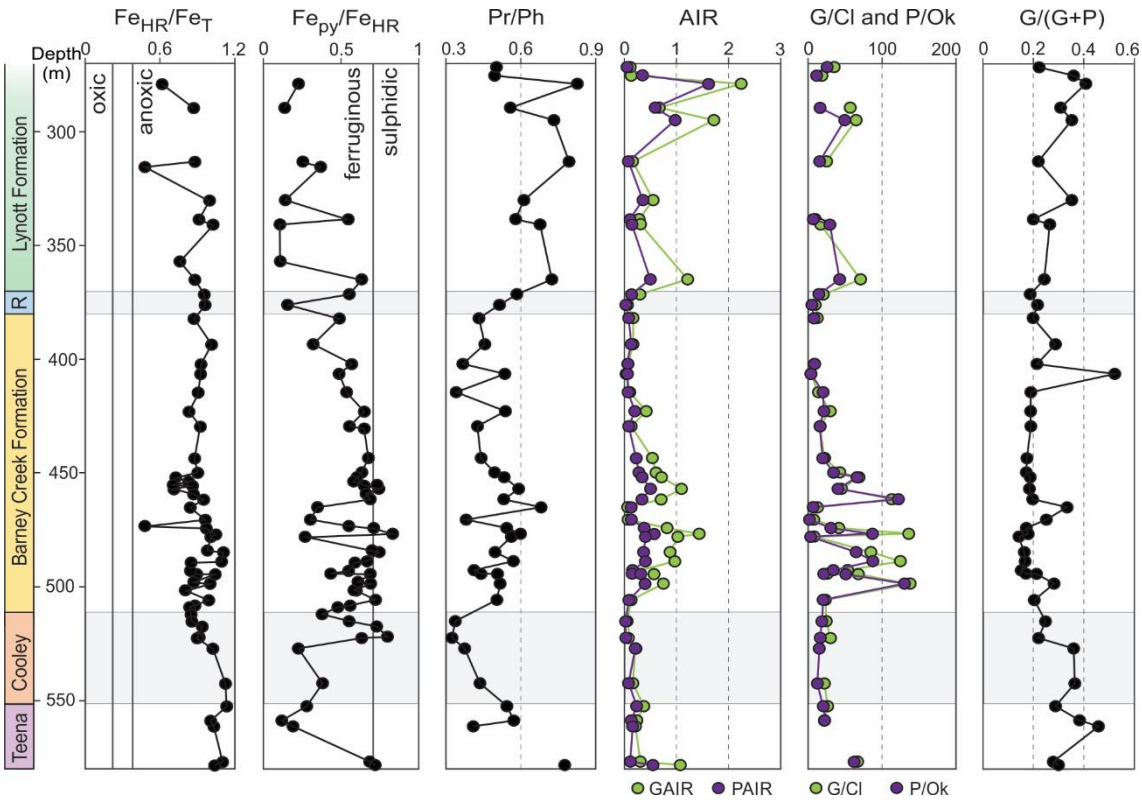

Figure 4.15. Redox parameters for LV09 drill core, including iron speciation ratios Fe_{HR}/Fe_T and Fe_{py}/Fe_{HR}, Pristane/Phytane, Aryl isoprenoid ratios for green (GAIR) and purple (PAIR) sulphur bacterial carotenoids, G/Cl and P/Ok, G/(G+P). R: Reward Dolostone.

Some biomarker parameters can be used as redox indicators. In the traditional interpretation, a low ratio of the regular isoprenoids pristane and phytane (Pr/Ph <1) points to minimal oxygen exposure of organic matter under reducing conditions (Didyk et al., 1978; Peters et al., 2005). In LV09 drill core, this proxy shows variations between 0.3 and 0.8 with an average of 0.5, consistent with low oxygen exposure in largely anoxic bottom waters (Figure 4.15). Pr/Ph values are slightly elevated in the Lynott Fm (avg. 0.65), which is in agreement with shallower water depth for this formation. Another redox proxy is the homohopane index (HHI, Figure 4.8). Generally, elevated values of HHI are interpreted as 'anoxia' (Peters et al., 2005), although it is poorly defined to which extent this refers to water column or sedimentary conditions. In the current study, HHI is generally low and varies only slightly around an average of 3.6% ± 0.7%.

Intact aromatic carotenoids, chlorobactane and okenane, and their breakdown products 2,3,6- and 2,3,4-AI in the Barney Creek Fm indicate activity of green and purple sulphur bacteria and the presence of photic zone euxinia (Brocks et al., 2005; Brocks & Schaeffer, 2008). Until recently, aromatic carotenoids of the 1.64 Ga Barney Creek Fm represented the oldest known biomarkers of that type. However, series of 2,3,6- and 2,3,4-AI were identified in the 1.73 Ga Wollogorang Fm in the southern McArthur Basin (Vinnichenko et al., 2020). Additionally, in the current study, chlorobactane and okenane were also detected in the 1.64 Ga Teena Dolostone, which underlies the Barney Creek Fm (Figure 4.14). Therefore, the Teena Dolostone contains currently the oldest known intact aromatic carotenoids. Diaromatic C_{40} carotenoids, previously detected in GR7 drill core, were also attributed to green (isorenieratane) and purple (renieratane and renierapurpurane) sulphur bacteria (Brocks & Schaeffer, 2008). However, recent studies by Cui et al. (2020) and Roussel et al. (2020) propose a possible additional cyanobacterial source for these diaromatic compounds based on the biosynthesis ability and presence of

diaromatic carotenoids in cultured cyanobacteria (*Synechococcus* sp., *Synechocystis* sp. and *Nostoc* sp.), with isorenieratene always being the least abundant isomer. Consequently, Cui et al. (2020) argue that isorenieratane can be used as biomarker for GSB only when it represents the dominant diaromatic carotenoid or co-occurs with chlorobactane and okenane. In LV09 drill core, diaromatic carotenoids were present only in trace amounts and were always accompanied by chlorobactane and okenane in higher abundances. Thus, we suggest that in LV09 chlorobactane is indicative of GSB and okenane of PSB.

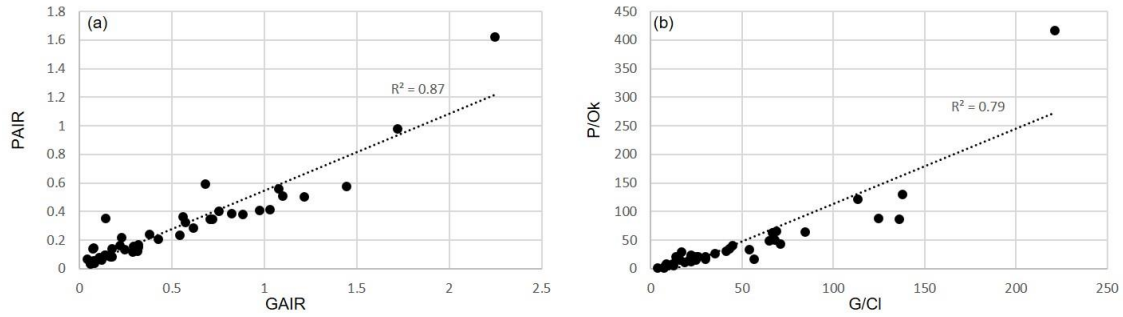

Figure 4.16. Cross plots of aryl isoprenoids ratios.

GSB are strictly anaerobic phototrophic organisms, which mostly use reduced sulphur species (sulphide and sulphur) as an electron donor and therefore inhabit anoxic waters within the photic zone (photic zone euxinia) (Brocks & Schaeffer, 2008). PSB have greater light requirements and higher oxygen tolerance than GSB and therefore commonly thrive just above GSB and directly below the oxic-anoxic interface within the light-penetrated zone at water depths of 12–25 m (Brocks & Schaeffer, 2008). Previous organic studies of the Barney Creek Fm interpreted aromatic carotenoids as biomarkers for planktonic sulphur bacterial communities (Brocks et al., 2005; Brocks & Schaeffer, 2008; Nettersheim, 2017). Alternatively, Lyons et al. (2012) suggested that PSB and GSB biomarkers in the deep water Barney Creek Fm belong to transported organic streaks from

shallow water microbial mats. However, the presence of okenane favours planktonic PSB, since these species represent a known source of okenone, while PSB in microbial mats produce carotenoids with a lycopene skeleton (Brocks & Schaeffer, 2008). Based on optical and chemical similarities between ripped-up organic streaks and intact laminated sediments in the Barney Creek Fm from LV09 drill core, Nettersheim (2017) proposed that these streaks were formed locally in deep water environments. Additionally, organic matter laminae resemble Phanerozoic planktonic-based lamalginite. Therefore, for the current study, we follow a planktonic interpretation of PSB and GSB. The G/(G+P) ratio for the LV09 varies slightly and averages at 0.25, favouring PSB over GSB communities (Figure 4.15). The presence of PSB throughout the whole LV09 drill core suggests a very shallow stratification of the basin during deposition of the McArthur Group.

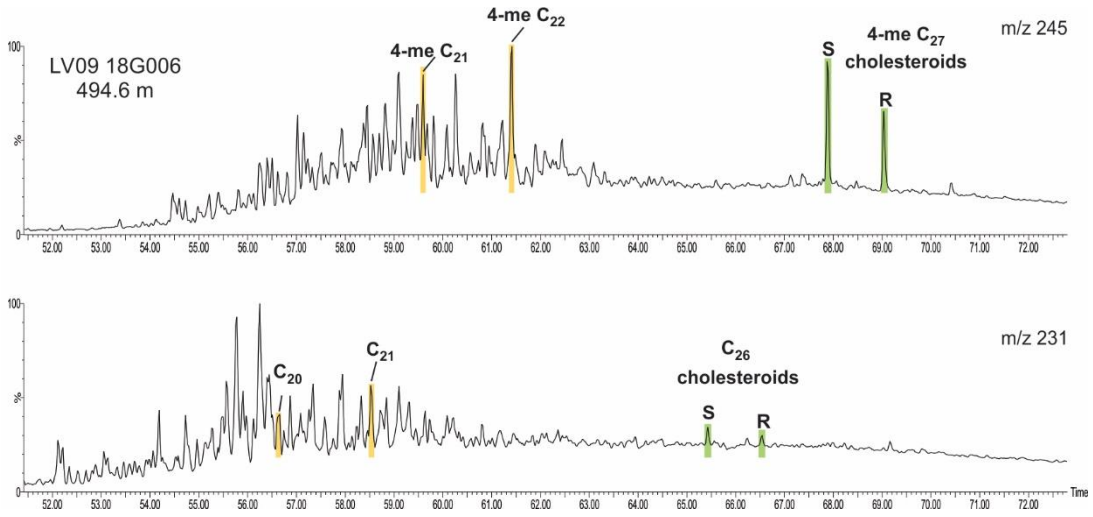

Figure 4.17. Distribution of the Triaromatic steroids (TAS) in LV09 drill core (sample 18G006, 494.6 m). *m/z* 245 trace illustrates 4-methylated C_{27} cholesteroids (S and R), C_{21} and C_{22} homologues TA(II). *m/z* 231 trace illustrates C_{26} cholesteroids (S and R), C_{20} and C_{21} homologues TA(II).

The AIR are considered to reflect the aerobic degradation of AI (Schwark & Frimmel, 2004), but theoretically these ratios can be also controlled by maturity and clay catalysis. LV09 sediments are exceptionally well preserved and GAIR and PAIR trends (Figure

4.15) illustrate no dependence on maturity parameters (Figure 4.13) or biodegradation (Figure 4.6). Additionally, AIR trends do not correlate with muddier facies (GR curve; Figure 4.1) or with the C_{30}DiaH/(DiaH+H) ratio (Figure 4.8), which is presumably controlled by diagenetic alteration. Therefore, we interpret AIR in LV09 as an indicator for aerobic degradation. According to Schwark and Frimmel (2004), low AIR values indicate that intermediate-chain compounds were preserved, suggesting relatively stable anoxic bottom waters. By contrast, elevated AIR values imply that aromatic carotenoids were exposed to more oxidizing conditions causing cleavage to shorter fragments. As GSB and PSB live below the oxic-anoxic interphase, such oxidation can be explained e.g. by currents that carry oxygenated waters into the deeper parts of the basin, including turbidity currents (Schwark & Frimmel, 2004).

In the Glyde River sub-basin (GR7), Nettersheim (2017) found correlations between carbonate content, iron speciation and biomarker parameters. Most proxies show two excursions in the intervals around 80 m and 220 m depth. Iron speciation data indicate dominantly ferruginous conditions throughout most of the Barney Creek Fm in GR7, while these two intervals approach or cross the euxinia threshold ($Fe_{py}/Fe_{HR} = 0.7$). PAIR and GAIR values in GR7 reach up to 2.9 and 3.2 respectively in probable euxinic intervals (Figure 4.18). In LV09 drill core, the AIR values are quite low (<1.5) in comparison to GR7 (Figure 4.18). Therefore, while the upper Barney Creek Fm in the Glyde River sub-basin saw at least two intermittent periods of elevated oxidation, the Barney Creek Fm in LV09 is consistent with more stable anoxic conditions. Elevated AIR in LV09 up to 2.2 are recorded mostly in the Lynott Fm, where Pr/Ph ratios also display higher values (Figure 4.15). The Lynott Fm was deposited in the shallowest depositional environments (Figure 4.1) and can be affected by intermittent oxygenation.

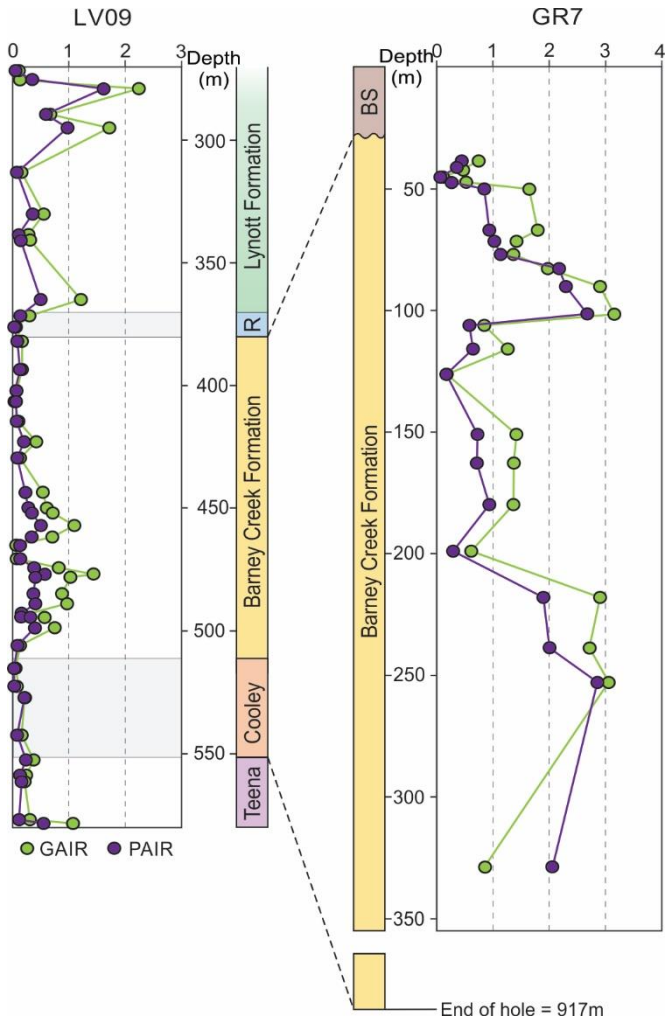

Figure 4.18. Comparison of aryl isoprenoid ratios for green (GAIR) and purple (PAIR) sulphur bacteria from LV09 and GR7 drill cores. Measurements for GR7 are from Nettersheim (2017) (the biomarker ratios are in Appendix A.3). R: Reward Dolostone; BS: Bukalara Sandstone.

The combination of iron speciation, bulk $\delta^{15}N$ and biomarker proxies reveal that the Teena Dolostone, Barney Creek Fm and Reward Dolostone sediments were deposited in stratified conditions with mildly oxygenated surface waters and anoxic, dominantly ferruginous bottom waters with occasional fluctuations to sulphidic environments. Elevated AIR and Pr/Ph ratios in the Lynott Fm are consistent with shallower water depth and higher oxygen exposure.

4.4.3 Paleo-environmental reconstructions and microbial communities

Based on the lithological features, the Barney Creek Fm is interpreted to be deposited in relatively deep sub-wave base marine environments, while the underlying Teena Dolostone and overlying Reward Dolostone were deposited in shallower marine conditions of the carbonate platform (Bull, 1998; Kunzmann et al., 2019; McGoldrick et al., 2010; Rawlings, 1999; Schmid, 2015). Based on the enriched sulphur isotopes of pyrite similar to typical seawater measurements, Johnston et al. (2008) suggested restricted marine environments for the Barney Creek Fm. This interpretation is supported by Sr and C isotope systematics for LV09 drill core reported by Farkas et al. (2018). In the formations above and below the Barney Creek Fm, the authors recorded typical mid-Proterozoic seawater values in $\delta^{13}C$ (~0‰; Strauss et al., 1992) and $^{87}Sr/^{86}Sr$ (~0.706; Kuznetsov et al., 2010) (Figure 4.4), indicative of open marine conditions. In contrast, the organic-rich Barney Creek Fm in LV09 drill core displayed a shift to lighter $\delta^{13}C$ and more radiogenic values of $^{87}Sr/^{86}Sr$ (Figure 4.4), which is consistent with deeper water depths and potential temporary basin restriction (Farkas et al., 2018). Substantial lateral thickness variations of the Barney Creek Fm also point to predominant deposition in the local sub-basins (McGoldrick et al., 2010).

Biomarker studies of the Barney Creek Fm from GR7 drill core also describe marine restricted environments in the local sub-basin with anoxic, sulphate-poor and stratified waters (Brocks et al., 2005; Brocks & Schaeffer, 2008; Nettersheim, 2017). The authors recorded a lack of typical eukaryotic saturated steranes, prevalence of bacterial hopanes (including high 3β-methylhopanes and low 2α-methylhopanes) and monoaromatic carotenoids (chlorobactane and okenane) with lower amounts of diaromatic carotenoids. The current study of LV09 drill core detects similar biomarker distributions and supports the previous findings. Additionally, the C_{26}/C_{25} tricyclic terpane ratio for the Barney

Creek Fm in LV09 favours marine environments (Figure 4.19), although it remains uncertain whether this ratio is applicable in the Precambrian.

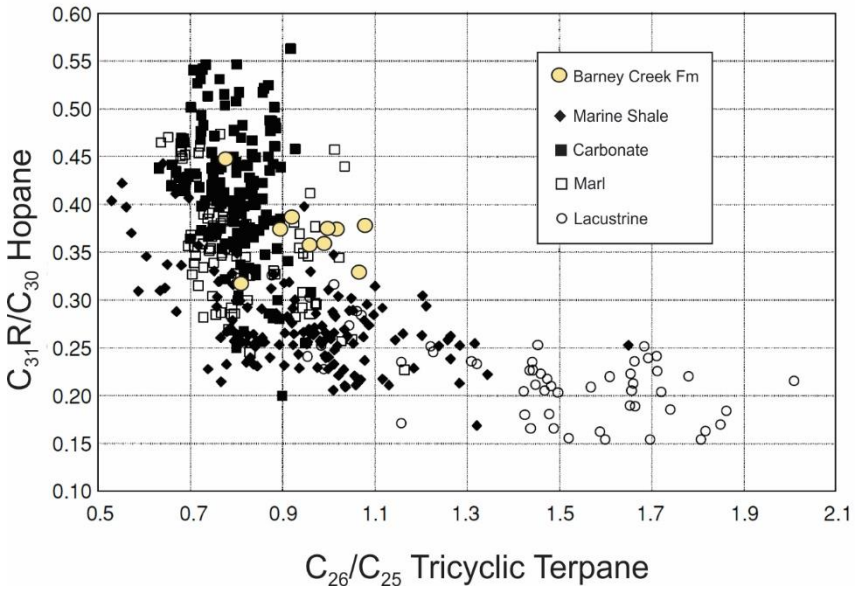

Figure 4.19. Cross plot of C_{26}/C_{25} tricyclic terpane ratio versus $C_{31}R/C_{30}$ hopane ratio distinguishing between lacustrine and marine oils (from Peters et al. (2005)) with Barney Creek Fm data from the current study.

Recently, a paper about the lacustrine Eocene Green River Fm by French et al. (2020) suggested a lacustrine depositional environment for the Barney Creek Fm. French et al. (2020) interpreted abundant 3β-methylhopanes coupled with low 2α-methylhopanes, low concentrations of isorenieratane relative to renierapurpurane and renieratane, and prevalence of 2,3,4-AI over 2,3,6-AI as indicators for lacustrine environments. However, such methylhopanes signatures are not exclusive to lacustrine settings and often present in shallow marine and restricted environments (Blumenberg et al., 2012; Cao et al., 2009; Gueneli, 2016; Lee et al., 2019; Luo et al., 2015; Rohrssen et al., 2013; Spaak et al., 2017). For example, in the Barney Creek Fm from LV09, 3-MHI averages at 4.5%, which is higher than average values in some marine Phanerozoic source rocks (1–3%) (Farrimond et al., 2004), but lower than in others (4–12%) (Cao et al., 2009; Rohrssen et al., 2013). On the methylhopane cross plot presented by French et al. (2020), our measurements of

the Barney Creek Fm fall outside of the Green River Fm area and instead display similar values to the Mesoproterozoic Xiamaling Fm (Luo et al., 2015) and Tourist Fm (Blumenberg et al., 2012), both interpreted as marine (Figure 4.20). Predominance of renierapurpurane and renieratane over isorenieratane is not typically lacustrine either, because such a pattern was also detected in restricted and open marine sediments (Cui et al., 2020; Roussel et al., 2020). Additionally, the distribution of aromatic carotenoids in the Barney Creek Fm is quite different from the Green River Fm (French et al., 2020). In LV09 drill core, chlorobactane and okenane are detected in high relative abundances (Figure 4.14) and diaromatic carotenoids are present in trace amounts, while the Green River Fm contains only occasional traces of okenane and displays comparable concentrations of chlorobactane and diaromatic carotenoids. Nettersheim (2017) illustrated that prevalence of 2,3,4-AI over 2,3,6-AI is not a strict characteristic of the Barney Creek Fm, since there are samples in GR7 drill core where 2,3,6-AI are dominant. Therefore, the similarity between the Barney Creek Fm and Green River Fm is much less pronounced than suggested by French et al. (2020). Finally, as sulphate levels were still much lower in Paleoproterozoic oceans than at present (Kah et al., 2004), the chemistry of marine waters was presumably more similar to modern lacustrine environments. Lower sulphate levels support methanogenesis and aerobic methanotrophy through type I methanotrophs, potentially explaining elevated 3-MHI values in the Barney Creek Fm (Brocks et al., 2005). A marine origin for the Barney Creek Fm is also more plausible based on lithological evidence (e.g., Kunzmann et al., 2019).

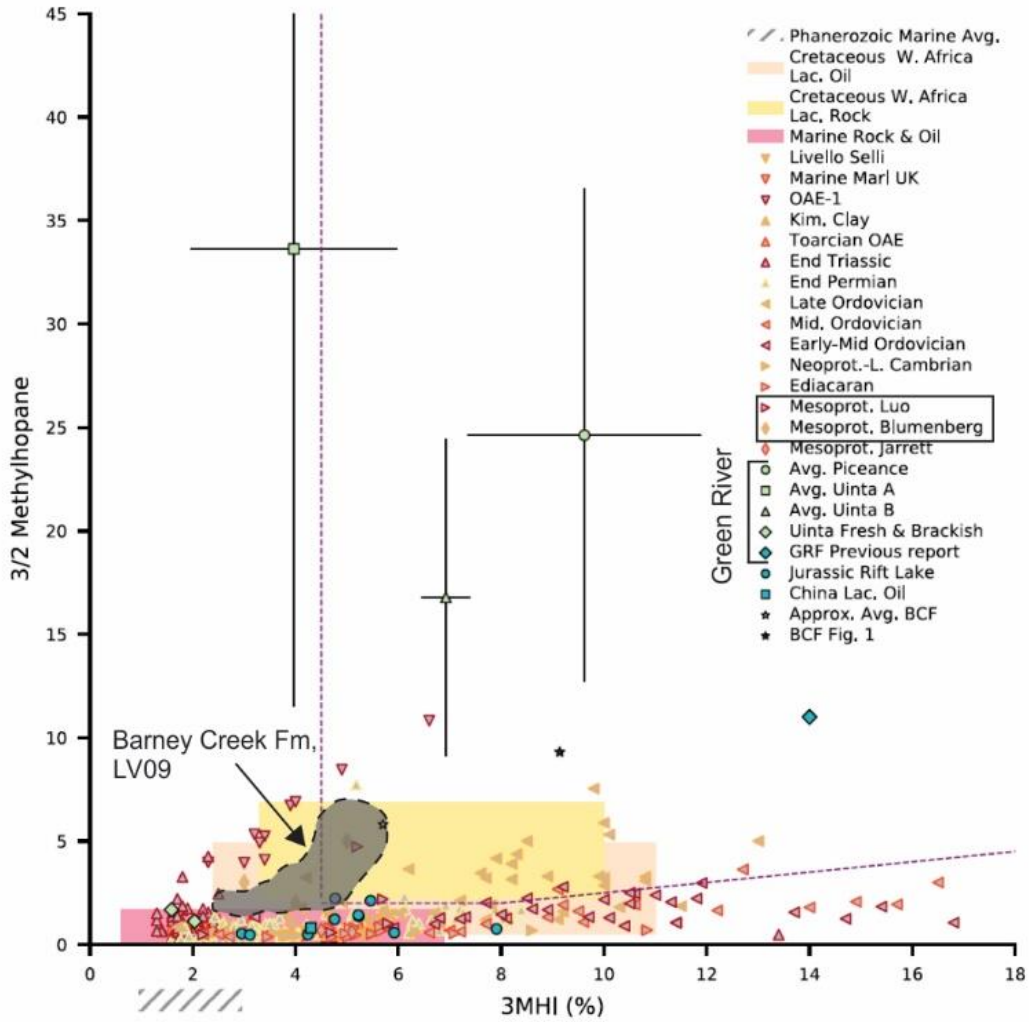

Figure 4.20. Methylhopane cross plot reproduced from French et al. (2020) with Barney Creek Fm data from the current study (black area). Literature data points are green to blue for lacustrine and red to orange for marine environments.

In the current study, we used biomarker parameters for reconstructions of paleo-environments and communities in LV09 drill core. According to the conventional view, diahopanes are formed through rearrangement of regular hopanoids on clay minerals, and high dia- versus regular hopane ratios are indicative of clay catalysis (Moldowan et al., 1991; Peters et al., 2005). However, the presence of an unknown biological precursor for these compounds cannot be excluded (Luo et al., 2015). Diahopanes have been detected in Proterozoic sediments previously (Blumenberg et al., 2012; Luo et al., 2015; Summons et al., 1988; Summons, Powell, & Boreham, 1988; Wang et al., 2018). In LV09, the

C_{30}DiaH/(DiaH+H) ratio ranges from 0.09 to 0.27 with higher values (0.18–0.27) in the Barney Creek Fm between 420–515 m depth (Figure 4.8). These values are similar to measurements in the 1.1 Ga Tourist Fm (Blumenberg et al., 2012) but lower than in the 1.38 Ga Xiamaling Fm (Luo et al., 2015). The observed C_{30}DiaH/(DiaH+H) trend displays no correlation with maturity parameters (Figure 4.13) and thus is not primarily caused by thermal alteration. Biodegradation also cannot be responsible for the formation of diahopanes, since C_{30}DiaH/(DiaH+H) ratios exhibit lower values in moderately biodegraded samples from LV09 drill core, while the highest values are recorded in the non-biodegraded section of the Barney Creek Fm (Figure 4.6; 4.8). However, an excursion to higher values of C_{30}DiaH/(DiaH+H) coincides with lighter $\delta^{13}C$ values (Figure 4.10) and muddier deeper water facies of the Barney Creek Fm based on GR log data (Figure 4.1). Additionally, while these muddier facies record the highest C_{30}DiaH/(DiaH+H) ratios (0.23–0.27), one Barney Creek Fm sample from 478.2 m depth (17G009), which contains 85% dolomite, illustrates a spike to a low value of 0.18 (Figure 4.10). Therefore, higher amounts of diahopanes in the Barney Creek Fm may be indeed formed through rearrangement of regular hopanoids in sediments with an elevated proportion of clay minerals. The rearrangement mechanism may be directly related to surface catalysis by clay minerals, but the connection might also be more indirect. For instance, high clay content can be associated with lower rates of deposition and thus longer exposure times of organic matter to oxidants and other chemicals that diffuse into the sediment from the water column.

The gammacerane index (GI) in the LV09 drill core is relatively low (≈5%) with no systematic stratigraphic trends or correlation with other parameters (Figure 4.8). High values of GI are commonly reported to indicate high salinity levels or a stratified water column as such ecosystems may harbour large populations of eukaryotic ciliates

producing tetrahymanol, a typical precursor of gammacerane (Peters et al., 2005; Sinninghe Damsté et al., 1995). However, other eukaryotes and bacteria, including aerobic methanotrophic bacteria (Banta et al., 2015; Cordova-Gonzalez et al., 2020), also can produce tetrahymanol. Since ciliates probably had not evolved by 1.64 Ga (Parfrey et al., 2011), a bacterial source for gammacerane in LV09 is more likely. Thus, GI does not represent an indicator for salinity and stratification in the Paleoproterozoic, yet the biosynthetic pathway to form tetrahymanol has already existed.

In the LV09 drill core, 3β-methylhopanes are the most abundant in the Lynott Fm (avg. 8%) and average around 4.5% in the Barney Creek Fm (Figure 4.8). According to Brocks et al. (2005), elevated abundances of 3β-methylhopanes in the Barney Creek Fm may indicate an activity of type I methanotrophic bacteria at an oxic-anoxic boundary and indirectly denote low marine sulphate concentrations in the McArthur Basin.

Contrary to the traditional view of abundant 2α-methylhopanes in the Proterozoic (Knoll et al., 2007; Summons et al., 1999), our results indicate that 2α-methylhopanes are low in LV09 drill core (average 2MHI = 1.3 ± 0.5%). These measurements are consistent with 2MHI reported for 1.1 Ga sediments from the Taoudeni Basin (≤2%; Blumenberg et al., 2012; Gueneli et al., 2018). Several biological sources were proposed for 2α-methylhopanes, such as cyanobacteria (Summons et al., 1999) and order Rhizobiales of α-proteobacteria (Ricci et al., 2015; Welander et al., 2010). However, Rhizobiales emerged only around 1.5 Ga (Wang et al., 2020). Therefore, a cyanobacterial origin for 2α-methylhopanes from 1.64 Ga McArthur Group is more likely. The 2MHI trend for LV09 drill core shows an apparent anti-correlation with $\delta^{13}C$ of carbonates (Figure 4.8) and thus may reflect a higher contribution from organisms in deeper water settings. Besides, the 2MHI trend also displays a co-variation with the C_{30} diahopane ratio (Figure 4.8), which might be associated with clay content. It is thus possible that clay catalysis,

at least in part, controls the 2MHI similar to the diahopane ratio. This observation implies that some part of the LV09 2α-methylhopanes is not of direct biological origin, but may instead be diagenetically generated from non-methylated hopanoids similar to methylsteranes (van Maldegem et al., 2020). Several samples from the Lynott Fm record the highest 2MHI values throughout the entire LV09 core (up to 2.4%), and display an excursion from a co-variation with the C_{30} diahopane ratio, which remains low (Figure 4.8). This excursion may indicate the presence of biological 2α-methylhopanes in addition to the diagenetic input at least for the Lynott Fm. However, a low abundance of 2α-methylhopanes in LV09 drill core does not preclude an important ecological role of cyanobacteria in Proterozoic oceans. For example, in modern marine environments, 2α-methylhopanoid production by cyanobacteria is scarce and mostly restricted to near-shore evaporitic conditions (Garby et al., 2013), while the majority of marine cyanobacteria do not produce 2α-methylhopanoids at all (Talbot et al., 2008). As a result, 2α-methylhopanes from LV09 drill core may reflect the presence of 2α-methylhopanoid-producing cyanobacteria in near-shore regions in mid-Proterozoic oceans, regardless of the total abundance of marine cyanobacteria.

In summary, exceptionally preserved LV09 drill core allows to analyse biomarkers for the first time in the lower Barney Creek Fm and underlying Teena Dolostone. The Teena Dolostone holds currently the oldest indigenous hopanes and intact C_{40} aromatic carotenoids. The lower Barney Creek Fm records elevated C_{30} diahopane ratios (relative to circumjacent formations) that coincide with lighter $\delta^{13}C$ values and muddier deeper water facies based on GR log data. Therefore, enhanced diahopanes in the Barney Creek Fm are most probably related to clay content either directly (clay catalysis) or indirectly (lower depositional rates and longer exposure to oxidation). Consistently low 2MHI co-vary in time series with diahopane ratios, indicating a possible diagenetic control on 2α-

methylhopanes. The absence of typical eukaryotic saturated steranes, prevalence of bacterial hopanes and aromatic carotenoids through all analysed formations indicate a bacteria-dominated marine ecosystem in the middle McArthur Group. Observed communities include anaerobic green and purple sulphur bacteria, cyanobacteria, tetrahymanol producing bacteria and aerobic methanotrophic bacteria. PSB are more abundant than GSB through the whole LV09 succession, while the Teena Dolostone and Lynott Fm contain slightly more GSB relative to other formations. This variety of bacterial communities can only occur in heterogeneous environments with stratified waters, which is also supported by inorganic iron speciation and $\delta^{15}N$ measurements.

4.4.4 Protosteroids and their possible producers

Previous biomarker studies on the 1.64 Ga Barney Creek Fm showed that diagnostic eukaryotic steranes were below detection limits (e.g. Brocks et al., 2005; Brooks & Schaeffer, 2008). Instead, 4-methylated triaromatic steroids (TAS) without side-chain alkylation were abundant (Brocks et al., 2005). In the Phanerozoic, steranes are generally present when aromatic steroids are found, therefore the Barney Creek Fm triaromatic steroids were attributed to a potential bacterial origin (methylotrophic bacteria) due to the apparent absence of saturated counterparts. However, Nettersheim (2017) found protosterane molecules in Barney Creek Fm sediments – lanostane (LA) and an unknown compound (CA), possibly derived from cycloartane (Figure 4.21). According to Nettersheim, the newly recognised Barney Creek Fm steranes are likely the saturated equivalents of the TAS, suggesting that TAS are derived from the same protosterol precursors as protosteranes, namely lanosterol and/or cycloartenol (Figure 4.21). Thus, it appears that at least in the Barney Creek Fm, but possibly in other Proterozoic formations,

steranes are not absent, but instead they are different from the typical Phanerozoic steranes and could record some of the earliest stages in sterol evolution.

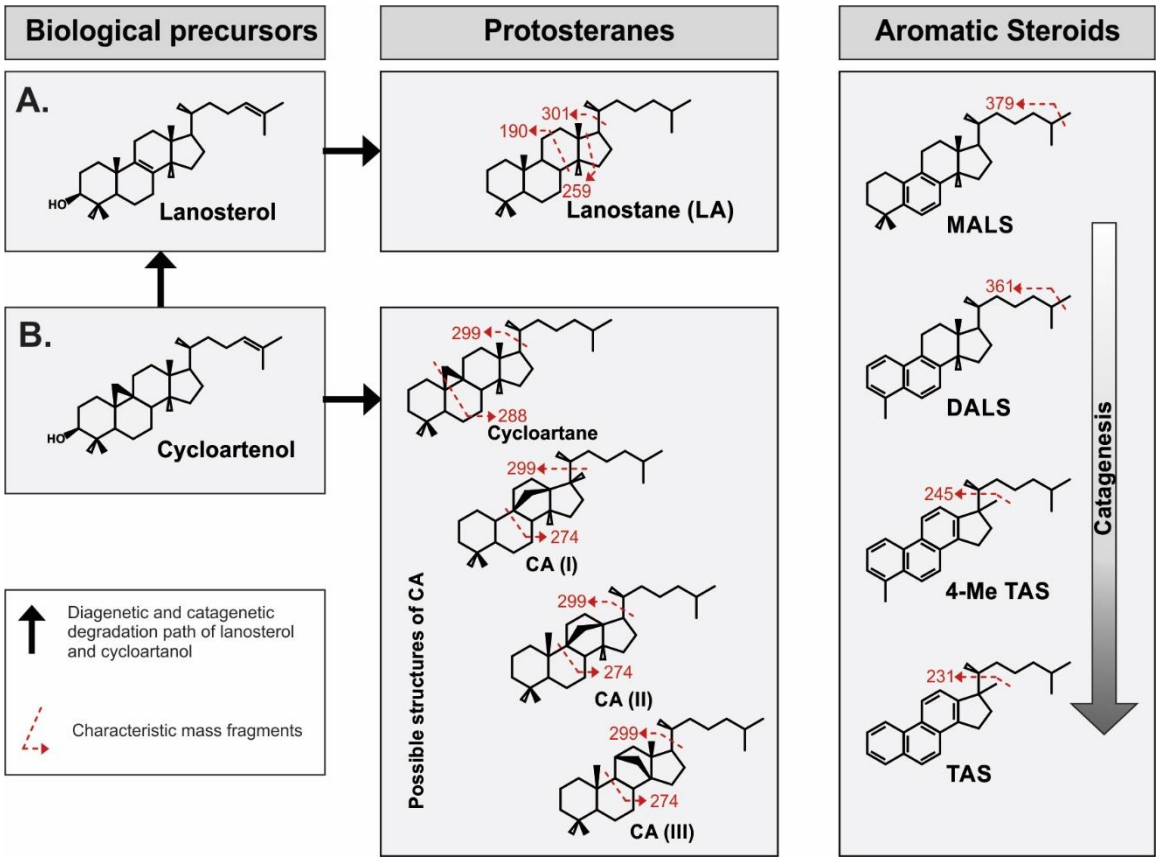

Figure 4.21. Molecular structures of lanosterol, cycloartenol and associated compounds detected in the Barney Creek Formation. (A) Lanosterol can preserve as lanostane (M^+414) with characteristic mass fragments of 301, 259, and 190. Further diagenesis of the molecules results in monoaromatic lanosteroids (MALS), diaromatic lanostroids (DALS), and triaromatic steroids (TAS). (B) The hydrocarbon skeleton of cycloartenol is cycloartane (M^+412), yet in the Barney Creek Fm a similar molecule is preserved with a suspected carbon-bridge in the C-ring (Nettersheim, 2017), referred to as cyclosterane (CA). CA has a characteristic 274 and 299 fragmentation. During aromatization of cycloartenol, the diagnostic three-ring breaks resulting in an aromatic steroid indistinguishable from an aromatized lanosterol.

Lanosterol compounds and its derivatives were isolated from a wide range of eukaryotic organisms, including vertebrates (Abe et al., 1993), yeasts and fungi (Abe et al., 1993; Connolly & Hill, 2000; Handa et al., 2010; Kamalov et al., 2000; Rösecke & König, 1999, 2000), higher plants (Alam et al., 2000; Hui et al., 1971; Kuroda et al., 2002; Kuroyanagi et al., 2000; Majumder et al., 2003; Ori et al., 2003; Rukachaisirikul et al.,

2000; Vieira et al., 2004). Cycloartenol represents an intermediate for sterol synthesis in plants (Abe et al., 1993; Summons et al., 2006). Cycloartenol and derivatives were also detected in modern microbial mats, sometimes in abundances up to 19% of total sterols (Edmunds & Eglinton, 1984). Even though sterols are widespread in eukaryotes, a limited number of bacteria can synthesize simple sterols (Lee et al., 2018; Pearson et al., 2003; Summons et al., 2006; Wei et al., 2016). For example, lanosterol was detected in methanotrophic bacteria *Methylococcus capsulatus* (Bird et al., 1971; Bouvier et al., 1976) and heterotrophic bacteria *Gemmata obscuriglobus* (Pearson et al., 2003), while some myxobacteria can produce both lanosterol and cycloartenol, as well as zymosterol (Bode et al., 2003). Genomic and phylogenetic studies suggest that bacteria may have obtained the ability to produce simple sterols through horizontal gene transfer from eukaryotes (Desmond & Gribaldo, 2009; Gold et al., 2017; Wei et al., 2016). Stem group eukaryotes represent deep branches of the evolutionary tree before the emergence of the last eukaryotic common ancestor (LECA) (Knoll, 2014). According to Desmond and Gribaldo (2009), LECA was able to synthesize a wide range of diverse sterols including more complex sterols with methylated side chain. Since complex steranes were not recorded in the Barney Creek Fm, crown group eukaryotes did not notably contribute sterols to the 1.64 Ga sediments. Therefore, protosteroid producers in the Barney Creek Fm may belong to stem group eukaryotes or bacteria.

Protosterane molecules were previously observed sporadically in Cenozoic and Cambrian sediments (Bao & Li, 2001; Birgel & Peckmann, 2008; Chen et al., 1989; Chen & Summons, 2001; Morales-Izquierdo et al., 1998; Parfenova, 2011; Peckmann et al., 2004). For example, the first discovery of lanostane molecules in the geological record happened in Paleogene dolomitic claystones (Eh2) from the Biyang Basin, China (Chen et al., 1989). Based on the scarce distribution of lanostanes in Phanerozoic sediments,

Parfenova (2011) suggested that these molecules might occur largely in carbonates or carbonate-rich sediments deposited in lacustrine and marine basins under reducing conditions. While the data for this observation are not statistically significant, it is possible that reducing environments enhance the preservation of protosteranes, which generally represent intermediate steps in sterol synthesis for modern organisms. In the mid-Proterozoic, however, protosteranes may be the end-products and reflect the abundance of stem group eukaryotes or bacteria.

4.4.5 Protosteroids, depositional environments

It is impossible at present to differentiate between stem group eukaryotes or bacteria as protosteroid producers in the mid-Proterozoic. However, LV09 drill core offers an opportunity to obtain some ecological information about the type of environments these organisms lived. By analogy to the classic ratio of steranes over hopanes, we plotted the concentrations of primordial steranes relative to hopanes versus depth in order to estimate the relative abundance of protosteroid producers (Figure 4.12a, LA/(LA+hop) and CA/(CA+hop)). In general, LA/(LA+hop) and CA/(CA+hop) parameters reflect a proportion and therefore can be caused by changes in protosteranes or hopanes. Based on the coefficient of variation (C_v = 100*standard deviation/average), the variation of hopane concentrations (C_v = 149%) is lower than the variation of CA concentrations (C_v = 155%) and greater than LA variations (C_v = 114%) in the dataset. Therefore, hopanes might have a stronger effect on the LA/(LA+hop) ratio. However, ratios of protosteranes versus different compounds (hopanes, diahopanes, cheilanthanes and gammacerane) illustrate similar depth trends (Figure 4.22). This observation suggests that variations in LA/(LA+hop) and CA/(CA+hop) ratios are largely controlled by protosteranes.

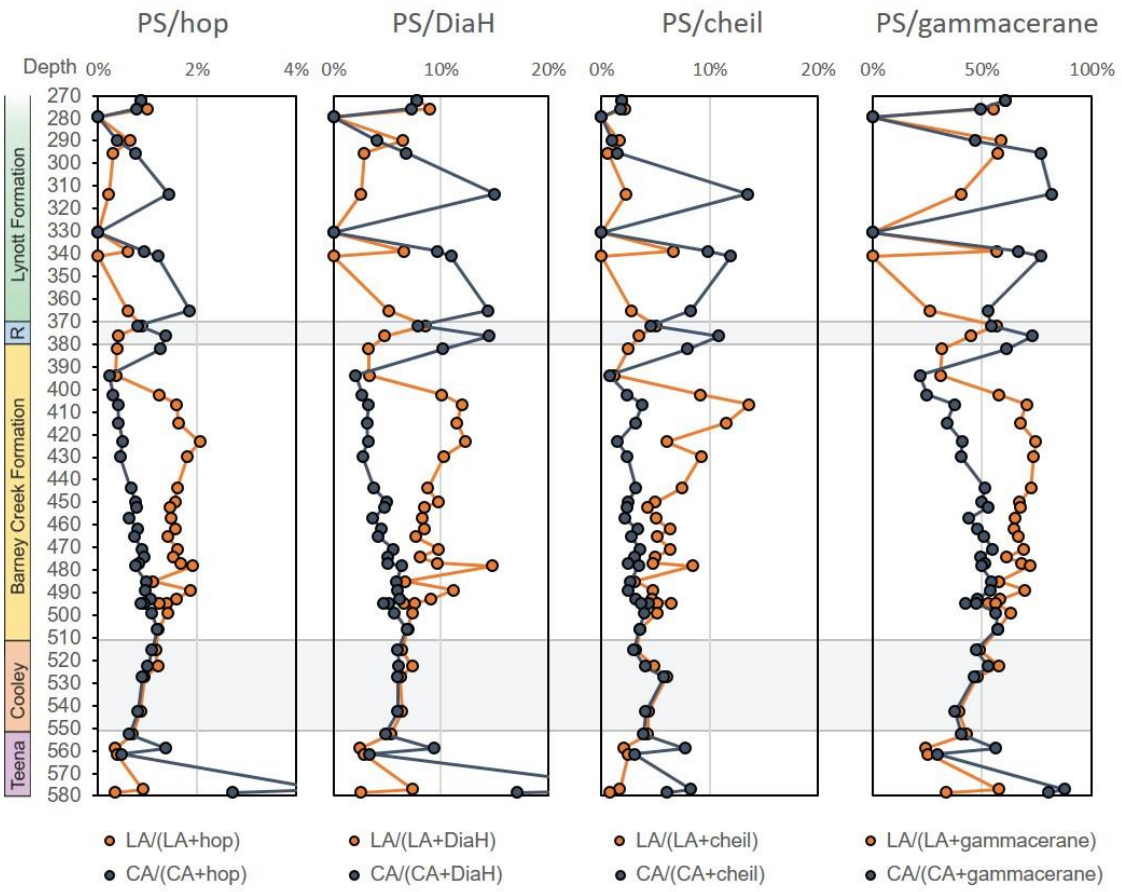

Figure 4.22. Similar depth trends of protosterane ratios for LV09 drill core versus hopanes, diahopanes, cheilanthanes and gammacerane. PS: protosteranes; R: Reward Dolostone.

Besides biological interpretations, biomarker distributions can be controlled by maturity, salinity, redox, biodegradation, clay catalysis, aromatization and lithology changes. However, relative concentrations of primordial steranes in LV09 drill core (Figure 4.12a) do not correlate with such parameters as Ts/(Ts+Tm), GI, HHI, Pr/Ph, AIR or (Pr+Ph)/(*n*-C_{17}+*n*-C_{18}). Furthermore, no relationship of primordial steranes (LA and CA) or aromatic steroids with TOC or carbonate content was found (Figure 4.4). Aromatic steroids (mono-, di- and triaromatic) are likely the aromatic equivalents of the protosteranes, derived from the same precursor. However, aromatic steroids lose part of their diagnostic properties during aromatization and, hence, it becomes impossible to resolve the actual precursor molecule – lanosterol or cycloartenol (Figure 4.21). Relative

aromatic steroid abundances versus protosteranes (ArS/(ArS+PS); Appendix A.1), which represents a degree of aromatization, shows no systematic changes in LV09 drill core and has no relationship with LA/(LA+hop) and CA/(CA+hop) trends. Therefore, variations in ratios of protosteranes relative to hopanes are independent from aromatization. There is, however, an apparent correlation of LA/(LA+hop) with C_{30}DiaH/(DiaH+H) ($R^2 = 0.5$; $p < 0.00001$), while CA/(CA+hop) ratios illustrate a completely independent trend (Figure 4.12a). However, the depths trends of LA/(LA+hop) and C_{30}DiaH/(DiaH+H) are not co-varying ideally. LA/(LA+hop) gradually increases from the bottom to the top of the drill core and reaches its maximum at 423 m depth, then decreases drastically at the top of the Barney Creek Fm; while C_{30}DiaH/(DiaH+H) ratio displays the highest values between 420–515 m depth (Figure 4.12a). Since LA are not rearrangement products of hopanes, the correlation between relative LA and diahopane abundances might be indirect. For example, different diagenesis and degradation conditions may enhance LA production in the Barney Creek Fm similar to diahopanes. While the conversion of lanosterol to cycloartenol is unlikely due to less stable molecular structures of cycloartenol with a three-ring (Figure 4.21), the transformation of cycloartenol to lanosterol during diagenesis is in principle possible by breaking this three-ring. In the Barney Creek Fm, CA/(CA+hop) and LA/(LA+hop) trends do not anti-correlate or anti-co-vary (Figure 4.12a), suggesting that there is no strong dependence between CA and LA. Nevertheless, we cannot completely exclude the possible degradation of CA to LA precursor molecules. If there are no diagenetic transformations between protosteranes, an alternative hypothesis for correlation between LA/(LA+hop) and C_{30}DiaH/(DiaH+H) is possible. Diahopanes are elevated in the muddier facies of the lower Barney Creek Fm deposited in the deepest waters and such depositional environments may be more suitable for LA producers. Below, we examine possible biological interpretations of LA/(LA+hop)

and CA/(CA+hop) trends in LV09 drill core, where these ratios can be explained by fluctuations in abundance of protosteroid producers.

In order to test the relative abundance of protosteroid producers in different depositional environments, we compared deeper marine facies of the Barney Creek Fm with shallower marine sediments of the overlying Reward Dolostone and underlying Teena Dolostone and also restricted lagoonal facies of the Lynott Fm. According to McGoldrick et al. (2010), the Reward and Teena Dolostone represent a carbonate platform facies shallower than the Barney Creek Fm. The concentrations of LA versus hopanes are low in the Lynott Fm, Reward and Teena Dolostone, and have the highest values in the Barney Creek Fm (Figure 4.22). This observation could mean that LA producers preferred deeper environments over relatively shallow carbonate platforms. At the same time, CA/(CA+hop) ratio is high in the Lynott Fm, Reward Dolostone and lower Teena Dolostone (Figure 4.22). The two lowermost Teena samples with high TOC (4.7 and 6.6%) record the highest values of CA/(CA+hop) in the drill core. Although biodegradation does not represent a controlling factor for protosteroid ratios, the Teena sample from 577 m depth is heavily or severely biodegraded with no *n*-alkanes or Pr and Ph preserved. This sample shows the highest CA/(CA+hop) value (4.55%), which could be explained by partly biodegraded hopanes, whereas CA compounds are more stable (Nettersheim, 2017). Overall CA/(CA+hop) trend behaviour suggests that CA producers were more abundant in shallow water environments. Since the concentrations of LA and CA relative to hopanes display different depth trends in LV09 drill core (Figure 4.22), protosterane producing biota may represent a mixture of distinct organisms, some of which prefer deeper environments (LA producers) and others thrive in shallower waters (CA producers). However, this hypothesis is not in agreement with protosterane data from GR7 drill core (the biomarker ratios for GR7 are in Appendix A.3). While LA/(LA+hop)

ratios illustrate comparable values for the Barney Creek Fm in LV09 and GR7, CA/(CA+hop) ratios in GR7 are substantially higher than in LV09 (Figure 4.23). The Barney Creek Fm facies in GR7 are deeper than in LV09 (Kunzmann et al., 2019). Therefore, the assumption that CA producers are more abundant in shallower environments is not supported.

Alternatively, different depth trends of relative LA and CA concentrations might be explained by geographically separated origins of LA and CA producers. For instance, some organisms may represent planktonic species, while others are benthic. However, we cannot confirm this hypothesis, since relative protosterane abundances do not show any correlation with community biomarker parameters (e.g., aromatic carotenoids, 3β-methylhopanes, 2α-methylhopanes, and gammacerane).

Redox conditions may also influence the presence of protosteroid producers. For example, in GR7, the concentrations of LA are below detection limit in euxinic intervals with Fe_{py}/Fe_{HR} >0.7 and GAIR >1.8 (Figure 4.23a). The LA/(LA+hop) ratios in GR7 display weak negative correlations with GAIR ($R^2 = 0.43$; $p < 0.00001$) and Fe_{py}/Fe_{HR} ($R^2 = 0.25$; $p < 0.00001$). In LV09, however, we observe a different pattern. There is no correlation between LA/(LA+hop) and GAIR (Figure 4.23b). While correlation between LA/(LA+hop) and Fe_{py}/Fe_{HR} is not strong ($R^2 = 0.35$; $p < 0.00001$), these parameters illustrate an apparent positive co-variation (Figure 4.23b). Additionally, relative LA abundances are quite high in euxinic intervals, unlike in GR7. Perhaps, the absence of LA in euxinic layers of GR7 is controlled by other factors, such as the overall preservation of biomarkers. Therefore, it is not possible at present to confidently conclude that abundance of LA producers is caused by fluctuations in redox conditions.

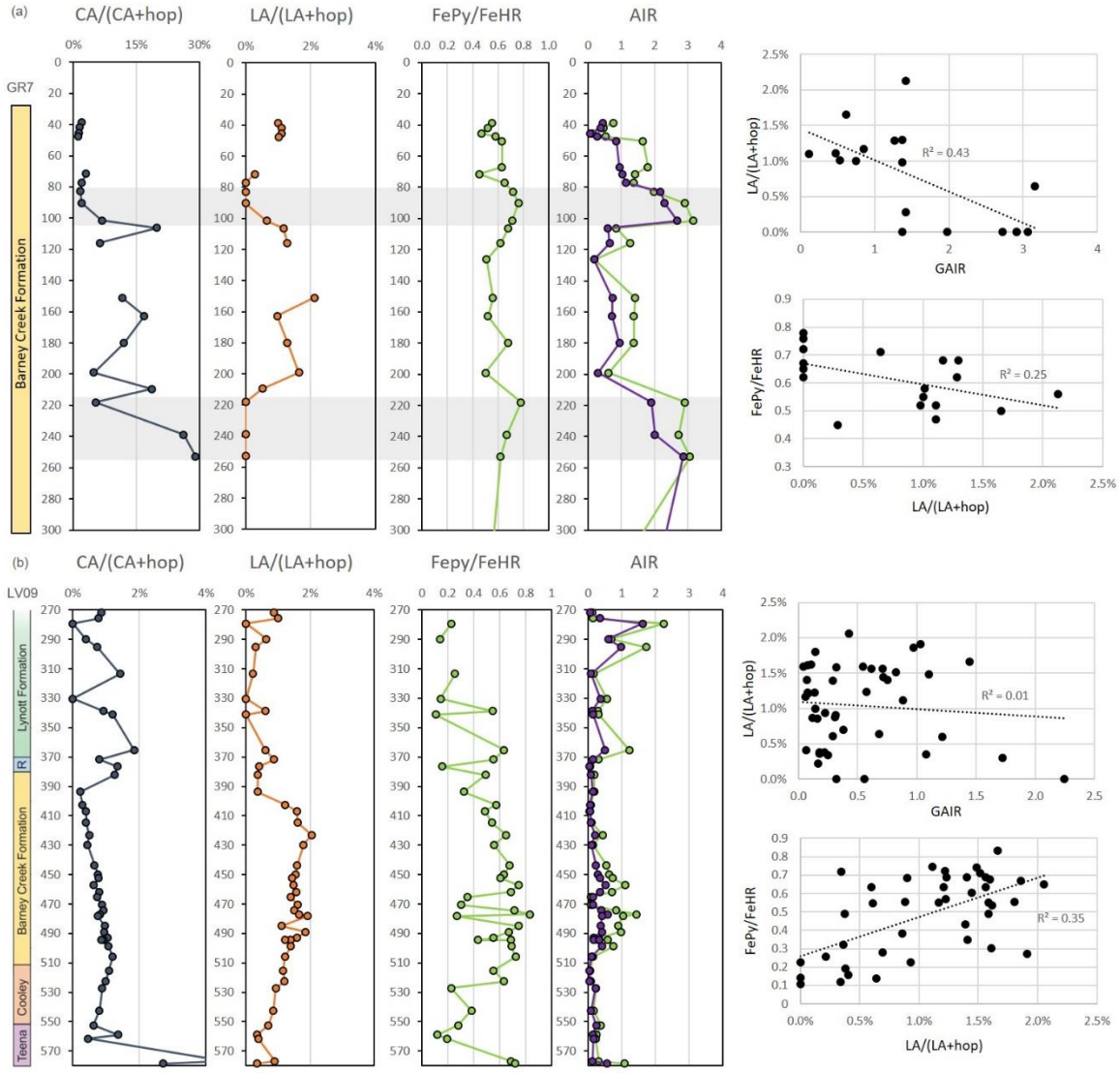

Figure 4.23. Protosteranes versus hopanes ratios, iron speciation (Fe_{py}/Fe_{HR}) and AIR for (a) GR7 and (b) LV09 drill cores. Grey zones in GR7 highlight euxinic intervals. R: Reward Dolostone.

In summary, protosteroid-producing biota may represent a mixture of distinct organisms, since the concentrations of LA and CA relative to hopanes display different depth trends. However, we cannot confidently evaluate what type of environments the protosteroid producers preferred, due to complex and contradictory patterns of relative LA and CA concentrations in GR7 and LV09 drill cores.

4.5 Conclusions

Immature to lower mature Paleoproterozoic sediments from LV09 drill core contain exceptionally well preserved indigenous biomarkers. This is the first study that investigates biomarkers throughout the whole Barney Creek Fm succession, reporting the currently oldest known hopanes and intact aromatic carotenoids in the underlying Teena Dolostone.

The combination of iron speciation, bulk $\delta^{15}N$ and biomarker proxies reveal that the Teena Dolostone, Barney Creek Fm and Reward Dolostone in LV09 drill core were deposited in stratified conditions with mildly oxygenated surface waters and anoxic, dominantly ferruginous bottom waters with occasional fluctuations to sulphidic environments, consistent with a previous study on GR7 drill core (Nettersheim, 2017). Elevated AIR and Pr/Ph ratios in the Lynott Fm are in agreement with shallower water depth and higher oxygen exposure.

Environmental cycles proposed by Nettersheim (2017) for GR7 are not recorded in LV09. Even though cyclicity of proxies is observed in LV09, these variations are of a different temporal scale than in GR7. While the upper Barney Creek Fm in the Glyde River sub-basin saw at least two intermittent periods of elevated oxidation, the Barney Creek Fm in LV09 is consistent with more stable anoxic conditions based on low AIR values. Enhanced diahopanes in the Barney Creek Fm of LV09 (relative to circumjacent formations) are most probably related to clay content either directly (clay catalysis) or indirectly (lower depositional rates and longer exposure to oxidation). Correlation and co-variation between diahopane ratios and 2MHI indicate a possible diagenetic control on 2α-methylhopane abundances.

Biomarkers in LV09 drill core represent a bacteria-dominated ecosystem. Observed bacterial communities include anaerobic green and purple sulphur bacteria (with PSB

predominance), cyanobacteria, tetrahymanol producing bacteria and aerobic methanotrophic bacteria. This variety of bacterial communities can only occur in heterogeneous environments with stratified waters, which is also supported by inorganic proxies.

Diagnostic eukaryotic steranes were below detection limits. Instead, we observe the protosteroids lanostane (LA) and cyclosterane (CA), and aromatic steroids derived from lanosterol and/or cycloartenol. Therefore, it appears that steroids in the Barney Creek Fm are not absent, but instead they are different from typical Phanerozoic steranes, possibly recording some of the earliest stages in sterol evolution. Stem group eukaryotes or bacteria can produce these molecules. In order to test the relative abundance of protosteroid producers in different depositional environments, we compared various formations in LV09 drill core and the Barney Creek Fm in GR7 drill core. Since the concentrations of LA and CA relative to hopanes display different depth trends in LV09 drill core, the protosteroid producing biota may represent a mixture of distinct organisms. However, we cannot confidently evaluate what type of environments the protosteroid producers preferred, due to complex and contradictory patterns of relative LA and CA concentrations in GR7 and LV09 drill cores. Nevertheless, protosterane distributions in the LV09 drill core are not controlled by maturity, biodegradation, redox, and aromatization.

Acknowledgements

We thank Janet Hope (ANU) for laboratory support. We are grateful to Ruslan Khamidullin (Lomonosov MSU) for help with Rock-Eval pyrolysis and Brooke Johnson (University of Oxford) for XRD measurements. We thank Michael Kipp (UW) for organic carbon and nitrogen isotope measurements and Jordan Kinsley (ANU) for iron speciation analysis. We thank Darryl Stacey from the Darwin Core Library (NTGS) for access to drill cores. We thank Marcus Kunzmann (CSIRO) for litho-stratigraphic interpretation of LV09 drill core. We are grateful to Lennart van Maldegem and Ilya Bobrovskiy (ANU) for helpful discussions. This research is funded by Australian Research Council grants DP160100607 and DP170100556.

References

Abe, I., Rohmer, M., & Prestwich, G. D. (1993). Enzymatic cyclization of squalene and oxidosqualene to sterols and triterpenes. *Chemical Reviews, 93*(6), 2189-2206.

Alam, M. S., Chopra, N., Ali, M., & Niwa, M. (2000). Normethyl pentacyclic and lanostane-type triterpenes from Adiantum venustum. *Phytochemistry, 54*(2), 215-220.

Banta, A. B., Wei, J. H., & Welander, P. V. (2015). A distinct pathway for tetrahymanol synthesis in bacteria. *Proceedings of the National Academy of Sciences, 112*(44), 13478-13483.

Bao, J., & Li, M. (2001). Unprecedented occurrence of novel C26–C28 21-norcholestanes and related triaromatic series in evaporitic lacustrine sediments. *Organic Geochemistry, 32*(8), 1031-1036.

Bird, C., Lynch, J., Pirt, F., Reid, W., Brooks, C., & Middleditch, B. (1971). Steroids and squalene in Methylococcus capsulatus grown on methane. *Nature, 230*(5294), 473-474.

Birgel, D., & Peckmann, J. (2008). Aerobic methanotrophy at ancient marine methane seeps: A synthesis. *Organic Geochemistry, 39*(12), 1659-1667.

Blumenberg, M., Thiel, V., Riegel, W., Kah, L. C., & Reitner, J. (2012). Biomarkers of black shales formed by microbial mats, Late Mesoproterozoic (1.1Ga) Taoudeni Basin, Mauritania. *Precambrian Research, 196-197*, 113-127. doi:10.1016/j.precamres.2011.11.010

Bode, H. B., Zeggel, B., Silakowski, B., Wenzel, S. C., Reichenbach, H., & Müller, R. (2003). Steroid biosynthesis in prokaryotes: identification of myxobacterial steroids and cloning of the first bacterial 2, 3 (S)-oxidosqualene cyclase from the myxobacterium Stigmatella aurantiaca. *Molecular Microbiology, 47*(2), 471-481.

Bouvier, P., Rohmer, M., Benveniste, P., & Ourisson, G. (1976). Δ8 (14)-steroids in the bacterium Methylococcus capsulatus. *Biochemical Journal, 159*(2), 267-271.

Brocks, J. J., Grosjean, E., & Logan, G. A. (2008). Assessing biomarker syngeneity using branched alkanes with quaternary carbon (BAQCs) and other plastic contaminants. *Geochimica et Cosmochimica Acta, 72*(3), 871-888.

Brocks, J. J., Love, G. D., Summons, R. E., Knoll, A. H., Logan, G. A., & Bowden, S. A. (2005). Biomarker evidence for green and purple sulphur bacteria in a stratified Palaeoproterozoic sea. *Nature, 437*, 866. doi:10.1038/nature04068

Brocks, J. J., & Schaeffer, P. (2008). Okenane, a biomarker for purple sulfur bacteria (Chromatiaceae), and other new carotenoid derivatives from the 1640Ma Barney Creek Formation. *Geochimica et Cosmochimica Acta, 72*(5), 1396-1414. doi:10.1016/j.gca.2007.12.006

Bull, S. (1998). Sedimentology of the Palaeoproterozoic Barney Creek formation in DDH BMR McArthur 2, southern McArthur basin, northern territory. *Australian Journal of Earth Sciences, 45*(1), 21-31.

Cao, C., Love, G. D., Hays, L. E., Wang, W., Shen, S., & Summons, R. E. (2009). Biogeochemical evidence for euxinic oceans and ecological disturbance presaging the end-Permian mass extinction event. *Earth and Planetary Science Letters, 281*(3-4), 188-201. doi:10.1016/j.epsl.2009.02.012

Chen, J., Philp, R., Fu, J., & Sheng, G. (1989). The occurrence and identification of C30-C32 lanostanes: A novel series of tetracyclic triterpenoid hydrocarbons. *Geochimica et Cosmochimica Acta, 53*(10), 2775-2779.

Chen, J., & Summons, R. E. (2001). Complex patterns of steroidal biomarkers in Tertiary lacustrine sediments of the Biyang Basin, China. *Organic Geochemistry, 32*(1), 115-126.

Clarkson, M., Poulton, S., Guilbaud, R., & Wood, R. (2014). Assessing the utility of Fe/Al and Fe-speciation to record water column redox conditions in carbonate-rich sediments. *Chemical Geology, 382*, 111-122.

Connolly, J. D., & Hill, R. A. (2000). Triterpenoids. *Natural Product Reports, 17*(5), 463-482.

Cordova-Gonzalez, A., Birgel, D., Kappler, A., & Peckmann, J. (2020). Carbon stable isotope patterns of cyclic terpenoids: A comparison of cultured alkaliphilic aerobic methanotrophic bacteria and methane-seep environments. *Organic Geochemistry, 139*, 103940. doi:10.1016/j.orggeochem.2019.103940

Cui, X., Liu, X.-L., Shen, G., Ma, J., Husain, F., Rocher, D., . . . Summons, R. E. (2020). Niche expansion for phototrophic sulfur bacteria at the Proterozoic–Phanerozoic transition. *Proceedings of the National Academy of Sciences, 117*(30), 17599-17606.

Dahl, B., Bojesen-Koefoed, J., Holm, A., Justwan, H., Rasmussen, E., & Thomsen, E. (2004). A new approach to interpreting Rock-Eval S2 and TOC data for kerogen quality assessment. *Organic Geochemistry, 35*(11-12), 1461-1477. doi:10.1016/j.orggeochem.2004.07.003

Desmond, E., & Gribaldo, S. (2009). Phylogenomics of sterol synthesis: insights into the origin, evolution, and diversity of a key eukaryotic feature. *Genome Biol Evol, 1*, 364-381. doi:10.1093/gbe/evp036

Didyk, B., Simoneit, B., Brassell, S. t., & Eglinton, G. (1978). Organic geochemical indicators of palaeoenvironmental conditions of sedimentation. *Nature, 272*(5650), 216-222.

Edmunds, K., & Eglinton, G. (1984). Microbial lipids and carotenoids and their early diagenesis in the Solar Lake laminated microbial mat sequence. *Microbial Mats: Stromatolites* (Vol. 3, pp. 343-390): Alan R. Liss New York.

Farkas, J., Bullen, M., Cox, G., Collins, A., Giuliano, W., Menpes, S., . . . Smith, B. (2018). Isotope Constraints on Intra-Basin Correlation and Depositional Settings of the Mid-Proterozoic Carbonates and Organic-Rich Shales in the Greater McArthur Basin, Northern Territory, Australia. *ASEG Extended Abstracts, 2018*(1), 1-6.

Farrimond, P., Talbot, H. M., Watson, D. F., Schulz, L. K., & Wilhelms, A. (2004). Methylhopanoids: Molecular indicators of ancient bacteria and a petroleum correlation tool. *Geochimica et Cosmochimica Acta, 68*(19), 3873-3882. doi:10.1016/j.gca.2004.04.011

French, K. L., Birdwell, J. E., & Berg, M. V. (2020). Biomarker similarities between the saline lacustrine Eocene Green River and the Paleoproterozoic Barney Creek Formations. *Geochimica et Cosmochimica Acta, 274*, 228-245.

Garby, T. J., Walter, M. R., Larkum, A. W., & Neilan, B. A. (2013). Diversity of cyanobacterial biomarker genes from the stromatolites of Shark Bay, Western Australia. *Environmental Microbiology, 15*(5), 1464-1475.

Gold, D. A., Caron, A., Fournier, G. P., & Summons, R. E. (2017). Paleoproterozoic sterol biosynthesis and the rise of oxygen. *Nature, 543*(7645), 420-423.

Gueneli, N. (2016). *Late Mesoproterozoic Microbial Communities.* (PhD Thesis), Australian National University, Canberra, ACT.

Gueneli, N., McKenna, A., Ohkouchi, N., Boreham, C., Beghin, J., Javaux, E., & Brocks, J. (2018). 1.1-billion-year-old porphyrins establish a marine ecosystem dominated by bacterial primary producers. *Proceedings of the National Academy of Sciences, 115*(30), E6978-E6986.

Handa, N., Yamada, T., & Tanaka, R. (2010). An unusual lanostane-type triterpenoid, spiroinonotsuoxodiol, and other triterpenoids from Inonotus obliquus. *Phytochemistry, 71*(14-15), 1774-1779.

Hui, W., Luk, K., Arthur, H., & Loo, S. (1971). Structures of three C 32 triterpenoids from Neolitsea pulchella. *Journal of the Chemical Society C: Organic*, 2826-2829.

Johnston, D. T., Farquhar, J., Summons, R. E., Shen, Y., Kaufman, A. J., Masterson, A. L., & Canfield, D. E. (2008). Sulfur isotope biogeochemistry of the Proterozoic McArthur Basin. *Geochimica et Cosmochimica Acta, 72*(17), 4278-4290.

Kah, L. C., Lyons, T. W., & Frank, T. D. (2004). Low marine sulphate and protracted oxygenation of the Proterozoic biosphere. *Nature, 431*(7010), 834-838.

Kamalov, L., Agzamova, M., Aripova, S., & Isaev, M. (2000). Low-molecular-weight mushroom metabolites V. Eburicoic acid fromPolyporus ailanthus. *Chemistry of Natural Compounds, 36*(1), 72-75.

Knoll, A. H. (2014). Paleobiological perspectives on early eukaryotic evolution. *Cold Spring Harb Perspect Biol, 6*(1). doi:10.1101/cshperspect.a016121

Knoll, A. H., Summons, R. E., Waldbauer, J. R., & Zumberge, J. E. (2007). The geological succession of primary producers in the oceans. *Evolution of primary producers in the sea* (pp. 133-163): Elsevier.

Kunzmann, M., Schmid, S., Blaikie, T. N., & Halverson, G. P. (2019). Facies analysis, sequence stratigraphy, and carbon isotope chemostratigraphy of a classic Zn-Pb host succession: The Proterozoic middle McArthur Group, McArthur Basin, Australia. *Ore Geology Reviews, 106*, 150-175.

Kuroda, M., Mimaki, Y., Ori, K., Koshino, H., Nukada, T., Sakagami, H., & Sashida, Y. (2002). Lucilianosides A and B, two novel tetranor-lanostane hexaglycosides from the bulbs of Chionodoxa luciliae. *Tetrahedron, 58*(33), 6735-6740.

Kuroyanagi, M., Sugiyama, K., Kanazawa, M., & Kawahara, N. (2000). Novel A-seco-rearranged lanostane triterpenoids from Abies sachalinensis. *Chemical and Pharmaceutical Bulletin, 48*(12), 1917-1920.

Kuznetsov, A., Melezhik, V., Gorokhov, I., Melnikov, N., Konstantinova, G., Kutyavin, E., & Turchenko, T. (2010). Sr isotopic composition of Paleoproterozoic 13C-rich carbonate rocks: the Tulomozero Formation, SE Fennoscandian Shield. *Precambrian Research, 182*(4), 300-312.

Kvalheim, O. M., Christy, A. A., Telnæs, N., & Bjørseth, A. (1987). Maturity determination of organic matter in coals using the methylphenanthrene distribution. *Geochimica et Cosmochimica Acta, 51*(7), 1883-1888.

Lee, A. K., Banta, A. B., Wei, J. H., Kiemle, D. J., Feng, J., Giner, J.-L., & Welander, P. V. (2018). C-4 sterol demethylation enzymes distinguish bacterial and eukaryotic sterol synthesis. *Proceedings of the National Academy of Sciences, 115*(23), 5884-5889.

Lee, C., Love, G. D., Hopkins, M. J., Kröger, B., Franeck, F., & Finnegan, S. (2019). Lipid biomarker and stable isotopic profiles through Early-Middle Ordovician carbonates from Spitsbergen, Norway. *Organic Geochemistry, 131*, 5-18.

Luo, G., Hallmann, C., Xie, S., Ruan, X., & Summons, R. E. (2015). Comparative microbial diversity and redox environments of black shale and stromatolite facies in the Mesoproterozoic Xiamaling Formation. *Geochimica et Cosmochimica Acta, 151*, 150-167.

Lyons, T. W., Reinhard, C. T., Love, G. D., & Xiao, S. (2012). Geobiology of the Proterozoic eon. *Fundamentals of Geobiology*, 371-402.

Majumder, P., Majumder, S., & Sen, S. (2003). Triterpenoids from the orchids Agrostophyllum brevipes and Agrostophyllum callosum. *Phytochemistry, 62*(4), 591-596.

McGoldrick, P., Winefield, P., Bull, S., Selley, D., & Scott, R. (2010). Sequences, synsedimentary structures, and sub-basins: the where and when of SEDEX zinc systems in the southern McArthur Basin, Australia. *Soc. Econ. Geol. Spec. Publ, 15*, 1-23.

Moldowan, J. M., Fago, F. J., Carlson, R. M., Young, D. C., an Duvne, G., Clardy, J., . . . Watt, D. S. (1991). Rearranged hopanes in sediments and petroleum. *Geochimica et Cosmochimica Acta, 55*(11), 3333-3353.

Morales-Izquierdo, A., Fu, J., Sheng, G., Hogg, A., & Strausz, O. P. (1998). Lanostane sulfides in an immature crude oil. *Organic Geochemistry, 28*(1-2), 125-134.

Nettersheim, B. J. (2017). *Reconstructing earth's alien ancient ecology - a multiproxy study of the 1.64 billion-years-old Barney Creek formation, northern Australia.* (PhD Thesis), Australian National University.

Ori, K., Koroda, M., Mimaki, Y., Sakagami, H., & Sashida, Y. (2003). Lanosterol and tetranorlanosterol glycosides from the bulbs of Muscari paradoxum. *Phytochemistry, 64*(8), 1351-1359.

Parfenova, T. (2011). Hydrocarbons of the lanostane homologous series in the Phanerozoic organic matter and their probable biologic sources. *Russian Geology and Geophysics, 52*(8), 773-780.

Parfrey, L. W., Lahr, D. J., Knoll, A. H., & Katz, L. A. (2011). Estimating the timing of early eukaryotic diversification with multigene molecular clocks. *Proceedings of the National Academy of Sciences, 108*(33), 13624-13629.

Pearson, A., Budin, M., & Brocks, J. J. (2003). Phylogenetic and biochemical evidence for sterol synthesis in the bacterium Gemmata obscuriglobus. *Proceedings of the National Academy of Sciences, 100*(26), 15352-15357. doi:10.1073/pnas.2536559100

Peckmann, J., Thiel, V., Reitner, J., Taviani, M., Aharon, P., & Michaelis, W. (2004). A microbial mat of a large sulfur bacterium preserved in a Miocene methane-seep limestone. *Geomicrobiology Journal, 21*(4), 247-255.

Peters, K. (1986). Guidelines for evaluating petroleum source rock using programmed pyrolysis. *AAPG Bulletin, 70*(3), 318-329.

Peters, K., Walters, C., & Moldowan, J. (2005). *The biomarker guide: Volume 2, Biomarkers and isotopes in petroleum exploration and earth history*: Cambridge University Press.

Poulton, S. W., & Canfield, D. E. (2005). Development of a sequential extraction procedure for iron: implications for iron partitioning in continentally derived particulates. *Chemical Geology, 214*(3-4), 209-221.

Poulton, S. W., & Canfield, D. E. (2011). Ferruginous Conditions: A Dominant Feature of the Ocean through Earth's History. *Elements, 7*(2), 107-112. doi:10.2113/gselements.7.2.107

Radke, M., & Welte, D. H. (1983). The methylphenanthrene index (MPI): a maturity parameter based on aromatic hydrocarbons. *Advances Organic Geochemistry 1981*, 504-512.

Rawlings, D. J. (1999). Stratigraphic resolution of a multiphase intracratonic basin system: The McArthur Basin, northern Australia. *Australian Journal of Earth Sciences, 46*(5), 703-723. doi:10.1046/j.1440-0952.1999.00739.x

Ricci, J., Michel, A., & Newman, D. (2015). Phylogenetic analysis of HpnP reveals the origin of 2-methylhopanoid production in Alphaproteobacteria. *Geobiology, 13*(3), 267-277.

Rohrssen, M., Love, G. D., Fischer, W., Finnegan, S., & Fike, D. A. (2013). Lipid biomarkers record fundamental changes in the microbial community structure of tropical seas during the Late Ordovician Hirnantian glaciation. *Geology, 41*(2), 127-130. doi:10.1130/g33671.1

Rösecke, J., & König, W. A. (1999). Steroids from the fungus Fomitopsis pinicola. *Phytochemistry, 52*(8), 1621-1627.

Rösecke, J., & König, W. A. (2000). Constituents of various wood-rotting basidiomycetes. *Phytochemistry, 54*(6), 603-610.

Roussel, A., Cui, X., & Summons, R. E. (2020). Biomarker stratigraphy in the Athel Trough of the South Oman Salt Basin at the Ediacaran-Cambrian Boundary. *Geobiology, 18*(6), 663-681.

Rukachaisirikul, V., Adair, A., Dampawan, P., Taylor, W. C., & Turner, P. C. (2000). Lanostanes and friedolanostanes from the pericarp of Garcinia hombroniana. *Phytochemistry, 55*(2), 183-188.

Schmid, S. (2015). *Sedimentological Review of the Barney Creek Formation in Drillholes LV09001, BJ2, McA5, McArthur Basin*: Northern Territory Geological Survey, Record 2015-006.

Schwark, L., & Frimmel, A. (2004). Chemostratigraphy of the Posidonia Black Shale, SW-Germany: II. Assessment of extent and persistence of photic-zone anoxia using aryl isoprenoid distributions. *Chemical Geology, 206*(3-4), 231-248.

Sigman, D., Altabet, M., McCorkle, D., Francois, R., & Fischer, G. (1999). The δ15N of nitrate in the Southern Ocean: Consumption of nitrate in surface waters. *Global Biogeochemical Cycles, 13*(4), 1149-1166.

Sinninghe Damsté, J. S., Kenig, F., Koopmans, M. P., Koster, J., Schouten, S., Hayes, J., & de Leeuw, J. W. (1995). Evidence for gammacerane as an indicator of water column stratification. *Geochimica et Cosmochimica Acta, 59*(9), 1895-1900.

Slotznick, S. P., Eiler, J. M., & Fischer, W. W. (2018). The effects of metamorphism on iron mineralogy and the iron speciation redox proxy. *Geochimica et Cosmochimica Acta, 224*, 96-115.

Spaak, G., Edwards, D. S., Foster, C. B., Pages, A., Summons, R. E., Sherwood, N., & Grice, K. (2017). Environmental conditions and microbial community structure during the Great Ordovician Biodiversification Event; a multi-disciplinary study from the Canning Basin, Western Australia. *Global and Planetary Change, 159*, 93-112.

Strauss, H., Des Marais, D. J., Hayes, J., & Summons, R. E. (1992). Proterozoic organic carbon—its preservation and isotopic record *Early Organic Evolution* (pp. 203-211): Springer.

Stüeken, E. E., Kipp, M. A., Koehler, M. C., & Buick, R. (2016). The evolution of Earth's biogeochemical nitrogen cycle. *Earth-Science Reviews, 160*, 220-239.

Summons, R. E., Bradley, A. S., Jahnke, L. L., & Waldbauer, J. R. (2006). Steroids, triterpenoids and molecular oxygen. *Philosophical Transactions of the Royal Society B: Biological Sciences, 361*(1470), 951-968.

Summons, R. E., Brassell, S. C., Eglinton, G., Evans, E., Horodyski, R. J., Robinson, N., & Ward, D. M. (1988). Distinctive hydrocarbon biomarkers from fossiliferous sediment of the late proterozoic Walcott member, Chuar Group, Grand Canyon, Arizona. *Geochimica et Cosmochimica Acta, 52*(11), 2625-2637.

Summons, R. E., Jahnke, L. L., Hope, J. M., & Logan, G. A. (1999). 2-Methylhopanoids as biomarkers for cyanobacterial oxygenic photosynthesis. *Nature, 400*(6744), 554-557.

Summons, R. E., Powell, T. G., & Boreham, C. J. (1988). Petroleum geology and geochemistry of the Middle Proterozoic McArthur Basin, Northern Australia: III. Composition of extractable hydrocarbons. *Geochimica et Cosmochimica Acta, 52*(7), 1747-1763. doi:https://doi.org/10.1016/0016-7037(88)90001-4

Talbot, H. M., Summons, R. E., Jahnke, L. L., Cockell, C. S., Rohmer, M., & Farrimond, P. (2008). Cyanobacterial bacteriohopanepolyol signatures from cultures and natural environmental settings. *Organic Geochemistry, 39*(2), 232-263.

van Maldegem, L. M., Nettersheim, B. J., Leider, A., Brocks, J. J., Adam, P., Schaeffer, P., & Hallmann, C. (2020). Geological alteration of Precambrian steroids mimics early animal signatures. *Nature Ecology & Evolution*, 1-5.

Veizer, J. (1989). Strontium isotopes in seawater through time. *Annual Review of Earth and Planetary Sciences, 17*(1), 141-167.

Vieira, L. M., Kijjoa, A., Silva, A. M., Mondranondra, O., Kengthong, S., Gales, L., . . . Herz, W. (2004). Lanostanes and friedolanostanes from the bark of Garcinia speciosa. *Phytochemistry, 65*(4), 393-398.

Vinnichenko, G., Jarrett, A. J. M., Hope, J. M., & Brocks, J. J. (2020). Discovery of the oldest known biomarkers provides evidence for phototrophic bacteria in the 1.73 Ga Wollogorang Formation, Australia. *Geobiology, 18*(5), 544-559. doi:10.1111/gbi.12390

Wang, S., Meade, A., Lam, H.-M., & Luo, H. (2020). Evolutionary Timeline and Genomic Plasticity Underlying the Lifestyle Diversity in Rhizobiales. *Msystems, 5*(4).

Wang, X., Zhao, W., Zhang, S., Wang, H., Su, J., Canfield, D. E., & Hammarlund, E. U. (2018). The aerobic diagenesis of Mesoproterozoic organic matter. *Scientific Reports, 8*(1), 1-10.

Wei, J. H., Yin, X., & Welander, P. V. (2016). Sterol Synthesis in Diverse Bacteria. *Front Microbiol, 7*, 990. doi:10.3389/fmicb.2016.00990

Welander, P. V., Coleman, M. L., Sessions, A. L., Summons, R. E., & Newman, D. K. (2010). Identification of a methylase required for 2-methylhopanoid production and implications for the interpretation of sedimentary hopanes. *Proceedings of the National Academy of Sciences, 107*(19), 8537-8542.

Chapter 5

Substantial maturity influence on carbon and hydrogen isotopic composition of *n*-alkanes in sedimentary rocks

Galina Vinnichenko, Amber J.M. Jarrett, Lennart M. van Maldegem, Jochen J. Brocks

Organic Geochemistry, 152, 2021.

Abstract

Carbon ($\delta^{13}C$) and hydrogen ($\delta^{2}H$) compound-specific isotope analyses on sedimentary hydrocarbons are widely used for ecological reconstructions and oil-source rock or oil-oil correlations. However, the effects of thermal alteration on isotopic composition are not fully understood, potentially imparting a bias on interpretation of older and more mature sedimentary sequences. We measured $\delta^{13}C$ and $\delta^{2}H$ of *n*-alkanes in 23 extracted bitumens from the 1.64 Ga Paleoproterozoic Barney Creek Formation in the southern McArthur Basin, Australia. The samples cover a wide range of thermal maturities with calculated vitrinite reflectance (Rc) values from 0.4 to 1.3%. Our results illustrate that while $\delta^{13}C$ of kerogen remains relatively constant, the $\delta^{13}C$ and $\delta^{2}H$ of *n*-alkanes have a strong positive correlation with thermal maturity. Average $\delta^{13}C_{alk}$ increase by 6.8‰ and $\delta^{2}H_{alk}$ by 69‰ among the samples in the analysed maturity range. At the same time, the carbon isotopic offset between *n*-alkanes and kerogen ($\Delta\delta^{13}C_{alk–ker}$) climbs from 1.3‰ to 8.5‰ with increasing maturity. Therefore, the substantial maturity influence on stable carbon and hydrogen isotopes of *n*-alkanes must be considered in palaeoecological and petroleum correlation studies.

In the initial stages of maturation, *n*-alkanes from the Barney Creek Formation display increasingly positive "isotope slopes" in plots of $\delta^{13}C_{alk}$ against carbon number. However, with further maturation, the slopes became increasingly negative. The isotope slope inversion indicates that the dominant mechanisms for *n*-alkane generation and degradation changed during the progression from early diagenesis to metagenesis. Numerical models suggest that the formation of positive and negative isotope slopes may be driven by the balance of the formation of *n*-alkanes from kerogen and their subsequent degradation, and by dependence of the degradation rate constant *k* on *n*-alkane chain length.

Keywords

Precambrian, McArthur Basin, Compound-specific isotope analysis (CSIA), $\delta^{13}C_{ker}$, biomarkers, Rock-Eval pyrolysis

5.1 Introduction

Compound-specific isotope analysis (CSIA) provides valuable information about biological sources of individual compounds, carbon cycling and geological processes in ancient sedimentary environments (Murray et al., 1994; Rooney et al., 1998; Odden et al., 2002; Sessions, 2016). CSIA is also a successful tool for oil-source rock and oil-oil correlations in Phanerozoic sequences (Pedentchouk & Turich, 2018). However, limited CSIA measurements are available for Precambrian samples, mainly due to the rare preservation of lipid biomarkers in rocks of this age (e.g., French et al., 2015).

One of the widely used approaches for CSIA on ancient sediments is tracking the differences between isotopic composition of *n*-alkyl lipid remains (*n*-alkanes), breakdown products of chlorophyll (pristane and phytane), and total organic carbon (e.g., Logan et al., 1995; Close et al., 2011; Williford et al., 2011; Schinteie & Brocks, 2017; van Maldegem, 2017). Typical Phanerozoic carbon isotope signatures on average follow the biosynthetic fractionation pattern with *n*-alkanes being ~4.5‰ ^{13}C-depleted relative to kerogen (Hayes, 2001) (throughout the text, the terminology isotopically 'depleted or enriched' refers to ^{13}C-depleted or ^{13}C-enriched). Inverse to this isotopic ordering, Proterozoic organic matter is characterised by ~1.5‰ ^{13}C-enrichment of extractable *n*-alkanes relative to kerogen and consequently by positive values of $\Delta\delta^{13}C_{alk-ker}$ (Logan et al., 1995; Logan et al., 1997). Logan et al. (1995) suggested that this inverse δ^{13}C pattern globally occurred in the Proterozoic through intensive heterotrophic reworking of slowly sinking primary biomass by bacteria and preferential preservation of heterotrophic lipids;

whereas in the Phanerozoic, faster-sinking fecal pellets produced by multicellular organisms preserve the signatures of primary biomass. An alternative explanation was proposed by Close et al. (2011). In their mixed community model for the Proterozoic, relatively ^{13}C-enriched prokaryotic phytoplankton represent major input for preserved lipids (e.g., *n*-alkanes), whereas kerogen dominantly retains the isotopically lighter signatures of eukaryotic biomass. A recent study by van Maldegem (2017) showed that changes in redox and community can affect $\delta^{13}C$ systematics, supporting elements of both existing models. However, based on highly variable $\Delta\delta^{13}C_{alk–ker}$ values across different Precambrian sedimentary basins, the author suggested that inverse $\delta^{13}C$ pattern between *n*-alkanes and kerogen is not a universal Proterozoic signal.

The hydrogen isotopic (δ^2H) composition of *n*-alkanes is controlled by a combination of environmental, biological, physical and chemical processes (Sessions, 2016). For thermally immature samples, a wide range of the δ^2H values can reveal information about water chemistry (e.g., meteoric, marine), organic matter source (e.g., marine algae versus terrestrial plants, or autotrophs versus heterotrophs) and biosynthetic fractionations (Sessions, 2016 and references therein). However, hydrogen exchange with water or clay minerals during diagenesis might complicate the original δ^2H signatures and lead to ^2H-enrichment of organic matter (Alexander et al., 1982; Sessions et al., 2004).

Over geological time, the primary carbon and hydrogen isotopic composition of bitumens can be significantly altered by diagenetic and catagenetic processes and especially by increasing thermal maturity (e.g., Clayton, 1991; Clayton & Bjorøy, 1994; Schimmelmann et al., 1999; Dawson et al., 2005, 2007; Radke et al., 2005; Tang et al., 2005; Pedentchouk et al., 2006; Maslen et al., 2012; Cheng et al., 2015; Sessions, 2016). For example, Tang et al. (2005) used anhydrous, closed-system pyrolysis experiments to show that thermal alteration alone can increase δ^2H_{alk} by ~50‰ and $\delta^{13}C_{alk}$ by ~4‰ at

vitrinite reflectance equivalent of 1.5%. Several Phanerozoic studies supported these experiments by showing a trend of increasing δ^2H of *n*-alkanes by up to ~71‰ with increasing maturity (e.g., Li et al., 2001; Dawson et al., 2005, 2007; Radke et al., 2005; Pedentchouk et al., 2006; Maslen et al., 2012), as well as $\delta^{13}C_{alk}$ values enriched by 2.0–4.5‰ in more mature samples (e.g., Clayton & Bjorøy, 1994; Odden et al., 2002; Dawson et al., 2007; Cheng et al., 2015). However, the number of studies that determine the maturity effect on $\delta^{13}C_{alk}$ and δ^2H_{alk} in natural systems is limited. Additionally, to our knowledge, there are no studies for the Phanerozoic and Precambrian that investigate $\delta^{13}C_{alk}$ across a wide range of maturities while keeping organic matter source constant. In this field-based study, we present the results of CSIA on extracted bitumens from the 1.64 Ga Barney Creek Formation (Fm) in the southern McArthur Basin, Australia. Since the Barney Creek Fm has a relatively constant organic matter source and covers a wide maturity range across the basin, we aim to test the effects of thermal alteration on Proterozoic carbon and hydrogen isotopic compositions of *n*-alkanes.

5.2 Geological setting and samples

The McArthur Basin is located in northern Australia and contains a Paleoproterozoic–Neoproterozoic succession of carbonate and siliciclastic rocks with minor volcanic horizons (Ahmad et al., 2013; Munson, 2016). The focus of this study is on the southern part of the basin, where the Paleoproterozoic section is stratigraphically subdivided into the Tawallah and McArthur groups (Jackson et al., 1987). The McArthur Group (~1690 to ~1614 Ma) is represented by shallow to deep marine succession of carbonates, shales, and sandstones (Jackson et al., 1987; Kunzmann et al., 2019). The 1640 ± 4 Ma Barney Creek Fm of the McArthur Group comprises laminated dolomitic, carbonaceous and pyritic siltstone and shale (Jackson et al., 1987; Page & Sweet, 1998).

The Barney Creek Fm is of particular scientific interest because it hosts potential petroleum resources (Powell et al., 1987; Johnson et al., 2013), world class Zn-Pb-Ag deposits, including the McArthur River 'HYC' Mine (Eldridge et al., 1993; Ireland et al., 2004), and it also contains indigenous lipid biomarkers of Paleoproterozoic age (Brocks et al., 2005).

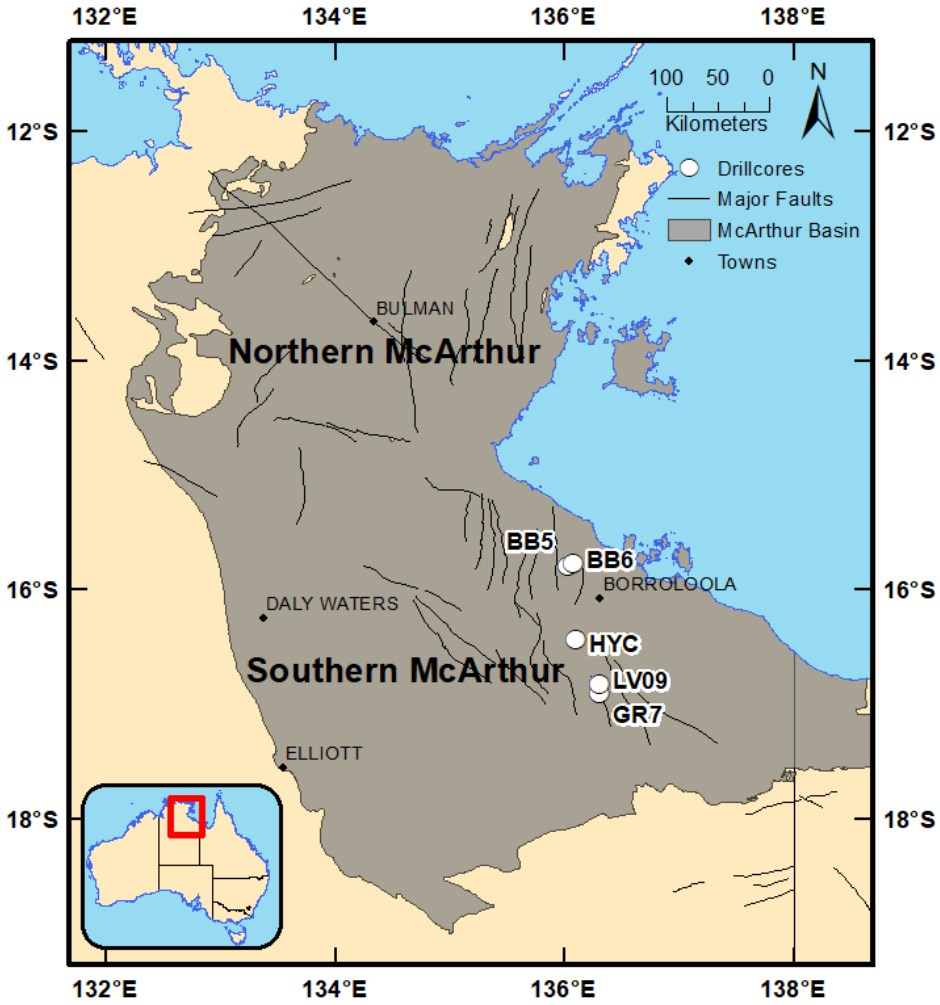

Figure 5.1. McArthur Basin in northern Australia with location of drill cores investigated in this study.

For the current study, a total of 23 Barney Creek Fm samples at different levels of maturity (assessed using hydrocarbon parameters and Rock-Eval pyrolysis) were selected for CSIA and organic carbon isotope analyses (Table 5.1). Samples were collected from

four open-source drill cores (LV09, GR7, BB5, BB6; Figure 5.1), stored at the Northern Territory Geological Survey core library in Darwin, Australia. The unmineralized HYC hanging wall (182 m, 157 m and 94 m above the ore body) and foot wall were also sampled from two drill holes, BS024-01 and MRM 2012-03. These unmineralized HYC samples were selected to avoid hydrothermal alteration effects. We further included published $\delta^{13}C$ and $\delta^{2}H$ values from five HYC ore body samples (Williford et al., 2011).

5.3 Methods

5.3.1 Biomarker analysis

Biomarker analysis was performed at the Australian National University and followed protocols allowing recognition and removal of contamination (e.g., Brocks et al., 2008; Brocks, 2011; French et al., 2015; Vinnichenko et al., 2020). Laboratory contaminants remained below detection limits in the cumulative system blanks that experienced the whole sequence of procedures along with samples. Since contamination from drilling fluids can affect the results of CSIA (Schinteie et al., 2019), the syngeneity of biomarkers was assessed by comparison of exterior and interior (E/I) hydrocarbon contents (Brocks et al., 2008). Therefore, ~3 mm of all external surfaces were removed using a solvent-cleaned precision diamond wafering saw (Buehler IsoMet 1000) or a wet table saw (Nortel Machinery Inc.), depending on sample size and shape. Then the exterior (E) and interior (I) rock portions were ground to < 240-mesh powder using a clean Rocklabs iron puck mill. Later, E and I rock powders were extracted with a Dionex Accelerated Solvent Extractor (ASE 200) using 90% DCM and 10% methanol. Prior to fractionation, elemental sulphur was removed from HYC extracts by filtration over freshly precipitated elemental copper. All extracted bitumens were fractionated into

saturated, aromatic, and polar fractions using microcolumn (Pasteur pipette) chromatography over annealed and dry-packed silica gel (7 cm). Saturated hydrocarbons were eluted with 1.5 ml of *n*-hexane, aromatic hydrocarbons with 4 ml of *n*-hexane:DCM (1:1, v/v) and polar hydrocarbons with 3 ml of DCM:methanol (1:1, v/v). Gas chromatography-mass spectrometry (GC–MS) analyses were carried out on an Agilent 6890 GC coupled to a Micromass Autospec Premier double-sector MS. The GC was equipped with a 60 m DB-5MS capillary column (0.25 mm ID, 0.25 µm; Agilent) and used helium as the carrier gas at a constant flow rate of 1 ml min^{-1}. Full Scan analyses were performed for saturated and aromatic fractions. Based on E/I criteria (e.g., Brocks et al., 2008), all analysed interior fractions contained indigenous biomarkers.

5.3.2 Compound-specific isotope analyses ($\delta^{13}C$ and $\delta^{2}H$)

Prior to CSIA, *n*-alkanes were separated from the saturated fractions (Figure 5.2) using 0.5 mg of 5Å zeolite molecular sieve (Grace Davison), which was activated at 300 ºC for 9 hours. The molecular sieve and corresponding saturated fractions were combined with 3.5 ml of cyclohexane, sealed, vigorously mixed and kept overnight at 90 ºC on a hot plate. The sieve was filtered, washed with cyclohexane, air-dried for 2 – 3 hours and digested in HF (32%, 3 ml) to release the *n*-alkanes, which were further extracted with 3 ml *n*-hexane. Total ion chromatograms of separated *n*-alkane fractions illustrate that branched/cyclic compounds and unresolved complex mixture were successfully removed during molecular sieving (Figure 5.2).

Stable carbon and hydrogen isotopic compositions of individual *n*-alkanes were measured at Geoscience Australia. For carbon isotopes, the instrument comprised a Thermo Trace gas chromatograph (GC) connected to a Finnigan MAT 253 isotope ratio mass spectrometer (IRMS) via a combustion furnace and water-removal assembly. The

on-column injector temperature was held at 150 ºC. The 1 µl of pentane solution with sample *n*-alkanes was injected either manually or with the GC PAL autosampler. Individual hydrocarbons were quantitatively converted to CO_2 and H_2O in the combustion reactor operated at 940 °C. Water was removed using a tubular Nafion™ membrane swept with helium. The GC was equipped with a DB-5 fused silica column (60 m x 0.32 mm ID, film thickness 0.25 µm). The oven was maintained at 40 °C for 4 min, ramped to 220 °C at 6 °C/min and then to 310 °C at 8 °C/min with a hold of 40 min. A mixture of perdeuterated *n*-C_{16} ($\delta^{13}C$ = –28.68‰), *n*-C_{20} ($\delta^{13}C$ = –34.04‰), and *n*-C_{24} ($\delta^{13}C$ = –26.85‰) alkanes was co-injected or separately injected with the sample. In general, a precision of less than 0.3‰ was obtained for perdeuterated *n*-alkanes with minimal background. Hydrogen isotopes were obtained using a Thermo Scientific Delta V Advantage IRMS, which was linked to Trace GC-TC. Before analysis, background scans and zero enrichment were performed to monitor the day-to-day performance of the GC-TC-IRMS system as a routine daily procedure. The H_3^+ factor (<10) was also calculated to ensure the linearity of results with responses within 0.5 to 10 V. Hydrocarbon components were resolved using a DB-5 capillary column (60 m x 0.32 mm ID, film thickness 0.25 µm) with Ultra High Purity (UHP) helium as a carrier gas at a constant flow rate of 1.2 ml min^{-1}. The on-column injector temperature was held at 150 ºC. The oven was maintained at 40 °C for 8 min, ramped to 200 °C at 10 °C/min and then to 310 °C at 8 °C/min with a hold of 40 min. The 2 µl of pentane solution with sample *n*-alkanes (more concentrated than for carbon isotopes) was injected either manually or with the GC PAL autosampler. A mixture of C_{20} (δ^2H = –177.8‰), C_{22} (δ^2H = –218.8‰), and C_{25} (δ^2H = –194.8‰) fatty acid methyl ester was separately injected with the sample as a standard to check the accuracy and repeatability of the GC-TC-IRMS system. The $\delta^{13}C$ and δ^2H values are reported in permil (‰) notation relative to VPDB and VSMOW

respectively. All analyses were run as a minimum in duplicate with an average standard deviation of individual compounds of 0.13‰ for $\delta^{13}C$ and 2‰ for $\delta^{2}H$.

5.3.3 Organic carbon isotope analyses

Organic carbon isotope analyses of kerogen ($\delta^{13}C_{ker}$) for LV09 samples followed the methods described in Stüeken (2013) and Kipp et al. (2018), and were measured at the IsoLab facilities in the Department of Earth and Space Sciences of the University of Washington. Rock powders were decarbonised with 6 N HCl, then samples were rinsed in 18 MΩ DI-H_2O and dried in an oven at 60 °C. Carbonate-free powders were analysed with a Costech ECS 4010 Elemental Analyser coupled to a Thermo Finnigan MAT 253 continuous flow IRMS.

Kerogen isolation for BB5, BB6 and HYC samples was performed at Geoscience Australia following the in-house protocol. The $\delta^{13}C_{ker}$ was measured with a Thermo Scientific MAT 253 IRMS for BB5 and BB6 samples, and with Sercon 20-20 combustion IRMS for HYC samples.

5.3.4 Rock-Eval pyrolysis

Total organic carbon (TOC) content and Tmax were measured on bulk rock powders using a Rock-Eval 6 Turbo™ (Vinci Technologies, France) at Geoscience Australia for BB5 and BB6 samples and Lomonosov Moscow State University for LV09 and HYC samples.

5.3.5 Numerical simulation of *n*-alkane degradation

To assess the trajectory of *n*-alkane concentrations and $\delta^{13}C$-profiles with increasing maturation, we constructed simple numerical models. The annotated code and accessory

files are available in the Supplementary Information (Appendix B). Input variables include initial concentrations of C_1 to C_{33} *n*-alkanes (in moles of carbon) and their carbon isotopic composition $\delta^{13}C$ *vs* VPDB. The models consider three principal mechanisms of *n*-alkane degradation and formation that may run in parallel. (1) Cleavage of *n*-alkanes along the carbon chain to shorter molecules that are returned to the reactant pool. The rate constant k_h (*h* = homolytic) and the $^{13}C/^{12}C$ fractionation factor α_h were assumed to be identical for each C–C bond within individual *n*-alkanes, except for terminal $–CH_2–CH_3$ bonds, which were neglected due to much higher activation energies of cleavage (Tang et al., 2000; Watanabe et al., 2001). In the input parameter file, rate constants $k_h(n)$ were set for each *n*-alkane homolog with carbon number *n*. For instance, to simulate thermal degradation of *n*-alkane homologs in a radical chain reaction in the gas phase, rate constants were set to follow the established equation $k_h \sim (n–2)*(n–3)^{1/2}$ (Watanabe et al., 2001). (2) The second type of reaction 'isomerizes' *n*-alkanes into new products and channels them into an 'isomer pool' but does not generate shorter *n*-alkanes. These reactions have the rate constant k_i (*i* = isomerization) and $^{13}C/^{12}C$ fractionation factor α_i. In the reaction examined in more detail in this manuscript, k_i was independent of *n*-alkane chain length *n*. (3) The third type of reaction is the generation of new *n*-alkanes through cleavage of *n*-alkyl moieties from kerogen. This reaction was simulated by cleaving *n*-C_{33} residues along the chain assuming that all C–C bonds have the same activation energy, except the terminal $–CH_2–CH_3$ bonds, which were neglected (see above).

5.4 Results

5.4.1 Biomarker distribution, thermal maturity and Rock-Eval data

Extracted Barney Creek Fm bitumens from drill core LV09 (n = 12) illustrate typical mid-Proterozoic (1.8–0.8 Ga) hydrocarbon distributions including a large unresolved complex mixture, relatively high methylalkane/*n*-alkane ratios, lack of saturated steranes and prevalence of hopanes and aromatic carotenoids (Brocks et al., 2005). The unimodal distribution of *n*-alkanes ranges from C_{10} to C_{32} with a maximum at C_{14} to C_{20} (Figure 5.2). The ratio of regular isoprenoids pristane and phytane (Pr/Ph) varies slightly between 0.3 and 0.6 and is consistent with minimal oxygen exposure of organic matter (Peters et al., 2005). Although samples from drill cores GR7, BB5, and BB6 and the HYC mine are too mature for preservation of polycyclic terpanes and carotenoids derivatives, the extracts demonstrate a non-biodegraded unimodal distribution of *n*-alkanes in the range $C_{10–30}$ with a maximum at $C_{14–16}$ and elevated methylalkane/*n*-alkane ratios compared with LV09 extracts (Figure 5.2).

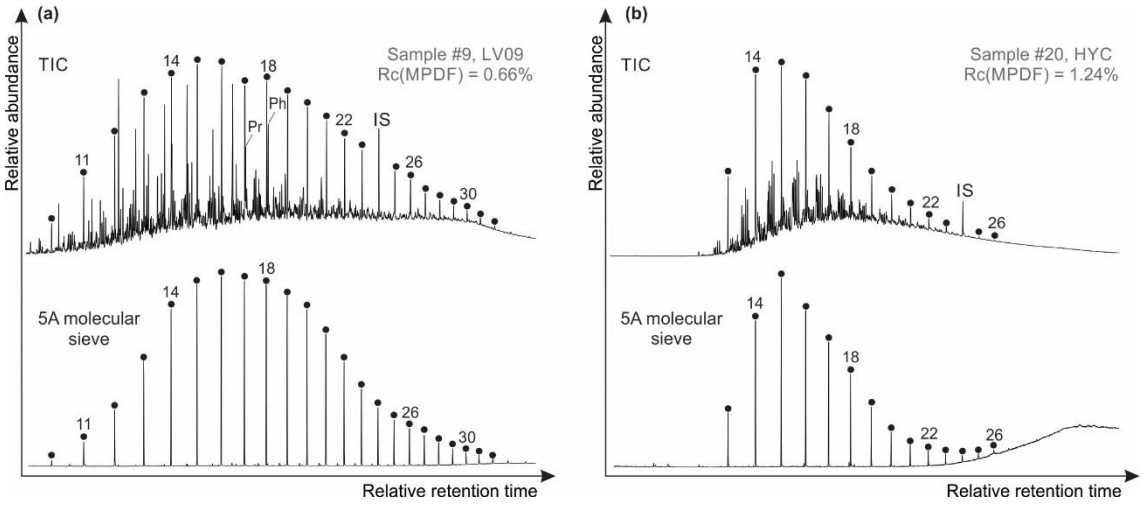

Figure 5.2. Total ion chromatograms (TIC) of saturated fractions and separated *n*-alkanes for Barney Creek Fm samples (a) #9 and (b) #22 of different maturity. Black circles represent *n*-alkanes. Pr: pristane; Ph: phytane; IS: internal standard, co-eluting with *n*-C_{24}.

The maturity level of Barney Creek Fm bitumens was assessed using the methylphenanthrene distribution factor (MPDF) (Kvalheim et al., 1987) (Table 5.1). Calculated vitrinite reflectance equivalent values Rc(MPDF) indicate variable thermal maturities that range from immature to early mature in LV09 (Rc = 0.44–0.71%), through the main oil window in GR7, BB5, and BB6 (Rc = 0.64–1.1%), and within the beginning of the gas window in the unmineralized HYC samples (Rc = 1.1–1.3%). Saturated hydrocarbon parameters based on polycyclic terpanes could not be applied in the current study since required compounds such as hopanes were not detected in the more mature samples.

The results of Rock-Eval pyrolysis are summarized in Table 5.1. Based on the classification scheme of Peters and Cassa (1994), the Barney Creek Fm has fair to excellent organic richness with TOC between 0.35% and 4.7% (Table 5.1). Since the hydrogen index (HI) is probably underestimated in the samples with low TOC due to mineral matrix effects (Espitalié et al., 1980; Dahl et al., 2004), in the following we only consider HI values in the samples with TOC >1%. In the least mature LV09 drill core with Tmax values from 424 °C to 438 °C, HI ranges between 344 and 515 mg HC/g TOC and indicates predominantly oil- and gas-prone marine kerogen (Table 5.1). In more mature BB5, BB6 and HYC samples, HI illustrates much lower values between 18 and 64 mg HC/g TOC (Table 5.1). S2 peaks of LV09, BB5 and unmineralized HYC samples illustrate well-formed Gaussian peaks (Appendix B.1, Supplementary Figure 1a–c). Tmax values for these samples vary from 424 °C to 468 °C (Table 5.1) and correlate positively with Rc(MPDF) (R^2 = 0.72, p = 0.0015). Accordingly, the methylphenanthrene-based maturity parameter and bulk rock Tmax are consistent and demonstrate immature to late mature source rock. Production index (PI) values around 0.1 for low maturity LV09 samples and ≤0.3 for more mature BB5 and HYC samples

suggest largely uncontaminated source rocks (Peters & Cassa, 1994). Oil saturation indices (S1/TOC) less than 100 mg of oil per gram of TOC indicate that all analysed samples are unaffected by migrated hydrocarbons (Jarvie, 2012). Tmax was also measured for BB6 samples. However, the results were not included in this study due to unreliable pyrograms displaying broad bimodal S2 peaks (Appendix B.1, Supplementary Figure 1d) and anomalously low Tmax. Such S2 shapes are common for heavy ends of bitumen, migrated oil, or drilling additives (Peters, 1986). Most probably, bulk BB6 rock powders used for Rock-Eval pyrolysis were affected by surficial contamination. Nevertheless, based on rigorous assessment of biomarker syngeneity using Exterior/Interior experiments (Brocks et al., 2008), the interior fractions of BB6 samples used for CSIA measurements remain unaffected by contamination.

5.4.2 Stable carbon isotopes

The stable carbon isotopic composition of Barney Creek Fm kerogen ($\delta^{13}C_{ker}$) is relatively constant across the Southern McArthur Basin, ranging from –32.5 to –33.5‰ in LV09, from –32.6 to –34.4‰ in BB5 and BB6, and from –33.1 to –34.0‰ in the unmineralized HYC samples (Table 5.1). These values are also consistent with previously published $\delta^{13}C_{ker}$ measurements of the Barney Creek Fm (Powell et al., 1987; Williford et al., 2011).

Table 5.1. Thermal maturity, TOC, Rock-Eval pyrolysis parameters and isotope ratios of Barney Creek Formation samples

Sample ID	Drill core[a]	Depth (m)	MPDF[b]	Rc (MPDF)[c]	Tmax[d] (°C)	TOC[e] (%)	S1[f]	S2[g]	PI[h]	S1/ TOC[i]	HI[j]	$\delta^{13}C$ ker[k] (‰)	$\delta^{13}C$ alk[l] (‰)	$\Delta\delta^{13}C_{alk-ker}$[m] (‰)	$\delta^{2}H$ alk[n] (‰)
#1	LV09	414.75	0.27	0.44	430	1.12	0.36	3.85	0.09	32	344	-33.1	-30.6	2.5	n.d.
#2	LV09	429.7	0.33	0.58	433	1.57	0.78	7.32	0.10	50	466	-32.6	-30.8	1.8	-108
#3	LV09	450.0	0.35	0.62	435	2.26	1.32	10.73	0.11	58	475	-32.8	-30.8	2.0	-112
#4	LV09	461.83	0.32	0.56	431	2.23	1.02	9.30	0.10	46	417	-33.4	-31.1	2.4	-111
#5	LV09	470.7	0.35	0.62	424	0.87	0.38	3.46	0.10	44	398	-33.0	-31.3	1.7	n.d.
#6	LV09	477.0	0.39	0.71	434	4.36	2.69	22.35	0.11	62	513	-32.6	-31.3	1.4	-120
#7	LV09	478.2	0.37	0.67	431	0.60	0.14	1.61	0.08	23	268	-33.1	-31.8	1.3	-106
#8	LV09	485.0	0.37	0.66	438	4.71	2.50	24.24	0.09	53	515	-33.5	-31.2	2.3	-116
#9	LV09	489.0	0.37	0.66	435	3.78	1.82	17.0	0.10	48	450	-33.5	-30.9	2.6	-118
#10	LV09	494.5	0.35	0.61	436	0.45	0.06	0.73	0.08	13	162	-32.7	-30.6	2.1	-103
#11	LV09	494.6	0.37	0.67	433	3.26	1.56	13.26	0.11	48	407	-33.0	-30.7	2.3	-120
#12	LV09	498.88	0.36	0.63	427	3.38	1.88	12.12	0.13	56	359	-32.5	-30.8	1.7	-113
#13	GR7	683.54	0.36	0.64	-	-	-	-	-		-	-	-	-	-117
#14	GR7	869.6	0.45	0.83	-	-	-	-	-		-	-	-	-	-115
#15	BB5	215.8	0.56	1.09	442	2.23	0.20	0.41	0.33	9	18	-33.6	-27.3	6.3	-88
#16	BB6	108.9	0.50	0.96	n.d.	0.62	0.10	0.28	0.27	16	44	-34.4	-28.6	5.8	-87
#17	BB6	125.75	0.48	0.90	n.d.	1.03	0.22	0.66	0.25	21	64	-33.5	-28.8	4.7	-87
#18	BB6	134.5	0.55	1.07	n.d.	1.09	0.27	0.67	0.29	25	61	-32.6	-28.6	4.0	-95
#19	BB6	142.67	0.56	1.10	n.d.	1.07	0.21	0.66	0.24	20	62	-33.6	-29.3	4.3	-96
#20	BS024-01	16.4	0.63	1.24	443	2.99	0.19	0.67	0.22	6	22	-33.4	-25.0	8.4	-51
#21	BS024-01	41.5	0.65	1.30	463	1.44	0.03	0.29	0.09	2	20	-34.0	-25.5	8.5	n.d.
#22	BS024-01	105.1	0.57	1.10	446	0.42	0.02	0.14	0.13	5	33	-33.3	-29.5	3.8	-75
#23	MRM 2012-03	210.8	0.62	1.22	468	0.35	0.01	0.04	0.20	3	11	-33.1	-26.2	6.9	n.d.
#24*	HYC		0.55	1.08	n.d.	0.79	n.d.	n.d.	n.d.	n.d.	6	-33.5	-27.4	6.1	-62
#25*	HYC		0.55	1.06	n.d.	0.48	n.d.	n.d.	n.d.	n.d.	4	-33.0	-27.8	5.2	-73
#26*	HYC	Mine pit	0.53	1.02	n.d.	0.48	n.d.	n.d.	n.d.	n.d.	13	-33.3	-27.7	5.6	-81
#27*	HYC		0.53	1.03	n.d.	0.48	n.d.	n.d.	n.d.	n.d.	2	-33.3	-26.8	6.5	-76
#28*	HYC		0.49	0.94	n.d.	0.56	n.d.	n.d.	n.d.	n.d.	12	-33.0	-27.2	5.8	-80

Table 5.1 [a]Drill core: LV09, GR7, BB5, BB6 – open source drill cores; BS024-01 and MRM 2012-03 are from the Here is Your Chance (HYC) mine. *#24–28: previously analysed Barney Creek Formation (BCF) samples from HYC (Williford et al., 2011). [b]Methylphenanthrene distribution factor MPDF = (3-MP+2-MP)/(3-MP+2-MP+9-MP+1-MP) (Kvalheim et al., 1987). [c]Calculated vitrinite reflectance Rc(MPDF) = 2.242*MPDF - 0.166 (Kvalheim et al., 1987). [d]Temperature at maximum of S2 peak. [e]Total organic carbon (%) from Rock-Eval pyrolysis. [f]Free hydrocarbons, mg HC/g rock. [g]Generative potential, mg HC/g rock. [h]Production index PI = S1/(S1+S2). [i]Oil saturation index = (S1/TOC)*100 mg HC/g TOC. [j]Hydrogen index HI = S2*100/TOC in mg HC/g TOC. [k]Organic carbon isotope values of kerogen. [l]Stable carbon isotopic composition of *n*-alkanes (average of *n*-$C_{16–23}$ for the current study and of *n*-$C_{18–21}$ for samples #24–28). [m]*n*-alkane–kerogen isotopic offset. [n]Stable hydrogen isotopic composition of *n*-alkanes (average of *n*-$C_{16–23}$ for the current study and of *n*-$C_{18–21}$ for samples #23–27). n.d. – not detectable or unreliable. "-" – not measured.

The carbon isotopic composition of *n*-alkanes ($\delta^{13}C_{alk}$), however, varies more widely. It ranges from –29.6‰ to –32.6‰ for LV09, from –26.9‰ to –27.5‰ for BB5, from –27.8‰ to –30.2‰ for BB6 and from –24.1‰ to –30.3‰ for HYC samples (Figure 5.3a, Table 5.2). Most LV09 samples display an increase of $\delta^{13}C_{alk}$ values by up to 3.5‰ with increasing carbon number in the range *n*-C_{12}–C_{31}, while no clear trend was observed for the BB5 and BB6 drill cores. Conversely, $\delta^{13}C_{alk}$ values in HYC samples generally decrease with increasing *n*-alkane carbon number (Figure 5.3a).

The discussion will focus on the non-weighted average of $\delta^{13}C$ of *n*-alkanes in the range *n*-C_{16} to *n*-C_{23} (Table 5.1), as carbon isotope data are available within that range for all samples. The average $\delta^{13}C_{alk}$ of *n*-$C_{16–23}$ for the Barney Creek Fm dataset increases from –31.8‰ to –25.0‰ with increasing Rc(MPDF). Similarly, the carbon isotopic offset between *n*-alkanes and kerogen ($\Delta\delta^{13}C_{alk–ker}$) increases from 1.3‰ in the early mature LV09 samples to 8.5‰ in the late mature HYC samples. Rc(MPDF) shows significant positive linear correlations with both $\Delta\delta^{13}C_{alk–ker}$ ($R^2 = 0.80$, $p < 0.00001$) and $\delta^{13}C_{alk}$ ($R^2 = 0.80$, $p < 0.00001$) (Figure 5.4a and c). Previously published carbon isotope values for HYC bitumens (Williford et al., 2011), included in Figure 5.4, fall on the trend line.

5.4.3 Stable hydrogen isotopes

The stable hydrogen isotopic composition of Barney Creek Fm *n*-alkanes (δ^2H_{alk}) is represented in Table 5.3 and Figure 5.3b. Analysed samples show progressive enrichment in $^2H_{alk}$ with increasing chain length of *n*-alkanes. To remain consistent with the reported average $\delta^{13}C_{alk}$ values, we use non-weighted average δ^2H_{alk} for *n*-C_{16} to *n*-C_{23}. Average δ^2H_{alk} of *n*-$C_{16–23}$ varies from –103‰ to –120‰ for LV09, from –115‰ to –117‰ for GR7, from –87‰ to –96‰ for BB6, reaches –88‰ for BB5 and from –75‰ to –51‰ for HYC samples (Table 5.1). Similar to carbon isotopes, average δ^2H_{alk} yields a strong linear correlation ($R^2 = 0.74$, $p < 0.0001$) with Rc(MPDF) across the sample set (Figure 5.4d). Additionally, average δ^2H_{alk} correlates positively with average $\delta^{13}C_{alk}$ ($R^2 = 0.83$, $p < 0.00001$, not shown).

Table 5.2. *n*-Alkane carbon isotopic composition of Barney Creek Formation bitumens

ID	$\delta^{13}C$ (‰), carbon number																			
	12	13	14	15	16	17	18	19	20	21	22	23	24	25	26	27	28	29	30	31
#1	n.d.	n.d.	n.d.	n.d.	-30.4 (0)	-30.4 (0.3)	-30.7 (0)	-30.8 (0.2)	-30.6 (0.1)	-30.5 (0.1)	-30.7 (0.1)	-30.4 (0.1)	-30.6 (0.1)	-30.7 (0)	-31.0 (0.2)	-30.8 (0.2)	-30.4 (0.1)	-30.7 (0.2)	-30.5 (0.1)	n.d.
#2	n.d.	n.d.	-31.6 (0)	-31.6 (0.1)	-31.4 (0.1)	-31.0 (0.1)	-30.9 (0.1)	-30.7 (0.1)	-30.6 (0.1)	-30.5 (0)	-30.8 (0.1)	-30.7 (0.2)	-30.7 (0.3)	-31.0 (0)	-30.5 (0.1)	-31.3 (0.3)	-30.4 (0)	-31.0 (0)	-30.5 (0.1)	-31.4 (0.3)
#3	n.d.	-30.2 (0.1)	-30.4 (0)	-30.8 (0.3)	-31.2 (0.3)	-31.0 (0.2)	-31.2 (0.2)	-30.9 (0.2)	-30.7 (0.2)	-30.5 (0.3)	-30.4 (0.2)	-30.4 (0.1)	-30.6 (0.2)	-30.1 (0.1)	-29.9 (0.3)	-30.4 (0.1)	-29.6 (0.3)	-29.6 (0.2)	-29.8 (0.1)	n.d.
#4	n.d.	n.d.	n.d.	-30.8 (0.2)	-30.6 (0.3)	-30.7 (0.3)	-30.8 (0.3)	-30.8 (0.3)	-31.0 (0.3)	-31.3 (0.1)	-31.6 (0)	-31.6 (0.1)	-31.7 (0)	-31.3 (0)	-31.4 (0.1)	-31.5 (0.2)	-31.5 (0.3)	-31.4 (0.2)	-31.1 (0.4)	n.d.
#5	n.d.	n.d.	n.d.	-31.8 (0.1)	-31.2 (0)	-31.5 (0.2)	-32.0 (0)	-31.3 (0)	-30.9 (0.1)	-31.1 (0.2)	-31.5 (0.2)	-30.7 (0.1)	-31.0 (0.2)	-30.9 (0.3)	-30.9 (0.1)	n.d.	n.d.	n.d.	n.d.	n.d.
#6	-32.6 (0)	-33.1 (0.1)	-32.3 (0.1)	-32.3 (0.1)	-32.0 (0.2)	-31.9 (0.1)	-31.8 (0)	-31.3 (0)	-31.0 (0.1)	-30.9 (0)	-30.6 (0)	-30.5 (0)	-30.2 (0.1)	-30.1 (0)	-29.8 (0.2)	-30.2 (0.4)	-29.8 (0.3)	-29.6 (0.1)	n.d.	n.d.
#7	n.d.	-32.0 (0.1)	-32.4 (0.1)	-32.3 (0.1)	-32.3 (0.1)	-32.0 (0.1)	-31.9 (0.1)	-31.9 (0)	-31.6 (0.1)	-31.5 (0.1)	-31.4 (0)	-31.5 (0.1)	-31.5 (0.1)	-31.4 (0)	-31.3 (0.3)	-31.4 (0.2)	-30.9 (0.2)	-31.0 (0.2)	n.d.	n.d.
#8	-31.8 (0)	-32.0 (0)	-31.5 (0.2)	-31.7 (0.1)	-31.5 (0)	-31.5 (0)	-31.5 (0.1)	-31.4 (0.1)	-31.5 (0.1)	-30.9 (0)	-30.8 (0.1)	-30.7 (0.2)	-30.6 (0.4)	-30.5 (0.5)	-30.3 (0.3)	-30.2 (0.5)	-30.0 (0)	-29.7 (0.1)	-30.2 (0.3)	-30.1 (0.3)
#9	n.d.	-32.4 (0.3)	-31.4 (0.1)	-31.2 (0.1)	-31.2 (0)	-31.2 (0)	-31.4 (0.1)	-31.0 (0)	-31.0 (0)	-30.7 (0)	-30.5 (0)	-30.4 (0)	-30.1 (0)	-29.9 (0.1)	-29.9 (0)	-30.0 (0)	-30.0 (0.1)	-29.8 (0)	-30.0 (0.1)	-29.9 (0.2)
#10	n.d.	n.d.	n.d.	-31.2 (0.3)	-31.1 (0)	-30.5 (0.2)	-30.5 (0.1)	-30.6 (0)	-30.4 (0)	-30.4 (0.1)	-30.7 (0.1)	-30.4 (0.2)	-30.6 (0.1)	-30.5 (0.2)	-31.0 (0.1)	-31.0 (0.3)	-29.9 (0.2)	-30.0 (0.1)	-29.8 (0.2)	n.d.
#11	n.d.	n.d.	-30.4 (0.1)	-30.6 (0.1)	-30.8 (0.1)	-31.0 (0.3)	-30.6 (0.2)	-30.6 (0.1)	-30.7 (0.2)	-30.3 (0.1)	-30.7 (0.1)	-30.7 (0.1)	-30.8 (0)	-30.6 (0)	-30.4 (0.3)	-30.6 (0.3)	-30.5 (0.2)	-30.6 (0.1)	-30.3 (0.1)	-30.4 (0)
#12	n.d.	-30.8 (0)	-30.9 (0.2)	-31.0 (0.1)	-30.8 (0)	-30.9 (0)	-31.1 (0)	-30.9 (0)	-30.7 (0)	-30.6 (0)	-30.6 (0.1)	-30.6 (0.1)	-30.4 (0.3)	-30.5 (0.1)	-30.2 (0)	-30.5 (0.3)	-30.0 (0.2)	-30.6 (0)	-30.3 (0.3)	n.d.
#13	n.d.	n.d.	n.d.	n.d.	n.d.	n.d.	n.d.	n.d.	n.d.	n.d.	n.d.	n.d.	n.d.	n.d.	n.d.	n.d.	n.d.	n.d.	n.d.	n.d.
#14	n.d.	n.d.	n.d.	n.d.	n.d.	n.d.	n.d.	n.d.	n.d.	n.d.	n.d.	n.d.	n.d.	n.d.	n.d.	n.d.	n.d.	n.d.	n.d.	n.d.
#15	n.d.	n.d.	n.d.	-27.1 (0)	-27.3 (0.2)	-27.5 (0.3)	-27.5 (0.3)	-27.1 (0.1)	-27.3 (0.3)	-27.2 (0.3)	-27.3 (0.4)	-27.2 (0.3)	-26.9 (0.1)	-27.1 (0.2)	-27.0 (0)	-26.9 (0)	-27.1 (0.2)	n.d.	n.d.	n.d.
#16	n.d.	n.d.	-27.8 (0.1)	-29.2 (0.5)	-28.7 (0.3)	-28.5 (0.3)	-28.5 (0.3)	-28.5 (0.2)	-28.7 (0.2)	-28.7 (0.2)	-28.4 (0.1)	-28.7 (0)	-28.6 (0.3)	-29.3 (0.1)	-29.2 (0)	n.d.	n.d.	n.d.	n.d.	n.d.
#17	n.d.	n.d.	-28.8 (0)	-28.9 (0)	-29.0 (0)	-28.6 (0.1)	-28.9 (0.2)	-28.8 (0.3)	-28.9 (0.2)	-28.9 (0.2)	-28.7 (0.3)	-28.8 (0.4)	-28.3 (0.3)	-28.1 (0)	-27.8 (0.2)	n.d.	n.d.	n.d.	n.d.	n.d.
#18	n.d.	n.d.	-29.2 (0.1)	-28.8 (0)	-28.6 (0.1)	-28.5 (0)	-28.7 (0)	-28.9 (0.1)	-28.8 (0.1)	-28.6 (0.1)	-28.4 (0.1)	-28.3 (0.1)	-28.0 (0.1)	-28.7 (0.1)	-29.6 (0)	-29.2 (0)	n.d.	n.d.	n.d.	n.d.
#19	n.d.	n.d.	-28.0 (0.1)	-28.1 (0.1)	-28.4 (0.1)	-28.4 (0.1)	-29.5 (0.1)	-29.9 (0.4)	-30.0 (0.3)	-29.4 (0.4)	-29.4 (0.2)	-29.3 (0)	-28.6 (0.1)	-28.9	-29.4	-30.2	n.d.	n.d.	n.d.	n.d.
#20	n.d.	-24.8 (0.3)	-25.5 (0.5)	-25.4 (0.1)	-25.4 (0.2)	-25.1 (0.1)	-25.9 (0)	-24.5 (0.1)	-24.4 (0.1)	-24.5 (0.1)	-25.2 (0.2)	-25.2 (0.4)	n.d.	n.d.	n.d.	n.d.	n.d.	n.d.	n.d.	n.d.
#21	n.d.	n.d.	-24.7 (0.3)	-24.1 (0.2)	-25.3 (0.1)	-24.4 (0.2)	-25.3 (0)	-25.0 (0.4)	-25.3 (0.2)	-25.5 (0)	-26.4 (0.1)	-26.8 (0.2)	n.d.	n.d.	n.d.	n.d.	n.d.	n.d.	n.d.	n.d.
#22	n.d.	n.d.	-29.0 (0.4)	-29.5 (0.2)	-30.1 (0.1)	-29.6 (0.2)	-29.8 (0.1)	-29.0 (0.1)	-29.2 (0.1)	-29.3 (0)	-29.2 (0)	-29.5 (0.1)	-29.7 (0.1)	-29.8 (0.1)	-29.7 (0)	-30.1 (0.1)	-30.1 (0)	-29.9 (0)	-30.3 (0)	n.d.
#23	n.d.	n.d.	-24.6 (0.1)	-24.6 (0.2)	-25.1 (0.1)	-25.4 (0)	-26.3 (0.1)	-26.0 (0.2)	-26.4 (0.2)	-26.5 (0)	-26.9 (0.1)	-27.0 (0.2)	n.d.	n.d.	n.d.	n.d.	n.d.	n.d.	n.d.	n.d.

LV09: samples #1–12; GR7: samples #13–14; BB5: sample #15; BB6: samples #16–19; BS024-01: samples #20–22; MRM 2012-03: sample #23. n.d. – not detectable. Numbers in parentheses are standard deviations. No standard deviation value means the result is collected from a single run.

Table 5.3. *n*-Alkane hydrogen isotopic composition of Barney Creek Formation bitumens

ID	δ^2H (‰), carbon number																		
	11	12	13	14	15	16	17	18	19	20	21	22	23	24	25	26	27	28	29
#1	n.d.	n.d.	n.d.	n.d.	n.d.	n.d.	n.d.	n.d.	n.d.	n.d.	n.d.	n.d.	n.d.	n.d.	n.d.	n.d.	n.d.	n.d.	n.d.
#2	n.d.	n.d.	n.d.	n.d.	n.d.	n.d.	-119 (2)	-110 (1)	-110 (1)	-105 (2)	-106 (2)	-105 (2)	-102 (1)	-103 (2)	-107 (3)	n.d.	n.d.	n.d.	n.d.
#3	n.d.	n.d.	n.d.	n.d.	-121 (2)	-125 (1)	-118 (0)	-114 (2)	-111 (5)	-109 (5)	-110 (3)	-102 (0)	-103 (1)	-93 (2)	-98 (3)	n.d.	n.d.	n.d.	n.d.
#4	n.d.	n.d.	n.d.	-123 (1)	-115 (0)	-114 (5)	-119 (3)	-115 (2)	-109 (1)	-107 (3)	-103 (4)	-111 (3)	-107 (5)	-102 (3)	-102 (1)	-99 (4)	n.d.	n.d.	n.d.
#5	n.d.	n.d.	n.d.	n.d.	n.d.	n.d.	n.d.	n.d.	n.d.	n.d.	n.d.	n.d.	n.d.	n.d.	n.d.	n.d.	n.d.	n.d.	n.d.
#6	n.d.	-135 (1)	-139 (1)	-139 (1)	-134 (0)	-132 (2)	-128 (2)	-122 (4)	-120 (3)	-119 (3)	-114 (2)	-112 (2)	-112 (2)	-102 (6)	-97 (2)	n.d.	n.d.	n.d.	n.d.
#7	n.d.	n.d.	n.d.	n.d.	n.d.	-115 (1)	-111 (4)	-106 (4)	-101 (3)	-102 (2)	-104 (2)	-101 (1)	n.d.	n.d.	n.d.	n.d.	n.d.	n.d.	n.d.
#8	n.d.	-127 (2)	-130 (0)	-132 (1)	-127 (1)	-124 (1)	-123 (1)	-120 (1)	-117 (2)	-116 (0)	-107 (1)	-109 (0)	-110 (3)	-100 (3)	-100 (4)	-94 (1)	-94 (0)	n.d.	n.d.
#9	n.d.	-130 (1)	-133 (1)	-133 (2)	-129 (0)	-129 (1)	-127 (3)	-122 (1)	-119 (2)	-119 (1)	-113 (1)	-110 (1)	-105 (2)	-110 (1)	-103 (5)	-101 (3)	-102 (2)	n.d.	n.d.
#10	n.d.	n.d.	n.d.	n.d.	n.d.	n.d.	n.d.	-105 (1)	-97 (1)	-102 (0)	-104 (1)	-107 (3)	-102 (2)	-109 (0)	n.d.	n.d.	n.d.	n.d.	n.d.
#11	n.d.	n.d.	-126 (1)	-121 (1)	-125 (2)	-124 (2)	-126 (2)	-122 (3)	-117 (3)	-119 (2)	-116 (1)	-116 (1)	-117 (2)	-112 (2)	-108 (3)	-113 (1)	-111 (2)	-110 (1)	-113 (0)
#12	n.d.	n.d.	n.d.	-117 (2)	-116 (2)	-115 (1)	-115 (3)	-117 (1)	-114 (4)	-112 (2)	-112 (3)	-112 (2)	-108 (4)	-112 (1)	-104 (1)	-107 (1)	n.d.	n.d.	n.d.
#13	-124 (1)	-127 (1)	-129 (1)	-126 (2)	-125 (3)	-121 (2)	-118 (2)	-117 (0)	-114 (2)	-118 (1)	-116 (2)	-117 (1)	-116 (1)	n.d.	n.d.	n.d.	n.d.	n.d.	n.d.
#14	-134 (1)	-133 (2)	-131 (2)	-128 (1)	-126 (2)	-123 (1)	-121 (0)	-118 (0)	-115 (2)	-113 (4)	-111 (1)	-113 (2)	-109 (4)	n.d.	n.d.	n.d.	n.d.	n.d.	n.d.
#15	n.d.	n.d.	n.d.	n.d.	-94 (4)	-97 (5)	-96 (5)	-94 (5)	-87 (2)	-83 (3)	-84 (3)	-82 (3)	-80 (3)	-75 (2)	-75 (5)	-75 (1)	-82 (0)	-89 (1)	-81 (0)
#16	n.d.	n.d.	n.d.	n.d.	-86 (2)	-91 (2)	-93 (2)	-89 (2)	-92 (1)	-88 (4)	-85 (0)	-82 (3)	-76 (1)	-81 (3)	n.d.	n.d.	n.d.	n.d.	n.d.
#17	n.d.	n.d.	n.d.	n.d.	-94 (1)	-90 (0)	-94 (2)	-90 (1)	-90 (4)	-88 (2)	-89 (5)	-80 (5)	-78 (3)	n.d.	n.d.	n.d.	n.d.	n.d.	n.d.
#18	n.d.	n.d.	n.d.	n.d.	-98 (1)	-100 (1)	-101 (0)	-98 (3)	-93 (2)	-95 (1)	-93 (4)	-90 (2)	-89 (5)	-83 (2)	n.d.	n.d.	n.d.	n.d.	n.d.
#19	n.d.	n.d.	n.d.	n.d.	-103 (1)	-104 (1)	-104 (1)	-101 (1)	-99 (0)	-95 (0)	-9 3(1)	-84 (4)	-89 (2)	-90 (0)	-84 (3)	n.d.	n.d.	n.d.	n.d.
#20	n.d.	n.d.	n.d.	-62 (1)	-55 (3)	-58 (2)	-48 (3)	-48 (3)	n.d.	n.d.	n.d.	n.d.	n.d.	n.d.	n.d.	n.d.	n.d.	n.d.	n.d.
#21	n.d.	n.d.	n.d.	n.d.	n.d.	n.d.	n.d.	n.d.	n.d.	n.d.	n.d.	n.d.	n.d.	n.d.	n.d.	n.d.	n.d.	n.d.	n.d.
#22	n.d.	-75 (5)	-75 (2)	-88 (1)	-83 (6)	-84 (6)	-83 (4)	-79 (1)	-69 (3)	-80 (3)	-65 (2)	-71 (0)	-70 (0)	n.d.	n.d.	n.d.	n.d.	n.d.	n.d.
#23	n.d.	n.d.	n.d.	n.d.	n.d.	n.d.	n.d.	n.d.	n.d.	n.d.	n.d.	n.d.	n.d.	n.d.	n.d.	n.d.	n.d.	n.d.	n.d.

LV09: samples #1 – 12; GR7: samples #13 – 14; BB5: sample #15; BB6: samples #16 – 19; BS024-01: samples #20 – 22; MRM 2012-03: sample #23. n.d. – not detectable. Numbers in parentheses are standard deviations.

5.5 Discussion

5.5.1 Thermal maturity

Based on Rc(MPDF), the Barney Creek Fm displays a wide range of thermal alteration intensities, from immature to the beginning of the gas window (Rc = 0.44–1.3%), with increasing maturity in the following order: LV09, GR7, BB6 and BB5, unmineralized HYC. Available bulk rock Tmax values for LV09, BB5, and HYC samples are consistent with biomarker-based maturity parameters, supporting the indigenous nature of the extracted hydrocarbons. Additionally, HI decreases with increasing Rc(MPDF). No correlation between maturity and TOC was observed (R^2 = 0.13). Unmineralized HYC samples show slightly higher maturity levels in comparison with previously published bitumens from the HYC ore body (Williford et al., 2011). This pattern may be related to varying thermal maturities in different mine locations.

5.5.2 Potential controlling factors for the $\delta^{13}C$ and $\delta^{2}H$ of *n*-alkanes

The isotopic composition of *n*-alkanes in source rocks or reservoirs potentially can be affected by a number of processes including thermal maturity, hydrocarbon migration, oil mixing, water washing, biodegradation and evaporative fractionation (e.g., Pedentchouk & Turich, 2018). In the current study, in order to minimize in-reservoir fractionation effects, we analysed extracted indigenous bitumens directly from the Barney Creek Fm source rock instead of oil samples. Consequently, water washing, evaporative fractionation and mix of several oils from multiple sources can be excluded as dominant controlling factors for $\delta^{13}C_{alk}$ and $\delta^{2}H_{alk}$ variability. Biodegradation can also be eliminated for the Barney Creek Fm bitumens based on the relative abundance and distribution of *n*-alkanes (Figure 5.2 and Pawlowska et al., 2013). Instead, significant linear correlations of average $\delta^{13}C_{alk}$ and $\delta^{2}H_{alk}$ with Rc(MPDF) (Figure 5.4) suggest that thermal maturity

is the major factor that controls changes in the isotopic composition of the Barney Creek Fm bitumens. Mechanisms of maturity control on $\delta^{13}C_{alk}$ and $\delta^{2}H_{alk}$ will be discussed below.

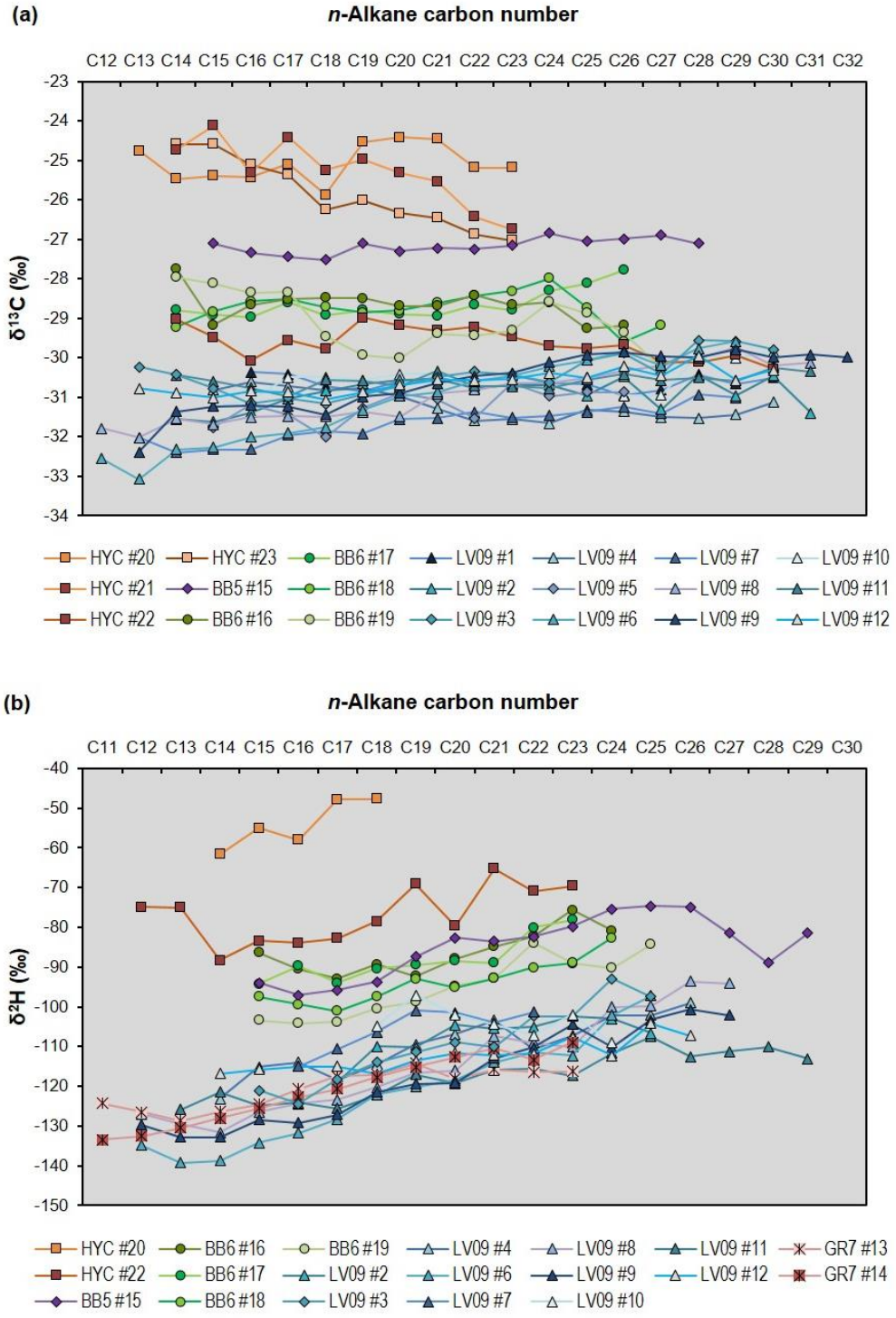

Figure 5.3. (a) $\delta^{13}C$ of *n*-alkanes and (b) $\delta^{2}H$ of *n*-alkanes from the Barney Creek Fm plotted against chain length.

5.5.3 Stable hydrogen isotopes

5.5.3.1 Maturity control on δ^2H of *n*-alkanes in previous studies

Under geological time and temperature, the primary hydrogen isotopic composition of lipids can be strongly modified by diagenetic hydrogen exchange processes and kinetic fractionation during thermal cracking (Sessions, 2016). The effects of these two processes on hydrogen isotopes might be hard to distinguish in natural samples, since both of them lead to ^2H-enrichment. To exclude the impact of hydrogen exchange reactions with water and only determine the effects of kinetic fractionation, Tang et al. (2005) performed anhydrous, closed-system pyrolysis experiments on North Sea petroleum and isolated *n*-alkanes from that oil. The study demonstrated that *n*-alkanes became heavier in ^2H by 53‰ with increasing maturity from 0.9 to 1.5% of vitrinite reflectance equivalent. Several Phanerozoic field-based studies are consistent with these results and illustrate an increase of average δ^2H_{alk} by up to ~71‰ with rising maturity (Table 5.4) (e.g., Li et al., 2001; Dawson et al., 2005, 2007; Radke et al., 2005; Maslen et al., 2012). Additionally, heating rate might influence the extent of $^2H_{alk}$-enrichment. For example, Radke et al. (2005) observed that in normal burial settings with maturity ranging from Rc(MPI) = 0.65 to 1.26%, δ^2H_{alk} increased by up to 52‰ for samples from the Permian Kupferschiefer, Poland. By contrast, the Jurassic Posidonia Shale from Germany, affected by heating from a magmatic intrusion, experienced a greater $^2H_{alk}$-enrichment by up to 67‰ in the smaller maturity range of Rc(MPI) = 0.64–1.04% (Radke et al., 2005).

5.5.3.2 δ^2H of *n*-alkanes in the Barney Creek Fm

In the current study, hydrogen isotopes of *n*-alkanes in the immature to early mature LV09 bitumens vary in the typical range for marine source rocks with average δ^2H_{alk} between –103‰ and –120‰ (Sessions, 2016). Analysed samples show an increase in δ^2H

values with increasing *n*-alkane carbon number (Figure 5.3b, Table 5.3). Samples #3, #6, #8 and #9 exhibit the most prominent "isotope slope" with up to 42‰ difference between low and high molecular weight *n*-alkanes. Such an effect has been associated with kinetic fractionation during thermal cracking (Tang et al., 2005). Observation of this pattern in LV09 bitumens indicates that the isotope slope may already become pronounced in samples of relatively low maturity with Rc(MPDF) <0.7%. Tang et al. (2005) also observed in their heating experiments a steepening of the δ^2H isotope slope with increasing thermal maturity from Rc = 0.9 to 1.5%. However, in the Barney Creek Fm, we detect no steepening effect in the maturity range of Rc(MPDF) = 0.56–1.1% (Figure 5.3b). It is unclear whether the most mature sample with Rc(MPDF) = 1.24% shows an increase in slope, since the δ^2H_{alk} measurements for this sample are available only for a limited range of *n*-alkanes (Figure 5.3b, HYC #20). Therefore, we cannot verify whether steepening of the δ^2H isotope slope observed in pyrolysis experiments at the highest thermal maturities also occurs in natural bitumens of the Barney Creek Fm.

Barney Creek Fm bitumens from several drill cores demonstrate an increase of average δ^2H_{alk} by 69‰ as maturity rises from Rc(MPDF) = 0.56 to 1.24% (Figure 5.4d). However, the actual $^2H_{alk}$ enrichment might be even higher because the long-chain *n*-alkanes, which are generally isotopically heavier, could not be measured for the most mature sample (Figure 5.3b). We also included published δ^2H values for HYC ore body bitumens in Figure 5.4. Williford et al. (2011) reported that HYC ore body *n*-alkanes are enriched in ^2H by up to 50–60‰ relative to *n*-alkanes from unmineralized, immature Barney Creek Fm sediments from the GR-10 core distal from the mine. The authors interpreted this apparently anomalous offset as a result of hydrogen exchange with the mineralizing fluid during ore genesis. However, we observe similar δ^2H values in ore body bitumens and bitumens from sediments of similar burial maturity not affected by

hydrothermal alteration (BB5, BB6, and unmineralized HYC samples), negating the evidence for anomalous $^{2}H_{alk}$ enrichment in the ore body (Figure 5.4d). The isotopic offset is fully consistent with a general $^{2}H_{alk}$ enrichment caused by increasing thermal maturity. The magnitude of average isotopic enrichment in the Barney Creek Fm is consistent with previously published empirical data from field-based studies on Phanerozoic sequences (Table 5.4).

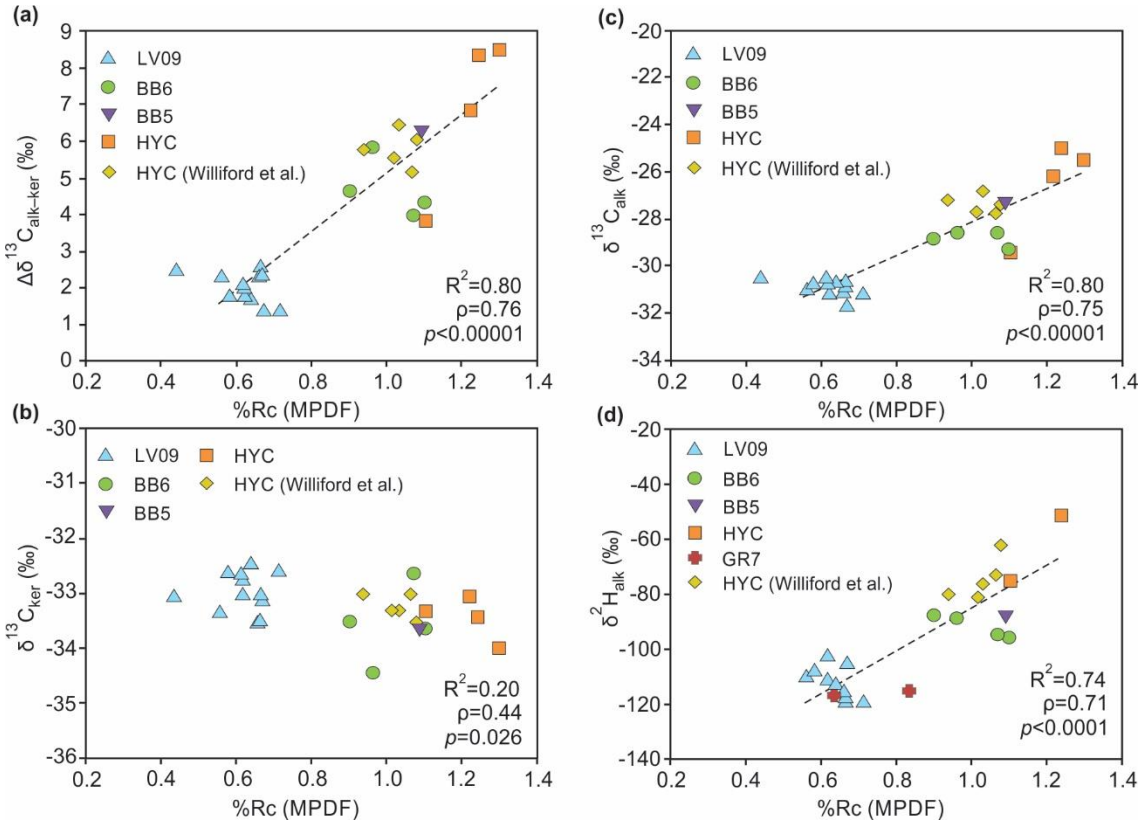

Figure 5.4. Plots of calculated vitrinite reflectance Rc(MPDF) for Barney Creek Formation extracted bitumens versus (a) carbon isotopic offset between *n*-alkanes and kerogen ($\Delta\delta^{13}C_{alk-ker}$), (b) carbon isotopes of kerogen ($\delta^{13}C_{ker}$), (c) average $\delta^{13}C$ of *n*-alkanes and (d) average $\delta^{2}H$ of *n*-alkanes. In addition to the R^2 values, we added Spearman's ρ and the corresponding p value because of non-normal distribution of the data. Note that previously published CSIA and $\delta^{13}C_{ker}$ values for HYC samples are included in the correlations (Williford et al., 2011).

Figure 5.5a compares correlations of average $\delta^{2}H_{alk}$ with maturity for Barney Creek Fm bitumens and an artificially heated Phanerozoic crude oil sample analysed by Tang et al. (2005). Even though Barney Creek Fm samples are shifted by ~20‰ to heavier values

of δ^2H_{alk}, maturity-related trends of average δ^2H_{alk} for both datasets experience almost the same slope (Figure 5.5a). In principle, the observed trend of increasing average δ^2H_{alk} with increasing maturity in the Barney Creek Fm may reflect a combination of kinetic fractionation caused by thermal cracking and hydrogen exchange effects. However, since Tang et al. (2005) record a similar $^2H_{alk}$ enrichment under exclusion of hydrogen exchange reactions, the data from the current study may be solely explained by fractionation during thermal cracking.

5.5.4 Stable carbon isotopes

5.5.4.1 Maturity control on $\delta^{13}C$ of *n*-alkanes in previous studies

Although it is widely accepted that thermal maturity influences the carbon isotopic composition of oils and *n*-alkanes, the precise mechanisms of such fractionation effects are not fully understood. According to Clayton (1991), oil generation and oil to gas cracking lead to increased $\delta^{13}C$ of residual bitumen caused by $^{13}C/^{12}C$ kinetic fractionation. Preferential breaking of $^{12}C–^{12}C$ bonds rather than $^{13}C–^{12}C$ bonds releases ^{13}C-depleted compounds and results in ^{13}C-enrichment of the remaining oil fraction (Clayton, 1991; Clayton & Bjorøy, 1994).

Previously published maturity-dependent $\delta^{13}C$ measurements of *n*-alkanes in experimental and field-based studies are summarised in Table 5.4. In the pyrolysis experiments on North Sea oil and isolated *n*-alkanes by Tang et al. (2005), mentioned in section 5.5.3.1, the average carbon isotopic composition of *n*-alkanes increased by 4.6‰ with increasing maturity from 0.9 to 1.5% vitrinite reflectance equivalent. In a similar experimental study, Tian et al. (2017) observed 5.5‰ average ^{13}C-enrichment for $C_{14–33}$ *n*-alkanes in anhydrous closed-system pyrolysis experiments at 250 ° to 450 °C on an oil sample from Maoming Basin in China, and 6.6‰ for the *n*-$C_{16–23}$ range (computed using

data from Table 2 in Tian et al. (2017)). Cheng et al. (2015) performed pyrolysis experiments on two immature source rock samples from Pearl River Mouth Basin in China and recorded enrichment of average $\delta^{13}C_{alk}$ by 3.3‰ (Enping Fm) and 5.7‰ (Wenchang Fm) in the maturity range of Rc = 0.64–1.24%.

There are few published Phanerozoic field-based studies that report systematic changes in $\delta^{13}C_{alk}$ with increasing maturity (Table 5.4) (e.g., Clayton & Bjorøy, 1994; Odden et al., 2002; Dawson et al., 2007; Cheng et al., 2015). For instance, Clayton and Bjorøy (1994) in a study of Jurassic North Sea oils showed an increase of average $\delta^{13}C_{alk}$ by 2.1‰ based on four samples in the narrow maturity range of Rc(MPI) = 0.77–0.86%. Dawson et al. (2007) analysed 15 upper-Jurassic bitumens from the Vulcan sub-Basin in Northern Australia with a wider maturity range of Ro = 0.7–1.6% and recorded ~4.5‰ enrichment of average $\delta^{13}C_{alk}$ (estimated from Fig. 3 in Dawson et al. (2007)). In one available Precambrian study with possible maturity influence on $\delta^{13}C_{alk}$, Jarret et al. (2019) examined 12 bitumens from the Mesoproterozoic Velkerri Fm, Australia, in the maturity range Rc(MPDF) = 0.54–1.16% and observed a maximum increase of average $\delta^{13}C_{alk}$ by up to 3‰. However, due to noticeable scatter in the data and absence of a clear correlation with maturity, the authors suggested that organic matter source might represent a greater control on $\delta^{13}C_{alk}$ variations than thermal alteration.

Table 5.4 (next page) [a]Thermal maturity estimated with vitrinite reflectance (Ro) and equivalent vitrinite reflectance (Rc) calculated from: T – temperature during pyrolysis experiments; Tmax – temperature at maximum of Rock-Eval S2 peak; MPI – methylphenanthrene index; MPDF – methylphenanthrene distribution factor. [b,c]Maximum enrichment in average hydrogen (^{2}H) or carbon (^{13}C) isotopic composition of *n*-alkanes with increasing maturity; the range of compounds is specified in parentheses. *n*: number of samples; *$\delta^{2}H$ or $\delta^{13}C$ data estimated from Figures.

Table 5.4. Summary of CSIA measurements for experimental and field-based studies

	Formation	Samples type	Age	Thermal maturity[a]	δ^2Halk increase[b]	δ^{13}Calk increase[c]	Reference
Experimental studies	North Sea	oil		T=390–445°C, Rc(T)=0.9–1.5%	53‰ ($C_{16–21}$), *n*=5	4.6‰ ($C_{16–21}$), *n*=4	Tang et al., 2005
	Enping Fm, China	source rock	Oligocene	T=300–380°C, Rc(T)=0.64–1.24%		3.3‰ ($C_{16–23}$), *n*=4	Cheng et al., 2015
	Wenchang Fm, China	source rock	Eocene	T=300–380°C, Rc(T)=0.64–1.24%		5.7‰ ($C_{16–23}$), *n*=4	Cheng et al., 2015
	Youganwo Fm, China	oil	Eocene-Oligocene	T=250–450°C		5.5‰ ($C_{14–33}$); 6.6‰ ($C_{16–23}$), *n*=6	Tian et al., 2017
Phanerozoic field-based studies	Enping Fm, China	bitumens	Oligocene	Increasing depth, 2550–4610 m		3‰ ($C_{16–23}$), *n*=10	Cheng et al., 2015
	Wenchang Fm, China	bitumens	Eocene	Increasing depth, 3254–3394 m		2.8‰ ($C_{16–23}$), *n*=6	Cheng et al., 2015
	North Sea	oils	Jurassic	Rc(MPI)=0.77–0.86%		2.1‰ ($C_{16–23}$), *n*=4	Clayton and Bjoroy, 1994
	Spekk Fm, Norway	bitumens	Late Jurassic	Ro=0.75–1.05%		1.8‰ ($C_{16–23}$), *n*=3	Odden et al., 2002
	Vulcan Fm, Australia	bitumens	Late Jurassic	Paqualin-1: Ro=0.7–1.6%; Vulcan-1B: Ro=0.7–1.2%	Paqualin-1: ~28‰, *n*=8; Vulcan-1B: ~36‰, *n*=8; ($C_{13–31}$)	*Paqualin-1: ~4.5‰, *n*=8; Vulcan-1B: ~2‰, *n*=7	Dawson et al., 2007
	Posidonia Shale, Germany	bitumens	Early Jurassic	Rc(MPI)=0.64–1.04%	67‰ ($C_{11–35}$); 68‰ ($C_{16–23}$), *n*=4		Radke et al., 2005
	Kockatea shale, Australia	oils and bitumens	Early Triassic	Rc=0.53–1.13%	42‰ ($C_{12–32}$), *n*=9		Dawson et al., 2005
	Kupferschiefer Shale, Poland	bitumens	Late Permian	Rc(MPI)=0.65–1.26%	52‰ ($C_{11–35}$); 71‰ ($C_{16–23}$), *n*=8		Radke et al., 2005
	Duvernay Fm, Canada	bitumens	Upper Devonian	Rc(Tmax)=0.38–0.78%	up to 71‰ ($C_{10–32}$), *n*=4		Maslen et al., 2012
	Western Canada	oils	Ordovician–Cretaceous	increasing maturity	*up to 40‰, *n*=5		Li et al., 2001
Precambrian field-based studies	Velkerri Fm, Australia	bitumens	Mesoproterozoic	Rc(MPDF)=0.54–1.16%		up to 3‰ ($C_{16–23}$), *n*=12	Jarrett et al., 2019
	Barney Creek Fm, Australia	bitumens	Paleoproterozoic	Rc(MPDF)=0.44–1.3%	up to 68.8‰ ($C_{16–23}$), *n*=19	up to 6.8‰ ($C_{16–23}$), *n*=21	Current study

5.5.4.2 $\delta^{13}C$ of *n*-alkanes in the Barney Creek Fm

Immature to early mature samples from LV09 drill core presumably most closely reflect the primary $\delta^{13}C$ values of Barney Creek Fm *n*-alkyl lipids. Average $\delta^{13}C_{alk}$ of extracted bitumens vary from –30.6‰ to –31.8‰. As a comparison, these values are ~3‰ enriched relative to *n*-alkanes of similar maturity from the overlying 1.38 Ga Velkerri Fm in the McArthur Basin (Jarrett et al., 2019). In the absence of terrestrial higher plants or detectable eukaryotic algae, the $\delta^{13}C_{alk}$ values of these Paleo- and Mesoproterozoic successions predominantly reflect bacterial biomass (e.g., Brocks, 2018; Gueneli et al., 2018). Analysed samples demonstrate an "inverse" isotopic ordering with ^{13}C-enrichment of extractable *n*-alkanes relative to kerogen and positive values of $\Delta\delta^{13}C_{alk–ker}$ between 1.3 and 2.6‰ (Figure 5.6c). Such inverse isotopic pattern is common in the Proterozoic but is opposite to typical isotopic ordering in the Phanerozoic (Figure 5.6a and b), a difference likely related to fundamental transformations in the ecology of primary producers and heterotrophs through time (Logan et al., 1995; Close et al., 2011).

Barney Creek Fm bitumens from several drill cores demonstrate an increase of average $\delta^{13}C_{alk}$ by up to 6.8‰ with increasing Rc(MPDF) from 0.44% to 1.3% (Figure 5.4c). Over that maturity range, $\delta^{13}C_{ker}$ values stay relatively constant (Figure 5.4b, Table 5.1). Therefore, the isotopic offset $\Delta\delta^{13}C_{alk–ker}$, which reaches 8.5‰ in the most thermally altered sample (Figure 5.4a, Figure 5.6c), is controlled by variations in *n*-alkanes and not the kerogen. To our knowledge, this is currently the highest recorded $^{13}C_{alk}$-enrichment caused by thermal maturation. Even though our results show ~2–4‰ greater $^{13}C_{alk}$-enrichment than other available field-based studies (Table 5.4, section 5.5.4.1), a meaningful comparison of the Paleoproterozoic Barney Creek Fm with Phanerozoic field data is not possible at present. High maturity-dependent $^{13}C_{alk}$-enrichment has not yet been recorded in the limited published Phanerozoic field-based studies, several of which

examine only narrow maturity ranges. However, the observed increase of $\delta^{13}C_{alk}$ values with rising thermal maturity in the Barney Creek Fm is similar to the pyrolysis experiments by Tang et al. (2005) and Cheng et al. (2015) on Phanerozoic oil and source rocks (compare slopes in Figure 5.5b). In principle, since these experimental studies were performed on Phanerozoic oil and source rocks, $\delta^{13}C_{alk}$ in Phanerozoic natural environments could be affected by thermal alteration to the same extent. Thus, it is generally important to consider possible extreme $\delta^{13}C_{alk}$ alterations upon maturation in environmental studies and oil-source rock correlations for both Proterozoic and Phanerozoic sequences. The Barney Creek Fm case study also highlights a substantial thermal maturity impact on $\Delta\delta^{13}C_{alk-ker}$ values (Figure 5.6c). Therefore, Precambrian community and redox reconstructions using $\Delta\delta^{13}C_{alk-ker}$ isotopic offsets (e.g., Logan et al., 1995; Close at al., 2011) must take thermal maturity into account.

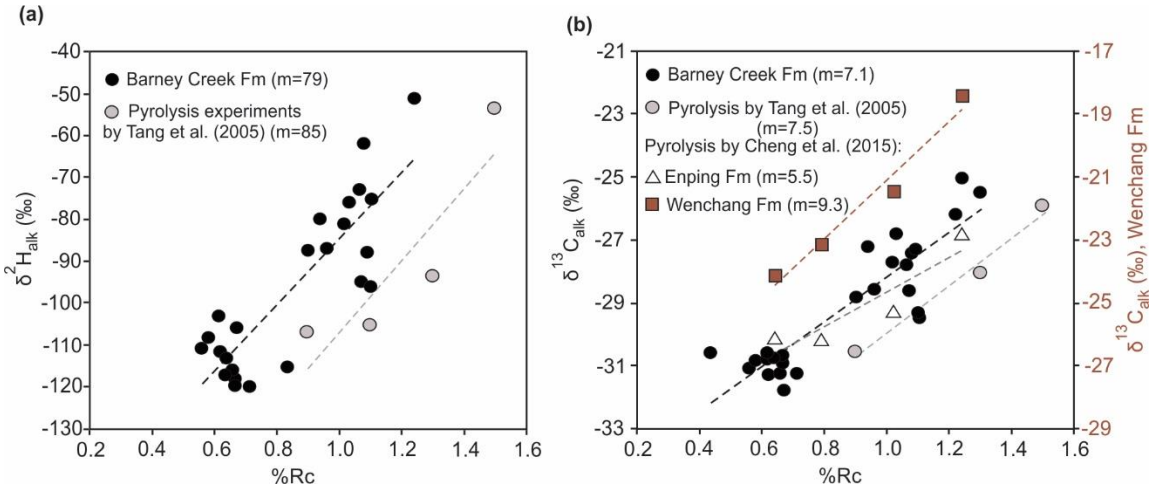

Figure 5.5. Comparison between maturity-related CSIA trends for Barney Creek Formation bitumens from the current study and artificially heated Phanerozoic crude oil sample (Tang et al., 2005) and source rocks (Cheng et al., 2015). The plots show calculated vitrinite reflectance Rc against (a) average δ^2H of *n*-alkanes and (b) average $\delta^{13}C$ of *n*-alkanes. Since the maturity of the unheated Phanerozoic oil sample is unknown in the experiments by Tang et al. (2005), here we provide CSIA measurements for the range of Rc = 0.9–1.5%. m: slope from linear equations.

5.5.4.3 Possible mechanisms for $\delta^{13}C_{alk}$-enrichment and the "isotope slope"

The precise mechanisms responsible for the increase of average $\delta^{13}C_{alk}$ with increasing thermal maturity are unresolved. One commonly discussed mechanism suggests that the carbon isotopic enrichment is caused by kinetic fractionation associated with the breaking of C–C bonds along the carbon chain of *n*-alkanes (e.g., Clayton, 1991). Due to preferential homolytic cleavage of $^{12}C–^{12}C$ bonds over $^{13}C–^{12}C$, the thermal cracking of an *n*-alkane should generate two isotopically depleted shorter chain *n*-alkanes, resulting in relative enrichment of the intact residue of the parent *n*-alkane. According to Clayton (1991), this enrichment has a proportionally larger effect on residual short chain *n*-alkanes than higher homologs, leading to progressive increase of $\delta^{13}C_{alk}$ with decreasing carbon number, creating a negative "isotope slope". The emergence of negative isotope profiles during increasing maturity was originally suggested by Silverman (1967) and later developed by Clayton (1991). However, the proposed mechanism does not account for changes in degradation rates with increasing carbon number. For example, the rate constant k_h for homolytic cleavage of *n*-alkanes in a radical chain reaction in the gas phase increases with chain length (Watanabe et al., 2001). As a consequence, long chain *n*-alkanes degrade faster than short chain homologs, resulting in faster enrichment of high molecular-weight compounds (Tang et al., 2005). This effect could be further enhanced by the addition of generated, isotopically depleted breakdown products to the short chain *n*-alkane pool. Thus, according to Tang et al. (2005), thermal cracking should lead to progressive ^{13}C (and ^{2}H) isotopic enrichment of *n*-alkanes with rising carbon number, creating a positive, not a negative, isotope slope. In their anhydrous pyrolysis experiments, Tang et al. (2005) observed a steepening of the $\delta^{2}H_{alk}$ isotope slope with increasing maturity. However, the predicted positive isotope slope in $\delta^{13}C_{alk}$ was not detected. Based on comparison with $\delta^{2}H_{alk}$, the most mature pyrolysate (Rc = 1.5%)

should have displayed a carbon isotopic difference of 1.4‰ between *n*-C_{13} and *n*-C_{21}. The authors argued that the expected positive $\delta^{13}C_{alk}$ slope was not observed due to low analytical precision of the measurements causing scattered $\delta^{13}C_{alk}$ values.

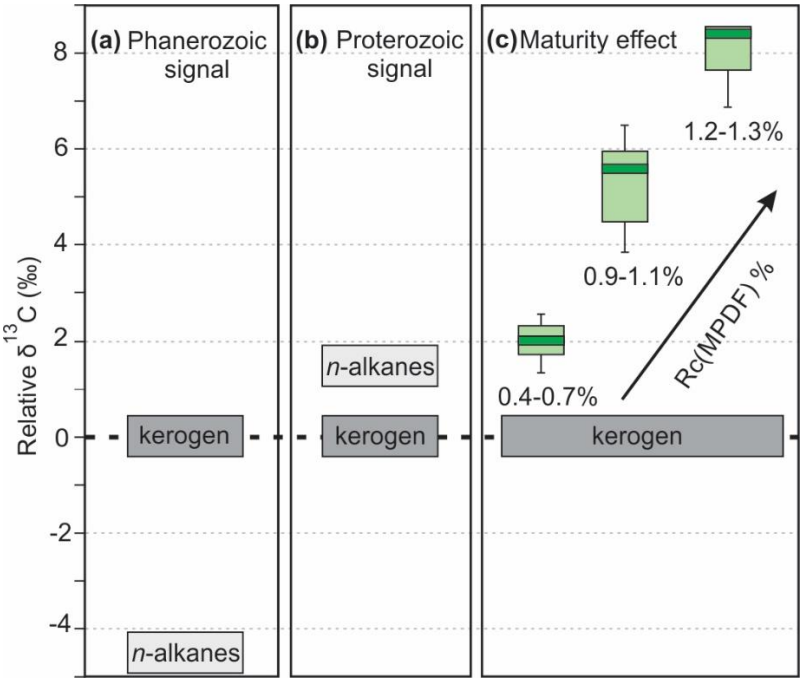

Figure 5.6. Schematic carbon isotope signatures of *n*-alkanes relative to kerogen for (a) Phanerozoic sediments, which are typically in agreement with the biosynthetic fractionation pattern (Hayes, 2001); and (b) Proterozoic sediments demonstrating an "inverse" isotopic ordering (Logan et al, 1995; Logan et al., 1997). (c) Whisker plots illustrating maturity effect on $\delta^{13}C$ of *n*-alkanes relative to kerogen in the Paleoproterozoic Barney Creek Formation. *n* = 12 in Rc = 0.4–0.7%, *n* = 11 in Rc = 0.9–1.1%, *n* = 3 in Rc = 1.2–1.3%.

While Tang et al. (2005) performed pyrolysis experiments on bitumen and isolated *n*-alkanes, Cheng et al. (2015) pyrolysed immature source rock samples, thus observing the combined effect of *n*-alkane generation from kerogen and *n*-alkane cracking. In these experiments, $\delta^{13}C_{alk}$ slopes started to increase at Rc >0.79%. An increase of the $\delta^{13}C_{alk}$ isotope slope was also detected in natural bitumens of the Enping Fm (Cheng et al., 2015), while in other published field-based studies the isotope slope either experienced no change (Odden et al., 2002; Cheng et al., 2015 for Wenchang Fm) or rotated to less positive values at higher maturities (Clayton & Bjorøy, 1994; Dawson et al., 2007).

In the current study, Barney Creek Fm bitumens display an inversion of the $\delta^{13}C_{alk}$ isotope slope from positive to negative with rising maturity (Figure 5.3a, 5.7). The least mature Barney Creek Fm bitumens (drill core LV09) show slightly increasing positive isotope slopes within the maturity range of Rc(MPDF) = 0.44–0.71% (Figure 5.7, R^2 = 0.52, p = 0.008). However, as maturity increases further from Rc(MPDF) = 0.9 to 1.3%, and the distributions of *n*-alkanes shift towards lower chain lengths due to near complete destruction of longer molecules (Figure 5.2), the $\delta^{13}C_{alk}$ isotope slopes start to flatten and then become more negative (Figure 5.3a, 5.7). Thus, cleavage of *n*-alkanes in radical chain reactions, which should generate increasingly positive isotope slopes (Tang et al., 2005), may not be the sole mechanism of ^{13}C-enrichment, and other reactions need to be considered.

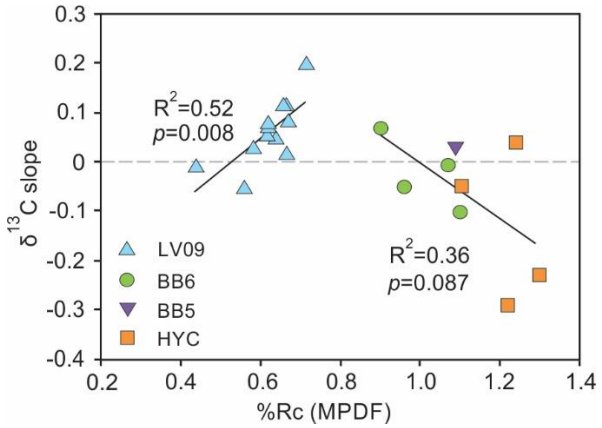

Figure 5.7. Carbon "isotope slope" inversion with increasing calculated vitrinite reflectance Rc(MPDF) for Barney Creek Formation extracted bitumens. Isotope slope values for each sample were obtained from plots of $\delta^{13}C$ of *n*-alkanes against chain length (Figure 5.3a). The full range of available carbon numbers was used for the computation of slope values. P values were calculated for R^2.

5.5.5 Simulation of $\delta^{13}C$ isotope slope behaviour

To explore the formation of positive and negative $\delta^{13}C_{alk}$ isotope slopes during organic matter maturation, we ran simple numerical models for three mechanisms: (1) *n*-alkane cleavage in a radical chain reaction, (2) reactions where the rate constant has

limited dependence on the *n*-alkane chain, and (3) generation of *n*-alkanes through degradation of kerogen. We do not imply that the particular reaction mechanisms in the models play a dominant role in *n*-alkane isotope slope formation in natural systems. Rather, the aim is to explore principal reaction characteristics that may be responsible for the generation of positive and negative slopes.

Figure 5.8a shows the progression of $\delta^{13}C$ profiles during cleavage of *n*-alkanes in a radical chain reaction in the gas-phase. In this model, *n*-alkanes are cleaved by β-scission, generating two shorter-chain *n*-alkane products that are isotopically depleted and returned to the *n*-alkane pool, and the intact residues of the parent compounds become isotopically enriched. Longer chain *n*-alkanes are cleaved considerably faster than shorter homologs as the rate constant increases with chain length *n* following $k_h \sim (n–2)(n–3)^{1/2}$ (Watanabe et al., 2001). We applied a $^{13}C/^{12}C$ fractionation factor $\alpha_h = 0.994$, a conservative estimate for homolytic mid-chain cleavage of *n*-alkanes (Tang et al., 2000), although the precise value is not critical for the purpose of the simulation. The isotopic values of all *n*-alkanes at the start of the reaction were set to $\delta^{13}C = –32‰$. After 20 iterations of arbitrary time units, 98.1% of *n*-alkanes in the range C_{13} to C_{31} were degraded, achieving an average isotopic enrichment comparable to the Barney Creek Fm. Moreover, as predicted by Tang et al. (2005) but unlike the Barney Creek Fm, the isotopic profiles develop increasingly positive isotope slopes (Figure 5.8a). According to Tang et al. (2005), two effects with unknown relative importance contribute to the progressively increasing $\delta^{13}C_{alk}$ slopes: (1) generation of isotopically depleted breakdown products that are added to the short chain *n*-alkane pool, and (2) higher rate constants k_h for longer chain *n*-alkanes. To determine the relative importance of these effects, we adjusted the model to discard the cleavage products rather than returning them to the *n*-alkane pool. Surprisingly, the removal of ^{13}C-

depleted products had only minimal impact on $^{13}C_{alk}$ enrichment. For instance, in the specific simulation shown in Figure 5.8a, after 20 iterations *n*-C_{13} becomes enriched by 3.78‰ if isotopically depleted products are removed, and by 3.41‰ if they are returned to the *n*-alkane pool. Moreover, withdrawal of the breakdown products had no visible influence on isotope slopes. Therefore, effect (1) is unimportant for the trajectory of $\delta^{13}C$ profiles in a radical chain reaction, and the formation of the positive isotope slope can be largely attributed to the dependence of the rate constant *k* on chain length *n*.

The second model examines the evolution of $\delta^{13}C$ profiles during hypothetical reactions where the rate constant k_i has only a weak dependence on *n*-alkane chain length, or where short chain *n*-alkanes may even react faster than longer homologs. For bitumen degradation under natural conditions, the dependence of rate constants on chain-lengths remains largely unexplored, so it is unclear which mechanisms have such characteristics. Plausible mechanisms include cracking and isomerization reactions where the reaction rate is controlled by access to limited sites on catalytic surfaces, or fast reactions in gas solution that favour homologs with lower evaporation energies. As an example, the simulation in Figure 5.8b keeps k_i constant with chain length. As $^{13}C/^{12}C$ fractionation factors α_i of such reactions, to our knowledge, have not been determined, we chose α_i = 0.994 to make the simulation comparable to the radical chain reaction in Figure 5.8a. After 20 iterations of arbitrary time units, 99.96% of *n*-alkanes in the range C_{13} to C_{31} were degraded, again achieving an average isotopic enrichment comparable to the Barney Creek Fm. Without changes in k_i with increasing carbon number, the enrichment of residual *n*-alkanes is now proportionally larger for short-chain homologs than for longer homologs as described by Clayton (1991). Consequently, and in contrast to the radical chain reaction, the isotopic profiles develop increasingly negative isotope slopes (Figure 5.8b).

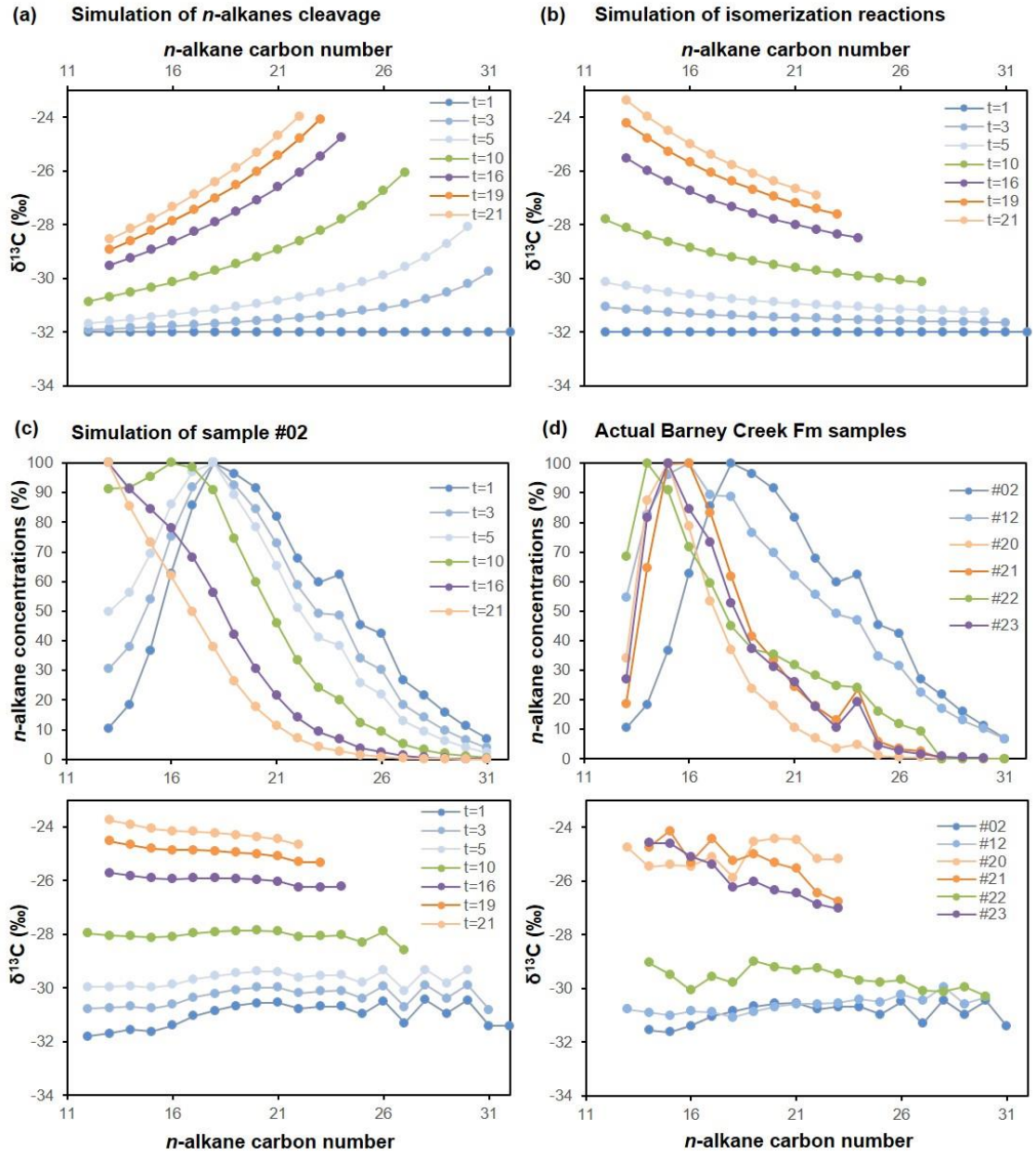

Figure 5.8. Comparison of measured and simulated *n*-alkane concentrations and $\delta^{13}C$ values. (a) Simulated progression of $\delta^{13}C$ for *n*-alkanes with increasing maturation during cleavage of *n*-alkanes to shorter *n*-alkanes in a gas-phase radical chain reaction where the rate constant follows $k_h \sim (n–2)*(n–3)^{1/2}$ (where n is chain length). At the end of the reaction, 1.9% of *n*-C_{13} to *n*-C_{31} remain. Average $k_h = 0.072$; fractionation factor $\alpha_h = 0.994$, 20 iterations, time steps = 5. (b) Simulation of isomerization or degradation of *n*-alkanes where the rate constant k_i is independent of chain length and the reaction products are not returned to the *n*-alkane pool. At the end of the reaction, 0.04% of *n*-C_{13} to *n*-C_{31} remain. $k_i = 0.072$; fractionation factor $\alpha_i = 0.994$, 20 iterations, time steps = 4.5. (c) Simulation of maturation based on actual *n*-alkane concentrations and $\delta^{13}C$ isotope data for Barney Creek Fm sample #02 (t = 1). In the simulation, the two reaction types shown in (a) and (b) were run simultaneously. At the end of the reaction, 1.8% of *n*-C_{13} to *n*-C_{31} remain. $k_h \sim (n–2)*(n–3)^{1/2}$, average $k_h = 0.072$; $k_i = 0.072$; $\alpha_h = 0.997$; $\alpha_i = 0.982$; 20 iterations, time steps = 1.7. (d) Actual Barney Creek Fm data for six selected samples

within the isotopic shift spectrum. The drop in absolute concentrations of *n*-alkanes (*n*-C_{13} to *n*-C_{31}) relative to TOC from the least (#02) to most mature (#21) Barney Creek Fm sample in the plot is 98.6%, i.e. 1.4% of initial concentrations remain.

To test whether competition between reactions with strong and weak dependence of *k* on *n* can reproduce the *n*-alkane abundances and isotope profiles of the Barney Creek Fm, we performed a simulation using actual *n*-alkane concentrations and isotope data for one of the least mature samples #02 (Figure 5.8c). In the model, as an arbitrary choice, both reaction types ran in parallel at the same average reaction rates but with different fractionation factors. Figure 5.8c–d compares the model results with actual $\delta^{13}C$ data and *n*-alkane abundance profiles of the Barney Creek Fm. Juxtaposition of the plots reveals that the magnitude of the isotope effect, the inversion of the isotope slope from positive to negative, the magnitude of decline in absolute *n*-alkane abundances as well as the shift of *n*-alkane carbon numbers towards lower molecular weight compounds were satisfactorily captured. However, formation of the increasingly positive isotope slopes in the earliest stages of maturation (Figure 5.7, LV09 samples) was not captured. It is plausible that the positive isotope slopes in LV09 samples formed during the early stages of *n*-alkane generation (rather than degradation) through cleavage of *n*-alkyl moieties from kerogen as illustrated in Figure 5.9. In this model, the inversion of the isotope slope from positive to negative is caused by the exhaustion of *n*-alkyl moieties in the kerogen and a shift from *n*-alkane formation to *n*-alkane degradation.

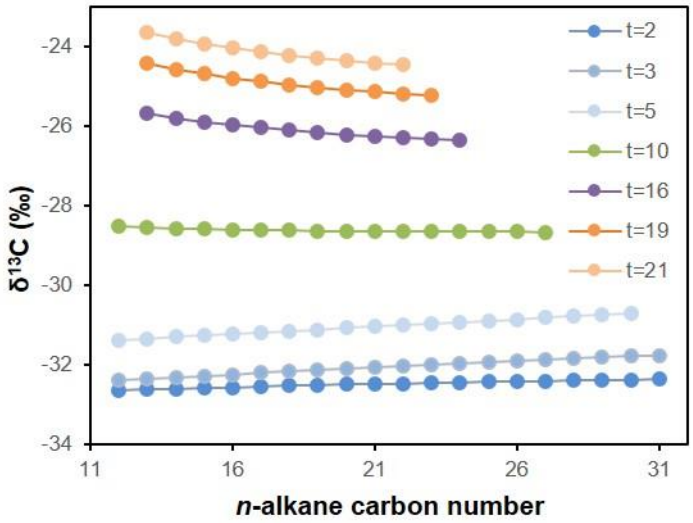

Figure 5.9. Simulation of generation of *n*-alkanes from kerogen and simultaneous *n*-alkane degradation following the two mechanisms in Figure 5.8c. Model parameters: kerogen cleavage (generation of all *n*-alkane homologs at same molarity; k = 0.17; α_h = 0.982), radical chain reaction (k_h ~ (n–2)*(n–3)$^{1/2}$; average k_h = 0.072; α_h = 0.982), isomerization (k_i = 0.27; α_i = 0.990); 20 iterations, time steps = 1.5; initial mass of *n*-alkyl carbon in kerogen = 100,000; initial carbon mass of *n*-C_2 to *n*-C_{31} = 500 each.

As mentioned, the numerical models shown in Figures 5.8 and 5.9 do not imply that the progression of *n*-alkane abundances and isotopes in the Barney Creek Fm, or any other natural system, were caused by these specific chemical mechanisms with the given rate constants and fractionation factors. Rather, the models suggest that the dependence of the rate constant k on chain length n, and the competition between *n*-alkane generation and degradation, may be the dominant drivers for *n*-alkane isotope slope behaviour. Therefore, future studies should aim to determine $k(n)$ for competing reactions in natural systems. More sophisticated models will need to include numerous effects that were excluded here, such as generation of *n*-alkanes from functionalized *n*-alkyl lipids, temperature dependencies of rate constants and isotope fractionation factors, the generation of *n*-alkanes through cleavage of methylalkanes, alkyl aromatics and similar compounds, and isotope effects associated with the expulsion of *n*-alkanes from source rocks.

5.6 Conclusions

Immature to early mature Paleoproterozoic Barney Creek Fm samples from LV09 drill core show ^{13}C-enrichment of extractable *n*-alkanes relative to kerogen, thus following an inverse isotopic pattern that was previously observed in Precambrian formations (Logan et al., 1995). The δ^2H_{alk} values vary in the typical range for marine source rocks and become heavier with increasing chain length of *n*-alkanes. The presence of this δ^2H_{alk} positive isotope slope demonstrate that kinetic fractionation effects already become evident at relatively low thermal maturities of Rc(MPDF) <0.7%.

Compound-specific carbon and hydrogen isotope values of Barney Creek Fm *n*-alkanes from several drill cores correlate significantly with maturity, demonstrating a ^{13}C and ^{2}H enrichment of *n*-alkanes by up to 6.8‰ and 69‰ respectively with increasing maturity from Rc(MPDF) = 0.4 to 1.3%. The carbon isotopic offset $\Delta\delta^{13}C_{alk-ker}$, which reaches 8.5‰ in the most mature bitumen, is controlled by variations in *n*-alkanes rather than the kerogen, since $\delta^{13}C_{ker}$ values stay relatively constant. The greater extent of $^{13}C_{alk}$-enrichment for Barney Creek Fm samples compared with available Phanerozoic empirical data may reflect the limited number of published studies about the thermal maturity influence on $\delta^{13}C_{alk}$. However, based on similar trends of increasing isotopic enrichment with maturity in pyrolysis experiments on Phanerozoic oils and source rocks, the isotopic composition of *n*-alkanes in Phanerozoic and Precambrian sequences might be affected by thermal alteration to a similar extent. As the observed thermal effect on $\delta^{13}C_{alk}$ and δ^2H_{alk} is high enough to have an impact on biological and environmental interpretations, it is important to consider maturity in oil-source rock correlations and ecological reconstructions for Proterozoic and Phanerozoic sediments. In particular, since thermal alteration can substantially affect the isotopic offset between *n*-alkanes and kerogen

($\Delta\delta^{13}C_{alk-ker}$), and presumably between *n*-alkanes and acyclic isoprenoids, it is crucial to take thermal maturity into account when isotope systematics are used to reconstruct Precambrian biological communities and trophic relationships.

In the Barney Creek Fm, the slope of $\delta^{13}C$ *n*-alkane profiles changes from positive to negative with increasing thermal maturity. Based on simple numerical simulations, we suggest that this slope behaviour is driven by the balance of the formation of *n*-alkanes from kerogen and their subsequent degradation, and the dependence of the degradation rate constant *k* on *n*-alkane chain length *n*. Initial generation of *n*-alkanes from kerogen forms a positive isotope slope. Degradation mechanisms where *k* strongly increases with chain length, such as radical chain reactions, also cause positive isotope slopes, while mechanisms with a lower dependence on chain length result in negative isotope slopes. The changing importance of these competing reactions in the progression from early diagenesis to metagenesis may be responsible for the observed isotope slope inversion in the Barney Creek Fm and other systems.

Acknowledgments

We thank Janet Hope (ANU) for laboratory support. We are grateful to Jacob Sohn and Junhong Chen for technical assistance with isotope measurements and Ian Long for isolation of kerogen in the Organic Geochemistry Laboratory at Geoscience Australia (GA). We thank Michael Kipp (UW) for organic carbon isotope measurements and Ruslan Khamidullin (Lomonosov MSU) for help with Rock-Eval pyrolysis. We thank Darryl Stacey from the Darwin Core Library (NTGS), Neil Williams and McArthur River Mining Pty Ltd for access to drill cores. We are grateful to Alex L. Sessions and Ilya Bobrovskiy for reviewing an earlier version of this manuscript, and Kliti Grice for scientific advice. This research was financially supported by Australian Research Council grants DP160100607 and DP170100556 (to JJB). GV acknowledges support from an Australian Government Research Training Program (RTP) Scholarship. AJMJ publishes with permission of the CEO, Geoscience Australia. The authors declare no conflicting interests, financial or otherwise. Daniel Dawson, Kenneth Peters, and two anonymous reviewers are thanked for their thoughtful comments and suggestions, which improved this manuscript. Andrew Murray and John Volkman are thanked for editorial assistance.

References

Ahmad, M., Dunster, J. N., & Munson, T. J. (2013). Chapter 15: McArthur Basin, In: Ahmad, M and Munson, T.J. (compilers), *Geology and mineral resources of the Northern Territory*. Northern Territory Geological Survey, Special Publication 5.

Alexander, R., Kagi, R. I., & Larcher, A. V. (1982). Clay catalysis of aromatic hydrogen-exchange reactions. *Geochimica et Cosmochimica Acta*, 46, 219-222.

Brocks, J. J. (2011). Millimeter-scale concentration gradients of hydrocarbons in Archean shales: Live-oil escape or fingerprint of contamination? *Geochimica et Cosmochimica Act,a* 75(11), 3196-3213.

Brocks, J. J. (2018). The transition from a cyanobacterial to algal world and the emergence of animals. *Emerging Topics in Life Sciences*, 2(2), 181-190.

Brocks, J. J., Grosjean, E., & Logan, G. A. (2008). Assessing biomarker syngeneity using branched alkanes with quaternary carbon (BAQCs) and other plastic contaminants. *Geochimica et Cosmochimica Acta*, 72, 871-888.

Brocks, J. J., Love, G. D., Summons, R. E., Knoll, A. H., Logan, G. A., & Bowden, S. A. (2005). Biomarker evidence for green and purple sulphur bacteria in a stratified Palaeoproterozoic sea. *Nature*, 437, 866.

Cheng, P., Xiao, X. M., Gai, H. F., Li, T. F., Zhang, Y. Z., Huang, B. J., & Wilkins, R. W. T. (2015). Characteristics and origin of carbon isotopes of *n*-alkanes in crude oils from the western Pearl River Mouth Basin, South China sea. *Marine and Petroleum Geology*, 67, 217-229.

Clayton, C. (1991). Effect of maturity on carbon isotope ratios of oils and condensates. *Organic Geochemistry*, 17, 887-899.

Clayton, C., & Bjorøy, M. (1994). Effect of maturity on $^{13}C/^{12}C$ ratios of individual compounds in North Sea oils. *Organic Geochemistry*, 21, 737-750.

Close, H. G., Bovee, R., & Pearson, A. (2011). Inverse carbon isotope patterns of lipids and kerogen record heterogeneous primary biomass. *Geobiology*, 9, 250-265.

Dahl, B., Bojesen-Koefoed, J., Holm, A., Justwan, H., Rasmussen, E., & Thomsen, E. (2004). A new approach to interpreting Rock-Eval S2 and TOC data for kerogen quality assessment. *Organic Geochemistry*, 35, 1461-1477.

Dawson, D., Grice, K., & Alexander, R. (2005). Effect of maturation on the indigenous δD signatures of individual hydrocarbons in sediments and crude oils from the Perth Basin (Western Australia). *Organic Geochemistry*, 36, 95-104.

Dawson, D., Grice, K., Alexander, R., & Edwards, D. (2007). The effect of source and maturity on the stable isotopic compositions of individual hydrocarbons in sediments and crude oils from the Vulcan Sub-basin, Timor Sea, Northern Australia. *Organic Geochemistry*, 38, 1015-1038.

Eldridge, C., Williams, N., & Walshe, J.L. (1993). Sulfur isotope variability in sediment-hosted massive sulfide deposits as determined using the ion microprobe SHRIMP; II, A study of the HYC Deposit at McArthur River, Northern Territory, Australia. *Economic Geology*, 88, 1-26.

Espitalié, J., Madec, M., & Tissot, B. (1980). Role of mineral matrix in kerogen pyrolysis: influence on petroleum generation and migration. *AAPG Bulletin*, 64(1), 59-66.

French, K. L., Hallmann, C., Hope, J. M., Schoon, P. L., Zumberge, J. A., Hoshino, Y., Peters, C. A., George, S. C., Love, G. D., Brocks, J. J., Buick, R., & Summons, R. E. (2015). Reappraisal of hydrocarbon biomarkers in Archean rocks. *Proceedings of the National Academy of Sciences*, 112, 5915-5920.

Gueneli, N., McKenna, A., Ohkouchi, N., Boreham, C., Beghin, J., Javaux, E., & Brocks, J. (2018). 1.1-billion-year-old porphyrins establish a marine ecosystem dominated by bacterial primary producers. *Proceedings of the National Academy of Sciences*, 115, E6978-E6986.

Hayes, J. M. (2001). Fractionation of carbon and hydrogen isotopes in biosynthetic processes. *Reviews in mineralogy and geochemistry*, 43, 225-277.

Ireland, T., Large, R.R., McGoldrick, P., & Blake, M. (2004). Spatial distribution patterns of sulfur isotopes, nodular carbonate, and ore textures in the McArthur River (HYC) Zn-Pb-Ag deposit, Northern Territory, Australia. *Economic Geology*, 99, 1687-1709.

Jackson, M., Muir, M. D., & Plumb, K. A. (1987). *Geology of the southern McArthur Basin, Northern Territory* (Vol. 220). Canberra: Australian Government Publishing Service.

Jarrett, A. J. M., Cox, G. M., Brocks, J. J., Grosjean, E., Boreham, C. J., & Edwards, D. S. (2019). Microbial assemblage and palaeoenvironmental reconstruction of the 1.38 Ga Velkerri Formation, McArthur Basin, northern Australia. *Geobiology*, 17, 360-380.

Jarvie, D. M. (2012). Shale resource systems for oil and gas: Part 2—Shale oil resource systems. In: Breyer, J. (Ed.), Shale reservoirs – Giant resources for the 21st century. *American Association of Petroleum Geologists Memoir*, 97, 89-119.

Johnson, R., Bluett, J., Titus, L., & Warner, D. (2013). Exploring and appraising the oldest gas accumulations in Australia. *The APPEA Journal*, 53, 470-470.

Kipp, M. A., Stüeken, E. E., Yun, M., Bekker, A., & Buick, R. (2018). Pervasive aerobic nitrogen cycling in the surface ocean across the Paleoproterozoic Era. *Earth and Planetary Science Letters*, 500, 117-126.

Kunzmann, M., Schmid, S., Blaikie, T. N., & Halverson, G. P. (2019). Facies analysis, sequence stratigraphy, and carbon isotope chemostratigraphy of a classic Zn-Pb host succession: The Proterozoic middle McArthur Group, McArthur Basin, Australia. *Ore Geology Reviews*, 106, 150-175.

Kvalheim, O. M., Christy, A. A., Telnæs, N., & Bjørseth, A. (1987). Maturity determination of organic matter in coals using the methylphenanthrene distribution. *Geochimica et Cosmochimica Acta*, 51, 1883-1888.

Li, M., Huang, Y., Obermajer, M., Jiang, C., Snowdon, L. R., & Fowler, M. G. (2001). Hydrogen isotopic compositions of individual alkanes as a new approach to petroleum correlation: case studies from the Western Canada Sedimentary Basin. *Organic Geochemistry*, 32, 1387-1399.

Logan, G. A., Hayes, J., Hieshima, G. B., & Summons, R. E. (1995). Terminal Proterozoic reorganization of biogeochemical cycles. *Nature*, 376, 53-56.

Logan, G. A., Summons, R. E., & Hayes, J. M. (1997). An isotopic biogeochemical study of Neoproterozoic and Early Cambrian sediments from the Centralian Superbasin, Australia. *Geochimica et Cosmochimica Acta*, 61, 5391-5409.

Maslen, E., Grice, K., Dawson, D., Wang, S., & Horsfield, B. (2012). Stable hydrogen isotopes of isoprenoids and *n*-alkanes as a proxy for estimating the thermal history of sediments through geological time. Analyzing the Thermal History of Sedimentary Basins: Methods and Case Studies. Society for Sedimentary Geology Special Publication 103, 29-43.

Munson, T. (2016). *Sedimentary Characterisation of the Wilton Package, Greater MacArthur Basin, Northern Territory*. Northern Territory Geological Survey, Record 2016-003.

Murray, A. P., Summons, R. E., Boreham, C. J., & Dowling, L. M. (1994). Biomarker and *n*-alkane isotope profiles for Tertiary oils: relationship to source rock depositional setting. *Organic Geochemistry*, 22, 521-IN526.

Odden, W., Barth, T., & Talbot, M. (2002). Compound-specific carbon isotope analysis of natural and artificially generated hydrocarbons in source rocks and petroleum fluids from offshore Mid-Norway. *Organic Geochemistry*, 33, 47-65.

Page, R. W., & Sweet, I. P. (1998). Geochronology of basin phases in the western Mt Isa Inlier, and correlation with the McArthur Basin. *Australian Journal of Earth Sciences*, 45, 219-232.

Pawlowska, M. M., Butterfield, N. J., & Brocks, J. J. (2013). Lipid taphonomy in the Proterozoic and the effect of microbial mats on biomarker preservation. *Geology*, 41, 103-106.

Pedentchouk, N., Freeman, K. H., & Harris, N. B. (2006). Different response of δD values of *n*-alkanes, isoprenoids, and kerogen during thermal maturation. *Geochimica et Cosmochimica Acta*, 70, 2063-2072.

Pedentchouk, N., & Turich, C. (2018). Carbon and hydrogen isotopic compositions of *n*-alkanes as a tool in petroleum exploration. *Geological Society*, London, Special Publications 468, 105-125.

Peters, K. (1986). Guidelines for evaluating petroleum source rock using programmed pyrolysis. *AAPG Bulletin*, 70(3), 318-329.

Peters, K., Walters, C., & Moldowan, J. (2005). *The biomarker guide: Volume 2, Biomarkers and isotopes in petroleum exploration and earth history.* Cambridge University Press.

Peters, K. E., & Cassa, M. R. (1994). Applied source rock geochemistry. In: Magoon, L. B., & Dow, W. G. (Eds.), The Petroleum System—From Source to Trap. *American Association of Petroleum Geologists Memoir*, 60, pp. 93-120.

Powell, T. G., Jackson, M. J., Sweet, I. P., Crick, I. H., Boreham, C. J., & Summons, R. E. (1987). *Petroleum geology and geochemistry, middle Proterozoic McArthur Basin.* Bureau of Mineral Resources Record 48, 286.

Radke, J., Bechtel, A., Gaupp, R., Püttmann, W., Schwark, L., Sachse, D., & Gleixner, G. (2005). Correlation between hydrogen isotope ratios of lipid biomarkers and sediment maturity. *Geochimica et Cosmochimica Acta*, 69, 5517-5530.

Rooney, M., Vuletich, A., & Griffith, C. (1998). Compound-specific isotope analysis as a tool for characterizing mixed oils: an example from the West of Shetlands area. *Organic Geochemistry*, 29, 241-254.

Schimmelmann, A., Lewan, M. D., & Wintsch, R. P. (1999). D/H isotope ratios of kerogen, bitumen, oil, and water in hydrous pyrolysis of source rocks containing kerogen types I, II, IIS, and III. *Geochimica et Cosmochimica Acta*, 63, 3751-3766.

Schinteie, R., & Brocks, J. J. (2017). Paleoecology of Neoproterozoic hypersaline environments: Biomarker evidence for haloarchaea, methanogens, and cyanobacteria. *Geobiology*, 15, 641-663.

Schinteie, R., Colangelo-Lillis, J. R., Hope, J. M., Chen, J., Nelson, D. B., Jarrett, A. J., & Brocks, J. J. (2019). Impact of drill core contamination on compound-specific carbon and hydrogen isotopic signatures. *Organic geochemistry*, 128, 161-171.

Sessions, A. L. (2016). Factors controlling the deuterium contents of sedimentary hydrocarbons. *Organic Geochemistry*, 96, 43-64.

Sessions, A. L., Sylva, S. P., Summons, R. E., & Hayes, J. M. (2004). Isotopic exchange of carbon-bound hydrogen over geologic timescales. *Geochimica et Cosmochimica Acta*, 68, 1545-1559.

Silverman, S. R. (1967). Carbon isotopic evidence for the role of lipids in petroleum formation. *Journal of the American Oil Chemists' Society*, 44(12), 691-695.

Stüeken, E. E. (2013). A test of the nitrogen-limitation hypothesis for retarded eukaryote radiation: nitrogen isotopes across a Mesoproterozoic basinal profile. *Geochimica et Cosmochimica Acta*, 120, 121-139.

Tang, Y., Huang, Y., Ellis, G. S., Wang, Y., Kralert, P. G., Gillaizeau, B., Ma, Q., & Hwang, R. (2005). A kinetic model for thermally induced hydrogen and carbon isotope fractionation of individual *n*-alkanes in crude oil. *Geochimica et Cosmochimica Acta*, 69, 4505-4520.

Tang, Y., Perry, J., Jenden, P., & Schoell, M. (2000). Mathematical modeling of stable carbon isotope ratios in natural gases. *Geochimica et Cosmochimica Acta*, 64, 2673-2687.

Tian, C., Xia, Y., Song, C., Ma, S., Gao, W., & Xing, L. (2017). Changes in the carbon isotope composition of pristane and phytane with increasing maturity. *Petroleum Science and Technology*, 35, 1270-1276.

van Maldegem, L. M. (2017). *Molecular and isotopic signatures of life surrounding the Neoproterozoic Snowball Earth events*. (Ph.D. Dissertation), Universität Bremen.

Vinnichenko, G., Jarrett, A. J. M., Hope, J. M., & Brocks, J. J. (2020). Discovery of the oldest known biomarkers provides evidence for phototrophic bacteria in the 1.73 Ga Wollogorang Formation, Australia. *Geobiology*, 18, 544-559.

Watanabe, M., Adschiri, T., & Arai, K. (2001). Overall rate constant of pyrolysis of *n*-alkanes at a low conversion level. *Industrial & Engineering Chemistry Research*, 40, 2027-2036.

Williford, K. H., Grice, K., Logan, G. A., Chen, J., & Huston, D. (2011). The molecular and isotopic effects of hydrothermal alteration of organic matter in the Paleoproterozoic McArthur River Pb/Zn/Ag ore deposit. *Earth and Planetary Science Letters*, 301, 382-392.

Chapter 6

Reassessment of the thermal preservation of organic matter in the Paleoproterozoic McArthur River (HYC) Zn-Pb ore deposit, Australia

Galina Vinnichenko, Janet M. Hope, Amber J.M. Jarrett, Neil Williams, Jochen J. Brocks

Ore Geology Reviews, 133, 2021.

Abstract

The 1.64 Ga old McArthur River (HYC) Zn-Pb deposit in northern Australia is one of the best preserved clastic-dominated, stratiform base-metal deposits. However, the mechanisms of ore formation are still controversial. To characterize the influence of metal-bearing fluids on organic matter in the McArthur River mine, we used lipid biomarkers in combination with compound-specific isotope analysis and Rock-Eval pyrolysis on a succession covering the hanging wall, orebody, inter-ore layers and foot wall. Aromatic and methyldiamantane maturity parameters indicate that bitumens through the entire succession, including the ore zone, fall into the beginning of the gas window (~160 ºC). The thermal maturity of kerogen in the hanging and foot wall is consistent with this degree of thermal alteration. By contrast, kerogen in the ore zone possesses extremely high thermal maturities that are inconsistent with the bitumen. This temperature anomaly shows that the extractable hydrocarbons migrated into the orebody after mineralization, most probably from surrounding sediments of the Barney Creek Formation. Polycyclic aromatic hydrocarbons (PAHs) found in the McArthur River orebody are also detected in similar distributions in the unmineralized hanging wall and foot wall and are thus not the products of hydrothermal activity, as previously assumed, but formed through burial-temperature processes. Therefore, the hydrocarbons in the McArthur River ore zone do not yield information about the temperature of mineralising fluids, negating earlier suggestions for temperatures of 200 ºC, or 250 to 400 ºC. Yet, based on kerogen maturity, the organic matter in ore lenses and inter-ore breccias is still severely altered. The data is most consistent with the flow of metal-bearing fluids with temperatures in the range of thermochemical sulphate reduction but inconsistent with the activity of bacterial sulphate reducers.

6.1 Introduction

The McArthur River (or HYC) clastic-dominated (CD) stratiform Zn-Pb deposit in northern Australia is one of the least altered CD Zn-Pb deposits yet discovered. Even though the deposit is 1.64 Ga old, primary-forming features are well preserved (Eldridge et al., 1993; Ireland et al., 2004), and the McArthur River deposit is therefore well suited for ore genesis investigations on the economically important CD-type of Zn-Pb mineralization. Although much research has been carried out to understand the McArthur River ore-forming processes, the precise mechanisms are still a topic of debate.

Two contrasting groups of ore-forming models have been proposed for the McArthur River deposit. The first are the relatively low temperature syngenetic synsedimentary models (Ireland et al., 2004; Large et al., 2002; Large et al., 1998; Large et al., 2001; McGoldrick et al., 2010), the most comprehensive of which is the brine-pool model of Ireland et al. (2004) where the three main sulphide minerals, pyrite, sphalerite and galena form from exhaled mineralizing fluids which pond in a brine pool. Sulphide precipitation in this model takes place mostly in response to bacterial sulphate reduction. The second are the much hotter post-sedimentary diagenetic to epigenetic models (Chen et al., 2003; Eldridge et al., 1993; Logan et al., 2001; Magnall et al., 2020; Spinks et al., 2020; Symons, 2007; Williford et al., 2011). The most detailed of these, initially developed by Eldridge et al. (1993) and subsequently refined by Logan et al. (2001) and Chen et al. (2003), involves the early diagenetic formation of pyrite by bacterial sulphate reduction in carbonaceous sediments and the later introduction of hot Zn- and Pb-rich fluids into the sediments from nearby faults. Ore formation is postulated to have occurred meters to tens of meters beneath the sediment-water interface by way of sulphate reduction. However, Logan et al. (2001) were ambivalent whether the reduction was bacterial or thermochemical. Subsequently Chen et al. (2003) proposed fluid temperatures of 250–

400 ºC, a range favouring thermochemical sulphate reduction, but also raising the possibility that the reduced sulphide sulphur may have been carried in by the mineralizing fluids, as initially suggested by Eldridge et al. (1993). A better understanding of the ore-forming fluids temperature is pivotal to determining the actual McArthur River processes.

The McArthur River orebody is hosted in the 1.64 Ga Paleoproterozoic Barney Creek Formation (Fm), which also contains dubious microfossils (Crick, 1992; Oehler, 1977) and biomarkers of Proterozoic age (Brocks et al., 2005; Brocks & Schaeffer, 2008; Summons et al., 1988). Previous studies on the McArthur River organic matter applied biomarker distributions and maturity indices to estimate the temperature of the ore-forming fluids (Logan et al., 2001; Chen et al. 2003; Williford et al. 2011). The suggested temperatures of 200–250 ºC (Williford et al. 2011) or even 250–400 ºC (Chen et al. 2003) were used to support an epigenetic model involving basin-derived hot mineralizing fluids. However, some of the previous biomarker studies were affected by contamination, based on the presence of diagnostic Phanerozoic sterane signals (e.g., Logan et al., 2001). Studies by Chen et al. (2003) and Williford et al. (2011) investigated samples along the horizontal trajectory of expected brine flow in individual ore bodies. The organic geochemistry of the McArthur River deposit was reviewed by Greenwood et al. (2013).

The current study provides the first hydrocarbon analysis of the full succession that harbours the McArthur River ore deposit, including the hanging wall, orebody, inter-ore layers and foot wall. The goal of this research is to compare organic matter in mineralized and unmineralized zones of the McArthur River mine using lipid hydrocarbons in combination with Rock-Eval pyrolysis and compound-specific isotope analysis, and to determine the impact the mineralizing fluids had on the organic geochemistry of the Barney Creek Fm.

6.2 Geological setting and samples

The McArthur River mine is located in the northern Australian McArthur Basin close to the Emu Fault. The Paleoproterozoic–Mesoproterozoic McArthur Basin contains predominantly shallow marine siliciclastic and carbonate succession that is subdivided into the Tawallah, McArthur, Nathan and Roper groups in the southern part of the basin (Figure 6.1) (Ahmad et al., 2013; Jackson et al., 1987; Munson, 2014). The McArthur Group (~1690 to ~1614 Ma) is represented by shallow to deep marine carbonates, shales and sandstones (Jackson et al., 1987; Kunzmann et al., 2019), deposited during predominant basin subsidence with occasional extensional and compressional periods (Blaikie & Kunzmann, 2020). The 1640 ± 4 Ma Barney Creek Fm of the McArthur Group occurs conformably between the Teena Dolostone (below) and the Reward Dolostone (above) and comprises laminated dolomitic, carbonaceous and pyritic siltstone and shale (Jackson et al., 1987; Page & Sweet, 1998). The Barney Creek Fm, which was deposited in a quiet, anoxic, sub-wave-base environment, records two maximum flooding surfaces and, together with the overlying Reward Dolostone, includes two transgressive-regressive sequences (Bull, 1998; Kunzmann et al., 2019). Jackson et al. (1987) subdivided the Barney Creek Fm into three members, from bottom to top the Cooley Dolostone, W-Fold Shale and HYC Pyritic Shale. Outside of the McArthur River mine, these three members are overlain by a thick, undifferentiated upper section that is not preserved in the HYC sub-basin (Kunzmann et al., 2019). The orebody is located within the HYC Pyritic Shale Member and consists of eight stacked ore lenses with average thicknesses ranging from ~2 to ~14 m, separated by unmineralized pyritic dolomitic shale or dolomitic breccia (Figure 6.1) (Eldridge et al., 1993). Sulphide mineralization occurs as mainly fine-grained bands and crystals of predominantly pyrite, galena and sphalerite, along with minor arsenopyrite and chalcopyrite (Ireland et al., 2004; Spinks et al., 2020).

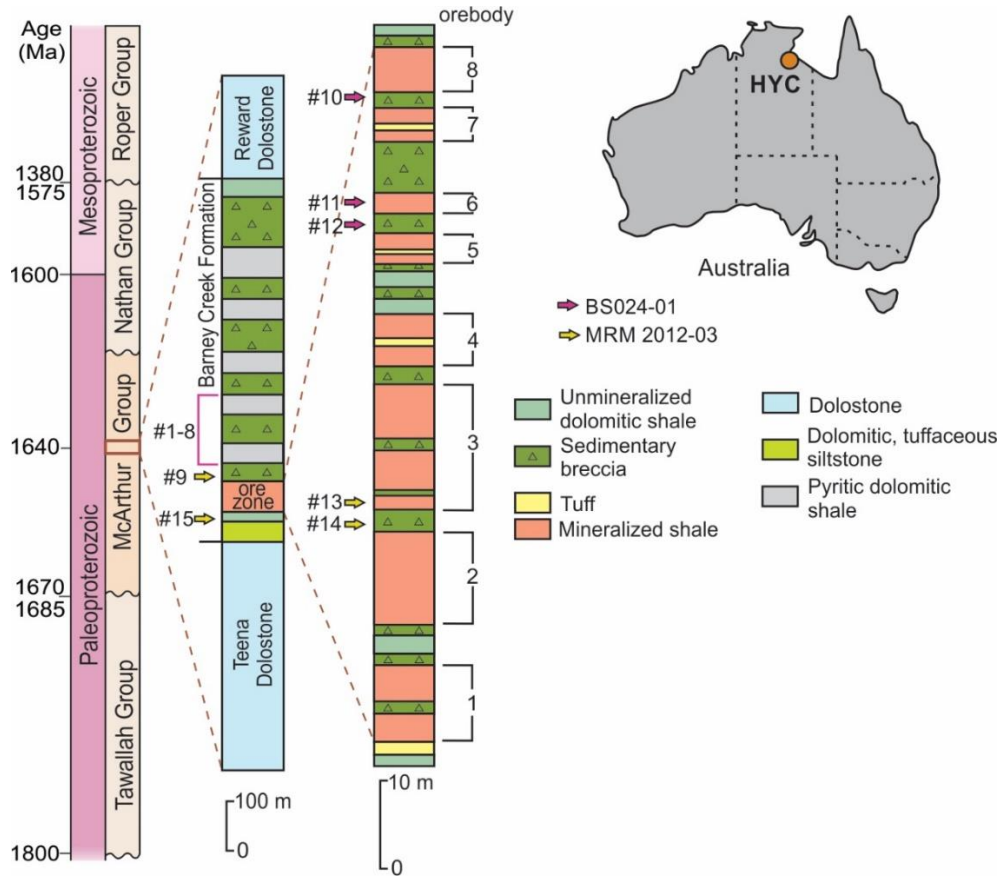

Figure 6.1. Simplified stratigraphy of the southern McArthur Basin and expanded McArthur River ore zone section (after Large et al., 1998) showing fifteen sampled intervals in two drill cores, BS042-01 and MRM 2012-03.

In the current study, fifteen samples (Figure 6.1, Table 6.1) were collected for organic geochemical analysis from the hanging wall, inter-ore, orebody and foot wall of two drill cores from the McArthur River Mine (MRM 2012-03 and BS024-01). Nine hanging wall samples, as well as one foot wall sample, consisted of unmineralized black shale, dolomitic siltstone and shale, pyritic shale and nodular dolomite (Table 6.1). Ore zone samples were represented by two mineralized shales, two inter-ore breccias and one nodular dolomite (Table 6.1). For comparison, we further included one low maturity unmineralized Barney Creek Fm sample (#16) from the LV09 drill core distal to the mine (Table 6.1).

6.3 Methods

6.3.1 Biomarker analysis

Since drilling fluids or other anthropogenic petroleum products can significantly compromise the results of biomarker analysis on Precambrian rocks, it is crucial to recognize and remove contaminants using exterior/interior experiments (Brocks et al., 2008) and only interpret demonstrably indigenous molecular fossils from McArthur River samples. Biomarker analysis was performed at the Australian National University and followed protocols and methods described in detail elsewhere (e.g., Brocks et al., 2008; Jarrett et al., 2013; Vinnichenko et al., 2020). First of all, ~3 mm were removed from the exterior of all drill core specimens using a solvent-cleaned precision diamond wafering saw (Buehler IsoMet 1000) or a wet table saw (Nortel Machinery Inc.), depending on sample size and shape. Then a clean Rocklabs iron puck mill was used to ground the exterior (E) and interior (I) rock portions to a < 240-mesh powder. Later, E and I rock powders were extracted with a Dionex Accelerated Solvent Extractor (ASE 200) using 90% DCM and 10% methanol. Prior fractionation, extracts were filtrated over freshly precipitated elemental copper to remove elemental sulphur. All extracted bitumens were separated into saturated, aromatic, and polar fractions with microcolumn (pasteur pipette) chromatography over annealed and dry-packed silica gel (7 cm) using 1.5 ml of *n*-hexane, 4 ml of *n*-hexane:DCM (1:1, v/v) and 3 ml of DCM:methanol (1:1, v/v) respectively. Gas chromatography-mass spectrometry (GC–MS) analyses were carried out on an Agilent 6890 GC coupled to a Micromass Autospec Premier double sector MS. The GC was equipped with a 60 m DB-5MS capillary column (0.25 mm ID, 0.25 µm; Agilent) and used helium as the carrier gas at a constant flow rate of 1 ml min^{-1}. Full Scan analyses were performed for saturated and aromatic fractions. Laboratory contaminants remained

below detection limits in the cumulative system blanks that experienced the whole sequence of procedures along with samples.

6.3.2 Isolation of kerogen

Kerogen isolation for McArthur River samples was undertaken at Geoscience Australia following the in-house protocol. The analysis was performed on 10–11g rock powder that had already undergone solvent extraction with ASE 200. Decarbonation of extracted powders was achieved using 15% hydrochloric acid (HCl), with samples then centrifuged 3 times with deionised water (2000 rpm for 5 minutes) for neutralising the HCl. 48% Hydrofluoric acid (HF) was used to remove silicate minerals. Samples were mixed with 100 ml of deionised water and 100 ml of HF and further stirred at room temperature on an agitator plate (150 rpm for 7 hours). The mixture was then allowed to stand for 6 hours, the dilute HF solution decanted, and fresh solution (50 ml of water and 50 ml of HF) added. The stirring procedure was repeated and 20 ml of warm (50 °C) saturated boric acid (H_3BO_3) solution was added to each sample, which was still immersed in HF solution. After the stirring procedure was repeated and samples were settled for 6 hours, the dilute HF/boric acid solution was siphoned off. Samples were washed with warm (50 °C) deionised water 4 times using centrifugation (2000 rpm for 5 minutes). Treatment with 15 ml of 15% HCl in a water bath set to 65 °C for 2 hours was used as an additional step to remove carbonates. To neutralise the HCl, samples were centrifuged with warm deionised water 3 times. For removal of heavy minerals, 20 ml of sodium polytungstate solution was added to each sample, mixed well and centrifuged. The floats and sinks were collected into separate test tubes and washed with warm deionised water. The kerogen concentrate was dried in an oven at 45 °C.

6.3.3 Rock-Eval pyrolysis

Total organic carbon (TOC) content and hydrocarbon potential were measured using a Rock-Eval 6 Turbo™ (Vinci Technologies, France) at Geoscience Australia and Moscow State University following the methodology, described in Jarret et al. (2018). The analyses were performed on 60 mg of bulk rock powder or 3 mg of concentrated kerogen. The initial pyrolysis oven temperature was set at 300 °C (held for 5 minutes) and then ramped to 650 °C with 25 °C per minute rate. The oxidation oven was held at 400 °C for 3 minutes followed by ramping to 850 °C at 20 °C per minute, with a final hold time of 5 minutes. The flame ionisation detector (FID) was calibrated by running the standard 'IFP 160000'. For each batch of samples, the analysis blanks were run and later automatically subtracted from sample data.

The main parameters obtained with this method are S1 (free hydrocarbons), S2 (hydrocarbon potential), S3 (CO_2 potential), Tmax (the pyrolysis temperature at the S2 peak maximum) and TOC (total organic carbon). Other parameters are defined in Table 6.3.

Table 6.1. McArthur River sample information and biomarker maturity parameters.

Sequence	Sample ID	Internal sample ID	Drill core	Depth, (m)	Relative depth[a], (m)	Sample description	MPI[b]	Rc (MPI)[c]	MPDF[d]	Rc (MPDF)[e]	MPR[f]	Rc (MPR)[g]	MDI[h] (%)
Hanging wall	#1	17G013	BS024-01	16.4	-182.6	Massive black shale	1.30	1.18	0.63	1.24	1.88	1.21	32
	#2	17G019	BS024-01	41.5	-157.7	Laminated black shale	1.40	1.24	0.65	1.30	2.19	1.28	30
	#3	19G019	BS024-01	63.5	-135.6	Dolomitic siltstone	1.26	1.16	0.61	1.20	1.86	1.21	37
	#4	19G020	BS024-01	85.7	-113.4	Dolomitic siltstone	1.29	1.17	0.62	1.22	1.95	1.23	39
	#5	17G020	BS024-01	105.1	-94.1	Pyritic shale	1.19	1.11	0.57	1.10	1.46	1.10	37
	#6	17G021	BS024-01	146.1	-53.1	Dolomitic siltstone	1.47	1.28	0.70	1.40	2.74	1.37	n.d.
	#7	19G023	BS024-01	167.5	-31.5	Dolomitic siltstone	1.24	1.14	0.69	1.37	2.77	1.38	n.d.
	#8	19G021	BS024-01	191.1	-7.9	Pyritic shale	1.44	1.26	0.68	1.36	2.58	1.35	37
	#9	17G011	MRM 2012-03	157.8	-3.0	Fine scale nodular dolomite	1.29	1.17	0.62	1.22	1.99	1.24	37
Interore 7/8	#10	17G018	BS024-01	201.1	2.1	Interore breccia	1.47	1.28	0.66	1.32	2.45	1.32	33
Orebody 6	#11	17G016	BS024-01	210.0	11.0	Mineralized shale	1.55	1.33	0.68	1.35	2.57	1.35	n.d.
Interore 5/6	#12	17G017	BS024-01	215.7	16.7	Interore breccia	1.44	1.27	0.70	1.40	2.83	1.39	32
Lower 3rd orebody	#13	17G014	MRM 2012-03	190.4	29.5	Mineralized shale	1.28	1.17	0.64	1.26	2.13	1.26	33
Interore 2/3	#14	17G015	MRM 2012-03	197.9	37.0	Nodular dolomite	1.22	1.13	0.59	1.16	1.71	1.17	41
Foot wall	#15	17G012	MRM 2012-03	210.8	49.9	Dolomitic shale	1.32	1.19	0.62	1.22	1.92	1.22	36
Unmineralized BCF	#16	17G008	LV09	477	-	Dolomitic siltstone	0.64	0.79	0.39	0.71	0.81	0.85	-

[a]Depth in meters relative to the top of the ore body. [b]Methylphenanthrene index MPI-1 = 1.5*(2-MP+3-MP)/(P+1-MP+9-MP), where P = phenanthrene, MP = methylphenanthrene (Radke & Welte, 1983). [c]Calculated vitrinite reflectance Rc(MPI-1) = 0.6*MPI-1+0.4 for absence of the MPI-1 reversal (Radke & Welte, 1983). [d]Methylphenanthrene distribution factor MPDF = (3-MP+2-MP)/(3-MP+2-MP+9-MP+1-MP) (Kvalheim et al., 1987). [e]Calculated vitrinite reflectance Rc(MPDF) = 2.242*MPDF - 0.166 (Kvalheim et al., 1987). [f]Methylphenanthrene ratio MPR = 2-MP/1-MP (Radke, 1988). [g]Calculated vitrinite reflectance Rc(MPR) = $1.1*\log_{10}$(MPR)+0.95 (Radke, 1988). [h]Methyldiamantane index MDI = 4-MD/(1-MD+3-MD+4-MD), where MD = methyldiamantane (Chen et al., 1996). n.d. – not detected.

6.3.4 Stable hydrogen and carbon isotopes

Stable hydrogen and carbon isotopic compositions of *n*-alkanes were analysed as duplicates using gas chromatography-isotopic ratio mass spectroscopy (GC-IRMS) at Geoscience Australia. Prior to isotope analyses, *n*-alkanes were separated from the saturated fraction using 0.5 mg of 5 Å zeolite molecular sieve (Grace Davison) in cyclohexane. The sieve was digested in HF (32%, 3 ml) to release the *n*-alkanes, which further were extracted with 3 ml *n*-hexane. All $\delta^{13}C$ and $\delta^{2}H$ values are reported in permil (‰) notation relative to VPDB and VSMOW respectively. Average standard deviation of individual compounds is 0.13‰ for $\delta^{13}C$ and 2‰ for $\delta^{2}H$. Organic carbon isotope analyses of kerogen ($\delta^{13}C_{ker}$) were measured with Sercon 20-20 combustion IRMS.

6.4 Results

6.4.1 Biomarker distributions and thermal maturity

Extracted Barney Creek Fm bitumens from fifteen mine samples illustrate typical mid-Proterozoic hydrocarbon distributions with large unresolved complex mixture and high methyl-alkane/*n*-alkane ratios (Pawlowska et al., 2013). Figure 6.2 compares the total ion chromatograms of the saturated and aromatic fractions of a hanging wall and orebody sample. Saturated fractions contain a unimodal distribution of *n*-alkanes ranging from C_{11} to C_{30} with a maximum at C_{13} to C_{17} (Figure 6.2a, b). The total ion chromatograms of the McArthur River aromatic fractions indicate the presence of polycyclic aromatic hydrocarbons (PAH) such as phenanthrene, pyrene, chrysene, benzo[e]pyrene, benzo[ghi]perylene and coronene in the ore zone as well as in the hanging wall (Figure 6.2c, d). Interestingly, even higher abundances of PAH (relative to TOC) were also detected in low maturity (Rc = 0.7–0.8%) unmineralized Barney Creek

Fm sediments from the LV09 drill hole, which is located 40 km south of the McArthur River mine (Table 6.2).

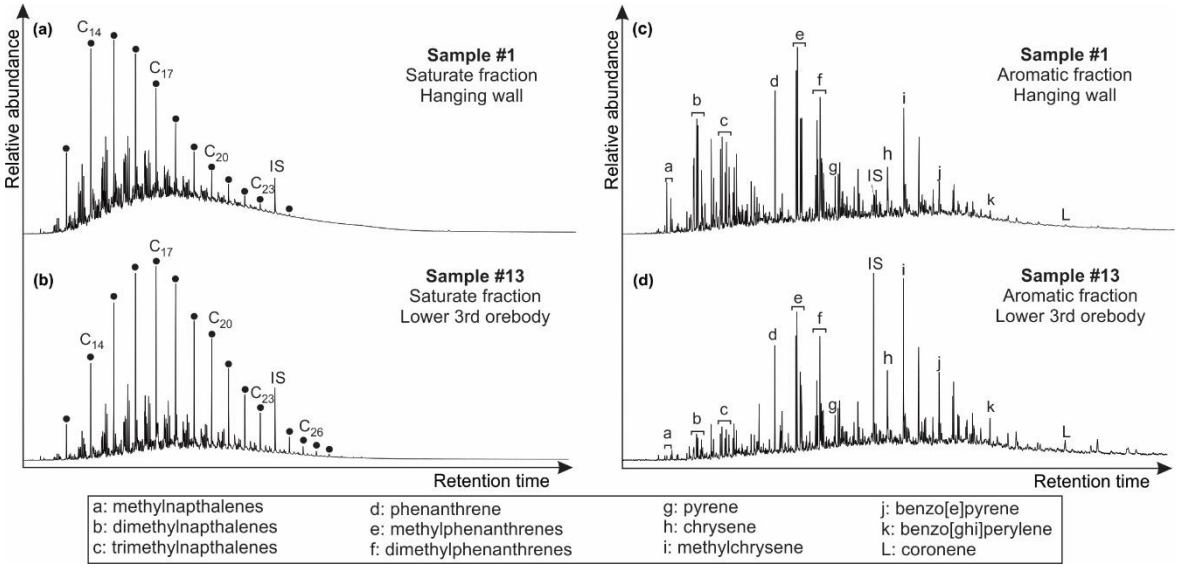

Figure 6.2. Total ion chromatograms of saturate (a, b) and aromatic (c, d) hydrocarbon fractions from hanging wall (182.6 m above orebody) and lower 3rd orebody samples. Black circles represent *n*-alkanes. IS = internal standard.

The maturity level of all McArthur River samples was too high for the preservation of polycyclic biomarkers such as hopanes or steranes. However, the McArthur River extracts contain diamondoids and phenanthrenes that can be used as maturity parameters. These compounds occur as various structural isomers with different thermal stabilities. Under thermal stress, the concentration of more stable isomers rises relative to less stable configurations (e.g., Greenwood et al., 2013). The relative abundances of these molecules may thus serve as thermal maturity indicators. Common hydrocarbon-based maturity indices, defined in Table 6.1, include the methyl diamantane index (MDI; Chen et al., 1996), methyl-phenanthrene index (MPI; Radke & Welte, 1983), methyl-phenanthrene distribution factor (MPDF; Kvalheim et al., 1987) and methyl-phenanthrene ratio (MPR; Radke, 1988). For sedimentary rock specimens of the Phanerozoic eon, vitrinite reflectance measurements (%Ro) represent a standard method to estimate thermal

maturity of solid organic matter. Since vitrinite, an organic maceral deriving from plants, did not exist in the Proterozoic, hydrocarbon parameters such as MDI, MPI, MPDF and MPR can be re-calculated to yield vitrinite reflectance equivalent values (Rc, where 'c' stands for calculated), making a comparison of different maturity parameters easier (formulas are provided in Table 6.1). Rc values between 0.6 and 1.2% correspond to thermally mature organic matter in the oil window zone, while values >1.2% denote overmature stage or gas window zone (Baskin, 1997)

Table 6.1 summarises the hydrocarbon-based maturity indices MDI, MPI, MPDF and MPR for McArthur River samples. MDI range from 30 to 41% and correspond to vitrinite reflectance equivalent (Rc) values between 1.1 and 1.3% (Chen et al., 1996), while Rc based on MPDF and MPR fall into the range 1.1–1.4% for the entire sediment package (Table 6.1, Figure 6.3b). Generally, MPI values rise with increasing maturity, but above a certain threshold (Rc = 1.7%), MPI values start to decrease again (Boreham et al., 1988). Such a reversal can be recognized by phenanthrene/methyl-phenanthrene (P/MP) ratios >1 (Brocks et al., 2003). The Rc(MPI) further must be calculated using two different formulas depending on the presence or absence of the reversal (Radke & Welte, 1983). Since P/MP ratios for the McArthur River samples vary from 0.3 to 0.5, the MPI is not reversed and the corresponding Rc(MPI) values fall into the range between 1.1 and 1.3%, consistent with other maturity parameters (Rc from MDI, MPDF and MPR). Orebody samples from this study show slightly higher maturity levels in comparison with previously published bitumens for the ore lens 5 that yielded Rc(MPDF) = 0.9–1.1% and Rc(MPR) = 0.9–1.0% (calculated from Table 1 in Williford et al. 2011). Although Williford et al. (2011) reported Rc(MPI) values up to 1.6%, the P/MP ratios in their study varied from 0.1 to 0.2, indicating that MPI reversal did not occur. Therefore, after applying the correct formula for absence of the reversal, Rc(MPI) in Williford et al. (2011)

should range between 1.1 and 1.2%, consistent with Rc(MPDF) and Rc(MPR) values from their study.

Table 6.2. PAH concentrations in ppb relative to organic carbon mass.

Sequence	Sample ID	Drill core	Depth, (m)	Relative depth[a], (m)	P[b]	Pyrene	Chrysene	Benzo[e] pyrene	Benzo[ghi] perylene	Coronene
Hanging wall	#1	BS024-01	16.4	-182.6	18 432	3 733	9 136	4 462	1 315	142
	#2	BS024-01	41.5	-157.7	20 870	5 025	12 954	6 056	2 069	502
	#5	BS024-01	105.1	-94.1	4 290	1 522	3 263	2 761	983	215
	#6	BS024-01	146.1	-53.1	22 726	5 084	15 872	8 023	3 559	894
	#9	MRM 2012-03	157.8	-3.0	8 918	1 903	5 501	2 888	1 188	n.d.
Interore 7/8	#10	BS024-01	201.1	2.1	11 026	2 211	5 581	2 444	987	310
Orebody 6	#11	BS024-01	210.0	11.0	11 195	2 540	5 810	2 910	1 203	353
Interore 5/6	#12	BS024-01	215.7	16.7	16 145	4 223	6 568	3 147	1 840	583
Lower 3rd orebody	#13	MRM 2012-03	190.4	29.5	14 489	3 080	11 305	8 499	3 270	766
Interore 2/3	#14	MRM 2012-03	197.9	37.0	1 673	468	920	617	303	136
Foot wall	#15	MRM 2012-03	210.8	49.9	4 393	817	2 045	1 191	411	n.d.
Unmineralized BCF	#16	LV09	477	-	83 339	12 786	30 010	14 068	1 887	n.d.

[a]Depth in meters relative to the top of the ore body. [b]Phenanthrene

6.4.2 Rock-Eval data

The results of Rock-Eval pyrolysis on bulk rock and kerogen concentrates of eleven samples are represented in Table 6.3. The majority of analysed whole rock samples have poor to fair TOC contents varying between 0.2% and 0.7%. Only upper hanging wall samples #2 and #1 record good to very good organic richness with bulk TOC of 1.4% and 3% respectively. Bulk Tmax measurements for the majority of samples are unreliable due to low TOC and low S2 peak (S2 < 0.2). The two most reliable Tmax values, from hanging wall samples #2 and #1, indicate a late oil window maturity level.

To reduce the matrix effect on low-TOC samples, we also performed Rock-Eval measurements on kerogen concentrates. S2 peaks of kerogen concentrates were 1.3 to 37 times higher than for bulk rock measurements. Tmax values for the hanging wall fell into the range 440–448 ºC, indicating maturities in the main oil window (Table 6.3, Figure 6.3a). By contrast, and despite reasonably high carbon contents (0.7 to 7.7%), the kerogen

concentrates from the underlying ore zone yielded inconsistently low Tmax values in the immature range from 386 to 424 ºC, and one sample with a low S2 peak (0.05) yielded 500ºC. Unreliable pyrograms (Appendix C, Supplementary Figure 1a, b) indicate that the unrealistically low and high Tmax values in the ore zone are an artefact and do not represent the actual maturity of the kerogen concentrates.

Table 6.3. Rock-Eval parameters for McArthur River samples.

Sequence	Sample ID	Bulk rock						Isolated kerogen					
		S1[a]	S2[b]	HI[c]	OI[d]	TOC[e] (%)	Tmax[f] (ºC)	S1	S2	HI	OI	TOC (%)	Tmax (ºC)
Hanging wall	#1	0.19	0.67	22	4	2.99	443	0.32	3.09	15	8	20.6	443
	#2	0.03	0.29	20	6	1.44	463	0.44	2.22	10	4	22.12	440
	#5	0.02	0.14	33	17	0.42	446*	0.91	2.85	30	6	9.58	440
	#6	0.01	0.03	9	34	0.32	467*	0.3	1.07	16	11	6.8	448
	#9	0.01	0.01	3	135	0.37	438*	0.1	0.41	21	7	1.98	442
Interore 7/8	#10	0.01	0.05	27	97	0.2	457*	0.24	0.64	8	8	7.74	424
Orebody 6	#11	0.01	0.1	22	52	0.48	441*	0.03	0.05	3	25	1.62	500*
Interore 5/6	#12	0	0.05	17	92	0.29	450*	0.05	0.21	11	5	1.87	422
Lower 3rd orebody	#13	0.03	0.1	20	32	0.52	413*	0.05	0.24	33	11	0.73	386
Interore 2/3	#14	0	0.04	7	59	0.68	442*	0.04	0.05	5	1	1.02	418*
Foot wall	#15	0.01	0.04	11	54	0.35	468*	0.78	1.49	10	2	14.2	436

[a]Free hydrocarbons, mg HC/g rock. [b]Generative potential, mg HC/g rock. [c]Hydrogen Index HI = S2*100/TOC, mg HC/g TOC. [d]Oxygen Index OI = S3*100/TOC, mg CO_2/g TOC. [e]Total Organic Carbon. [f]Temperature at maximum of S2 peak. * – low S2 (<0.2), Tmax is unreliable.

6.4.3 Stable hydrogen and carbon isotopes

We measured the stable hydrogen isotopic composition (δ^2H) of *n*-alkanes from two ore zone samples and three hanging wall samples in the McArthur River mine. Non-weighted average δ^2H of orebody *n*-alkanes *n*-C_{16} to *n*-C_{20} range from -78 ‰ to -82‰, whereas hanging wall *n*-alkanes range from -78‰ to -79‰ for samples #3 and #5 and reach -51‰ in sample #1 (Table 6.4). Figure 6.4 illustrates the comparison of δ^2H values measured in the current study with previously published *n*-alkane values from the ore lens 5 (Williford et al., 2011) and an unmineralized Barney Creek Fm sample from LV09 drill core distal to the McArthur River deposit. Our measurements demonstrate that *n*-alkanes

from the ore sequence and hanging wall are around 40‰ enriched in ^{2}H compared to *n*-alkanes from the unmineralized sample from the LV09 drill core (Figure 6.4).

Stable carbon isotopes of Barney Creek Fm kerogen ($\delta^{13}C_{ker}$) only show slight variability, ranging from -32.8‰ to -34.0‰ (Table 6.4). The similarities between $\delta^{13}C_{ker}$ values in the orebody and unmineralized hanging wall and foot wall demonstrate that hydrothermal fluids did not significantly affect the isotopic composition of the orebody kerogen. Measurements of the stable carbon isotopic composition ($\delta^{13}C$) of *n*-alkanes are available for two samples from the ore zone, three from the hanging wall and one from the foot wall. Non-weighted average $\delta^{13}C$ of orebody *n*-alkanes *n*-C_{16} to *n*-C_{23} range from -29.3‰ to -30.8‰, whereas hanging wall and foot wall *n*-alkanes range from -25.0‰ to -29.5‰ (Table 6.4).

Table 6.4. Hydrogen and carbon isotope values for McArthur River samples.

Sequence	Sample ID	Internal sample ID	Relative depth[a], (m)	$\delta^{2}H$ alk[b] (‰)	$\delta^{13}C$ ker[c] (‰)	$\delta^{13}C$ alk[d] (‰)
Hanging wall	#1	17G013	-182.6	-51	-33.4	-25.02
	#2	17G019	-157.7	n.d.	-34.0	-25.50
	#3	19G019	-135.6	-78	n.d.	n.d.
	#5	17G020	-94.1	-79	-33.3	-29.45
Lower 3rd orebody	#13	17G014	29.5	-78	-33.4	-29.34
Interore 2/3	#14	17G015	37.0	-82	-32.8	-30.76
Foot wall	#15	17G012	49.9	n.d.	-33.1	-26.18

[a]Depth in meters relative to the top of the ore body. [b]Stable hydrogen isotopic composition of *n*-alkanes (average of *n*-$C_{16–20}$). [c]Organic carbon isotope values of kerogen. [d]Stable carbon isotopic composition of *n*-alkanes (average of *n*-$C_{16–23}$). N.d. – not determined.

6.5 Discussion

6.5.1 Thermal maturity and origin of the bitumen

The solid black circles in Figure 6.3a summarize previously published Rock-Eval data for the McArthur River deposit (Logan et al., 2001). While hanging wall samples indicate a normal burial maturity trend in the oil window (450–470 ºC), the ore succession yields strongly elevated Tmax values (>520 ºC). Figure 6.3b illustrates organic matter reflectance measurements (random Ro) up to 2.4% in the orebody (Logan et al., 2001). At the same time, unmineralized layers within the ore zone have random Ro values that are consistent with burial maturities in the oil window (Figure 6.3b). These observations were used in support of an epigenetic model, where hot fluids percolated through permeable sedimentary layers forming the ore lenses but did not affect intercalated low permeability muddier beds (Logan et al., 2001). However, it seems questionable that inter-ore layers of millimetre to centimetre-scale could have escaped thermal alteration during ore genesis while hot brines flowed through the adjacent metal-rich layers. Additionally, since no information about S2 values is available for the published Rock-Eval data, and as the orebody is generally kerogen poor, the reliability of the Tmax values in the ore zone is uncertain.

In the current study, we obtained Rock-Eval data on kerogen concentrates uncompromised by possible mineral matrix effects and low TOC. Newly acquired Tmax values reconfirm oil window maturity in the hanging wall and also the foot wall. However, kerogen concentrates from the orebody yield unreliable pyrograms and/or low S2 values (Appendix C, Supplementary Figure 1a, b). Tmax measurements obtained from these pyrograms are significantly below (386–424 ºC) or above (500 ºC) the oil window (Figure 6.3a, Table 6.3) and do not indicate the actual maturity of the kerogen concentrates. Since the carbon content of the kerogen concentrates of the orebody is high enough to preclude

detection limit problems, the low S2 peaks and unrealistic Tmax values must have a different explanation. We interpret the random variable Tmax values as an indicator for severely altered organic matter, likely related to locally elevated temperatures in the ore zone. The presence of pyrolytic kerogen in the orebody is in agreement with previous Rock-Eval and organic matter reflectance data from Logan et al. (2001) and high temperatures (~310 ºC) estimated by Symons (2007) based on the orebody organic matter reflectance (Rmax) measurements of Crick (1992). Such temperatures are above the bacterial sulphate reduction range and are most consistent with thermochemical sulphate reduction.

Bitumen based maturity parameters from our study are inconsistent with kerogen based maturity data (Figure 6.3). Rc(MPDF) values in the range 1.1 to 1.4% indicate normal burial maturities within the beginning of the gas window for the entire sediment package from the hanging wall, through the orebody and into the foot wall (Figure 6.3c). Moreover, within the ore zone, maturities do not vary between mineralized and non-mineralized layers. The new and previous (e.g., Williford et al., 2011) bitumen Rc(MPDF) values contradict the Tmax and reflectance data from Logan et al. (2001) and Tmax from the current study that all suggest strongly elevated maturities in the ore zone (Figure 6.3). The discrepancy between bitumen-based and kerogen-based parameters is best explained by a thermal anomaly during ore formation accompanied by alteration of the kerogen and destruction of indigenous hydrocarbons. The detected hydrocarbons in the orebody, which indicate normal burial maturities, must then represent migrated bitumen.

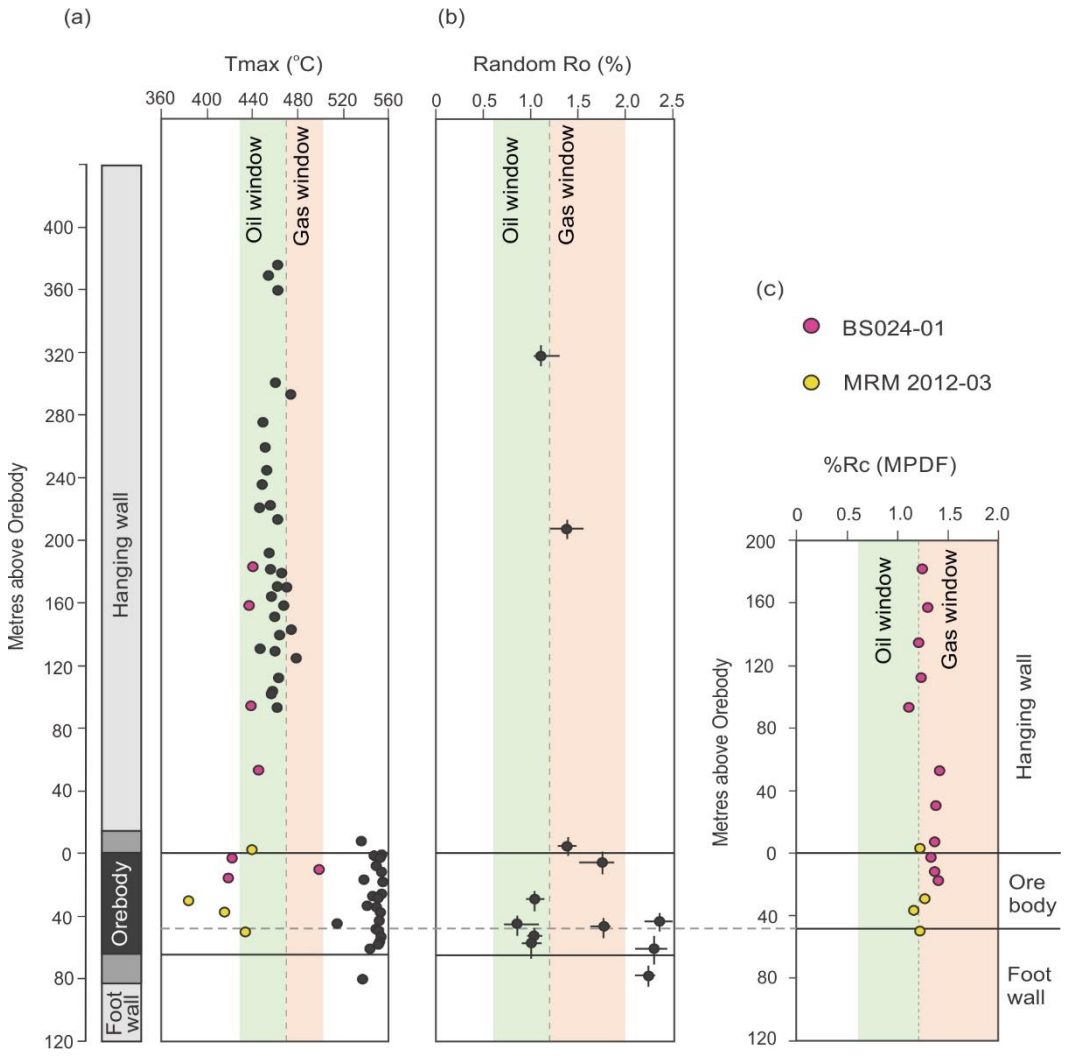

Figure 6.3. Previous Tmax (a) and organic matter reflectance (b) data in black from drill hole and mine samples around HYC deposit, plotted relative to the orebody (modified from Logan et al., 2001); and Tmax data on isolated kerogen from the current study (pink and yellow circles). (c) Calculated vitrinite reflectance Rc(MPDF) for the extracted hydrocarbons from two HYC drill cores. Oil window: Rc between 0.6% and 1.2%, Tmax between 435 and 470 ºC. Gas window: Rc between 1.2% and 2%, Tmax between 470 and 500 ºC.

In order to obtain additional information about organic sources and geological processes in the McArthur River mine, we measured stable hydrogen (δ^2H) and carbon ($\delta^{13}C$) isotopic compositions of *n*-alkanes in orebody and hanging wall samples. Williford et al. (2011) demonstrated that McArthur River orebody *n*-alkanes are enriched in ^2H by up to 50–60‰ relative to *n*-alkanes in unmineralized Barney Creek Fm sediments from the GR-10 core distal from the mine. Williford et al. (2011) interpreted this as a result of

equilibrium hydrogen exchange during ore genesis with a highly ^{2}H-enriched fluid, presumably coming from evaporites of the underlying Tawallah Group. However, due to limited sample availability, Williford et al. (2011) were not able to test this hypothesis by comparing the $\delta^{2}H$ composition of *n*-alkanes from the orebody with samples from the hanging wall. A strong $\delta^{2}H$ compositional difference of saturated hydrocarbons in the hanging wall and orebody would confirm the existence of isotopically heavy ore-forming brines ascending from the nearby fault system and exchanging hydrogen with McArthur River organic matter in the orebody. However, even though our measurements confirm that *n*-alkanes from the ore sequence are enriched in ^{2}H compared to immature and non-altered *n*-alkanes from the LV09 drill core, we detected similarly heavy isotopic compositions in the hanging wall above the ore (Figure 6.4). This observation is more consistent with a general ^{2}H-enrichment of *n*-alkanes caused by kinetic fractionation effects at relatively high thermal maturities in the full McArthur River succession (e.g., Tang et al., 2005; Vinnichenko et al., 2021). Accordingly, heavy $\delta^{2}H$ values of *n*-alkanes in the orebody are not necessarily related to hydrogen exchange with evaporitic hydrothermal fluids, as was proposed by Williford et al. (2011). Instead, similar $\delta^{2}H$ values of orebody and hanging wall *n*-alkanes are consistent with the hypothesis that hydrocarbons in the ore zone migrated from surrounding unmineralized Barney Creek Fm sediments. Similarities in the distributions of saturated (Figure 6.2a, b) and aromatic (Figure 6.2c, d) fractions in the hanging wall and orebody also support this hypothesis.

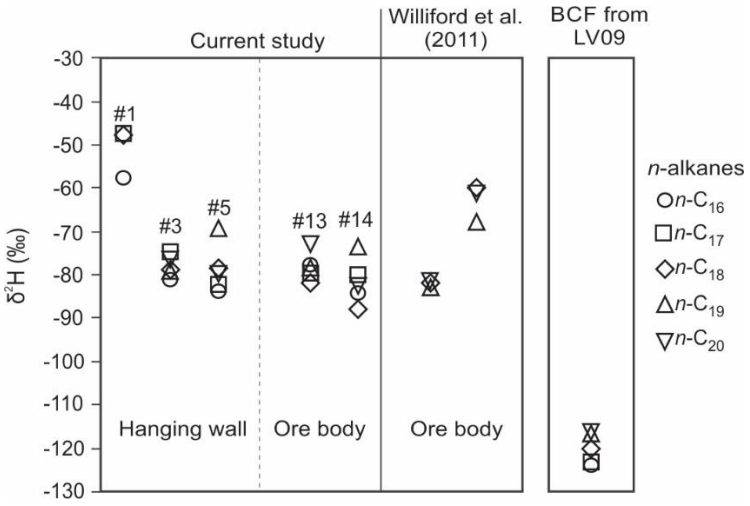

Figure 6.4. Comparison of hydrogen isotope values (δ^2H) of *n*-alkanes from hanging wall and orebody samples from the current study, previously reported values from the ore lens 5 (samples 3 and 1; Williford et al., 2011) and a low maturity unmineralized Barney Creek Formation sample from LV09 drill core (485 m depth).

The $\delta^{13}C$ composition of *n*-alkanes in the orebody is harder to explain. *n*-Alkanes in the orebody are depleted in ^{13}C relative to the hanging wall and foot wall *n*-alkanes by 1–5‰ (Table 6.4). A recent study by Vinnichenko et al. (2021) demonstrated a strong positive correlation between $\delta^{13}C$ of *n*-alkanes and thermal maturity in the unmineralized Barney Creek Fm (Figure 6.5). Figure 6.5 illustrates that $\delta^{13}C$ values of *n*-alkanes from the lower ore lens 3 and 2/3 inter-ore layer fall outside of this correlation, while values from the ore lens 5 measured by Williford et al. (2011) follow the expected trend. The data suggest that the McArthur River orebody contains more than one charge of migrated hydrocarbons that were expelled from their source rock at different stages of maturation and/or are from different stratigraphic levels. Moreover, it is possible that migrated hydrocarbons in the orebody have varied $\delta^{13}C$ values of *n*-alkanes due to different maturation mechanisms acting on in-situ bitumens and migrated oils. The complex isotope systematics of the McArthur River warrant further study.

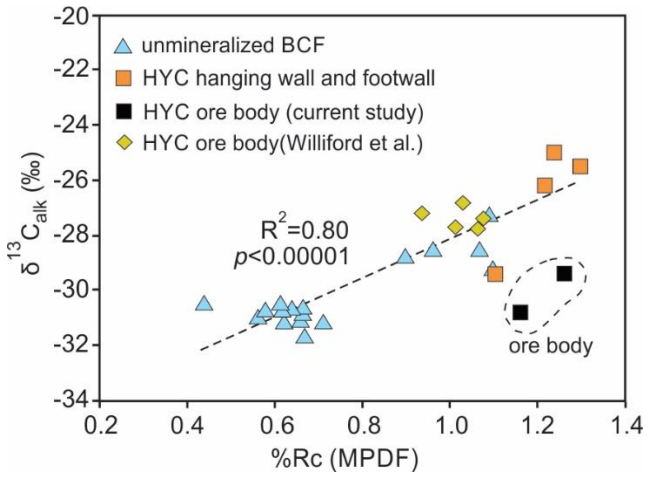

Figure 6.5. Comparison of bitumens from McArthur River orebody and unmineralized Barney Creek Formation in a cross plot of $\delta^{13}C$ of *n*-alkanes (average of *n*-$C_{16–23}$) and calculated vitrinite reflectance Rc(MPDF) (after Vinnichenko et al., 2021).

We can draw two conclusions from the kerogen and bitumen maturity data. Firstly, organic matter in ore zone sediments suffered severe thermal alteration during the ore forming process and, secondly, the hydrocarbons in the orebody largely represent bitumens that migrated from surrounding sediments at a later stage. Therefore, the orebody hydrocarbons do not reflect the temperature and activity of the metal-bearing fluids.

6.5.2 Polycyclic aromatic hydrocarbons (PAH) and temperature of the ore-forming fluid

In support of an epigenetic model, a study by Chen et al. (2003) found distributions of PAH in the McArthur River ore zone similar to those seen in hydrothermal petroleum from the Guaymas Basin in the Gulf of California and north American Middle Valley (Kawka & Simoneit, 1990; Simoneit, 1994), proposing high formation temperatures of 250–400 ºC. The authors observed that PAH concentrations decrease with distance from the source of the mineralizing fluids. This was explained by the theory that the PAH in

the McArthur River were distributed laterally by ore-forming fluids through permeable layers in the sediment and precipitated during cooling of the fluids.

A follow-up study by Williford et al. (2011) suggested that a significant portion of PAH in the orebody likely originated in black shales of the underlying Tawallah Group at a depth of 6 km and temperatures of 250 ºC and later migrated into the McArthur River deposit. The fluids containing PAH migrated along a flower structure associated with the Emu Fault and cooled to 200 ± 20 °C before reaching the Barney Creek Fm sediments. However, the temperature of 200 ± 20 °C was estimated based on reported Rc(MPI) values up to 1.6% for the ore lens 5. As described in section 6.4.1, Rc(MPI) in Williford et al. (2011) in fact range between 1.1–1.2%, which is also consistent with other maturity indices Rc(MPDF) = 0.9–1.1% and Rc(MPR) = 0.9–1.0%. Therefore, bitumen based maturity parameters for the ore lens 5 correspond more to a temperature around 160 °C. Additionally, if the PAH formation temperatures of 250 ºC proposed by Williford et al. (2011) are correct, then methyl-phenanthrene based indices (MPI, MPDF and MPR) should reflect higher maturity values consistent with such temperatures (Rc ~ 3–3.5% for T = 250 ºC). However, this is contradicted by the lower maturity of the hydrocarbons found by Williford et al. (2011) and in the current study. Since orebody samples show the same bitumen maturity values as in the hanging wall and foot wall (Figure 6.3c), we propose that PAH in the orebody migrated from a more proximal source than the Tawallah Group, possibly the Barney Creek Fm itself. According to Chen et al. (2003), some PAH are two to three times more abundant in ore relative to enclosing inter-ore layers (in ppb over TOC). We did not observe such PAH distributions in our sample set (Figure 6.6, Table 6.2). However, it is possible that the PAH in the orebody observed by Chen et al. (2003) may represent a mixture between small amounts of syngenetic high-

maturity PAH and PAH that migrated into the orebody during a later event from surrounding sediments.

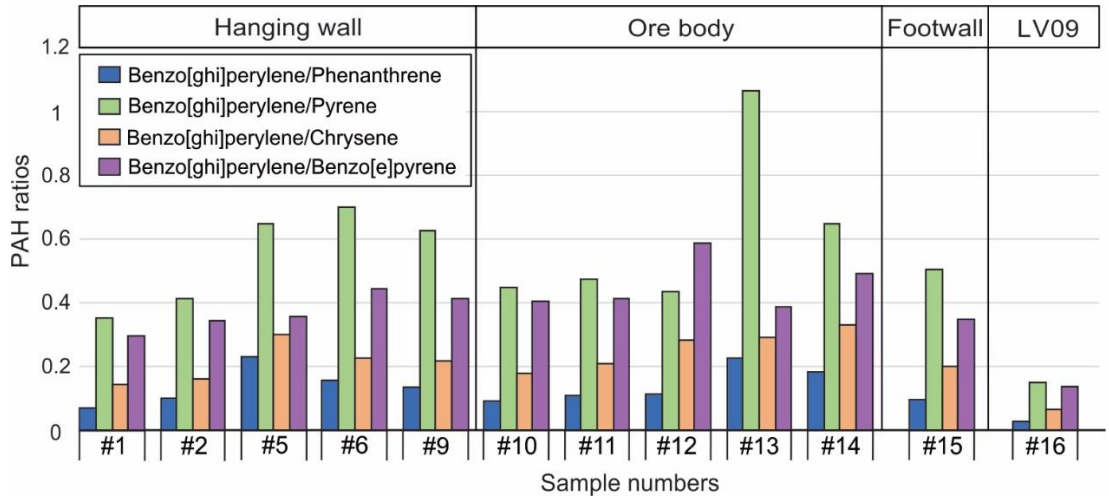

Figure 6.6. Ratios of benzo[ghi]perylene to other PAH compounds in samples from McArthur River mine and immature unmineralized LV09 sample.

In the current study, we detected similar distributions of PAH in the ore zone and in the hanging wall up to 180 meters above the ore (Figure 6.2, 6.6). Several interpretations could explain the presence of PAH in the hanging wall: (1) These molecules migrated into the hanging wall from other stratigraphic levels in the Barney Creek Fm; (2) the PAH are indigenous and formed at high temperatures due to continuous influx of hydrothermal, base metal-poor but Fe-rich fluids into the hanging wall sediments after the cessation of ore formation; (3) the PAH are indigenous and formed through burial-temperature processes independent of hydrothermal fluids. To test the first hypothesis, we plotted the concentrations of individual PAH in hanging wall and foot wall bitumens against TOC (Figure 6.7). The plot reveals significant linear correlations (R^2 = 0.88–0.95; n = 6), demonstrating that the PAH in the hanging wall are indigenous and that hypothesis (1) is false. If the second hypothesis is correct, then organic matter in the hanging wall should have experienced the same thermal alteration as organic matter in the orebody. However, this is not compatible with Tmax data that reveals a normal burial maturity trend in the

hanging wall but highly elevated maturities in the ore zone (Figure 6.3a). Hypothesis (3), suggesting a low-temperature origin of the PAH, is supported by the observation that low maturity Barney Creek Fm sediments from drill hole LV09 distal to the McArthur River mine contain even higher abundances of PAH (relative to TOC) than the McArthur River orebody (Table 6.2), including the same type of compounds and in broadly similar distributions despite considerable maturity differences (Figure 6.6). It is thus clear that the PAH in the hanging wall are a component of the original bitumen that formed through burial-temperature processes, while the bulk of PAH in the orebody migrated from surrounding sediments. As a result, PAH distributions in the McArthur River mine cannot be used as an indication for high temperatures (250–400 ºC) of ore-forming fluids.

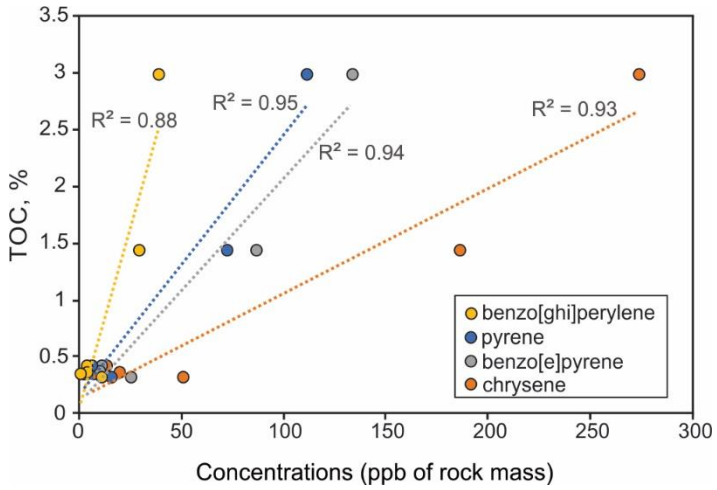

Figure 6.7. Correlation of TOC with concentrations of various polycyclic aromatic hydrocarbons in hanging wall samples.

6.6 Conclusions

A comparison of kerogen and bitumens in the McArthur River orebody with the hanging and foot wall indicates that the original organic matter in the orebody was altered by pyrolytic temperatures and/or thermochemical sulphate reduction. However, the extractable hydrocarbons in the ore zone demonstrate much lower thermal maturities than the kerogen and must have migrated into the Zn-Pb deposit from surrounding sediments after mineralization. PAH found in the McArthur River orebody are also detected in similar amounts and distributions in the unmineralized hanging wall. Thus, the bulk of these compounds migrated into the orebody and formed through burial temperature processes and not during hydrothermal activity, as previously assumed. However, a small proportion of PAH in the ore might be an indigenous residue of hydrothermal processes.

As the hydrocarbons migrated into the orebody, they cannot provide information about the temperature of mineralising fluids, negating evidence for temperatures of 250 to 400 ºC (Chen et al., 2003) or 200 ºC (Williford et al., 2011). Yet, new and previous Rock-Eval data and reflectance measurements indicate that the organic matter in the orebody was severely altered, including the ore lenses and inter-ore breccia. The data is most consistent with the activity of metal-bearing fluids with temperatures in the range of thermochemical sulphate reduction but inconsistent with bacterial sulphate reduction.

Acknowledgments

We are grateful to Jacob Sohn and Junhong Chen for technical assistance with isotope measurements and Ian Long for isolation of kerogen in the Organic Geochemistry laboratory at Geoscience Australia. We thank Ruslan Khamidullin (Lomonosov MSU) for help with Rock-Eval analysis. We thank Darryl Stacey from the Darwin Core Library (NTGS) for access to McArthur Basin drill cores. JJB and NW thank McArthur River Mining Pty Ltd for their support of this study and, in particular, Christopher Hy and Ed Morris for facilitating sample collection. We are grateful to two anonymous reviewers and Marcus Kunzmann for their helpful comments. This research was financially supported by Australian Research Council grants DP160100607 and DP170100556 (to JJB). GV acknowledges support from an Australian Government Research Training Program (RTP) Scholarship. AJMJ publishes with permission of the CEO, Geoscience Australia. The authors declare no conflicting interests, financial or otherwise.

References

Ahmad, M., Dunster, J. N., & Munson, T. J. (2013). Chapter 15: McArthur Basin: in Ahmad M and Munson TJ (compilers).'. *Geology and mineral resources of the Northern Territory'. Northern Territory Geological Survey, Special Publication, 5*.

Baskin, D. K. (1997). Atomic H/C ratio of kerogen as an estimate of thermal maturity and organic matter conversion. *AAPG Bulletin, 81*(9), 1437-1450.

Blaikie, T., & Kunzmann, M. (2020). Geophysical interpretation and tectonic synthesis of the Proterozoic southern McArthur Basin, northern Australia. *Precambrian Research, 343*, 105728.

Boreham, C., Crick, I., & Powell, T. (1988). Alternative calibration of the Methylphenanthrene Index against vitrinite reflectance: Application to maturity measurements on oils and sediments. *Organic geochemistry, 12*(3), 289-294.

Brocks, J. J., Buick, R., Logan, G. A., & Summons, R. E. (2003). Composition and syngeneity of molecular fossils from the 2.78 to 2.45 billion-year-old Mount Bruce Supergroup, Pilbara Craton, Western Australia. *Geochimica et Cosmochimica Acta, 67*(22), 4289-4319.

Brocks, J. J., Grosjean, E., & Logan, G. A. (2008). Assessing biomarker syngeneity using branched alkanes with quaternary carbon (BAQCs) and other plastic contaminants. *Geochimica et Cosmochimica Acta, 72*(3), 871-888.

Brocks, J. J., Love, G. D., Summons, R. E., Knoll, A. H., Logan, G. A., & Bowden, S. A. (2005). Biomarker evidence for green and purple sulphur bacteria in a stratified Palaeoproterozoic sea. *Nature, 437*, 866. doi:10.1038/nature04068

Brocks, J. J., & Schaeffer, P. (2008). Okenane, a biomarker for purple sulfur bacteria (Chromatiaceae), and other new carotenoid derivatives from the 1640Ma Barney Creek Formation. *Geochimica et Cosmochimica Acta, 72*(5), 1396-1414. doi:10.1016/j.gca.2007.12.006

Bull, S. (1998). Sedimentology of the Palaeoproterozoic Barney Creek formation in DDH BMR McArthur 2, southern McArthur basin, northern territory. *Australian Journal of Earth Sciences, 45*(1), 21-31.

Chen, J., Fu, J., Sheng, G., Liu, D., & Zhang, J. (1996). Diamondoid hydrocarbon ratios: novel maturity indices for highly mature crude oils. *Organic geochemistry, 25*(3-4), 179-190.

Chen, J., Walter, M. R., Logan, G. A., Hinman, M. C., & Summons, R. E. (2003). The Paleoproterozoic McArthur River (HYC) Pb/Zn/Ag deposit of northern Australia: organic geochemistry and ore genesis. *Earth and Planetary Science Letters, 210*(3-4), 467-479. doi:10.1016/s0012-821x(03)00171-7

Crick, I. H. (1992). Petrological and maturation characteristics of organic matter from the Middle Proterozoic McArthur Basin, Australia. *Australian Journal of Earth Sciences, 39*(4), 501-519.

Eldridge, C., Williams, N., & Walshe, J. L. (1993). Sulfur isotope variability in sediment-hosted massive sulfide deposits as determined using the ion microprobe SHRIMP; II, A study of the HYC Deposit at McArthur River, Northern Territory, Australia. *Economic Geology, 88*(1), 1-26.

Greenwood, P. F., Brocks, J. J., Grice, K., Schwark, L., Jaraula, C. M. B., Dick, J. M., & Evans, K. A. (2013). Organic geochemistry and mineralogy. I. Characterisation

of organic matter associated with metal deposits. *Ore Geology Reviews, 50*, 1-27. doi:10.1016/j.oregeorev.2012.10.004

Ireland, T., Large, R. R., McGoldrick, P., & Blake, M. (2004). Spatial distribution patterns of sulfur isotopes, nodular carbonate, and ore textures in the McArthur River (HYC) Zn-Pb-Ag deposit, Northern Territory, Australia. *Economic Geology, 99*(8), 1687-1709.

Jackson, M., Muir, M. D., & Plumb, K. A. (1987). *Geology of the southern McArthur Basin, Northern Territory* (Vol. 220): Australian Government Publishing Service.

Jarrett, A., Cox, G., Southby, C., Hong, Z., Palatty, P., Carr, L., & Henson, P. (2018). Source rock geochemistry of the McArthur Basin, northern Australia: Rock-Eval pyrolysis data release. Record 2018/024. *Geoscience Australia, Canberra*.

Jarrett, A. J. M., Schinteie, R., Hope, J. M., & Brocks, J. J. (2013). Micro-ablation, a new technique to remove drilling fluids and other contaminants from fragmented and fissile rock material. *Organic geochemistry, 61*, 57-65. doi:10.1016/j.orggeochem.2013.06.005

Kawka, O. E., & Simoneit, B. R. (1990). Polycyclic aromatic hydrocarbons in hydrothermal petroleums from the Guaymas Basin spreading center. *Applied Geochemistry, 5*(1-2), 17-27.

Kunzmann, M., Schmid, S., Blaikie, T. N., & Halverson, G. P. (2019). Facies analysis, sequence stratigraphy, and carbon isotope chemostratigraphy of a classic Zn-Pb host succession: The Proterozoic middle McArthur Group, McArthur Basin, Australia. *Ore Geology Reviews, 106*, 150-175.

Kvalheim, O. M., Christy, A. A., Telnæs, N., & Bjørseth, A. (1987). Maturity determination of organic matter in coals using the methylphenanthrene distribution. *Geochimica et Cosmochimica Acta, 51*(7), 1883-1888.

Large, R., Bull, S., Selley, D., Yang, J., Cooke, D., Garven, G., & McGoldrick, P. (2002). Controls on the formation of giant stratiform sediment-hosted Zn-Pb-Ag deposits: with particular reference to the north Australian Proterozoic. *University of Tasmania, Centre for Special Ore Deposit and Exploration (CODES) Studies Publication, 4*, 107-149.

Large, R. R., Bull, S. W., Cooke, D. R., & McGoldrick, P. J. (1998). A genetic model for the HYC Deposit, Australia; based on regional sedimentology, geochemistry, and sulfide-sediment relationships. *Economic Geology, 93*(8), 1345-1368.

Large, R. R., Bull, S. W., & Winefield, P. R. (2001). Carbon and oxygen isotope halo in carbonates related to the McArthur River (HYC) Zn-Pb-Ag deposit, north Australia: Implications for sedimentation, ore genesis, and mineral exploration. *Economic Geology, 96*(7), 1567-1593.

Logan, G. A., Hinman, M. C., Walter, M. R., & Summons, R. E. (2001). Biogeochemistry of the 1640 Ma McArthur River (HYC) lead-zinc ore and host sediments, Northern Territory, Australia. *Geochimica et Cosmochimica Acta, 65*(14), 2317-2336. doi:https://doi.org/10.1016/S0016-7037(01)00599-3

Magnall, J. M., Gleeson, S., Hayward, N., & Rocholl, A. (2020). Massive sulfide Zn deposits in the Proterozoic did not require euxinia. *Geochemical Perspectives Letters, 13*, 19-24.

McGoldrick, P., Winefield, P., Bull, S., Selley, D., & Scott, R. (2010). Sequences, synsedimentary structures, and sub-basins: the where and when of SEDEX zinc systems in the southern McArthur Basin, Australia. *Soc. Econ. Geol. Spec. Publ, 15*, 1-23.

Munson, T. (2014). *Petroleum geology and potential of the onshore Northern Territory, 2014*: Northern Territory Geological Survey.

Oehler, J. H. (1977). Microflora of the HYC pyritic shale member of the Barney Creek Formation (McArthur Group), middle Proterozoic of northern Australia. *Alcheringa, 1*(3), 315-349.

Page, R. W., & Sweet, I. P. (1998). Geochronology of basin phases in the western Mt Isa Inlier, and correlation with the McArthur Basin. *Australian Journal of Earth Sciences, 45*(2), 219-232. doi:10.1080/08120099808728383

Pawlowska, M. M., Butterfield, N. J., & Brocks, J. J. (2013). Lipid taphonomy in the Proterozoic and the effect of microbial mats on biomarker preservation. *Geology, 41*(2), 103-106. doi:10.1130/g33525.1

Radke, M. (1988). Application of aromatic compounds as maturity indicators in source rocks and crude oils. *Marine and Petroleum Geology, 5*(3), 224-236.

Radke, M., & Welte, D. H. (1983). The methylphenanthrene index (MPI): a maturity parameter based on aromatic hydrocarbons. *Advances Organic Geochemistry 1981*, 504-512.

Simoneit, B. R. (1994). Lipid/bitumen maturation by hydrothermal activity in sediments of Middle Valley, Leg 139.

Spinks, S. C., Pearce, M. A., Liu, W., Kunzmann, M., Ryan, C. G., Moorhead, G. F., . . . Schaubs, P. M. (2020). Carbonate Replacement as the Principal Ore Formation Process in the Proterozoic McArthur River (HYC) Sediment-Hosted Zn-Pb Deposit, Australia. *Economic Geology*.

Summons, R. E., Powell, T. G., & Boreham, C. J. (1988). Petroleum geology and geochemistry of the Middle Proterozoic McArthur Basin, Northern Australia: III. Composition of extractable hydrocarbons. *Geochimica et Cosmochimica Acta, 52*(7), 1747-1763. doi:https://doi.org/10.1016/0016-7037(88)90001-4

Symons, D. (2007). Paleomagnetism of the HYC Zn-Pb SEDEX Deposit, Australia: evidence of an epigenetic origin. *Economic Geology, 102*(7), 1295-1310.

Tang, Y., Huang, Y., Ellis, G. S., Wang, Y., Kralert, P. G., Gillaizeau, B., . . . Hwang, R. (2005). A kinetic model for thermally induced hydrogen and carbon isotope fractionation of individual n-alkanes in crude oil. *Geochimica et Cosmochimica Acta, 69*(18), 4505-4520. doi:10.1016/j.gca.2004.12.026

Vinnichenko, G., Jarrett, A. J., van Maldegem, L. M., & Brocks, J. J. (2021). Substantial maturity influence on carbon and hydrogen isotopic composition of n-alkanes in sedimentary rocks. *Organic geochemistry, 152*, 104171.

Vinnichenko, G., Jarrett, A. J. M., Hope, J. M., & Brocks, J. J. (2020). Discovery of the oldest known biomarkers provides evidence for phototrophic bacteria in the 1.73 Ga Wollogorang Formation, Australia. *Geobiology, 18*(5), 544-559. doi:10.1111/gbi.12390

Williford, K. H., Grice, K., Logan, G. A., Chen, J., & Huston, D. (2011). The molecular and isotopic effects of hydrothermal alteration of organic matter in the Paleoproterozoic McArthur River Pb/Zn/Ag ore deposit. *Earth and Planetary Science Letters, 301*(1-2), 382-392. doi:10.1016/j.epsl.2010.11.029

Chapter 7

Discovery of the oldest known biomarkers provides evidence for phototrophic bacteria in the 1.73 Ga Wollogorang Formation, Australia

Galina Vinnichenko, Amber J.M. Jarrett, Janet M. Hope, Jochen J. Brocks

Geobiology, 18(5), 2020

Abstract

The discovery of mid-Proterozoic (1.8 – 0.8 billion years ago, Ga) indigenous biomarkers is a challenge, since biologically informative molecules of such antiquity are commonly destroyed by metamorphism or overprinted by drilling fluids and other anthropogenic petroleum products. Previously, the oldest clearly indigenous biomarkers were reported from the 1.64 Ga Barney Creek Formation in the northern Australian McArthur Basin. In this study, we present the discovery of biomarker molecules from carbonaceous shales of the 1.73 Ga Wollogorang Formation in the southern McArthur Basin, extending the biomarker record back in time by ~90 million years. The extracted hydrocarbons illustrate typical mid-Proterozoic signatures with a large unresolved complex mixture, high methyl-alkane/*n*-alkane ratios and absence of eukaryotic steranes. Acyclic isoprenoids, saturated carotenoid derivatives, bacterial hopanes and aromatic hopanoids and steroids also were below detection limits. However, continuous homologous series of low molecular weight C_{14}–C_{19} 2,3,4- and 2,3,6-trimethyl aryl isoprenoids (AI) were identified, and C_{20}–C_{22} AI homologs were tentatively identified. Based on elevated abundances relative to abiogenic isomers, we interpret the 2,3,6-AI isomer series as biogenic molecules, and the 2,3,4-AI series as possibly biogenic. The biological sources for the 2,3,6-AI series include carotenoids of cyanobacteria and/or green sulphur bacteria (Chlorobiaceae). The lower concentrated 2,3,4-AI series may be derived from purple sulphur bacteria (Chromatiaceae). These degradation products of carotenoids are the oldest known clearly indigenous molecules of likely biogenic origin.

Keywords

Molecular fossils, aryl isoprenoids, Chromatiaceae, Chlorobiaceae, McArthur Basin, mid-Proterozoic

7.1 Introduction

The mid-Proterozoic interval is characterised by apparent stable environmental conditions with few remarkable changes in the chemistry of the oceans and atmosphere (Holland, 2006). While marine surface waters were mildly oxygenated, the ocean interior remained dominantly anoxic and ferruginous, and continental margins and slope settings experienced occasional sulphidic (euxinic) conditions (Canfield, 1998; Johnston et al., 2010; Lyons et al., 2014; Planavsky et al., 2011; Poulton & Canfield, 2011; Poulton et al., 2010). In the past few decades, microfossil studies have greatly advanced our knowledge of the mid-Proterozoic biosphere (e.g. Knoll & Nowak, 2017; Beghin et al., 2017; Butterfield & Smith, 2015), including the discovery of the oldest-known microfossil of probable eukaryotic origin in the 1.67 Ga Changzhougou Formation, China (Lamb et al., 2009; Li et al., 2013) and of the first alga, the rhodophyte *Bangiomorpha* from 1.05 Ga silicified carbonates in Arctic Canada (Butterfield, 2000; Gibson et al., 2017). However, as most microfossils lack diagnostic characteristics, reconstruction of marine community structures based on fossils alone remains problematic. Hydrocarbon biomarkers represent a complementary source of information for ancient ecosystems for which body fossil are scarce. Based on molecular fossils, mid-Proterozoic marine ecosystems were dominated by bacteria (Blumenberg et al., 2012; Brocks et al., 2005; Gueneli et al., 2018; Jarrett et al., 2019; Luo et al., 2015; Luo et al., 2016; Nguyen et al., 2019; Pawlowska et al., 2013), while biomarkers diagnostic for eukaryotic life only become detectable around 0.8 Ga ago (Brocks et al., 2016; Brocks et al., 2017; Hoshino et al., 2017). Currently, the oldest known clearly indigenous lipid biomarkers come from the 1.64 Ga Barney Creek Formation (BCF) of the McArthur Group in the northern Australian McArthur Basin (Figure 7.1a). The lack of saturated diagnostic eukaryotic steranes and prevalence of bacterial hopanes and aromatic carotenoids in the BCF indicate a marine ecosystem

dominated by bacteria (Brocks et al., 2005). Discovering older biologically informative molecules is a challenge, as most Paleoproterozoic sedimentary sequences have suffered burial metamorphism. Even relatively mild thermal alteration beneath prehnite-pumpellyite facies is incompatible with the preservation of biomarkers (French et al., 2015). The recognition of indigenous biomarkers in mid-Proterozoic rocks is also often affected by overprint with contaminants from drilling fluids and other anthropogenic petroleum products (Brocks et al., 2008). Worldwide, there are currently only 6 geological sequences ≥ 1.0 Ga that yield demonstrably indigenous biomarkers: the 1.0 Ga Nonesuch Formation (Gueneli, 2016), 1.1 Ga El Mreïti Group (Blumenberg et al., 2012; Gueneli et al., 2018), 1.38 Ga Xiamaling Formation (Luo et al., 2015), 1.38 Ga Roper Group (Jarrett et al., 2019; Nguyen et al., 2019), 1.4 Ga Hongshuizhuang Formation (Luo et al., 2016), and the aforementioned 1.64 Ga BCF (Brocks et al., 2005). In this study, we aim to extend the biomarker record back in time by investigating carbonaceous shales of the 1.73 Ga Wollogorang Formation (Fm) of the Tawallah Group, which unconformably underlies the McArthur Group in the southern McArthur Basin.

7.2 Geological setting and samples

The Paleoproterozoic-Mesoproterozoic McArthur Basin in northern Australia contains a 10–12 km thick succession of carbonates, siliciclastics and some volcanics (Ahmad et al., 2013). In the southern part of the basin, the stratigraphy is subdivided into four major groups, in stratigraphic order the Tawallah, McArthur, Nathan and Roper groups (Figure 7.1b) (Jackson et al., 1987). The lowermost Tawallah Group (~1850 to ~1715 Ma) consists of shallow marine to fluvial sandstones with minor carbonates and shales and rare volcanic rocks intercalated with the sediments (Rawlings, 1999). The

Wollogorang Fm is located in the middle of the Tawallah Group and comprises a 160 m thick dolostone, sandstone and mudstone succession (Ahmad et al., 2013). The upper sandstone-rich part of the formation appears be separated from the underlying dolostone-shale section by a sequence boundary (Page et al., 2000). Tuffaceous beds from black shales below the suspected sequence boundary provide ages of 1730 ± 3 Ma and 1729 ± 4 Ma using the U-Pb zircon method, whereas a tuff sample from the overlying sandstone is dated at 1723 ± 4 Ma (Page et al., 2000). The Wollogorang Fm was deposited in shallow marine to near-shore environments under predominantly euxinic conditions (Spinks et al., 2016). Organic-rich beds have been described in the Wollogorang Fm previously with up to 6% total organic carbon (TOC) content (Munson, 2014). Generally, the thermal maturity of the formation is affected by the Settlement Creek Dolerite, a sill that intruded the formation at its base, and overlying Gold Creek Volcanics. However, regional coverage of Gold Creek Volcanics is sporadic and there are areas where the Wollogorang Fm is overlain by the Warramana Sandstone.

Nine Wollogorang Fm samples were selected for organic geochemical analysis from two open source drill cores, 14MCDDH001 and 14MCDDH002 (Figure 7.1a). These stratigraphic diamond cores were drilled in the southern McArthur Basin in 2014 by Enigma Mining Limited and stored at the Northern Territory Geological Survey (NTGS) core library in Darwin, Australia.

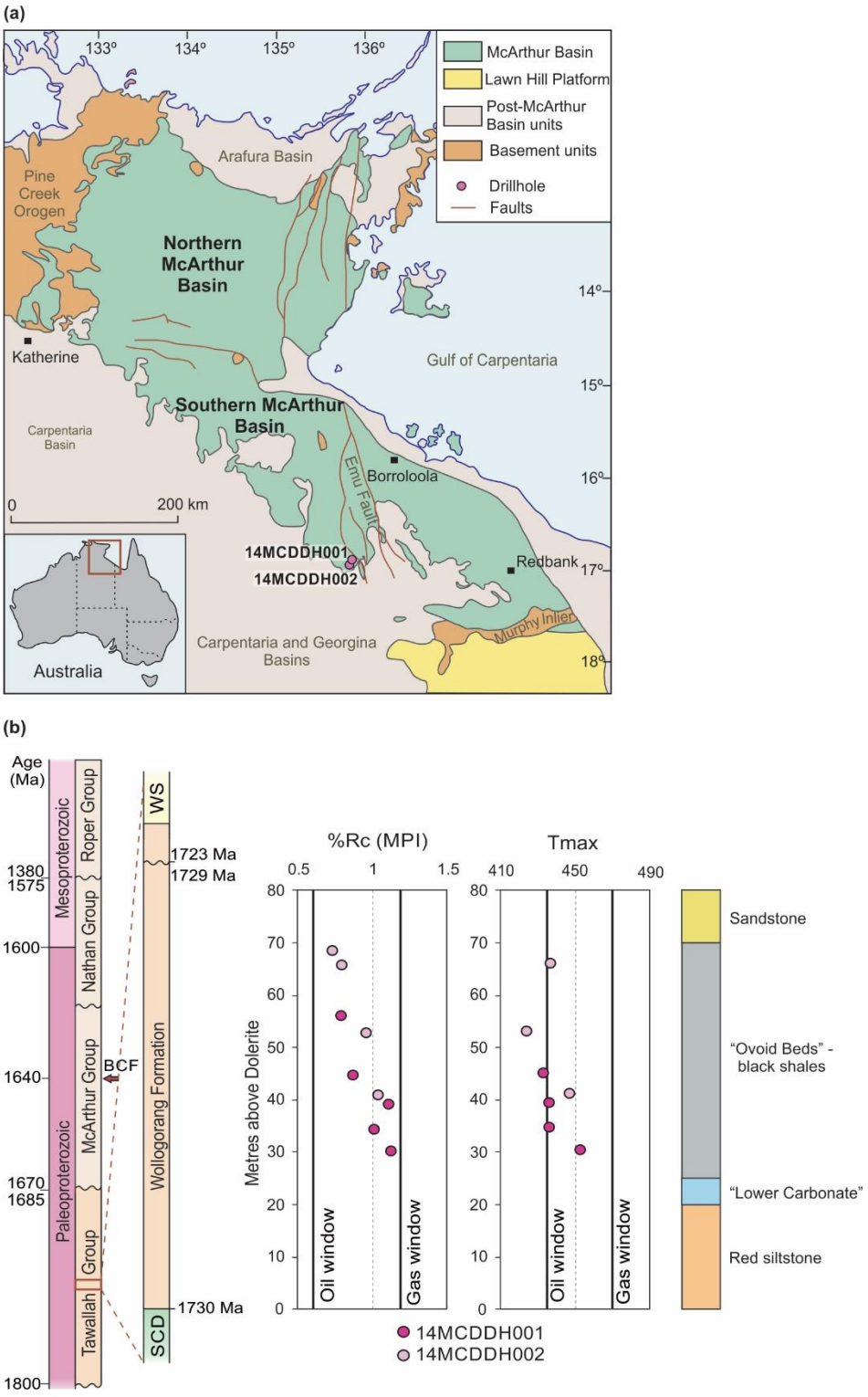

Figure 7.1. (a) McArthur Basin in northern Australia with location of drill cores investigated in this study (modified after Ahmad et al. (2013)); (b) simplified stratigraphy of the southern McArthur Basin, calculated vitrinite reflectance Rc(MPI) and Tmax for two drill cores intersecting the Wollogorang Fm and lithology column. Oil window: Rc between 0.6 – 1.2%, Tmax between 435 – 470ºC. BCF: Barney Creek Formation; WS: Warramana Sandstone; SCD: Settlement Creek Dolerite; ages for the Wollogorang Formation are from Page et al. (2000).

The two drill holes intersected 94 and 110 m of the Wollogorang Fm, directly overlain by the Warramana Sandstone. Absence of the Gold Creek Volcanics may be responsible for the good thermal preservation of the underlying black shales. Based on the drilling report (Wetherley, 2014), the Wollogorang Fm is represented by 20 – 25 m of red siltstone at its base, 4 – 12 m of "Lower Carbonate" sequence, 36 m of black shales with carbonate nodules, the so called "Ovoid Beds", and 22 – 49 m of Upper Sandstone facies (Figure 7.1b). For the current study, samples were collected from the black shales of the "Ovoid Beds" that fall into the lower half of the Wollogorang Fm with an age of 1730 Ma. Kerogen atomic H/C ratios of three black shale samples from the current study were available on the NTGS database. Two samples from 14MCDDH001 have H/C ratios of 0.67 and 0.78 and one sample from 14MCDDH002 yields 0.73 (Table 7.2). Additionally, we included solid bitumen reflectance values available on the NTGS database for equivalents of samples #6 and #7 of this study (14MCDDH002, 96.0–96.1 m depth and 14MCDDH001, 70.5–70.58 m depth respectively). The lowermost ~30 m of the Wollogorang Fm were not suitable for biomarker analyses as they displayed an oxidized red colouration and are strongly affected by the heat aureole of the underlying Settlement Creek Dolerite.

7.3 Methods

Protocols and methods for contamination-free biomarker analysis were described in detail by Brocks et al. (2017). In order to evaluate laboratory contaminants, cumulative laboratory system blanks were analysed. These blanks captured the whole sequence of procedures from rock crushing, solvent extraction, column chromatography to instrumental analyses. To evaluate and remove contaminants that may have been introduced to rock specimens during drilling and storage, ~3 mm of all external surfaces

were removed using a solvent-cleaned wet table saw (Nortel Machinery Inc.). The exterior (E) and interior (I) rock portions were ground to a < 240-mesh powder using a clean Rocklabs iron puck mill. Bitumen was extracted from E and I rock powders with a Dionex Accelerated Solvent Extractor (ASE 200) using 90% DCM and 10% methanol. Extracts were fractionated into saturated, aromatic, and polar fractions using microcolumn (pasteur pipette) chromatography over annealed and dry-packed silica gel (7 cm). Saturated hydrocarbons were eluted with 1.5 ml of *n*-hexane, aromatic hydrocarbons with 4 ml of *n*-hexane:DCM (1:1 v/v) and polar hydrocarbons with 3 ml of DCM:methanol (1:1 v/v). Gas chromatography-mass spectrometry (GC–MS) analyses were carried out on an Agilent 6890 GC coupled to a Micromass Autospec Premier double sector MS. The GC was equipped with a 60 m DB-5MS capillary column and used helium (1 ml/min constant flow) as the carrier gas. Additionally, a 60 m VF-200MS capillary column was used to confirm elution positions of aryl isoprenoids with the same flow rate and carrier gas. Full Scan (FS) analyses were performed for saturated and aromatic fractions. Concentrations of *n*-alkanes were determined by integration of GC-MS *m/z* 85 signals. Hopanes and steranes were quantified using Metastable Reaction Monitoring (MRM) in $M^+ \rightarrow 191$ and $M^+ \rightarrow 217$ precursor–product transitions respectively. Trimethyl aryl isoprenoids (AI) were analysed by MRM using $M^+ \rightarrow 134$ transitions with a cycle time of ~430 ms and identified by comparison with elution positions in bitumens of the 1.64 Ga BCF (Brocks & Schaeffer, 2008) on two different capillary columns, DB-5MS and VF-200MS. Additionally, the AI isomers were compared with authentic chemical standards of C_{14} 2,3,4-, 2,3,6-, 2,3,5-, 2,4,5- and 2,4,6-AI, kindly provided by Roger Summons (Summons & Powell, 1987). The 3,4,5-AI series (e.g. Clifford et al., 1998) was identified by comparison with bitumens of the Ordovician Utica Shale. The trimethyl alkyl benzene (TMAB) isomers were tentatively identified by comparison with

chromatographic m/z 176 → 134 signals in bitumen reference standards rich in aromatic carotenoids (2,3,6- and 2,3,4-TMAB in the BCF; 3,4,5-TMAB in the Utica Shale).

Stable carbon and hydrogen isotopic compositions of *n*-alkanes were analysed as duplicates using gas chromatography-isotopic ratio mass spectroscopy (GC-IRMS) at Geoscience Australia (Jarrett et al., 2019). *n*-Alkanes were separated from the saturated fraction using 0.5 mg of 5 Å zeolite molecular sieve (Grace Davison) in cyclohexane. The sieve was digested in HF (32%, 3 ml) to release the *n*-alkanes, which further were extracted with 3 ml *n*-hexane. All $\delta^{13}C$ and δD values are reported in permil (‰) notation relative to VPDB and VSMOW respectively. The average standard deviation of individual compounds was 0.12‰ for $\delta^{13}C$ and 1.7‰ for δD.

Total organic carbon (TOC) content and hydrocarbon potential were measured for all interior rock samples using a Source Rock Analyzer (SRA) TPH-TOC Workstation (Weatherford Laboratories) at the University of Adelaide.

7.4 Results

7.4.1 Programmed pyrolysis data

The results of programmed pyrolysis for the interior of Wollogorang Fm samples are summarized in Table 7.1. The TOC content ranges from 0.55% to 8.63% with an average of 2.7% and indicates a fair to excellent source rock potential. Hydrogen index (HI) values vary from 16 to 138 mg HC/g TOC. However, HI is probably underestimated in the samples with low TOC due to mineral matrix effects (Dahl et al., 2004). Production index (PI) values around 0.1 suggests immature organic matter and absence of migrated hydrocarbons or drilling fluid contaminants in the interior rock powders (Peters, 1986). Tmax measurements for samples #1 and #3 are unreliable due to low S2 peak (S2 < 0.2). In the other seven samples, Tmax ranges from 424ºC to 453ºC and suggests a downcore

maturity trend from immaturity to the main oil window, albeit with considerable scatter (Figure 7.1b).

Table 7.1. Programmed pyrolysis parameters for Wollogorang Formation samples.

Sample ID	Relative depth (m)[a]	Drill core[b]	Depth (m)	TOC (%wt)[c]	S2[d]	Tmax[e] (°C)	HI[f]	PI[g]	Rc (Tmax)[h]
#1	68.85	2	72.15	0.55	0.09	n.d.	16	0.1	n.d
#2	66.0	2	75.0	0.61	0.20	437	33	0.09	0.71
#3	56.48	1	53.52	0.68	0.13	n.d.	19	0.07	n.d.
#4	53.1	2	87.9	1.41	1.37	424	97	0.12	0.47
#5	45.0	1	65.0	2.79	3.86	433	138	0.07	0.64
#6	41.25	2	99.75	8.63	11.6	447	135	0.05	0.89
#7	39.4	1	70.6	2.02	1.59	436	79	0.12	0.69
#8	34.6	1	75.4	2.13	1.77	436	83	0.13	0.68
#9	30.3	1	79.7	5.69	5.18	453	91	0.06	0.99

[a]Depth in meters above the top of the Settlement Creek Dolerite. [b]Drill core 1: 14MCDDH001; 2: 14MCDDH002. [c]Total Organic Carbon. [d]Generative potential, mg HC/g rock. [e]Temperature at maximum of S2 peak. [f]Hydrogen index HI = S2*100/TOC, mg HC/g TOC. [g]Production index PI = S1/(S1+S2), where S1 represents volatile hydrocarbons. [h]Calculated vitrinite reflectance Rc(Tmax) = 0.0180*Tmax – 7.16 (Jarvie et al., 2001). n.d. – low S2, Tmax is unreliable.

7.4.2 Syngeneity of biomarkers

Biomarkers remained below detection limits in the cumulative laboratory blanks that were run alongside two batches of samples. The syngeneity of biomarkers was further assessed using exterior/interior (E/I) experiments, which involve comparison of absolute concentrations of individual compounds in the outer 3 mm of each rock sample (E) with the interior portion (I). These experiments provide information about surficial contamination levels and the presence of indigenous hydrocarbons. Generally, the presence of surface contamination is recognised by $E/I >> 1$, while $E/I \approx 1$ commonly indicates indigenous hydrocarbons and $E/I < 1$ evaporation from surfaces or during solvent removal from hydrocarbon extracts. An interpretation of different E/I patterns is given in Brocks et al. (2008) and Jarrett et al. (2013).

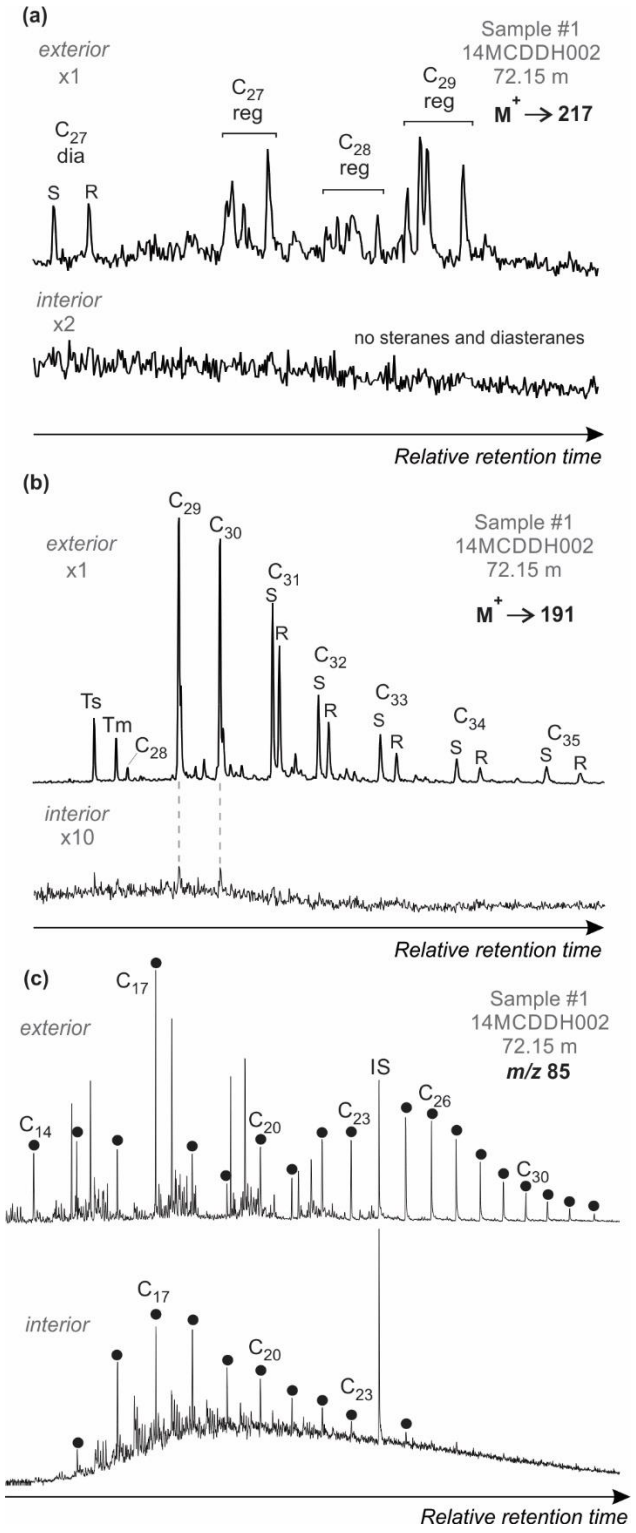

Figure 7.2. Chromatograms illustrating the results of exterior/interior experiments on sample #1, 72.15 m depth from drill core 14MCDDH002. (a) Summed $M^+ \rightarrow 217$ MRM chromatogram showing sterane distribution. (b) Summed $M^+ \rightarrow 191$ MRM chromatogram showing hopane distribution. (c) Partial *m/z* 85 chromatogram highlighting the distribution of *n*-alkanes. 'x10' indicates that interior chromatogram has been magnified by a factor of 10 relative to extract yields per gram of rock.

Figure 7.2 juxtaposes the distribution of steranes, hopanes and *n*-alkanes in the interior and exterior fractions of sample #1 (14MCDDH002, 72.15 m depth). Steranes were only detectable in the exterior parts of all samples and are thus considered contaminants (Figure 7.2a). The exteriors of all samples also contained relatively high concentrations of hopanes (Figure 7.2b). However, in the interiors, hopanes were generally below detection limits with the exception of sample #1 where traces of C_{29} and C_{30} hopanes were visible (Figure 7.2b). As the concentration of individual hopanes in the exterior of sample #1 was ~100 times higher than in the interior (E/I ≈100), it is possible that some hopanes permeated into the rock interior from its surfaces. Erring on the side of caution, we do not interpret these hopanes as indigenous. Six samples showed indigenous distributions of *n*-alkanes in exterior and interior portions with E/I ≈ 1, for instance sample #7 (14MCDDH001. 70.6 m depth) shown in Figure 7.3b with E/I = 0.74 – 1.05. *n*-Alkanes on the exteriors of the remaining 3 samples were contaminated (Figure 7.2c, 7.3a). Figure 7.3a represents sample #1 with E/I ranging from 3.5 to 86. Overall, Figure 7.2 indicates that the E/I experiments were very efficient in the removal of surficial contaminants and the interior portions of the samples remained largely unaffected.

Figure 7.3c summarizes the results of the E/I experiment for aryl isoprenoids (AI) for sample #7, with E/I = 0.84 – 1.24 in the range $C_{13–22}$, and sample #1 with E/I = 0.84 – 1.57 in the range $C_{15–22}$. The two elevated E/I data points of sample #1, E/I = 7.6 and 4.5 for the C_{14} 2,3,6- and 2,3,4-AI isomers respectively, can be explained by evaporation of these low molecular weight compounds from the interior fraction during solvent removal. The AI were generally considered indigenous, since E/I values were close to 1 in clean samples (#7) but also in surficially contaminated samples (#1), indicating that the surficial contaminants did not include AI. In the following we only discuss hydrocarbons that are clearly indigenous based on these E/I criteria.

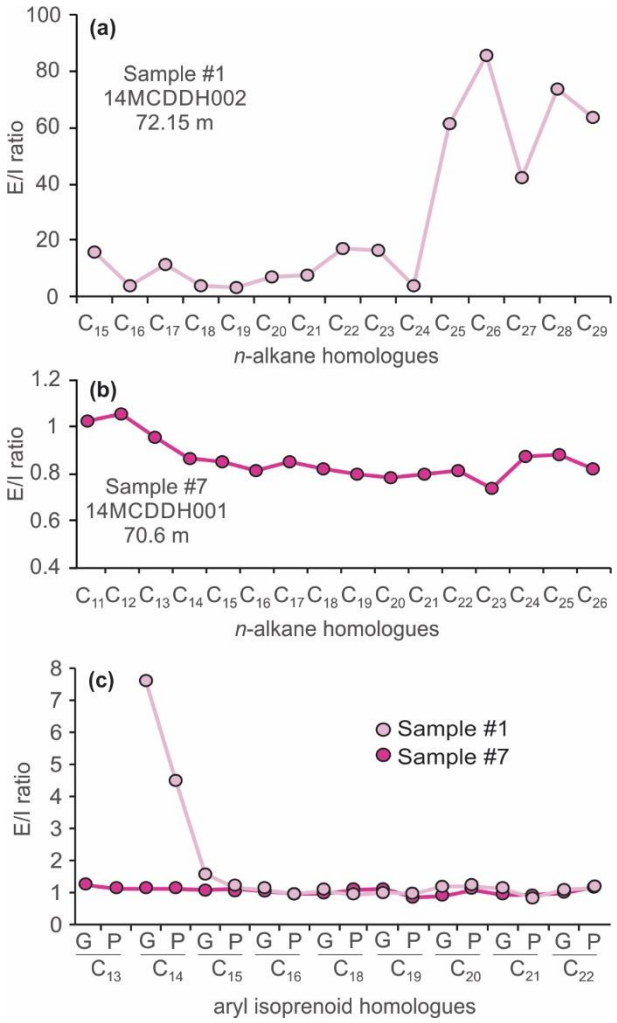

Figure 7.3. Exterior/interior (E/I) ratios of *n*-alkane homologues for (a) sample #1, 72.15 m depth from drill core 14MCDDH002 and (b) sample #7, 70.6 m depth from drill core 14MCDDH001. (c) E/I ratios of aryl isoprenoid (AI) homologues for samples #1 and #7. G: 2,3,6-AI; P: 2,3,4-AI.

7.4.3 General biomarker distribution and thermal maturity

GC-MS analyses of the interior fractions illustrate typical indigenous mid-Proterozoic hydrocarbon distributions, including a large unresolved complex mixture (UCM) relative to *n*-alkane signal heights, and high methyl-alkane/*n*-alkane ratios (Figure 7.2c, 7.4a) (Pawlowska et al., 2013). Saturated fractions contain unimodal distribution of *n*-alkanes ranging from C_{10} to C_{28} with a maximum at C_{13} to C_{17} (Figure 7.4a). Clearly indigenous acyclic isoprenoids, saturated carotenoid derivatives, tri- and tetra cyclic

terpanes, hopanes, and steranes were not observed in any sample. Diamondoids were present in some samples in trace amounts, but were too low to calculate maturity ratios. The aromatic hydrocarbon fraction was dominated by parent and methylated naphthalenes and phenanthrenes, as well as pyrene, chrysene and other polyaromatic hydrocarbons (Figure 7.4b). However, polycyclic aromatic compounds of known biological origin, such as benzohopanoids and aromatic steroids, were not detected.

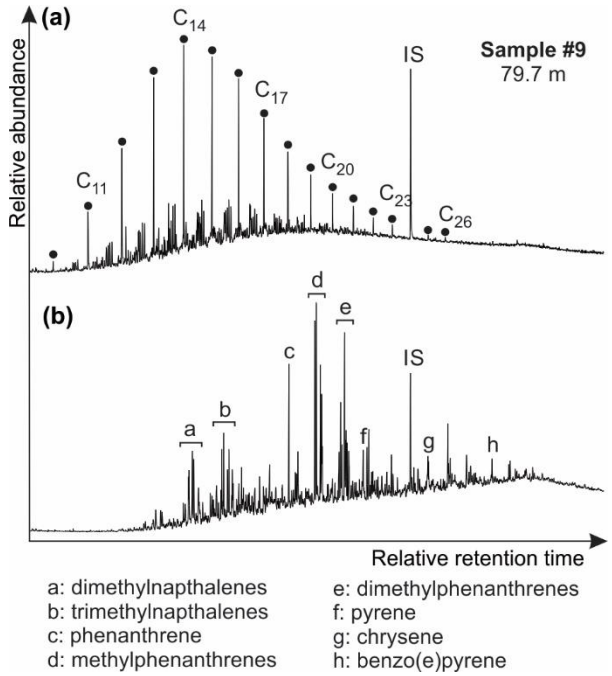

Figure 7.4. Total ion chromatograms of (a) saturated and (b) aromatic hydrocarbon fractions from sample #9, drill core 14MCDDH001, 79.7 m depth. Black circles represent *n*-alkanes, IS: internal standard.

The thermal maturity of the Wollogorang bitumens was estimated using the trimethylnaphthlene ratio (TNR) and the methyl phenanthrene based parameters MPI, MPR and MPDF (Alexander et al., 1985; Kvalheim et al., 1987; Radke, 1988; Radke & Welte, 1983) (Table 7.2). Figure 7.1b plots calculated vitrinite reflectance values Rc(MPI) relative to the distance from the top of the Settlement Creek Dolerite. The data reveals a maturity trend that ranges from Rc = 0.7% 69 m above the dolerite sill to Rc = 1.1% 30 m above the intrusion. These values fall within the oil generation window (Table 7.2).

The steep increase in Rc by 0.4% over 39 metres suggests that maturation was caused by the heating aureole of the dolerite intrusion and not by burial.

7.4.4 Aryl isoprenoids

The breakdown products of aromatic carotenoids, aryl isoprenoids (AI) with 2,3,4- and 2,3,6-methylation patterns, are commonly identified in *m/z* 134 selected ion recording chromatograms. However, in thermally mature samples, AI may be difficult to detect due to low abundances and co-elution with straight chain trimethyl alkyl benzenes (TMAB) and other compounds (Jarrett et al., 2019). Therefore, to minimize co-elution, we identified AI using more selective MRM $M^+ \rightarrow 134$ transitions and compared elution positions with a BCF reference sample on two different capillary columns, DB-5MS and VF-200MS (Figure 7.5). The MRM chromatograms reveal a continuous series of signals in the correct elution positions on the DB-5MS column for C_{13} to C_{22} AI with 2,3,4- and 2,3,6-methylation patterns (Figure 7.5a). Higher molecular weight (C_{22+}) AI and intact C_{40} aromatic carotenoid derivatives were not detected. Clear signals were recorded for 2,3,4- and 2,3,6-AI in the range C_{13}–C_{19}, while 2,3,4-AI signals in the C_{20}–C_{22} range were partly or entirely obscured by co-elution. The MRM chromatograms on the VF-200MS column support the presence of AI and illustrate a series of 2,3,6-AI in the correct elution positions for C_{13} to C_{19} homologs; whereas clear signals of 2,3,4-AI were detected for C_{13}–C_{16} and C_{19}, with the C_{18} homolog masked by co-elution (Figure 7.5b). Starting from the C_{20} homolog, the peaks of the two series begin to merge on the VF-200MS column. Since concentrations of 2,3,6-AI are higher than 2,3,4-AI in the Wollogorang Fm, an additional BCF sample with equally predominant 2,3,6-AI (blue line) was added as a reference to the 274→134 and 302→134 chromatograms, showing that the 2,3,6-series

Table 7.2. Maturity parameters of Wollogorang Formation bitumens.

Sample ID	Relative depth (m)[a]	Drill core[b]	Depth (m)	MPI[c]	Rc (MPI)[d]	MPDF[e]	Rc (MPDF)[f]	MPR[g]	Rc (MPR)[h]	TNR[i]	H/C ratio[j]	Rb (%)[k]
#1	68.85	2	72.15	0.55	0.72	0.36	0.64	0.80	0.84	0.62		
#2	66.0	2	75.0	0.66	0.79	0.39	0.72	0.85	0.87	0.54		
#3	56.48	1	53.52	0.65	0.79	0.43	0.80	1.01	0.95	0.76		
#4	53.1	2	87.9	0.93	0.96	0.45	0.85	1.12	1.01	0.67		
#5	45.0	1	65.0	0.79	0.87	0.38	0.70	0.87	0.88	0.68	0.78	
#6	41.25	2	99.75	1.06	1.04	0.55	1.08	1.63	1.18	0.92	0.73	1.01–1.34
#7	39.4	1	70.6	1.18	1.11	0.51	0.97	1.34	1.09	0.84		0.95–1.25
#8	34.6	1	75.4	1.02	1.01	0.42	0.78	0.99	0.94	0.95		
#9	30.3	1	79.7	1.20	1.12	0.61	1.20	1.98	1.28	1.13	0.67	

[a]Depth in meters above the top of the Settlement Creek Dolerite. [b]Drill core 1: 14MCDDH001; 2: 14MCDDH002. [c]Methylphenanthrene index MPI-1 = 1.5*(2-MP+3-MP)/(P+1-MP+9-MP) (Radke & Welte, 1983). [d]Calculated vitrinite reflectance Rc(MPI-1) = 0.6*MPI-1+0.4 (Radke & Welte, 1983). [e]Methylphenanthrene distribution factor MPDF = (3-MP+2-MP)/(3-MP+2-MP+9-MP+1-MP) (Kvalheim et al., 1987). [f]Calculated vitrinite reflectance Rc(MPDF) = 2.242*MPDF - 0.166 (Kvalheim et al., 1987). [g]Methylphenanthrene ratio MPR = 2-MP/1-MP (Radke, 1988). [h]Calculated vitrinite reflectance Rc(MPR) = 1.1*$\log_{10}$(MPR)+0.95 (Radke, 1988). [i]Trimethylnaphthalene ratio TNR-1 = 2,3,6-TMN/(1,4,6-TMN+1,3,5-TMN) (Alexander et al., 1985). [j]Publicly available kerogen atomic H/C ratios (Northern Territory Geological Survey database). [k]Publicly available solid bitumen reflectance values for equivalents of samples #6 and #7 of this study (Northern Territory Geological Survey database).

elutes a little bit earlier than the 2,3,4-series (Figure 7.5b). Based on that observation, it was possible to confirm the presence of chromatographic signals for C_{20} 2,3,6-AI in the correct elution positions on the VF-200MS column. Additionally, Figure 7.5 demonstrates the distribution of C_{13}–C_{18} homologs of the 3,4,5-AI series, identified by comparison with Ordovician Utica Shale.

Figure 7.5 illustrates that on both columns the C_{13} homologs of 3,4,5-, 2,3,6- and 2,3,4-AI cannot be distinguished from the C_{13} 3,4,5-, 2,3,6- and 2,3,4-TMAB homologs (open circles in the 176→134 traces). This is expected as the C_{13} AI lack side-chain methylation and have the same hydrocarbon skeleton as the corresponding TMAB (i.e. they are the same compounds). By contrast, the C_{15} homolog of 2,3,4-AI that co-elutes with tentatively identified 3,4,5-TMAB on the DB-5MS column, is well resolved on the VF-200MS column. We also note that the signal intensity of C_{20} 2,3,4-AI relative to C_{20} 2,3,6-AI is unusually high on the DB-5MS column, revealing that C_{20} 2,3,4-AI is also affected by a co-eluting compound. Generally, when identifying AI, it is important to detect unbroken series of homologs as the apparent presence of individual isomers is meaningless, and to note that the C_{13} homologs are identical to TMAB and the C_{15} 2,3,4-AI co-elutes with 3,4,5-TMAB on DB-5MS capillary columns.

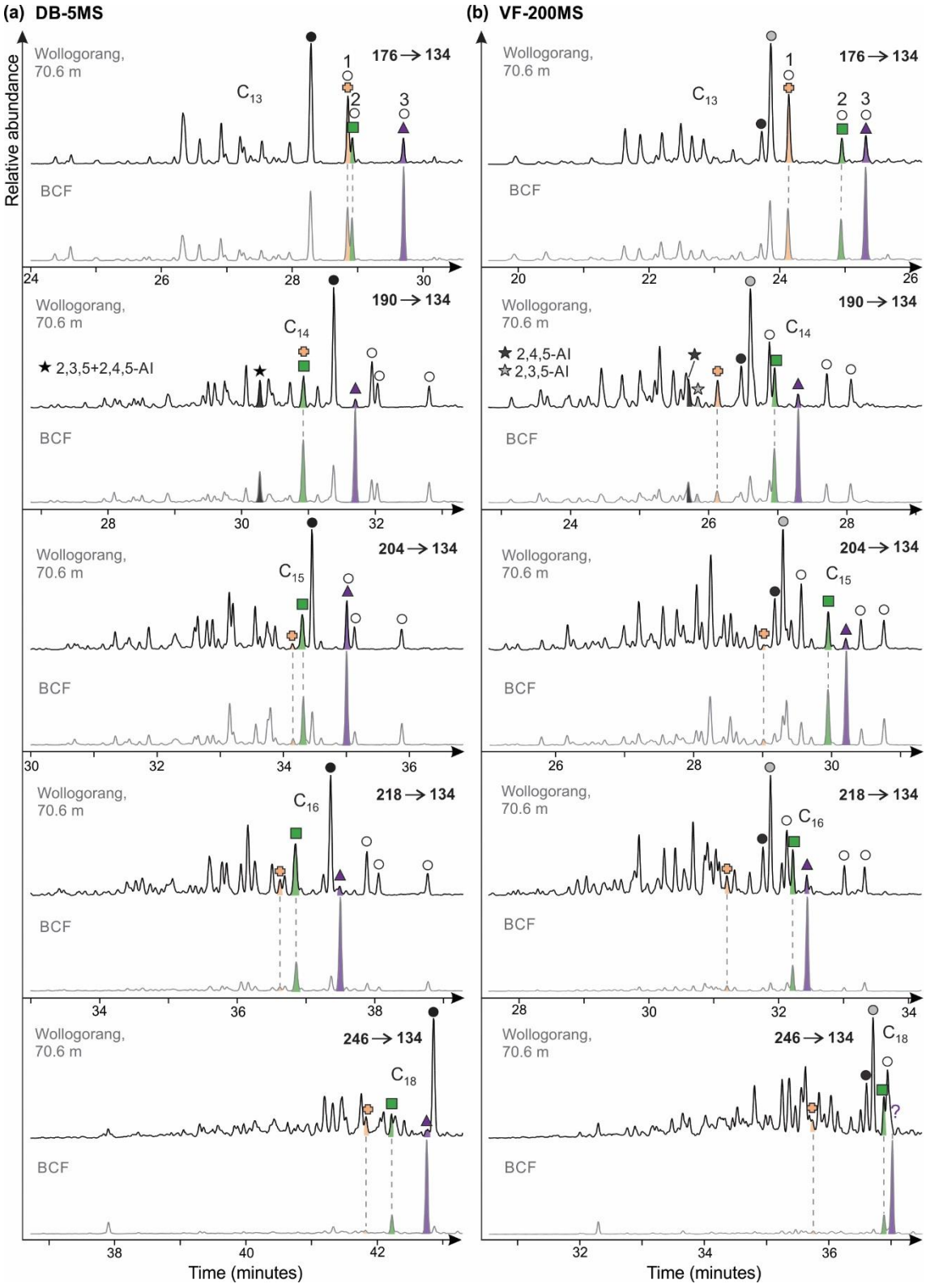
(a) DB-5MS
(b) VF-200MS
Relative abundance
Wollogorang, 70.6 m
176 → 134
190 → 134
204 → 134
218 → 134
246 → 134
C13
C14
C15
C16
C18
1
2
3
BCF
★ 2,3,5+2,4,5-AI
☆ 2,3,5-AI
★ 2,4,5-AI
?
Time (minutes)

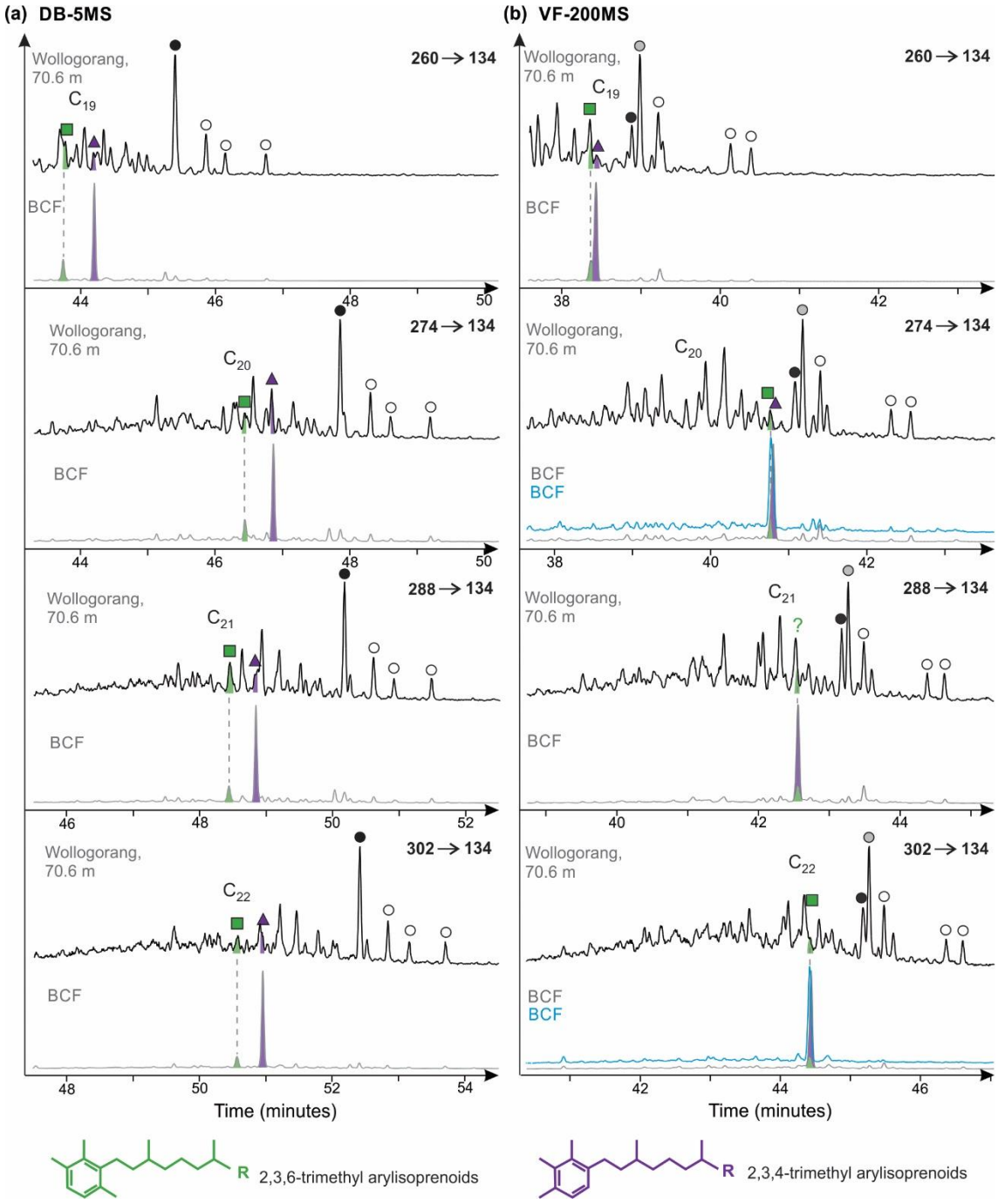

Figure 7.5. MRM chromatograms of $M^+ \rightarrow 134$ illustrating the aryl isoprenoid (AI) distribution of the Wollogorang Fm (drillcore 14MCDDH001, sample #7, 70.6 m) with a BCF reference sample on (a) DB-5MS and (b) VF-200MS capillary columns and chemical structures of the 2,3,6- and 2,3,4-AI. Additional BCF sample with predominance of 2,3,6-AI (blue line) is added to the 274→134 and 302→134 chromatograms. Orange crosses, green squares and purple triangles denote 3,4,5-AI, 2,3,6-AI and 2,3,4-AI respectively. The C_{14} homologs of 2,3,5- and 2,4,5-AI isomers are indicated in the 190→134 chromatograms (see Figure 7.6 for details). Solid circles indicate the trimethyl *n*-alkylbenzene (TMAB) series reported in Jarrett et al. (2019) (see Figure 7.6 for details); empty circles represent 3 additional TMAB isomer series (1 – 3,4,5-TMAB; 2 – 2,3,6-TMAB; 3 – 2,3,4-TMAB). These TMAB series are identified in

the current study by comparison with chromatographic m/z 176 → 134 signals in BCF and Utica Shale bitumen reference standards. The chromatogram of 232→134 is not shown due to low concentrations of C_{17} that represents a branching position. Sample #7 was selected for this figure due to its low thermal maturity (Tmax = 436ºC), reasonably high organic content (TOC = 2.02%), and clear AI peak resolutions for both 2,3,4- and 2,3,6-AI series.

Figure 7.6 compares the Wollogorang Fm and BCF extracts with C_{14} synthetic AI standards (Summons & Powell, 1987) on two capillary columns and demonstrates the presence of five AI isomers in the analyzed samples (2,3,5-, 2,4,5-, 3,4,5-, 2,3,6-, 2,3,4-AI). The sixth isomer, 2,4,6-AI, is generally not observed in *m/z* 190 → 134 traces due the absence of free *ortho* and *para* positions at the aryl-moiety, which are required to form the *m/z* 134 fragment. Thus, 2,4,6-AI isomers are not further discussed here. The 2,3,5- and 2,4,5-AI isomers co-elute on the DB-5MS column and are separated on the VF-200MS column (Figure 7.6). Pseudohomologues of the 3,4,5-AI series normally elute slightly to the left of 2,3,6-AI (Figure 7.5). However, the C_{14} homolog of the 3,4,5-AI series is an exception as it co-elutes with C_{14} 2,3,6-AI on the DB-5MS column (Figure 7.6a). Nevertheless, it is well resolved on the VF-200MS column (Figure 7.6b). Since the co-eluting compounds on the DB-5MS column (2,3,5- with 2,4,5-AI and 2,3,6- with 3,4,5-AI) are well resolved on the VF-200MS column, it was possible to calculate the relative abundances of the C_{14} AI isomers (Figure 7.7c). The series of 2,3,4- and 2,3,6-AI were detected in all nine Wollogorang Fm samples. The abundances of 2,3,6-AI relative to TMAB and other isomers in M^+ → 134 chromatograms decrease downcore with increasing thermal maturity (e.g. Figure 7.7a and c for the C_{14} homologs). However, no clear trend in relative abundances was observed for the 2,3,4-AI series.

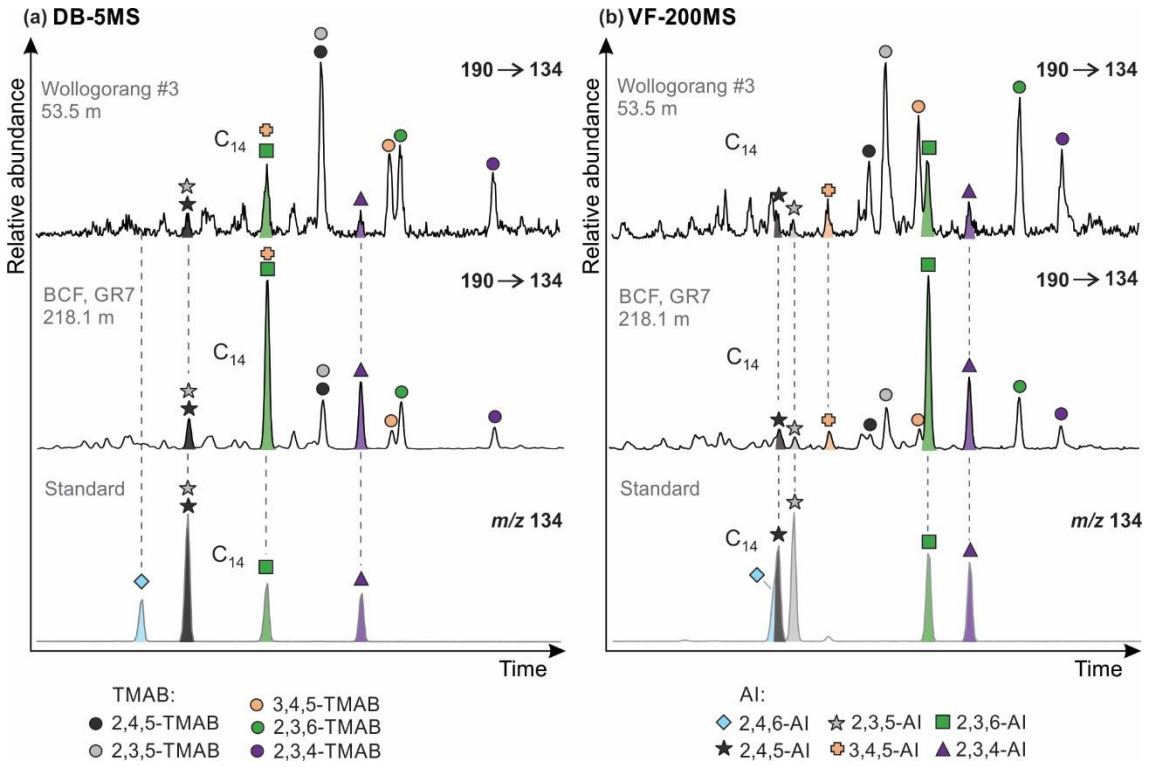

Figure 7.6. *m/z* 190→134 MRM chromatograms with the C_{14} aryl isoprenoid (AI) distribution of the Wollogorang Fm (sample #3, 53.5 m) and BCF (GR7 drillcore, 218.1 m) on (a) DB-5MS and (b) VF-200MS capillary columns. The AI were identified by comparison with partial *m/z* 134 chromatograms with synthetic standards of C_{14} 2,3,4-, 2,3,6-, 2,3,5-, 2,4,5- and 2,4,6-AI isomers (courtesy Roger Summons; Summons & Powel, 1987) and 3,4,5-AI in the Utica Shale.

In summary, the identification of the 2,3,6-AI series in the Wollogorang Fm samples is strong based on the presence of 8 chromatographic signals that are in the correct elution positions on both DB-5MS and VF-200MS columns (C_{14} to C_{22}, excluding C_{17} that is always low due to branching), although some signals are partly co-eluting with unknown compounds. The recognition of the 2,3,4-AI series is less strong, but still fair, based on the correct elution positions of 4 well resolved signals on both capillary columns (C_{14}, C_{15}, C_{16}, C_{19}) and a clear C_{18} signal on the DB-5MS column, which is masked by closely eluting compounds on VF-200MS.

7.4.5 Stable carbon and hydrogen isotopes

Stable carbon and hydrogen isotopes of *n*-alkanes were measured for the two samples with high extract yields (#6 and #7). The two extracts were similar, with $\delta^{13}C$ values ranging between -25 and -27‰, and δD values from -89 to -106‰ (Table 7.3). *n*-Alkanes of the Wollogorang Fm are ^{13}C-enriched by ~6‰ relative to the 1.38 Ga Roper Group (Jarrett et al., 2019), but comparable with BCF values from the McArthur River Mine (Williford et al., 2011).

Table 7.3. *n*-Alkane carbon and hydrogen isotopic composition of Wollogorang Formation bitumens

Carbon number	Sample #6		Sample #7	
	$\delta^{13}C$ (‰)	δD (‰)	$\delta^{13}C$ (‰)	δD (‰)
12	-25.94	-97.1	-27.48	
13	-25.38	-95.55	-27.18	-99.76
14	-25.19	-96.22	-27.04	-98.26
15	-25.26	-96.76	-26.90	-97.98
16	-25.47	-94.63	-26.79	-95.31
17	-25.53	-96.46	-26.64	-95.52
18	-25.77	-93.07	-26.67	-96.01
19	-26.03	-91.79	-26.80	-101.28
20	-26.34	-89.91	-26.98	-99.01
21	-26.40	-88.65	-27.09	-99.36
22	-26.63	-90.63	-27.11	-103.6
23	-26.52		-27.17	-104.87
24	-26.69		-27.37	-104.64
25	-26.39		-27.18	-106.37
26	-26.51		-27.22	-103.43
27			-27.05	
28			-26.87	

7.5 Discussion

7.5.1 Thermal maturity and syngeneity of biomarkers

Based on clean laboratory blanks and successful removal of surficial contamination (Figure 7.2), hydrocarbons detected in the interior fractions extracted from the 1.73 Ga Wollogorang Fm are indigenous. The observation of steeply increasing thermal maturities towards the underlying dolerite provides additional evidence for the syngeneity of

phenanthrenes and naphthalenes (Figure 7.1 b; Table 7.2; Appendix D, Supplementary Figure 1).

Programmed pyrolysis data (Table 7.1) indicate that the thermal maturity of the Wollogorang Fm samples ranges from the early oil window (Tmax = 424 – 437ºC in five samples) to the main oil window (Tmax of 447ºC and 453ºC in two samples with the highest TOC content). At the same time, the phenanthrene-based maturity parameters of the Wollogorang Fm bitumens suggest a wider maturity range to the end of the oil window (e.g. Rc(MPI)=0.7–1.1%, Table 7.2). However, conventional maturity parameters are poorly calibrated in the vicinity of intrusions, and close alignment of different indices is not necessarily expected (Illing et al., 2019). Available kerogen atomic H/C ratios (Table 7.2) correspond to the late oil window for samples #5 and #6 and to the beginning of wet gas window for sample #9 (Vandenbroucke & Largeau, 2007). These H/C ratios are consistent with solid bitumen reflectance values and biomarker-based maturity parameters (Table 7.2). Therefore, based on combined H/C, organic petrography and phenanthrene data, the maturity level for samples #4 – #9 ranges from the late oil window to the beginning of wet gas window, whereas the shallowest samples #1 – #3 are within the main oil window.

Absence of steranes and hopanes in the analysed samples may, in principle, be related to intense heterotrophic reworking of the original biomass, low abundances of sterol and hopanol producing organisms, or thermal decay caused by the dolerite intrusion. In a recent study of the 1.38 Ga Velkerri Fm from the McArthur Basin, Jarrett et al. (2019) illustrated the disappearance of hopanes downcore as a result of thermal degradation. According to presented data (Table 2 in Jarrett et al. (2019)), hopane concentrations dropped below detection limits at MPDF > 0.39 and MPR > 1.03. Based on MPDF, the majority of Wollogorang Fm bitumens from the current study demonstrate higher

maturity levels (Table 7.1). However, hopanes could still be expected based on MPR, particularly in the shallowest samples. The thermal maturity assessment based on phenanthrenes is thus not precise enough to obtain an unambiguous picture, and it remains unclear whether the lack of hopanes in the three least mature samples (#1–3) is related to ecology or thermal degradation.

Lee and Brocks (2011) demonstrated that 2,3,4- and 2,3,6-AI are preserved to Tmax values of at least 440 to 445ºC in the 1.64 Ga Barney Creek Fm, McArthur Basin. These Tmax values correspond to calculated vitrinite reflectance equivalents of Rc(Tmax)=0.76–0.85% (Jarvie et al., 2001). Therefore, the preservation of indigenous AI in the Wollogorang Fm bitumens is not unexpected, since at least three samples have Rc(MPI) and Rc(MPDF)<0.85%.

Schwark and Frimmel (2004) introduced the aryl isoprenoid ratio (AIR), which evaluates the proportion of short versus intermediate chain-length AI and apparently reflects the aerobic degradation of these molecules. However, reduction in average AI chain length might be also induced by increasing maturity. Therefore, the absence of AI with more than 22 carbon atoms in the Wollogorang Fm could be related to intermittent oxygenation of the bottom sediments, but may also simply reflect elevated maturity. Thus, without quantitative knowledge of the maturity-dependence of AIR, it is not yet possible to apply this ratio to estimate the exposure of organic matter to oxygen.

7.5.2 Biological versus abiological origins of the aryl isoprenoids

The 2,3,6- and 2,3,4-AI are commonly attributed to distinct photosynthetic bacterial sources (Brocks & Schaeffer, 2008). However, random isomerization reactions could theoretically also invoke the formation of AI. Random isomerization has the potential to create a large number of molecular structures. In *m/z* 190 → 134 traces alone, over 100

possible products with different alkylation patterns at the aromatic ring and the side chain are possible, of which only six would be trimethylated AI (i.e. 2,3,4-, 2,3,5-, 2,3,6-, 2,4,6-, 2,4,5-, and 3,4,5-AI (Figure 7.7d; (Summons & Powell, 1987)). These six AI may be formed abiologically via reshuffling of methyl groups at the aromatic ring, as observed for methyl phenanthrenes and methyl naphthalenes (Bastow et al., 2000; Szczerba & Rospondek, 2010; van Aarssen et al., 1999); via side-chain methylation of straight-chain TMAB, or demethylation, methylation and transmethylation reactions of other related structures. However, in the least mature Wollogorang Fm samples the relative abundances of TMAB and AI are entirely different (e.g. sample #3 in Figure 7.7a). For instance, while 2,3,5+2,4,5 TMAB represent the biggest peak in the *m/z* 190→134 chromatogram, these two isomers are the lowest among AI. Therefore, we can exclude that five of the detected AI isomers formed through side chain isomerization of respective TMAB precursors.

Unless a metastable equilibrium is reached, the generation of abiogenic AI isomers through re-arrangement of biogenic precursors would initially result in dominant biogenic isomers and lower abundances of more or less equally distributed abiogenic products. This can be observed in low maturity sediments of the Barney Creek Formation (BCF), where the biological 2,3,6- and 2,3,4-AI are significantly elevated in comparison to other detected AI isomers (e.g. 218.1 m sample in Figure 7.7b and c). However, at elevated maturities, increasing abundances of abiogenic isomers are generated, presumably through isomerization of methyl groups at the aryl-moiety (Szczerba & Rospondek, 2010). In the most mature BCF sample (683.5 m), the relative abundance of AI isomers is probably close to metastable equilibrium (Figure 7.7b, c) where the abiogenic 2,3,5-, 2,4,5- and 3,4,5- isomers are all more abundant than the biogenic 2,3,4- and 2,3,6-AI isomers. A similar pattern is observed in the Wollogorang Fm (Figure 7.7a and c). For

the least mature Wollogorang Fm sample (#3) in the 14MCDDH001 drillcore, the 2,3,6-AI is elevated by a factor of at least ~4 in comparison to other detected AI isomers and also relative to all unassigned peaks in the *m/z* 190 → 134 chromatogram. Moreover, as in the BCF, with increasing maturity (samples #7 and #9) the relative abundance of 2,3,6-AI drops towards a metastable equilibrium with the other isomers (Figure 7.7a and c). Thus, while the AI in the most mature Wollogorang Fm samples must be interpreted as thermal rearrangement products, the strongly elevated relative abundance of the 2,3,6-AI isomer in the least mature sample argues for the existence of a biological precursor.

The origin of the 2,3,4-AI series is less certain. In the least mature sample #3, 2,3,4-AI is elevated over the abiological 2,3,5-, 2,4,5- and 3,4,5-AI isomers, and thus more abundant than expected for an equilibration product (compare BCF sample 683.5 m; Figure 7.7c). However, due to its low absolute abundance and inconsistent behaviour down-core (Fig. 7.7c), an abiological origin cannot be excluded.

7.5.3 Biomarker interpretation at the biological/abiological boundary

The increasing isomerisation of AI in the Wollogorang Fm close to the volcanic intrusion highlights a challenge in the search for the oldest biomarker molecules on Earth, and possibly on other planets: at some degree of (thermal) alteration and somewhere in deep geological time, we will encounter an unresolved overlap between biomarker assemblages and thermodynamic ambiguities. In such an uncertain boundary scenario, the biomarker molecules, although correctly identified, might not indicate the presence of biological precursors but represent random catagenetic products. In other words, the chemical structure of a molecule ceases to be a biomarker, and only distributions far from metastable equilibrium (and possibly isotopic compositions) may provide clues about biogenic origins.

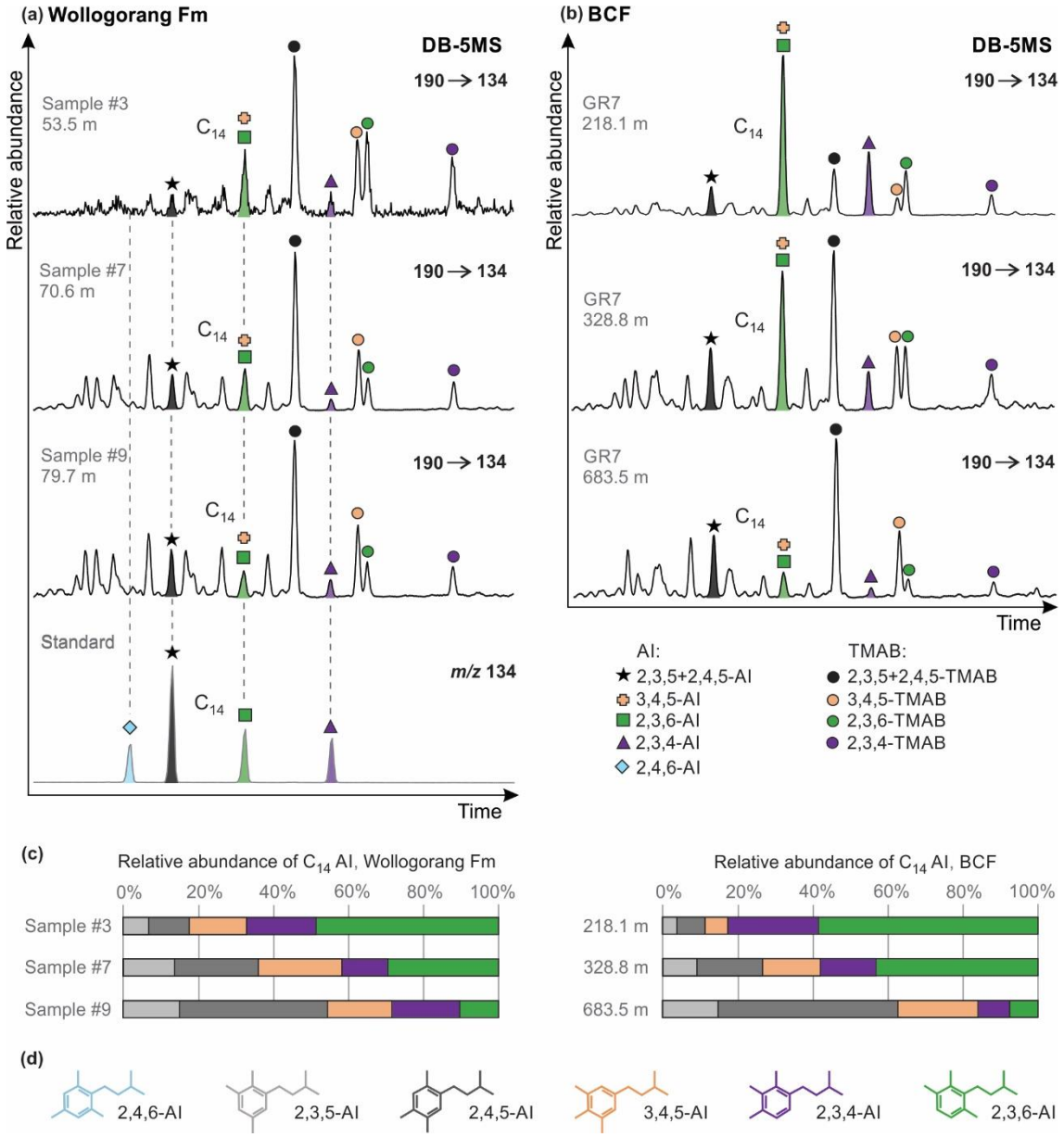

Figure 7.7. *m/z* 190→134 MRM chromatograms illustrating the C_{14} aryl isoprenoid (AI) distribution of the Wollogorang Fm, 14MCDDH001 drillcore (a) and BCF, GR7 drillcore (b) with increasing maturity. The AI were identified by comparison with synthetic standards of C_{14} 2,3,4-, 2,3,6-, 2,3,5-, 2,4,5- and 2,4,6-AI isomers (Summons & Powel, 1987) and 3,4,5-AI in the Utica Shale. (c) Relative abundances of five C_{14} AI isomers in the Wollogorang Fm and BCF with increasing depth (the sixth isomer 2,4,6-AI is not visible in *m/z* 190→134). (d) Colour coded structures of the six possible C_{14} AI isomers.

The current study provides an example of such a border scenario. Series of 2,3,4- and 2,3,6-AI were detected in all analysed samples. However, in the most mature Wollogorang Fm samples with distribution of AI isomers close to metastable equilibrium,

the 2,3,4- and 2,3,6-AI series must be interpreted as abiogenic random isomerization products. Moreover, due to the low absolute and relative abundance, the nature of the 2,3,4-AI series remains ambiguous in the entire maturity range. The biogenic record of 2,3,6-AI disappears in the approximate maturity window with Rc of 0.8–1% (calculated from biomarker-based maturity parameters). Conversely, 2,3,6-AI from the least mature Wollogorang Fm samples with Rc(MPI)<0.8% have not reached a metastable equilibrium with other isomers and, therefore, can be interpreted as biogenic.

7.5.4 Biological interpretation of the aryl isoprenoids

Compounds of the 2,3,6-AI series are commonly interpreted as degradation products of chlorobactene or isorenieratene, originating from green sulphur bacteria (GSB, Chlorobiaceae) (Brocks & Schaeffer, 2008). However, Koopmans et al. (1996) demonstrated that 2,3,6-AI can also be produced by oxidation of non-aromatic β-carotene. In the absence of algae in the mid-Proterozoic (Gueneli et al., 2018), carotenoids with the β-carotane skeleton are most likely derived from cyanobacteria (Lee & Brocks, 2011). In principle, 2,3,6-AI of Chlorobiaceae can be distinguished from other biological sources by a relative ^{13}C-enrichment of ~15‰ (Koopmans et al., 1996). Unfortunately, $\delta^{13}C$ measurements were not possible in the current study due to low concentrations of AI. Therefore, in the absence of reliable additional information, we conclude that the 2,3,6-AI in the Wollogorang Fm are the degradation products of carotenoids, likely from cyanobacteria and/or green sulphur bacteria.

If the compounds of the 2,3,4-AI series are not isomerization products but derived from a biological precursor, then more far reaching conclusions are possible. 2,3,4-AI are the typical breakdown products of C_{40} aromatic carotenoids with the okenane, renieratane and renierapurpurane skeletons, which are regarded as diagnostic pigments of purple

sulphur bacteria (PSB) of the family Chromatiaceae. The co-occurrence of 2,3,6-AI with 2,3,4-AI would then suggests that GSB represent a major source for 2,3,6-AI, as GSB always thrive in environments where PSB are found. GSB are strictly anaerobic phototrophic organisms, which mostly use reduced sulphur species (sulphide and sulphur) as electron donors but can also oxidize ferrous iron. In restricted planktonic ecosystems such as the black shale facies of the Wollogorang Fm, GSB inhabit anoxic waters within the photic zone of the water column to depths of up to 100 m (Brocks & Schaeffer, 2008). PSB have greater light requirements and higher oxygen tolerance than GSB and therefore commonly thrive just above GSB and directly below the oxic-anoxic interface within the light-penetrated zone. PSB are most commonly observed at water depths of 12 to 25 m (Brocks & Schaeffer, 2008), suggesting at least temporary very shallow stratification of the McArthur Basin at 1.73 Ga. In this interpretation, the McArthur Basin was stratified and anoxic at 1.73 Ga and inhabited by GSB and PSB, which is consistent with euxinic bottom waters proposed by Spinks et al. (2016) based on trace element proxies.

In summary, in the least mature Wollogorang Fm samples, 2,3,4-AI may be derived from PSB or formed by abiogenic isomerization, whereas 2,3,6-AI reveal the presence of cyanobacteria and/or GSB.

7.6 Conclusions

The 1.73 Ga Wollogorang Fm of the Tawallah Group in the southern McArthur Basin contains the currently oldest known clearly indigenous molecular fossils. Previously, the oldest biomarkers were reported from the 1.64 Ga Barney Creek Formation (Brocks et al., 2005). Our findings thus extend the biomarker record by ~90 million years. The bitumens of the Wollogorang Formation experienced heating by an underlying dolerite sill, and this is reflected by a steep thermal maturity trend from the main oil window to

the beginning of the wet gas window at 70 to 30 meters above the sill. Extracted hydrocarbons illustrate typical indigenous mid-Proterozoic signatures with large unresolved complex mixtures, high methyl alkane/*n*-alkane ratios, and the absence of acyclic isoprenoids, saturated carotenoids and eukaryotic steranes. Bacterial hopanes were also below detection limits. The thermal maturity of the shallowest bitumens is in the range where polycyclic biomarkers start to disappear, so it remains unclear whether lack of hopanes is primary or caused by the heating aureole of the dolerite sill. However, continuous homologous series of low molecular weight 2,3,6- and 2,3,4-trimethyl aryl isoprenoids (AI) were identified. While the AI in the most mature Wollogorang Fm samples reach a metastable equilibrium and represent thermal rearrangement products, in the least mature samples with Rc(MPI)<0.8% we interpret the 2,3,6-AI compound series as diagenetic derivatives from biogenic precursor molecules based on its elevated abundance relative to co-occurring abiogenic isomeric series, and the 2,3,4-AI series as possibly biogenic. These degradation and isomerization products of carotenoids are currently the oldest detected molecules of biological origin, revealing the presence of phototrophic bacteria in the 1.73 Ga Wollogorang Fm.

Acknowledgments

We thank Jacob Sohn for technical assistance with isotope measurements in the Organic Geochemistry laboratory (GA) and Darryl Stacey from the Darwin Core Library (NTGS) for access to drill cores. We thank Roger Summons (MIT) for synthetic standards of aryl isoprenoids. We are grateful to Lennart van Maldegem and Ilya Bobrovskiy (ANU) for helpful discussions. This research is funded by Australian Research Council grants DP160100607 and DP170100556 (to JJB). GV acknowledges support from an Australian Government Research Training Program (RTP) Scholarship. AJMJ publishes with

permission of the CEO, Geoscience Australia. The authors declare no conflicting interests, financial or otherwise.

References

Ahmad, M., Dunster, J. N., & Munson, T. J. (2013). Chapter 15: McArthur Basin: in Ahmad M and Munson TJ (compilers).'. *Geology and mineral resources of the Northern Territory'. Northern Territory Geological Survey, Special Publication, 5*.

Alexander, R., Kagi, R., Rowland, S., Sheppard, P., & Chirila, T. (1985). The effects of thermal maturity on distributions of dimethylnaphthalenes and trimethylnaphthalenes in some ancient sediments and petroleums. *Geochimica et Cosmochimica Acta, 49*(2), 385-395.

Bastow, T. P., Alexander, R., Fisher, S. J., Singh, R. K., van Aarssen, B. G., & Kagi, R. I. (2000). Geosynthesis of organic compounds. Part V—methylation of alkylnaphthalenes. *Organic geochemistry, 31*(6), 523-534.

Beghin, J., Guilbaud, R., Poulton, S. W., Gueneli, N., Brocks, J. J., Storme, J.-Y., . . . Javaux, E. J. (2017). A palaeoecological model for the late Mesoproterozoic–early Neoproterozoic Atar/El Mreïti Group, Taoudeni Basin, Mauritania, northwestern Africa. *Precambrian Research, 299*, 1-14.

Blumenberg, M., Thiel, V., Riegel, W., Kah, L. C., & Reitner, J. (2012). Biomarkers of black shales formed by microbial mats, Late Mesoproterozoic (1.1Ga) Taoudeni Basin, Mauritania. *Precambrian Research, 196-197*, 113-127. doi:10.1016/j.precamres.2011.11.010

Brocks, J. J., Grosjean, E., & Logan, G. A. (2008). Assessing biomarker syngeneity using branched alkanes with quaternary carbon (BAQCs) and other plastic contaminants. *Geochimica et Cosmochimica Acta, 72*(3), 871-888.

Brocks, J. J., Jarrett, A. J., Sirantoine, E., Kenig, F., Moczydlowska, M., Porter, S., & Hope, J. (2016). Early sponges and toxic protists: possible sources of cryostane, an age diagnostic biomarker antedating Sturtian Snowball Earth. *Geobiology, 14*(2), 129-149. doi:10.1111/gbi.12165

Brocks, J. J., Jarrett, A. J. M., Sirantoine, E., Hallmann, C., Hoshino, Y., & Liyanage, T. (2017). The rise of algae in Cryogenian oceans and the emergence of animals. *Nature, 548*(7669), 578-581. doi:10.1038/nature23457

Brocks, J. J., Love, G. D., Summons, R. E., Knoll, A. H., Logan, G. A., & Bowden, S. A. (2005). Biomarker evidence for green and purple sulphur bacteria in a stratified Palaeoproterozoic sea. *Nature, 437*, 866. doi:10.1038/nature04068

Brocks, J. J., & Schaeffer, P. (2008). Okenane, a biomarker for purple sulfur bacteria (Chromatiaceae), and other new carotenoid derivatives from the 1640Ma Barney Creek Formation. *Geochimica et Cosmochimica Acta, 72*(5), 1396-1414. doi:10.1016/j.gca.2007.12.006

Butterfield, N. J. (2000). Bangiomorpha pubescens n. gen., n. sp.: implications for the evolution of sex, multicellularity, and the Mesoproterozoic/Neoproterozoic radiation of eukaryotes. *Paleobiology, 26*(3), 386-404.

Butterfield, N. J., & Smith, A. (2015). Early evolution of the Eukaryota. *Palaeontology, 58*(1), 5-17. doi:10.1111/pala.12139

Canfield, D. E. (1998). A new model for Proterozoic ocean chemistry. *Nature (London), 396*(6710), 450-453. doi:10.1038/24839

Clifford, D. J., Clayton, J. L., & Damsté, J. S. S. (1998). 2, 3, 6-/3, 4, 5-Trimethyl substituted diaryl carotenoid derivatives (Chlorobiaceae) in petroleums of the Belarussian Pripyat River Basin. *Organic geochemistry, 29*(5-7), 1253-1267.

Dahl, B., Bojesen-Koefoed, J., Holm, A., Justwan, H., Rasmussen, E., & Thomsen, E. (2004). A new approach to interpreting Rock-Eval S2 and TOC data for kerogen quality assessment. *Organic geochemistry, 35*(11-12), 1461-1477. doi:10.1016/j.orggeochem.2004.07.003

French, K. L., Hallmann, C., Hope, J. M., Schoon, P. L., Zumberge, J. A., Hoshino, Y., . . . Summons, R. E. (2015). Reappraisal of hydrocarbon biomarkers in Archean rocks. *Proc Natl Acad Sci U S A, 112*(19), 5915-5920. doi:10.1073/pnas.1419563112

Gibson, T. M., Shih, P. M., Cumming, V. M., Fischer, W. W., Crockford, P. W., Hodgskiss, M. S., . . . Skulski, T. M. (2017). Precise age of Bangiomorpha pubescens dates the origin of eukaryotic photosynthesis. *Geology, 46*(2), 135-138.

Gueneli, N. (2016). *Late Mesoproterozoic Microbial Communities.* (PhD Thesis), Australian National University.

Gueneli, N., McKenna, A., Ohkouchi, N., Boreham, C., Beghin, J., Javaux, E., & Brocks, J. (2018). 1.1-billion-year-old porphyrins establish a marine ecosystem dominated by bacterial primary producers. *Proceedings of the National Academy of Sciences, 115*(30), E6978-E6986.

Holland, H. D. (2006). The oxygenation of the atmosphere and oceans. *Philos Trans R Soc Lond B Biol Sci, 361*(1470), 903-915. doi:10.1098/rstb.2006.1838

Hoshino, Y., Poshibaeva, A., Meredith, W., Snape, C., Poshibaev, V., Versteegh, G. J. M., . . . Hallmann, C. (2017). Cryogenian evolution of stigmasteroid biosynthesis. *Science Advances, 3*.

Illing, C. J., Hallmann, C., Scott, A. C., Collinson, M. E., Briggs, D. E. G., Strauss, H., & Summons, R. E. (2019). Heterogeneity of free and occluded bitumen in a natural maturity sequence from Oligocene Lake Enspel. *Geochimica et Cosmochimica Acta, 245*, 240-265. doi:10.1016/j.gca.2018.10.021

Jackson, M., Muir, M. D., & Plumb, K. A. (1987). *Geology of the southern McArthur Basin, Northern Territory* (Vol. 220): Australian Government Publishing Service.

Jarrett, A. J. M., Cox, G. M., Brocks, J. J., Grosjean, E., Boreham, C. J., & Edwards, D. S. (2019). Microbial assemblage and palaeoenvironmental reconstruction of the 1.38 Ga Velkerri Formation, McArthur Basin, northern Australia. *Geobiology, 17*(4), 360-380. doi:10.1111/gbi.12331

Jarrett, A. J. M., Schinteie, R., Hope, J. M., & Brocks, J. J. (2013). Micro-ablation, a new technique to remove drilling fluids and other contaminants from fragmented and fissile rock material. *Organic geochemistry, 61*, 57-65. doi:10.1016/j.orggeochem.2013.06.005

Jarvie, D., Claxton, B., Henk, F., & Breyer, J. (2001). Oil and shale gas from the Barnett Shale, Fort Worth Basin, Texas: AAPG Annual Meeting Program, v. 10, p. *A100*.

Johnston, D. T., Poulton, S. W., Dehler, C., Porter, S., Husson, J., Canfield, D. E., & Knoll, A. H. (2010). An emerging picture of Neoproterozoic ocean chemistry: Insights from the Chuar Group, Grand Canyon, USA. *Earth and Planetary Science Letters, 290*(1-2), 64-73. doi:10.1016/j.epsl.2009.11.059

Knoll, A. H., & Nowak, M. A. (2017). The timetable of evolution. *Science Advances, 3*(5). doi:10.1126/sciadv.1603076

Koopmans, M. P., Schouten, S., Kohnen, M. E., & Damsté, J. S. S. (1996). Restricted utility of aryl isoprenoids as indicators for photic zone anoxia. *Geochimica et Cosmochimica Acta, 60*(23), 4873-4876.

Kvalheim, O. M., Christy, A. A., Telnæs, N., & Bjørseth, A. (1987). Maturity determination of organic matter in coals using the methylphenanthrene distribution. *Geochimica et Cosmochimica Acta, 51*(7), 1883-1888.

Lamb, D. M., Awramik, S. M., Chapman, D. J., & Zhu, S. (2009). Evidence for eukaryotic diversification in the ~1800 million-year-old Changzhougou Formation, North China. *Precambrian Research, 173*(1-4), 93-104. doi:10.1016/j.precamres.2009.05.005

Lee, C., & Brocks, J. J. (2011). Identification of carotane breakdown products in the 1.64 billion year old Barney Creek Formation, McArthur Basin, northern Australia. *Organic geochemistry, 42*(4), 425-430.

Li, H., Lu, S., Su, W., Xiang, Z., Zhou, H., & Zhang, Y. (2013). Recent advances in the study of the Mesoproterozoic geochronology in the North China Craton. *Journal of Asian Earth Sciences, 72*, 216-227.

Luo, G., Hallmann, C., Xie, S., Ruan, X., & Summons, R. E. (2015). Comparative microbial diversity and redox environments of black shale and stromatolite facies in the Mesoproterozoic Xiamaling Formation. *Geochimica et Cosmochimica Acta, 151*, 150-167.

Luo, Q., George, S. C., Xu, Y., & Zhong, N. (2016). Organic geochemical characteristics of the Mesoproterozoic Hongshuizhuang Formation from northern China: implications for thermal maturity and biological sources. *Organic geochemistry, 99*, 23-37.

Lyons, T. W., Reinhard, C. T., & Planavsky, N. J. (2014). The rise of oxygen in Earth's early ocean and atmosphere. *Nature, 506*(7488), 307.

Munson, T. (2014). *Petroleum geology and potential of the onshore Northern Territory, 2014*: Northern Territory Geological Survey.

Nguyen, K., Love, G. D., Zumberge, J. A., Kelly, A. E., Owens, J. D., Rohrssen, M. K., . . . Lyons, T. W. (2019). Absence of biomarker evidence for early eukaryotic life from the Mesoproterozoic Roper Group: Searching across a marine redox gradient in mid-Proterozoic habitability. *Geobiology, 17*(3), 247-260. doi:10.1111/gbi.12329

Page, R. W., Jackson, M. J., & Krassay, A. A. (2000). Constraining sequence stratigraphy in north Australian basins: SHRIMP U–Pb zircon geochronology between Mt Isa and McArthur River. *Australian Journal of Earth Sciences, 47*(3), 431-459. doi:10.1046/j.1440-0952.2000.00797.x

Pawlowska, M. M., Butterfield, N. J., & Brocks, J. J. (2013). Lipid taphonomy in the Proterozoic and the effect of microbial mats on biomarker preservation. *Geology, 41*(2), 103-106. doi:10.1130/g33525.1

Peters, K. (1986). Guidelines for evaluating petroleum source rock using programmed pyrolysis. *AAPG Bulletin, 70*(3), 318-329.

Planavsky, N. J., McGoldrick, P., Scott, C. T., Li, C., Reinhard, C. T., Kelly, A. E., . . . Lyons, T. W. (2011). Widespread iron-rich conditions in the mid-Proterozoic ocean. *Nature, 477*(7365), 448-451. doi:10.1038/nature10327

Poulton, S. W., & Canfield, D. E. (2011). Ferruginous Conditions: A Dominant Feature of the Ocean through Earth's History. *Elements, 7*(2), 107-112. doi:10.2113/gselements.7.2.107

Poulton, S. W., Fralick, P. W., & Canfield, D. E. (2010). Spatial variability in oceanic redox structure 1.8 billion years ago. *Nature Geoscience, 3*(7), 486-490. doi:10.1038/ngeo889

Radke, M. (1988). Application of aromatic compounds as maturity indicators in source rocks and crude oils. *Marine and Petroleum Geology, 5*(3), 224-236.

Radke, M., & Welte, D. H. (1983). The methylphenanthrene index (MPI): a maturity parameter based on aromatic hydrocarbons. *Advances Organic Geochemistry 1981*, 504-512.

Rawlings, D. J. (1999). Stratigraphic resolution of a multiphase intracratonic basin system: The McArthur Basin, northern Australia. *Australian Journal of Earth Sciences, 46*(5), 703-723. doi:10.1046/j.1440-0952.1999.00739.x

Schwark, L., & Frimmel, A. (2004). Chemostratigraphy of the Posidonia Black Shale, SW-Germany: II. Assessment of extent and persistence of photic-zone anoxia using aryl isoprenoid distributions. *Chemical Geology, 206*(3-4), 231-248.

Spinks, S. C., Schmid, S., Pagés, A., & Bluett, J. (2016). Evidence for SEDEX-style mineralization in the 1.7 Ga Tawallah Group, McArthur Basin, Australia. *Ore Geology Reviews, 76*, 122-139. doi:10.1016/j.oregeorev.2016.01.007

Summons, R., & Powell, T. (1987). Identification of aryl isoprenoids in source rocks and crude oils: biological markers for the green sulphur bacteria. *Geochimica et Cosmochimica Acta, 51*(3), 557-566.

Szczerba, M., & Rospondek, M. J. (2010). Controls on distributions of methylphenanthrenes in sedimentary rock extracts: critical evaluation of existing geochemical data from molecular modelling. *Organic geochemistry, 41*(12), 1297-1311.

van Aarssen, B. G., Bastow, T. P., Alexander, R., & Kagi, R. I. (1999). Distributions of methylated naphthalenes in crude oils: indicators of maturity, biodegradation and mixing. *Organic geochemistry, 30*(10), 1213-1227.

Vandenbroucke, M., & Largeau, C. (2007). Kerogen origin, evolution and structure. *Organic geochemistry, 38*(5), 719-833.

Wetherley, C. (2014). 2014 Stratigraphic diamond drilling program EL 27711 and EL 30085.

Williford, K. H., Grice, K., Logan, G. A., Chen, J., & Huston, D. (2011). The molecular and isotopic effects of hydrothermal alteration of organic matter in the Paleoproterozoic McArthur River Pb/Zn/Ag ore deposit. *Earth and Planetary Science Letters, 301*(1-2), 382-392. doi:10.1016/j.epsl.2010.11.029

Chapter 8

Conclusions

The current dissertation aimed to extend our knowledge about mid-Proterozoic ecosystems and challenges related to the preservation of ancient organic matter. For these purposes, I analysed Paleoproterozoic samples from the ~1.64 Ga middle McArthur Group and ~1.73 Ga Tawallah Group in the northern Australian McArthur Basin. Rigorous exterior/interior experiments allowed recognition and removal of surficial contaminants where present and subsequent analysis of indigenous Paleoproterozoic biomarker signatures. The main findings of this thesis are outlined below.

(1) Exceptionally well-preserved organic matter and biomarkers were recorded through the middle McArthur Group from the Teena Dolostone to the Lynott Fm in the LV09 drill core (Chapter 4). A multi-proxy analysis suggests a bacteria-dominated ecosystem within heterogeneous environments with stratified waters for the whole succession, where bacterial communities include anaerobic green and purple sulphur bacteria, cyanobacteria, tetrahymanol producing bacteria and aerobic methanotrophic bacteria.

(2) Protosteroid molecules, previously detected in the GR7 drill core, were also identified in LV09 sediments. Stem group eukaryotes or bacteria may have produced these molecules in the Paleoproterozoic. I compared relative protosterane concentrations in different depositional environments from deep to shallow marine and lagoonal. However, due to complex and contradictory patterns of relative abundances in GR7 and LV09 drill cores, I cannot confidently evaluate what environments the protosteroid producers preferred. Nevertheless, protosterane distributions in the LV09 drill core are not controlled by maturity, biodegradation, redox, and aromatization.

(3) Thermal maturity may substantially affect the compound-specific carbon and hydrogen isotopic composition of *n*-alkanes. Chapter 5 illustrates strong linear correlations between maturity and compound-specific isotopes in the 1.64 Ga Barney

Creek Formation and demonstrates a ^{13}C and ^{2}H enrichment of *n*-alkanes by up to 6.8‰ and 69‰ respectively. This is the first study describing maturity influence on compound-specific isotopes in the Proterozoic. Based on similar isotopic enrichments caused by thermal maturation in the Barney Creek Fm and pyrolysis experiments on Phanerozoic oils and source rocks, the results of my research are important for Phanerozoic sequences as well. As the observed thermal effect on $\delta^{13}C$ and $\delta^{2}H$ of *n*-alkanes is high enough to have an impact on biological and environmental interpretations, it is important to consider maturity in oil-source rock correlations and ecological reconstructions for Proterozoic and Phanerozoic sediments. Chapter 5 also demonstrates the $\delta^{13}C$ *n*-alkane slope inversion from positive to negative in the Barney Creek Fm with increasing thermal maturity. Using simple numerical simulations, I suggest that this isotope slope inversion is controlled by changing importance of different generation and degradation processes.

(4) Preservation of organic matter associated with the 1.64 Ga McArthur River (HYC) zinc/lead ore deposit was reassessed in Chapter 6. This project represents the first hydrocarbon analysis through the full succession of the McArthur River sulphide deposit, including the foot wall, orebody, inter-ore layers and hanging wall. Based on the comparison of organic matter between the orebody and unmineralized sections, I demonstrate that hydrocarbons in the orebody migrated from surrounding sediments and therefore do not record the temperature of mineralizing fluids, negating earlier temperature estimates.

(5) A successful extension of the known biomarker record back in time is provided in Chapters 4 and 7. Chapter 4 presents the discovery of the oldest known hopanes and intact aromatic carotenoids (chlorobactane and okenane) in the ~1.64 Ga Teena Dolostone, which underlies the Barney Creek Formation. Chapter 7 records series of the low molecular weight 2,3,4- and 2,3,6-trimethyl aryl isoprenoids (AI) in the 1.73 Ga

Wollogorang Formation. These compounds represent the oldest known biogenic aromatic carotenoids on Earth and reveal the activity of phototrophic bacteria at 1.73 Ga ago in the McArthur Basin.

(6) This thesis also outlines the limitations of biomarker analysis at the edge of detectability. At some degree of thermal alteration and somewhere in deep geological time, we may encounter an unresolved overlap between biological signatures and thermodynamic ambiguities. In this uncertain boundary scenario, the detected hydrocarbons might not indicate the presence of biological precursors but represent random abiogenic products. Chapter 7 provides an example of such a scenario. The Wollogorang Fm experienced heating by an underlying dolerite sill, and this is reflected by a steep thermal maturity trend in the biomarkers and Rock-Eval pyrolysis. Extracted bitumens contain series of AI, which show a systematic change in isomer distributions with increasing maturity. While in the least mature samples the 2,3,6-AI series have a biogenic origin based on their elevated abundances relative to abiogenic isomers, the AI in the most mature samples reach a metastable equilibrium and represent thermal rearrangement products. Therefore, the biological interpretation of biomarkers in ancient and thermally mature sediments should be made cautiously.

This thesis provides a detailed overview of the oldest preserved indigenous biomarkers on Earth. The biomarker distributions observed throughout Paleoproterozoic formations of the McArthur Basin indicate a bacteria-dominated ecosystem, comparable to other mid-Proterozoic formations around the world. This study also investigates the source and distribution of potential eukaryotic biomarkers (protosteranes), and while progress has been achieved by recognizing distinct trends in preservation of these molecules (unrelated to maturity, redox and biodegradation), no absolute determination

could be made about their biological origin. For future studies, I suggest pursuing isotopic measurements of isolated protosterane molecules in order to obtain more information about the source organisms. The current research also advances the understanding of thermal alteration effects on ancient organic matter preservation. These findings provide a valuable insight for recognition of indigenous biological signatures in future mid-Proterozoic studies.

APPENDIX A

Supplementary material for Chapter 4

Appendix A.1

Table: Biomarker ratios for LV09 drill core

Formation	Sample ID	Depth, m	Pr/Ph	Pr/C_{17}	Ph/C_{18}	(Pr+Ph)/(C_{17}+C_{18})	Ts/(Ts+Tm)	C_{29}Ts/(Ts+H)	Moretane ratio
Lynott	19G016i	271.95	0.5	0.43	1.36	0.79	0.47	0.29	0.07
	19G017i	275.76	0.5	0.19	1.15	0.43	0.48	0.32	0.07
	18G014i	279.35	0.8	0.07	0.36	0.13	0.21	0.19	0.11
	18G015i	289.85	0.6	0.12	0.70	0.26	0.35	0.24	0.06
	19G018i	295.3	0.7	0.18	0.47	0.27	0.32	0.22	0.07
	19G001i	313.43	0.8	0.36	0.48	0.41	0.36	0.26	0.07
	19G002i	330.4	0.6	0.38	0.76	0.55	0.30	0.12	0.19
	19G003i	338.8	0.6	2.89	3.59	3.30	0.41	0.30	0.06
	19G004i	341.1	0.7	0.53	0.78	0.65	0.37	0.21	0.07
	19G005i	365.2	0.7	0.30	0.47	0.38	0.45	0.30	0.06
Reward	19G006i	371.76	0.6	1.23	2.07	1.65	0.49	0.33	0.06
	19G007i	376.4	0.5	1.68	3.08	2.40	0.46	0.30	0.05
Barney Creek	12B117	382.22	0.4	1.54	3.13	2.38	0.52	0.01	0.06
	18G001i	393.7	0.5	0.46	1.23	0.80	0.64	0.42	0.05
	18G002i	402.4	0.4	1.43	3.30	2.44	0.56	0.38	0.05
	18G003i	406.7	0.5	0.42	0.96	0.67	0.57	0.07	0.05
	18G004i	414.75	0.3	0.96	2.21	1.66	0.57	0.39	0.05
	12B118	423.1	0.5	0.55	1.04	0.79	0.58	0.45	0.06
	18G005i	429.7	0.4	0.66	1.32	1.01	0.57	0.44	0.06
	18G008i	443.7	0.4	0.70	1.50	1.11	0.57	0.42	0.06
	17G002i	450.0	0.5	0.56	1.05	0.81	0.56	0.46	0.05
	19G008i	452.1	0.5	0.36	0.75	0.54	0.56	0.43	0.09
	19G009i	457.2	0.6	0.32	0.64	0.47	0.56	0.45	0.06
	18G009i	461.83	0.5	0.47	0.97	0.71	0.56	0.38	0.06
	19G010i	465.3	0.7	0.37	1.16	0.62	0.57	0.38	0.06
	17G007i	470.7	0.4	0.47	1.12	0.81	0.57	0.47	0.04
	19G011i	474.4	0.5	0.47	0.97	0.70	0.58	0.48	0.06
	17G008i	477.0	0.6	0.33	0.65	0.48	0.57	0.42	0.05
	17G009i	478.2	0.6	0.50	1.04	0.75	0.60	0.49	0.05
	17G001i	485.0	0.5	0.46	0.92	0.69	0.58	0.44	0.05
	17G010i	489.0	0.6	0.46	0.88	0.66	0.57	0.41	0.06
	12B119	492.98	0.4	0.54	1.08	0.84	0.59	0.39	0.06
	18G007i	494.5	0.4	0.67	1.26	0.99	0.56	0.48	0.05
	18G006i	494.6	0.5	0.91	1.54	1.25	0.57	0.44	0.05
	18G010i	498.88	0.5	0.61	1.18	0.89	0.59	0.43	0.07
	19G012i	506.0	0.5	0.96	1.86	1.42	0.59	0.43	0.06
Cooley	19G013i	515.35	0.3	2.33	4.29	3.54	0.62	0.43	0.06
	18G016i	522.68	0.3	3.44	10.89	7.11	0.61	0.43	0.04
	18G017i	527.32	0.4	0.84	2.52	1.63	0.60	0.41	0.04
	18G018i	542.61	0.4	0.77	2.43	1.47	0.62	0.37	0.04
Teena	18G019i	552.62	0.5	1.16	2.24	1.69	0.63	0.39	0.06
	19G014i	558.9	0.6	3.50	6.57	4.98	0.63	0.35	0.06
	18G020i	561.5	0.4	0.63	2.14	1.26	0.66	0.35	0.04
	17G005i	577.0	n.d.	n.d.	n.d.	n.d.	0.66	0.46	0.04
	19G015i	578.5	0.8	1.33	1.68	1.50	0.64	0.40	0.05

n.d. – not detected. Moretane ratio = C_{30} βα-hopane/(C_{30} βα-hopane+C_{30} αβ-hopane).

Sample ID	GI, %	2MHI, %	3MHI, %	C_{30}DiaH/ (DiaH+H)	HHI, %	3MeHHI %	C_{26}T/ C_{25}T	C_{19}T/ C_{23}T	T(C_{20}+C_{21})/ (C_{23}+C_{24})
19G016i	3.1	2.3	8.3	0.15	2.3	4.2	0.79	0.84	1.48
19G017i	4.2	2.4	6.6	0.14	3.5	6.5	0.76	0.21	0.76
18G014i	2.1	n.d.	16.3	0.14	2.5	3.5	0.45	0.33	1.28
18G015i	2.3	0.8	9.7	0.12	2.5	5.7	0.65	0.29	1.08
19G018i	1.2	2.3	10.2	0.14	2.7	4.4	0.81	0.20	0.57
19G001i	1.5	0.5	8.5	0.09	2.6	4.2	n.a.	1.38	1.26
19G002i	5.5	n.d.	4.1	0.11	n.d.	n.d.	n.a.	2.72	1.27
19G003i	2.2	0.3	7.2	0.10	3.6	5.3	n.a.	0.80	1.05
19G004i	1.7	0.9	2.4	0.13	4.1	n.d.	n.a.	1.52	1.77
19G005i	8.1	1.0	6.8	0.16	3.5	5.4	n.a.	1.17	1.22
19G006i	3.3	0.8	5.4	0.12	3.6	5.4	n.a.	0.95	1.07
19G007i	2.2	0.5	5.8	0.09	3.5	5.4	n.a.	0.64	0.99
12B117	3.6	n.d.	8.6	0.14	3.9	6.0	0.81	0.39	0.77
18G001i	4.5	1.3	5.1	0.13	5.4	6.1	0.78	0.40	1.04
18G002i	5.0	0.8	5.1	0.14	3.4	6.7	0.92	0.76	0.88
18G003i	3.5	0.9	4.7	0.14	3.7	6.3	1.0	0.56	0.68
18G004i	4.4	1.1	5.5	0.17	3.2	6.5	1.02	0.84	0.85
12B118	4.4	n.d.	4.1	0.22	2.7	5.1	n.a.	1.82	1.33
18G005i	4.1	1.7	4.9	0.23	3.9	6.7	1.0	1.11	0.96
18G008i	3.8	1.5	4.3	0.25	3.3	6.9	1.08	1.07	0.92
17G002i	4.4	1.6	3.1	0.24	3.2	3.9	n.a.	1.57	1.16
19G008i	4.5	1.6	4.8	0.23	3.2	n.d.	n.a.	1.90	1.18
19G009i	5.0	1.2	5.2	0.24	2.9	5.0	n.a.	1.89	1.23
18G009i	5.4	1.4	2.7	0.25	4.0	7.2	0.90	0.97	0.93
19G010i	4.4	1.7	4.7	0.26	3.9	6.8	n.a.	0.93	0.89
17G007i	4.2	2.1	4.6	0.24	4.4	6.1	n.a.	1.15	1.03
19G011i	6.1	1.8	4.8	0.27	3.6	6.4	n.a.	1.70	1.11
17G008i	4.8	1.6	4.0	0.26	3.2	5.7	n.a.	1.57	1.25
17G009i	4.2	1.5	3.4	0.18	5.0	8.4	n.a.	1.22	1.02
17G001i	4.9	n.d.	2.9	0.26	2.8	4.1	n.a.	1.67	1.25
17G010i	4.9	1.1	4.6	0.26	2.8	5.5	n.a.	1.44	1.16
12B119	6.9	1.8	3.8	0.25	3.7	5.9	n.a.	1.16	1.05
18G007i	7.5	1.0	5.5	0.25	4.3	6.9	0.96	0.84	0.89
18G006i	5.9	1.3	3.9	0.26	3.6	6.3	0.99	0.98	0.96
18G010i	5.1	1.6	3.9	0.25	3.9	6.8	1.07	0.97	0.97
19G012i	5.6	1.3	4.1	0.26	3.7	5.8	n.a.	1.47	1.04
19G013i	7.3	1.5	4.6	0.26	3.4	4.6	n.a.	1.36	1.01
18G016i	5.1	1.4	4.3	0.22	3.6	5.2	0.90	0.83	0.88
18G017i	6.0	1.3	4.5	0.21	3.9	5.3	1.09	0.45	0.73
18G018i	6.6	0.8	3.1	0.18	4.3	5.5	0.91	0.56	0.71
18G019i	4.7	0.6	2.7	0.17	4.2	8.6	0.88	0.89	0.87
19G014i	5.5	1.0	3.6	0.17	4.7	6.1	n.a.	0.46	0.60
18G020i	5.5	0.8	3.0	0.17	4.5	7.7	0.94	0.55	0.80
17G005i	3.8	n.d.	2.4	0.19	2.3	4.4	n.a.	1.69	1.42
19G015i	3.9	1.2	3.7	0.20	3.2	5.0	n.a.	2.52	1.17

n.d. – not detected (below detection limit). n.a. – not available (extended tricyclics were not run in the method). GI = Gammacerane/(gammacerane+C_{30}αβ-hopane). 2MHI = C_{31} 2α-methyl-hopane/(C_{31} 2α-methyl-hopane+C_{30} αβ-hopane). 3MHI = C_{31} 3β-methyl-hopane/(C_{31} 3β-methyl-hopane+C_{30} αβ-hopane). C_{30}DiaH/(DiaH+H) = C_{30} diahopane/(C_{30} diahopane+C_{30} αβ+βα hopane). HHI = 100*C_{35}(S+R)/Σ$C_{31–35}$(S+R) using 17α,21β(H)-homohopanes. 3MeHHI = 100*C_{35}(S+R)/Σ$C_{31–35}$(S+R) using 3β-methylhopanes. T = tricyclic terpanes (cheilanthanes).

Sample ID	G/ Cl	P/ Ok	Cl/ (Cl+Ok)	G/ (G+P)	GAIR	PAIR	MPI	%Rc (MPI)	MPDF	%Rc (MPDF)
19G016i	35	26	0.18	0.23	0.12	0.06	0.79	0.9	0.47	0.9
19G017i	18	11	0.26	0.36	0.14	0.35	0.56	0.7	0.44	0.8
18G014i	n.d.	n.d.	n.d.	0.40	2.25	1.62	0.71	0.8	0.37	0.7
18G015i	57	16	0.11	0.31	0.68	0.59	0.57	0.7	0.37	0.7
19G018i	65	49	0.29	0.35	1.72	0.98	0.65	0.8	0.35	0.6
19G001i	25	15	0.15	0.22	0.17	0.08	0.18	0.5	0.24	0.4
19G002i	n.d.	n.d.	n.d.	0.35	0.56	0.36	n.d.	n.d.	n.d.	n.d.
19G003i	9	6	0.13	0.20	0.29	0.12	0.52	0.7	0.29	0.5
19G004i	17	29	0.38	0.27	0.32	0.15	0.26	0.6	0.21	0.3
19G005i	71	43	0.16	0.24	1.22	0.50	0.66	0.8	0.33	0.6
19G006i	21	14	0.14	0.19	0.31	0.14	0.46	0.7	0.26	0.4
19G007i	9	5	0.13	0.22	0.07	0.04	0.51	0.7	0.31	0.5
12B117	12	8	0.14	0.20	0.18	0.08	0.58	0.7	0.31	0.5
18G001i	n.d.	n.d.	n.d.	0.29	0.18	0.14	0.54	0.7	0.38	0.7
18G002i	9	8	0.20	0.21	0.08	0.05	0.63	0.8	0.37	0.7
18G003i	4	2	0.34	0.52	0.04	0.07	n.d.	n.d.	n.d.	n.d.
18G004i	14	20	0.26	0.19	0.11	0.08	0.51	0.7	0.27	0.4
12B118	30	21	0.14	0.19	0.43	0.21	0.56	0.7	0.29	0.5
18G005i	16	16	0.19	0.19	0.14	0.09	0.60	0.8	0.33	0.6
18G008i	22	20	0.16	0.18	0.54	0.23	0.61	0.8	0.30	0.5
17G002i	43	34	0.14	0.17	0.61	0.29	0.65	0.8	0.35	0.6
19G008i	69	66	0.18	0.19	0.72	0.35	0.57	0.7	0.33	0.6
19G009i	45	40	0.17	0.19	1.10	0.51	0.58	0.8	0.36	0.6
18G009i	113	122	0.21	0.20	0.71	0.34	0.67	0.8	0.32	0.6
19G010i	12	6	0.19	0.33	0.07	0.14	n.a.	n.a.	n.a.	n.a.
17G007i	7	2	0.07	0.25	0.08	0.14	0.55	0.7	0.35	0.6
19G011i	42	31	0.13	0.17	0.82	0.39	n.a.	n.a.	n.a.	n.a.
17G008i	136	87	0.12	0.18	1.44	0.58	0.64	0.8	0.39	0.7
17G009i	8	3	0.07	0.14	1.03	0.41	0.61	0.8	0.37	0.7
17G001i	85	65	0.13	0.16	0.88	0.38	0.66	0.8	0.37	0.7
17G010i	125	87	0.12	0.17	0.97	0.41	0.66	0.8	0.37	0.7
12B119	54	34	0.10	0.15	0.32	0.17	0.72	0.8	0.37	0.7
18G007i	25	21	0.15	0.17	0.29	0.16	0.67	0.8	0.35	0.6
18G006i	68	50	0.17	0.21	0.57	0.32	0.73	0.8	0.37	0.7
18G010i	138	129	0.27	0.28	0.75	0.40	0.73	0.8	0.36	0.6
19G012i	23	20	0.18	0.20	0.14	0.09	n.a.	n.a.	n.a.	n.a.
19G013i	24	19	0.20	0.25	0.06	0.03	n.a.	n.a.	n.a.	n.a.
18G016i	30	16	0.13	0.22	0.08	0.04	0.56	0.7	0.32	0.6
18G017i	n.d.	15	n.d.	0.36	0.23	0.22	0.54	0.7	0.26	0.4
18G018i	22	13	0.25	0.36	0.16	0.09	0.75	0.8	0.40	0.7
18G019i	26	20	0.24	0.29	0.38	0.24	0.71	0.8	0.37	0.7
19G014i	22	24	0.40	0.38	0.25	0.13	n.a.	n.a.	n.a.	n.a.
18G020i	n.d.	n.d.	n.d.	0.46	0.22	0.16	0.77	0.9	0.40	0.7
17G005i	67	62	0.27	0.28	0.32	0.12	0.41	0.6	0.24	0.4
19G015i	221	417	0.45	0.30	1.08	0.56	n.a.	n.a.	n.a.	n.a.

n.d. – not detected (below detection limit). n.a. – not available. Cl = chlorobactane. Ok = okenane. G = $\Sigma C_{13–39}$ 2,3,6- trimethyl aryl isoprenoids (AI) and P = $\Sigma C_{13–39}$ 2,3,4-AI. GAIR = $\Sigma(C_{13–17})/\Sigma(C_{18–22})$ 2,3,6-AI. PAIR = $\Sigma(C_{13–17})/\Sigma(C_{18–22})$ 2,3,4-AI. MPI-1 = 1.5*(2MP+3MP)/(P+1MP+9MP). %Rc(MPI) = 0.6MPI-1+0.4. MPDF = (3-MP+2-MP)/(3-MP+2-MP+9-MP+1-MP). %Rc(MPDF) = 2.242*MPDF - 0.166.

Sample ID	% LA/ (LA+ hop)	% CA/ (CA+ hop)	% PS/ (PS+ hop)	% LA/ (LA+ DiaH)	% CA/ (CA+ DiaH)	% LA/ (LA+ cheil)	% CA/ (CA+ cheil)	% LA/ (LA+ gam)	% CA/ (CA+ gam)
19G016i	0.9	0.9	1.7	7.7	7.8	1.9	1.9	60.8	60.8
19G017i	1.0	0.8	1.8	9.0	7.2	2.2	1.7	55.2	49.3
18G014i	n.d.	n.d.	n.d.	n.d.	n.d.	n.d.	n.d.	n.d.	n.d.
18G015i	0.6	0.4	1.0	6.4	4.1	1.6	1.0	58.8	46.8
19G018i	0.3	0.7	1.0	2.8	6.8	0.6	1.5	57.1	76.7
19G001i	0.2	1.4	1.6	2.6	15.0	2.3	13.5	40.2	81.7
19G002i	n.d.	n.d.	n.d.	n.d.	n.d.	n.d.	n.d.	n.d.	n.d.
19G003i	0.6	0.9	1.5	6.6	9.7	6.7	9.8	56.5	66.4
19G004i	n.d.	1.2	1.2	n.d.	10.9	n.d.	12.0	n.d.	77.0
19G005i	0.6	1.8	2.4	5.1	14.4	2.8	8.2	26.2	52.5
19G006i	0.9	0.8	1.7	8.6	7.9	5.0	4.6	56.5	54.1
19G007i	0.4	1.4	1.7	4.8	14.5	3.5	10.9	44.6	73.1
12B117	0.4	1.3	1.6	3.2	10.2	2.3	7.9	31.8	61.2
18G001i	0.4	0.2	0.6	3.3	2.0	1.2	0.7	31.0	21.6
18G002i	1.2	0.3	1.5	10.1	2.7	9.2	2.4	57.4	24.8
18G003i	1.6	0.4	2.0	11.9	3.3	13.6	3.8	70.4	37.3
18G004i	1.6	0.4	2.0	11.5	3.1	11.5	3.1	67.3	33.8
12B118	2.1	0.5	2.5	12.3	3.2	6.0	1.5	74.5	41.1
18G005i	1.8	0.4	2.2	10.3	2.7	9.2	2.4	73.5	40.3
18G008i	1.6	0.7	2.2	8.8	3.8	7.4	3.2	72.2	51.5
17G002i	1.6	0.8	2.3	9.7	4.9	5.0	2.5	67.2	49.6
19G008i	1.4	0.8	2.2	8.5	4.7	4.2	2.3	67.6	52.9
19G009i	1.5	0.6	2.1	8.3	3.7	5.0	2.2	65.1	44.0
18G009i	1.6	0.8	2.3	8.4	4.5	6.3	3.3	64.3	47.9
19G010i	1.4	0.7	2.1	7.6	4.1	5.1	2.8	66.6	51.0
17G007i	1.6	0.9	2.5	9.8	5.5	6.4	3.6	69.1	54.8
19G011i	1.5	0.9	2.4	8.0	5.1	5.0	3.1	61.4	49.2
17G008i	1.7	0.8	2.5	9.6	5.0	4.8	2.4	68.1	51.3
17G009i	1.9	0.8	2.6	14.8	6.3	8.4	3.4	71.8	49.7
17G001i	1.1	1.0	2.1	6.7	5.9	3.1	2.7	57.8	54.5
17G010i	1.9	0.9	2.8	11.1	6.0	4.7	2.5	69.6	53.7
12B119	1.6	1.0	2.6	9.1	6.2	4.6	3.1	58.3	48.0
18G007i	1.4	0.9	2.3	7.5	5.1	6.5	4.4	52.8	42.5
18G006i	1.2	0.9	2.1	6.5	4.6	5.2	3.7	56.3	47.3
18G010i	1.4	1.1	2.4	7.3	5.7	5.1	4.0	62.8	56.4
19G012i	1.2	1.2	2.4	6.9	6.8	3.6	3.5	57.4	57.0
19G013i	1.2	1.1	2.2	6.4	6.0	3.2	3.0	48.9	47.2
18G016i	1.2	1.0	2.2	7.3	6.1	4.9	4.0	57.7	52.8
18G017i	0.9	0.9	1.8	6.2	6.0	6.0	5.8	47.7	46.5
18G018i	0.9	0.8	1.6	6.4	6.0	4.3	4.1	39.3	37.7
18G019i	0.7	0.6	1.3	5.3	4.8	4.3	3.9	43.1	40.5
19G014i	0.3	1.4	1.7	2.5	9.3	2.0	7.7	24.0	56.2
18G020i	0.4	0.5	0.8	2.8	3.4	2.5	3.0	25.4	29.4
17G005i	0.9	4.5	5.4	7.4	29.4	1.7	8.2	57.5	87.7
19G015i	0.3	2.7	3.0	2.5	17.1	0.8	6.0	33.6	80.3

n.d. – not detected (below detection limit). LA = $\Sigma peaks_{\mathbf{1\text{-}4}}$ lanostane. CA = $\Sigma peaks_{\mathbf{5–6}}$ cyclosterane. PS = LA+CA. Hop = dia($C_{29–35}$)+αβ($C_{27–35}$)+βα($C_{29–30}$) hopanes. DiaH = $\Sigma C_{29–35}$ diahopanes. Cheil = $\Sigma C_{19–25}$ cheilanthanes. Gam = gammacerane.

Sample ID	ArS/ (ArS+PS)	Mals/ (Mals+TAS)	Dals/ (Dals+TAS)	TAS/ (TAS+ArH)	ArS/ (ArS+ArH)
19G016i	0.98	0.06	0.16	0.67	0.72
19G017i	0.93	0.11	0.24	0.45	0.54
18G014i	n.d.	n.d.	0.04	0.91	0.92
18G015i	0.97	0.05	0.13	0.64	0.68
19G018i	0.97	0.03	0.09	0.51	0.55
19G001i	0.78	0.07	0.13	0.35	0.40
19G002i	n.d.	0.06	0.08	0.72	0.75
19G003i	0.81	0.12	0.19	0.35	0.42
19G004i	0.86	0.06	0.16	0.37	0.42
19G005i	0.93	0.05	0.16	0.57	0.62
19G006i	0.94	0.09	0.18	0.55	0.62
19G007i	0.79	0.11	0.20	0.34	0.42
12B117	0.91	0.06	0.27	0.51	0.59
18G001i	0.98	0.05	0.07	0.65	0.67
18G002i	0.98	0.13	0.20	0.55	0.63
18G003i	0.79	0.04	0.06	0.36	0.39
18G004i	0.92	0.06	0.08	0.55	0.58
12B118	0.95	0.10	0.12	0.68	0.73
18G005i	0.94	0.06	0.08	0.57	0.61
18G008i	0.96	0.06	0.10	0.66	0.70
17G002i	n.d.	n.d.	n.d.	n.d.	n.d.
19G008i	0.94	0.03	0.06	0.70	0.72
19G009i	0.97	0.04	0.08	0.72	0.74
18G009i	0.96	0.03	0.08	0.71	0.73
19G010i	0.79	0.04	0.06	0.48	0.50
17G007i	0.90	0.11	0.17	0.45	0.52
19G011i	0.94	0.04	0.10	0.66	0.69
17G008i	0.98	0.05	0.11	0.72	0.76
17G009i	0.92	0.11	0.19	0.56	0.63
17G001i	n.d.	n.d.	n.d.	n.d.	n.d.
17G010i	0.97	0.04	0.11	0.74	0.77
12B119	0.82	0.04	0.11	0.66	0.69
18G007i	0.97	0.02	0.07	0.67	0.69
18G006i	0.99	0.05	0.13	0.77	0.80
18G010i	0.98	0.01	0.02	0.90	0.90
19G012i	0.94	0.04	0.12	0.65	0.68
19G013i	0.96	0.04	0.12	0.68	0.71
18G016i	0.93	0.06	0.16	0.60	0.65
18G017i	0.85	0.08	0.21	0.38	0.46
18G018i	0.85	0.05	0.18	0.37	0.43
18G019i	0.87	0.03	0.12	0.43	0.47
19G014i	0.62	0.11	0.21	0.15	0.19
18G020i	0.60	0.05	0.10	0.18	0.20
17G005i	0.80	0.01	0.05	0.73	0.74
19G015i	0.97	0.01	0.03	0.86	0.86

n.d. – not detected. PS = LA+CA. ArS – sum of aromatic steroids, ArS = (C_{29}(S+R) Mals+C_{28}(S+R) Dals+$C_{26–27}$ TAS); Mals – C_{29} monoaromatic steroids, Dals – C_{28} diaromatic steroids, TAS – C_{26} triaromatic cholesteroids and 4-methylated C_{27} triaromatic cholesteroids. ArH – aromatic hopanoids, ArH = $\Sigma C_{32–35}$ benzohopanoids+$\Sigma C_{28–30}$(S+R) 28-nor regular monoaromatic 8,14-secohopanoids+$\Sigma C_{29–30}$ regular monoaromatic 8,14-secohopanoids.

Appendix A.2

Table: XRD data for LV09 drill core

Formation	Sample ID	Depth, m	Quartz	Pyrite	gypsum	microcline	orthoclase	dolomite	KNiAlSiO	Sanidine	Siderite	Illite	Hematite
Lynott	18G014i	279.35	56					15	3	26			
	18G015i	289.85	53			29		15	3				
Barney Creek	18G001i	393.7	39			35		22	4				
	18G002i	402.4	43					37	2	17			1
	18G003i	406.7	37			29		33					1
	18G004i	414.75	42			36		22					1
	18G005i	429.7	35				42	23					
	18G008i	443.7	56	2		35		6	1				
	17G002i	450.0	55	1				18	3	23			
	18G009i	461.83	45				38	16					2
	17G007i	470.7	30			30		39					1
	17G008i	477.0	40	20		36		4					
	17G009i	478.2	10					85			5		
	17G001i	485.0	40	12		31		13	3				
	17G010i	489.0	39	9		32		20					
	18G007i	494.5	43			22		33	2				
	18G006i	494.6	54	9	6		22	7	2				
	18G010i	498.88	57	18	5	18			2				
Cooley	18G016i	522.68	47			52							1
	18G017i	527.32	29					55		15			
	18G018i	542.61	30			32		37					1
Teena	18G019i	552.62	37			16		41	5				
	18G020i	561.5	24			27		50					
	17G005i	577.0	43	2		28		12	1			14	

Appendix A.3

Table: Biomarker ratios for GR7 drill core

Formation	Depth, m	% LA/ (LA+hop)	% CA/ (CA+hop)	GAIR	PAIR	Fe_{py}/ Fe_{HR}
Barney Creek	38.7	1.0	1.9	0.75	0.45	0.55
	41.8	1.1	1.5	0.47	0.37	0.52
	45.35	1.1	1.3	0.12	0.07	0.47
	47.55	1.0	1.2	0.53	0.27	0.58
	50.3	n.a.	n.a.	1.65	0.85	0.63
	67.14	n.a.	n.a.	1.8	0.94	0.63
	71.65	0.3	3.0	1.42	1.03	0.45
	77.20	n.d.	2.0	1.37	1.14	0.65
	82.95	n.d.	1.7	1.98	2.18	0.72
	90.30	n.d.	2.0	2.91	2.3	0.76
	101.60	0.6	6.8	3.16	2.68	0.71
	106.28	1.2	19.9	0.85	0.59	0.68
	116.0	1.3	6.3	1.27	0.65	0.62
	126.4	n.a.	n.a.	0.19	0.18	0.51
	151.1	2.1	11.7	1.42	0.73	0.56
	162.85	1.0	16.9	1.37	0.72	0.52
	180.0	1.3	12.0	1.37	0.94	0.68
	199.08	1.7	4.9	0.62	0.32	0.50
	209.6	0.5	18.6	n.a.	n.a.	n.a.
	218.1	n.d.	5.3	2.91	1.9	0.78
	238.8	n.d.	26.2	2.72	2.01	0.67
	252.9	n.d.	29.1	3.06	2.86	0.62
	328.8	n.a.	n.a.	0.86	2.06	0.54

n.d. – not detected (below detection limit). n.a. – not available. LA = $\Sigma peaks_{\mathbf{1\text{-}4}}$ lanostane. CA = $\Sigma peaks_{\mathbf{5\text{–}6}}$ protosterane. Hop = dia($C_{29–35}$)+αβ($C_{27–35}$)+βα($C_{29–30}$) hopanes. GAIR = $\Sigma(C_{13–17})/\Sigma(C_{18–22})$ 2,3,6-trimethyl aryl isoprenoids (AI). PAIR = $\Sigma(C_{13–17})/\Sigma(C_{18–22})$ 2,3,4-AI. Fe_{py} = pyrite iron. Fe_{HR} = highly reactive iron. Measurements for GAIR, PAIR and Fe_{py}/Fe_{HR} are from Nettersheim (2017). Protosteranes and hopanes are integrated by the author.

Appendix A.4

The annotated Python code to extract C_{30} DiaH/(DiaH+H) values.

```
# Extract C30 DiaH/(DiaH+H) values at d13C depths.
import numpy as np
import matplotlib.pyplot as plt
from sklearn.metrics import r2_score

# First trend (\sigma^13C,%)
depth1 = np.genfromtxt('trend1.dat')[:,0] #take the first column of
trend1.dat and save it as depth1
data1 = np.genfromtxt('trend1.dat')[:,1] #take the second column of
trend1.dat and save it as data1

# Second trend (C30 DiaH/(DiaH+H)
depth2=np.genfromtxt('trend2.dat')[:,0] #take the first column of
trend2.dat and save it as depth2
data2=np.genfromtxt('trend2.dat')[:,1] #take the second column of
trend2.dat and save it as data2

# Trend1 has 42 depth values, Trend2 has 45 depth values
# We will take the "42" same depth values of trend1 and extract the
information from trend2 at the same depth values. Loop below will do
that. np.interp() command does this:

''' One-dimensional linear interpolation. Returns the one-dimensional
piecewise linear interpolant to a function with given discrete data
points (xp, fp), evaluated at x. '''

# We take the depth1 values (depth1[i]) and give the x and y
coordinates where we want to do linear interpolation (depth2,data2).
This will give us the values on that exact depth (datainterp).
datainterp = np.zeros(42)
for i in range(0,42):
datainterp[i] = np.interp(depth1[i],depth2,data2)

#Save the new interpolated "red" C30 DiaH/(DiaH+H) data points into a
file.
new_points = np.array([depth1,datainterp]) # First column is depth,
second column is data points
np.savetxt('new_points.txt', new_points.T, fmt='%s') # save it to a
txt file
```

APPENDIX B

Supplementary material for Chapter 5

Appendix B.1

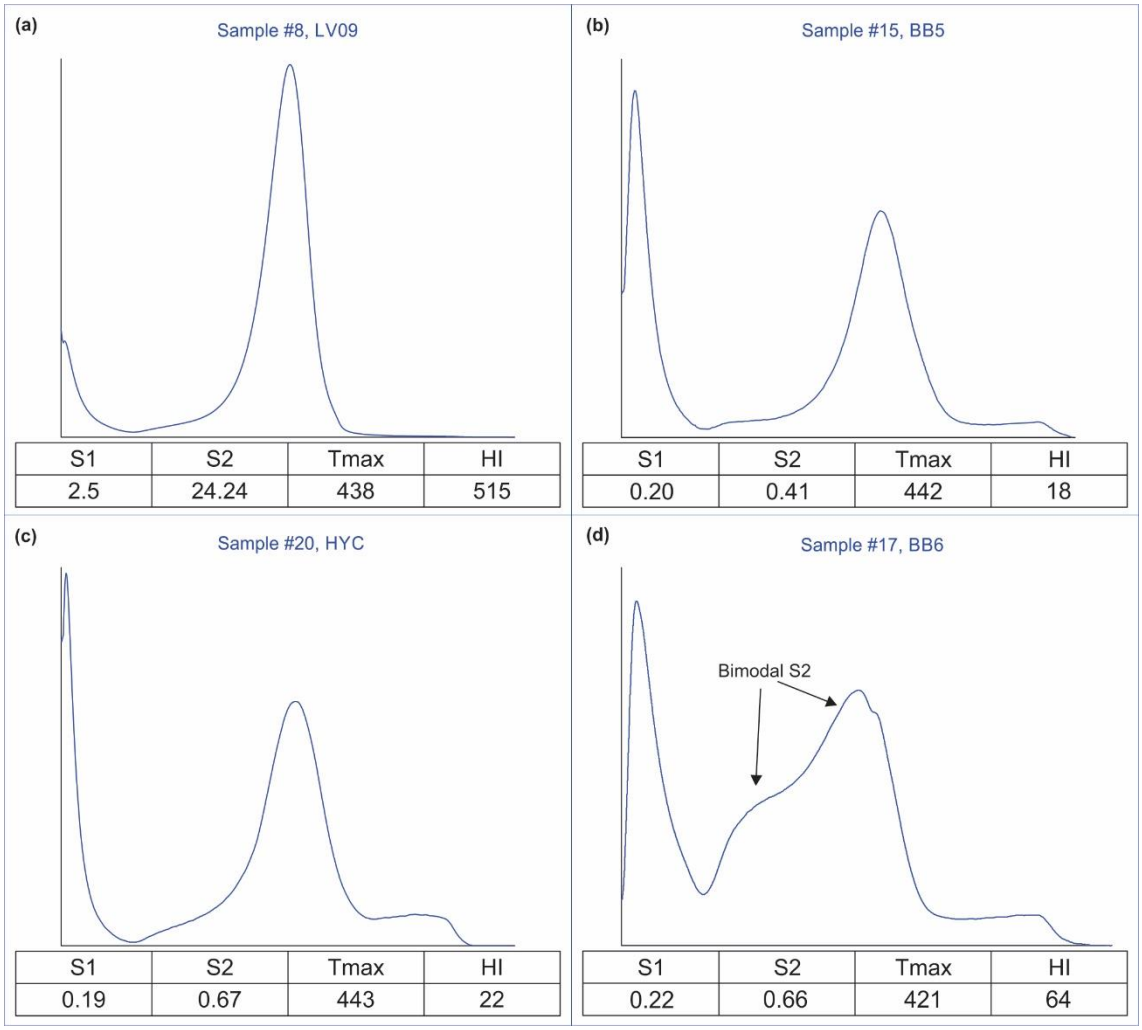

S1	S2	Tmax	HI
2.5	24.24	438	515

S1	S2	Tmax	HI
0.20	0.41	442	18

S1	S2	Tmax	HI
0.19	0.67	443	22

S1	S2	Tmax	HI
0.22	0.66	421	64

Supplementary Figure 1. Rock-Eval pyrograms of representative samples from (a) LV09, (b) BB5, (c) HYC and (d) BB6 drill cores. BB6 samples display broad bimodal S2 peaks.

Appendix B.2 The annotated Python code and input parameters

C	m0	d13C	kh	ki
			0.001	
1	240	-31.9	0	0
2	240	-31.9	0	0
3	240	-31.9	0	0
4	240	-31.9	0.002	0.28892
5	240	-31.9	0.004243	0.28892
6	240	-31.9	0.006928	0.28892
7	240	-31.9	0.01	0.28892
8	240	-31.9	0.013416	0.28892
9	240	-31.9	0.017146	0.28892
10	240	-31.9	0.021166	0.28892
11	240	-31.9	0.025456	0.28892
12	250	-31.8	0.03	0.28892
13	262.191	-31.7	0.034785	0.28892
14	463.6134	-31.56	0.039799	0.28892
15	924.4207	-31.63	0.045033	0.28892
16	1583.143	-31.39	0.050478	0.28892
17	2159.086	-31.04	0.056125	0.28892
18	2521.857	-30.85	0.061968	0.28892
19	2431.975	-30.67	0.068	0.28892
20	2308.859	-30.56	0.074216	0.28892
21	2061.839	-30.54	0.08061	0.28892
22	1712.221	-30.78	0.087178	0.28892
23	1505.187	-30.69	0.093915	0.28892
24	1574.725	-30.69	0.100817	0.28892
25	1143.293	-30.97	0.10788	0.28892
26	1069.196	-30.49	0.1151	0.28892
27	676.6984	-31.31	0.122474	0.28892
28	545.9536	-30.44	0.13	0.28892
29	400.8278	-30.96	0.137674	0.28892
30	284.201	-30.45	0.145492	0.28892
31	172.5726	-31.41	0.153454	0.28892
32	104.7895	-31.41	0.161555	0.28892
33	63.63028	-31.41	0.3	0.28892

```
# -*- coding: utf-8 -*-
"""
Created on Fri May 8 13:19:08 2020
@author: Jochen Brocks
"""
import numpy as np
import pandas as pd
""" Global variables and functions """
VPDB = 0.0112372
def R13_from_d13(d13C): # R13 = 13C/12C
return (d13C/1000+1)*VPDB
def d13_from_R13(ratio):
return (ratio/VPDB-1)*1000
def F13_from_d13(d13C): # F13 = 13C/(12C + 13C)
ratio = R13_from_d13(d13C)
return ratio/(1+ratio)
def F13_from_R13(ratio):
return ratio/(1+ratio)
""" Import parameters from excel file and create dataframes """
Parameters_file = "Input data and results graphs.xlsx"
Empty_dataframe_file = "Empty Dataframe.xlsx"
Target_file = "Output data.xlsx"
# Read excel sheets with starting parameters
df_parameters = pd.read_excel(Parameters_file, sheet_name='Sheet1')
# Generate empty DataFrames for all outputs
# 12C moles of n-alkanes through time
df_n_12C = pd.read_excel(Empty_dataframe_file, sheet_name='n_12C')
# 13C moles of n-alkanes through time
df_n_13C = pd.read_excel(Empty_dataframe_file, sheet_name='n_13C')
# 12C moles of isoalkanes through time
df_i_12C = pd.read_excel(Empty_dataframe_file, sheet_name='i_12C')
# 13C moles of isoalkanes through time
df_i_13C = pd.read_excel(Empty_dataframe_file, sheet_name='i_13C')
# d13C of n-alkanes
df_d13C_n = pd.read_excel(Empty_dataframe_file, sheet_name='d13C_n')
# d13C of isomerization products
df_d13C_i = pd.read_excel(Empty_dataframe_file, sheet_name='d13C_i')
# masses of n-alkanes through time (in C-moles)
df_n_masses = pd.read_excel(Empty_dataframe_file,
sheet_name='n_masses')
# masses of i-alkanes through time (in C-moles)
df_i_masses = pd.read_excel(Empty_dataframe_file,
sheet_name='i_masses')
# total moles as consistency check (total moles need to stay constant)
df_all_masses = pd.read_excel(Empty_dataframe_file,
sheet_name='all_masses')
# IMPORTANT: moles 'm' in the excel sheet are given in moles of carbon
# atoms. Thus, to get moles of molecules: moles(molecules) = m/C
(where
# C is chain length). The rate constants kh and ki refer to the
reaction speed
# per mole of molecules. Thus, to get the reacted mass (moles of
carbon) per
# time unit t: product_mass = moles * k * t * C = (m/C) * k * t * C =
m * k * t
# Thus, it is crucial that the rate constants in the Excel sheet
reflect the
# reaction rate of molecules. Any chain-length dependence of k is
# included in the Excel file k data.
""" Adjustable variables """
```

```
#Switching different mechanisms on and off
mid_chain_cleavage = True
branching = False # a percentage of cleavage products is isomerized
and removed
if branching:
br = 4
else:
br = 1.0
isomerization = False
ramping = False
# td = rate at which kn and ki increase per iteration cycle
# to e.g. simulate the temperature dependence of k
if ramping:
td_h = 2.7 #start proportion
td_i = 0.07 # start proportion
td_h_rate = 0.8
td_i_rate = 1.2
else:
td_h = 1
td_i = 1
td_h_rate = 1
td_i_rate = 1
# Introducing time dependence for competing reactions
# The rate constants k are in units of 1/sec. 'timesteps' determines
the size
# of the time step for each iteration.
timesteps = 4
# Number of reaction cycles plus one
iterations = 20+1
# Range of n-alkane chain lengths considered in model
C_min = 3
C_max = 33
# fractionation factor for mid-chain homolytic (h) cleavage of n-
alkane chain
alpha_h = 0.994
# fractionation factor for isomerization (i) of n-alkanes
alpha_i = 0.994
""" Variable preparation """
# Write starting moles for t = 0 into the 13C and 12C DataFrames
df_n_12C.iloc[:,1] = df_parameters['m0']*(1-
F13_from_d13(df_parameters['d13C']))
df_n_13C.iloc[:,1] =
df_parameters['m0']*F13_from_d13(df_parameters['d13C'])
# Create dataframe for prelim cracking data: total moles, 12C, 13C,
F13
df_prelim = pd.DataFrame(np.zeros((C_max+1,4)),columns =
['moles','12C',
'13C','F13'])
# j is the counter for the chain lengths of cleavage products
df_prelim['j'] = np.arange(C_max+1)
# Set reaction time to zero and record it
t = 0
df_n_12C.iat[0,1] = t
""" Start of time cycles """
for i in range(1,iterations):
# Make copy of carbon moles from t to t + 1
df_n_12C.iloc[:,i+1] = df_n_12C.iloc[:,i]
df_n_13C.iloc[:,i+1] = df_n_13C.iloc[:,i]
df_i_12C.iloc[:,i+1] = df_i_12C.iloc[:,i]
df_i_13C.iloc[:,i+1] = df_i_13C.iloc[:,i]
```

```
t = t + timesteps
df_n_12C.iat[0,i+1] = t
print('Cycle =',i)
""" Start of carbon number cycles """
for C in range(C_max, C_min-1,-1):
# Get moles and isotopes of reactants
m13 = df_n_13C.iat[C,i]
m12 = df_n_12C.iat[C,i]
m = m13 + m12 # carbon moles of reactant in pool
# R13 and F13 are the isotopic ratio and isotopic fraction of
# the reactant respectively. Assuming an even distribution of isotopes
# across the molecule, this is also the isotopic composition of
# each carbon position in the molecule.
R13_uncleaved = m13/m12
F13_uncleaved = m13/m
""" Mid-chain cleavage generating two shorter n-alkanes """
if mid_chain_cleavage:
kh = df_parameters.at[C,'kh']
mh = m*kh*timesteps * td_h # C moles of cleavage products
# Cleavage of an n-alkane forms shorter products with 2 to C-2
# carbon atoms in a total of C-3 different shorter-chain products.
# The following equation computes the fraction of carbon moles for
# each product with length j that is generated in this process:
# For instance C-3 = 7 molecules nC10 are cleaved into 2*C2 + 2*C3
#+ 2*C4 + 2*C5 + 2*C6 + 2*C7 +2*C8. These are nc = (C-3)*C produced
# moles of carbon (70 atoms).
nc = (C-3)*C
# Each product has the same molar concentration. The carbon-mole
# fraction of each product with chain length j is then 2*j/nc, and
# the number of generated carbon moles is
df_prelim.loc[2:C-2,'moles'] = mh*2*df_prelim.loc[2:C-2,'j']/nc
# Isotopic composition of carbon atoms adjacent to cleavage point
F13_cleaved = F13_from_R13(R13_uncleaved * alpha_h)
# The isotopic composition of an n-alkane product with j carbon
# atoms is [(j-1)*F13_uncleaved + 1*F13_cleaved] / j.
# The following computes for each fragment j the amount of
# 13C and 12C in total moles.
df_prelim.loc[2:C-2,'F13'] = ((df_prelim.loc[2:C-2,'j']-1)*
F13_uncleaved + 1*F13_cleaved) / df_prelim.loc[2:C-2,'j']
df_prelim.loc[2:C-2,'13C'] = df_prelim.loc[2:C-2,'moles']*\
df_prelim.loc[2:C-2,'F13']
df_prelim.loc[2:C-2,'12C'] = df_prelim.loc[2:C-2,'moles']*\
(1-df_prelim.loc[2:C-2,'F13'])
# Add the products to the dataframes
# The reactants go from 2 to C-2 (i.e. if C=33, from 2 to 31)
# Careful: this is iloc[2:C-1], but loc[2:C-2]
if branching:
df_n_12C.iloc[2:C-1,i+1] += (1-br)*df_prelim.loc[2:C-2,'12C']
df_n_13C.iloc[2:C-1,i+1] += (1-br)*df_prelim.loc[2:C-2,'13C']
df_i_12C.iloc[2:C-1,i+1] += br*df_prelim.loc[2:C-2,'12C']
df_i_13C.iloc[2:C-1,i+1] += br*df_prelim.loc[2:C-2,'13C']
else:
df_n_12C.iloc[2:C-1,i+1] += df_prelim.loc[2:C-2,'12C']
df_n_13C.iloc[2:C-1,i+1] += df_prelim.loc[2:C-2,'13C']
# Add up the generated 12C and 13C and subtract from reactant
df_n_12C.iloc[C,i+1] -= df_prelim.loc[2:C-2,'12C'].sum()
df_n_13C.iloc[C,i+1] -= df_prelim.loc[2:C-2,'13C'].sum()
""" End-chain isomerization removing n-alkanes from pool """
if isomerization:
# rate constant for end-chain isomerization
```

```
ki = df_parameters.at[C,'ki']
# moles of isomerized product
mi = m*ki*timesteps * td_i # computes total moles cleavage product
# Isotopic composition of C atoms at cleavage point
F13_isomerized = F13_from_R13(R13_uncleaved * alpha_i)
# Isotopes of the product containing 2 fractionated C-atoms
F13 = ((C-2)*F13_uncleaved + 2*F13_isomerized) / C
# Add the isomerized depleted product to the isomers dataframes
df_i_13C.iat[C,i+1] += mi * F13
df_i_12C.iat[C,i+1] += mi * (1-F13)
# Remove the isomerized n-alkane from the parent pool
df_n_13C.iat[C,i+1] -= mi * F13
df_n_12C.iat[C,i+1] -= mi * (1-F13)
# Write isotope values into d13C sheet
df_d13C_n.iloc[C,i+1] = d13_from_R13(df_n_13C.iloc[C,i+1]/
df_n_12C.iloc[C,i+1])
td_h *= td_h_rate
td_i *= td_i_rate
""" Preparing data for reporting """
# Creates data frame with total moles
df_n_masses.iloc[1:C_max+1,1:iterations+1] =
df_n_13C.iloc[1:C_max+1,1:
iterations+1]+df_n_12C.iloc[1:C_max+1,1:iterations+1]
# Add a DataFrame 'df_norm' where moles are normalized to the highest
# n-alkane peak in the carbon number range nC13 to nC31 for each cycle
df_norm = df_n_masses.copy()
df_norm.loc['Max'] = df_norm.iloc[13:31+1,1:].max()
df_norm.iloc[1:C_max+1,1:] *= 100/df_norm.loc['Max',1:]
# Add a Column 'Remains%' with precentage n-alkanes remaining
df_n_masses['Remains%'] =
df_n_masses.iloc[:,iterations]/df_n_masses.iloc[:,1]\
*100# Masses of generated isomers
df_i_masses.iloc[1:C_max+1,1:iterations+1] =
df_i_13C.iloc[1:C_max+1,1:
iterations+1]+df_i_12C.iloc[1:C_max+1,1:iterations+1]
# Add percentage of nC13 to nC31 that are remaining (for comparison
with BCF)
df_norm.loc['Max',iterations-1] = 'nC13-31% remaining'
df_norm.loc['Max',iterations] =
100*df_n_masses.loc[13:31,iterations].sum()/\
df_n_masses.loc[13:31,1].sum()
# Masses of isomerization products
df_i_masses.iloc[1:C_max+1,1:iterations+1] =
df_i_13C.iloc[1:C_max+1,1:
iterations+1]+df_i_12C.iloc[1:C_max+1,1:iterations+1]
# Creates dataframe with d13C values
df_d13C_n.iloc[1:C_max+1,1:iterations+1] = d13_from_R13(df_n_13C.iloc[
1:C_max+1,1:iterations+1]/df_n_12C.iloc[1:C_max+1,1:iterations+1])
df_d13C_i.iloc[1:C_max+1,1:iterations+1] = d13_from_R13(df_i_13C.iloc[
1:C_max+1,1:iterations+1]/df_i_12C.iloc[1:C_max+1,1:iterations+1])
# Creates dataframe of sum of all masses to keep tally of reactants
and
# products to varify that the end products maintain mass and isotope
balance.
df_all_masses.iloc[1:C_max+1,1:iterations+1] =
df_n_masses.iloc[1:C_max+1,1:
iterations+1]+df_i_masses.iloc[1:C_max+1,1:iterations+1]
""" Writing results to Excel file """
# Create new excel file with multiple sheets / will overwrite old one
with
```

```
# same name.
# Create a Pandas Excel writer using XlsxWriter as the engine.
writer = pd.ExcelWriter(Target_file, engine='xlsxwriter')
# Write each dataframe to a different worksheet. Exclude index column.
df_n_12C.to_excel(writer, sheet_name='n_12C', index = False)
df_n_13C.to_excel(writer, sheet_name='n_13C', index = False)
df_i_12C.to_excel(writer, sheet_name='i_12C', index = False)
df_i_13C.to_excel(writer, sheet_name='i_13C', index = False)
df_n_masses.to_excel(writer, sheet_name='n_masses', index = False)
df_i_masses.to_excel(writer, sheet_name='i_masses', index = False)
df_d13C_n.to_excel(writer, sheet_name='d13C_n', index = False)
df_d13C_i.to_excel(writer, sheet_name='d13C_i', index = False)
df_all_masses.to_excel(writer, sheet_name='all_masses', index = False)
df_norm.to_excel(writer, sheet_name='normalized', index = False)
# Close the Pandas Excel writer and output the Excel file.
writer.save()
```

APPENDIX C

Supplementary material for Chapter 6

Appendix C

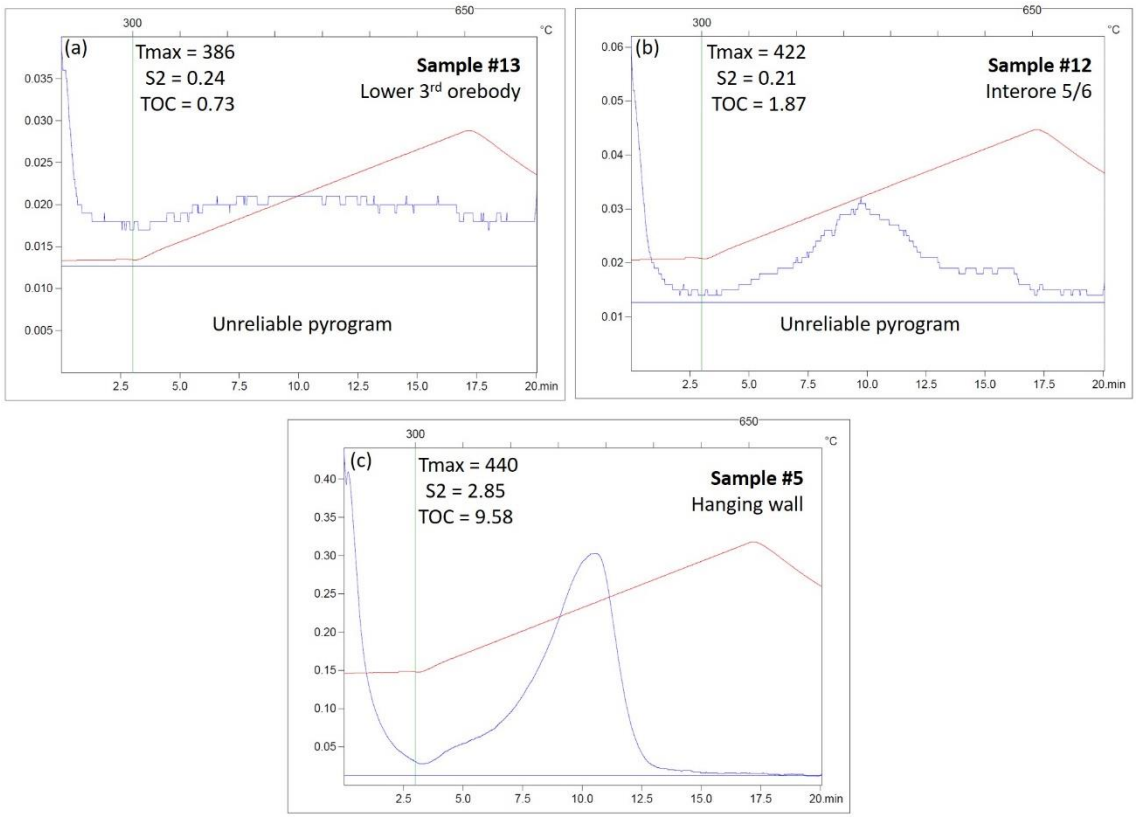

Supplementary Figure 1. Representative Rock-Eval pyrograms of kerogen concentrates from the (a, b) ore zone and (c) hanging wall.

APPENDIX D

Supplementary material for Chapter 7

Appendix D

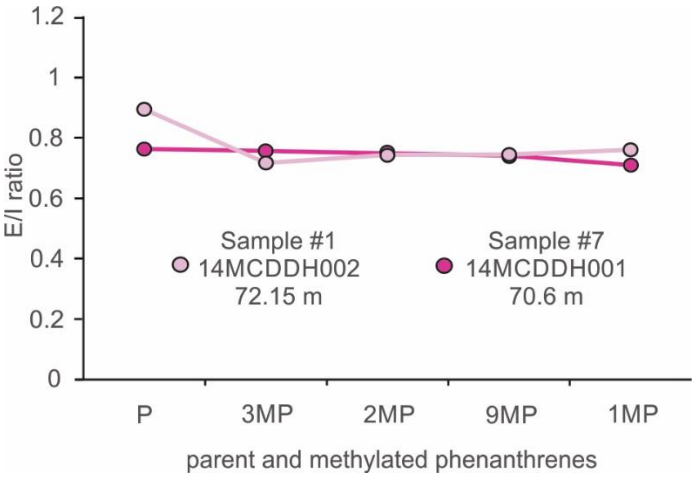

Supplementary Figure 1. Exterior/interior (E/I) ratios of parent (P) and methylated (MP) phenanthrenes for samples #1 and #7. Phenanthrenes were considered indigenous, since E/I values were close to 1 in clean samples (#7) but also in surficially contaminated samples (#1).